

Utilizing malachite green derivatives to diversify fluorogen-activating proteins (FAPs)' applications

A Dissertation by

Jianjun He

Submitted to the Faculty of the

Department of Chemistry, Carnegie Mellon University

in partial fulfillment of the requirements for the degree of

DOCTOR OF PHILOSOPHY

April 26, 2016

Acknowledgement

The past five-year of Ph.D. study has been one of the most exciting experiences in my life, which are highlighted by the continuous flow of inspiration, excitement and support. Firstly, I would like to express my sincere gratitude to my advisor Dr. Marcel P. Bruchez for his continuous support of my Ph.D study and related research, for his instruction, patience, and motivation. His guidance helped me in all the time of graduate research and writing of this thesis. His enthusiasm towards science and life has always been the inspiration for me, which is critical to shape my scientific thinking and experimental performance.

I would like to thank Dr. Danith Ly, Dr. Kevin Noonan and Dr. Alexander Deiters for being on my committee, for helpful discussion, comments and guidance on my research and thesis writing.

My sincere thanks also go to the former and current members of Bruchez's lab: Dr Yi Wang, Dr. Cheryl Telmer, Dr. Qi Yan, Dr. Saumya Saurabh, Dr. Anmol Grove, Dr. Suvrajit Maji, Dr. Richa Verma, Dr. Xiaohong Tan, Christopher Pratt, Matharishwan Naganbabu, Alexandra Carpenter, Lydia Perkins, Taylor Canady, Jonathan Dewed and Dmytro Kolodieznyi. I would like to express my great thanks to Dr. Alan Waggoner and the colleagues from Molecular Biosensor and Imaging Center (MBIC): Dr. Brigitte Schmidt, Dr. Chris Szent-Gyorgyi, Dr. Byron Ballou, Dr. Haibing Teng, Dr. Lauren Ernst, Dr. Greg Fisher, Dr. Matthew J. Saunders, Dr. Ming Zhang, Susan Andreko, Yehuda Creeger and Allison Dempsey.

I would also like to appreciate my collaborators: Dr. Simon Watkins, Dr. Gregory A. Gibson, Dr. Claudette M St Croix, Dr. Michael Tsang, Dr. Maria A. Missinato, Dr. Ezenwa Onuoha at University of Pittsburgh.

Last but not the least, I would like to thank my friends and my family for supporting me throughout writing this thesis and my life in general. They are very important in my life for sharing and encouraging.

Abstract

The field of cell imaging has been greatly advanced through the use of genetically encoded fluorescent probes. By genetically expressing to proteins of interest, fluorescent proteins have enabled noninvasively imaging of live cells to study protein-protein interaction, protein trafficking and protein expression and localization. In our group, we are dedicated to the development of protein reporters (FAPs) that can activate fluorescence from originally dark molecules (fluorogens). Among these fluoromodules, FAP_{dL5**} is a 25 kDa binder for malachite green (MG) derivatives that functions throughout living cells with thousands fold fluorescence activation and a low-picomolar dissociation constant. With rational designed MG derivatives, distinct applications have been found in single molecule imaging, physiological pH measurements and protein detection as recombinant affinity probes. However, in previous applications, developments of functionalized MG derivatives were focused on energy-transfer pairs which a donor that signals the environmental change is usually covalently linked to MG molecule. Little modification has been done with MG chromophore itself.

In this thesis, we explored the effects brought by introduction of different modifications on MG. First, by varying the charge of the linker, we have proposed and synthesized a series of MG derivatives with different net charge that directly alters the cell permeability. Secondly, a series of fluorinated MG derivatives were synthesized to investigate fluorination effect on spectra and affinity of MG-dL5**. Thirdly, a number of MG analogues with distinct absorption spectra were made to serve the purpose of multi-color imaging. Finally, a heavy-atom substituted MG (MG-2I) was made, which greatly increases singlet oxygen quantum yield upon binding to dL5**. This MG-2I/dL5** complex enables protein inactivation and targeted cell killing and rapid targeted lineage ablation in living larval and adult zebrafish.

Table of Content

Abstract

Chapter 1----- Fluorescence imaging and fluorogen activating proteins

Chapter 2----- Charge dependent cell permeability and specificity of Malachite Green derivatives

Introduction

Characterization of charged MG derivatives

Charge-dependent cell permeability

Experimental details

Chapter 3----- Study of fluorinated malachite green

Introduction

Characterization of fluorinated MG derivatives with dL5**

Experimental details

Chapter 4----- From One, Many: Structurally derived malachite green analogues for multicolor cell labeling using dL5**

Introduction

Characterization of MHN derivatives with dL5**

Dual-color imaging of FAP-BK α HEK293 cells

Experimental details

Chapter 5----- MG-2I/dL5** as a targetable and activatable photosensitizer

Introduction

Synthesis route for MG-2I

Characterization of MG-2I/dL5** complex

FAP-TAPs mediated CALI of the PLC δ 1 PH domain

FAP-TAPs mediated cellular photoablation

FAP-TAPs mediated cardiac ablation in larval zebrafish

Targeting FAP-TAPs to selective ablate cancer cells

Chapter 6----- Thesis summary and future directions

Appendix

Abbreviations used:

NIR: near-infrared;

GFP: green fluorescent protein;

FAP: fluorogen activating protein;

scFv: single-chain variable fragment

MG: malachite green;

EM: electron microscopy;

FRET: Förster resonance energy transfer

TM: transmembrane

ROS: reactive oxygen species;

PS: Photosensitizer;

PDT: photodynamic therapy;

TAPs: targetable and activatable photosensitizer;

CALI: chromophore-assisted light inactivation;

λ_{\max} : the extinction coefficient of the maximum absorption peak;

λ_{ex} : the maximum excitation peak of the complex;

ϵ : extinction coefficient;

λ_{em} : the maximum emission peak of the complex;

K_d : dissociation constant;

Φ_F : fluorescence quantum yield;

Φ_{Δ} : singlet oxygen quantum yield;

AR: activation ratio;

Chapter 1: Fluorescence imaging and fluorogen activating proteins

Background

In order to address many of the fundamental and challenging questions in life science, scientists are often required to observe such relevant key processes at a sensitivity level down to single molecules (1-5 nm), within a functioning, living cell¹⁻³. Fluorescence imaging provides an exceptional approach in studies of sub-cellular structure or cellular events because of its high sensitivity, vast flexibility and minimal perturbations⁴⁻⁸. With the continuous emergence of both new fluorescent probes and microscopic approaches, the resolution and timescales acquired by fluorescence imaging have been greatly advanced⁹⁻¹¹, making fluorescence imaging an indispensable technology in bringing molecules of importance into the light (Figure 1.1)^{12,13}.

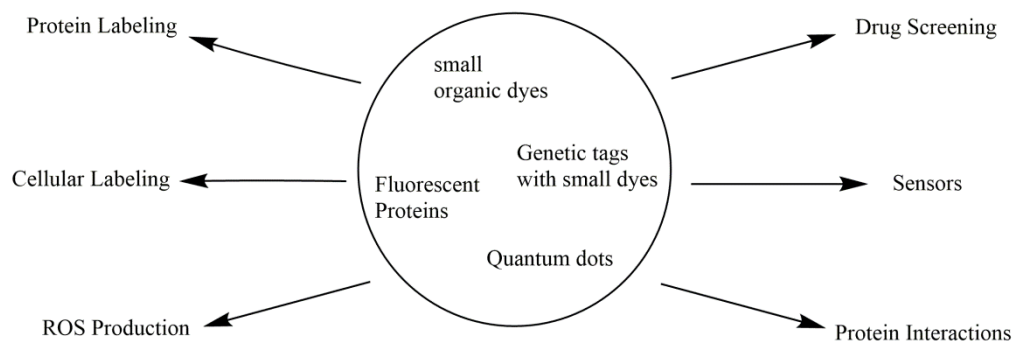


Figure 1.1: Fluorescent probes and their applications in molecular biology, chemical biology and cell biology.

Small organic dyes

Originally, fluorescent tools were mainly small synthetic organic dyes (Figure 1.2) used as a mean to visualize locations of cellular compartments¹⁴, or as a probe to signal concentrations of metal ions¹⁵, change of pH¹⁶, enzyme activities¹⁷, and reactive oxygen species¹⁸ and so on.

Precisely imaging proteins of interest is often achieved by attaching the fluorophore to an antibody or peptide¹⁹⁻²¹ that can be specifically recognized by their protein partners since, except

in rare cases, the fluorophore itself lacks protein-binding specificity^{22,23}. Luckily, with countless functionalized fluorescent compounds and rapidly developed conjugation methods in the field, direct attachment has been adapted to a wide range of applications in labeling target proteins, including fluorophores such as BODIPY, rhodamine, Alexa dyes and cyanine dyes^{14,24,25}. These small organic fluorescent dyes offer different spectral properties, molecular brightness and photostability and are very useful tools for target labeling from cultured cells, tissue slices to whole animal models²⁶. However, this labeling approach is often limited to specific applications such as biochemical protein-protein interaction or extracellular protein trafficking, which do not require delivery of conjugates into cells, a fundamental barrier to broader use of labeled proteins or peptides.

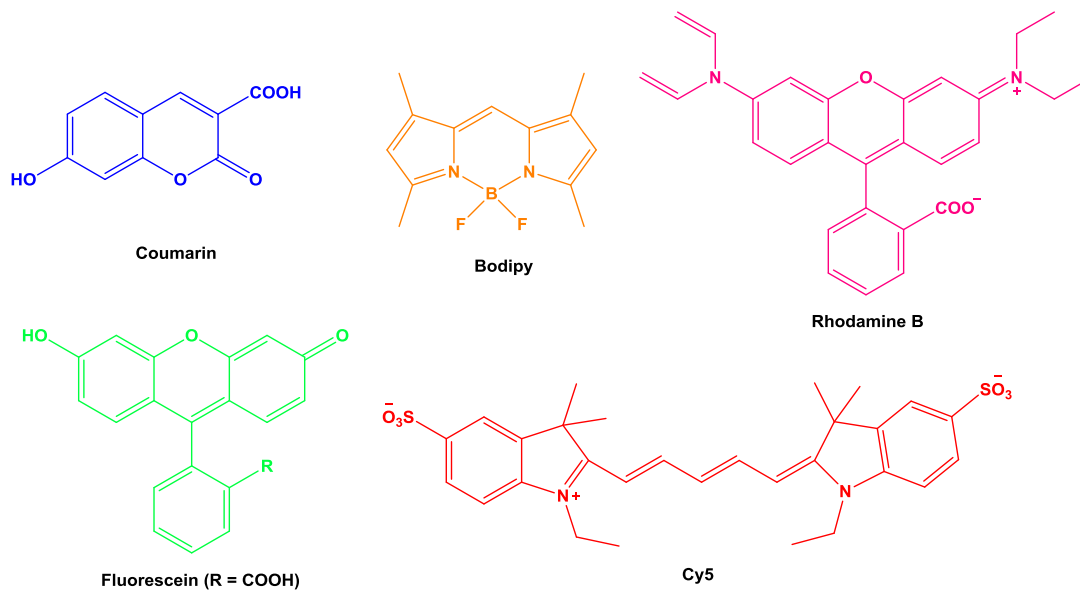


Figure 1.2: Representative core structures of commonly used small organic fluorophores including coumarin, fluorescein, BODIPY, rhodamine, and Cy5.

Fluorescent proteins

Later, with the revolutionary discovery and re-engineering of green fluorescent protein (GFP) from jellyfish *Aequorea victoria*, biologists realized specific labeling by genetically fusing the fluorescent protein to the protein of interest²⁷⁻²⁹. Two features make GFP an especially powerful

labeling tool: GFP derived fluorescent proteins are relatively stable and form the chromophore through an autocatalytic cyclization that requires no exogenous cofactors³⁰; and the fusion of GFP to a protein does not usually alter its function or location, which enabled researchers to use GFP in living systems to study cell dynamics and development⁸. In addition, with different colors available from various fluorescent proteins engineered from laboratory directed evolution³¹, fluorescent proteins have been widely used in cell and molecular biology as reporters of expression to study protein trafficking and signaling^{32,33}. Moreover, with structure-guided, site-directed mutagenesis, many fluorescent proteins that are responsive to physiological changes have been successfully developed, such as pH-sensitive pHluorins³⁴ that monitors vesicle exocytosis and recycling, photosensitizing KillerRed³⁵ that can inactivate protein and kill cells, and calcium indicator GCaMP6³⁶ that can track neuronal activity. Despite tremendous efforts and successes in the development of fluorescent proteins, the fundamental limitations in terms of brightness and emission wavelength are still desired to be improved³⁷.

Hybrid Tags

Alternatively, genetic targeting of fluorescent reporters can be achieved through hybrid approaches, where small molecules can be covalently targeted to genetically expressed proteins on or in the cells, either by site-specific reaction or enzymatic recognition^{38,39}. In this way, the ‘turn-on’ fluorescent signal of targeted cellular molecules is activated by adding the small molecules. Hybrid tags including Halo-tag⁴⁰, SNAP-tag⁴¹, and tetracysteine tags⁴² often provide more functional diversity compared to fluorescent proteins due to the versatility of small synthetic molecules. For example, in the tetracysteine-biarsenical hybrid system, a genetically targetable small peptide (12 amino acids) containing a tetracysteine motif that binds FIASH and ReAsH with picomolar affinity have been used to pulse-chase label new copies of proteins⁴³, to

correlate EM localization⁴⁴ and to inactivate proteins of interest using chromophore-assisted light inactivation (CALI)⁴⁵. However, these tags typically require high substrate concentrations (> 1 μM), which require extensive wash-off of unbound fluorophores for high signal-to-background imaging.

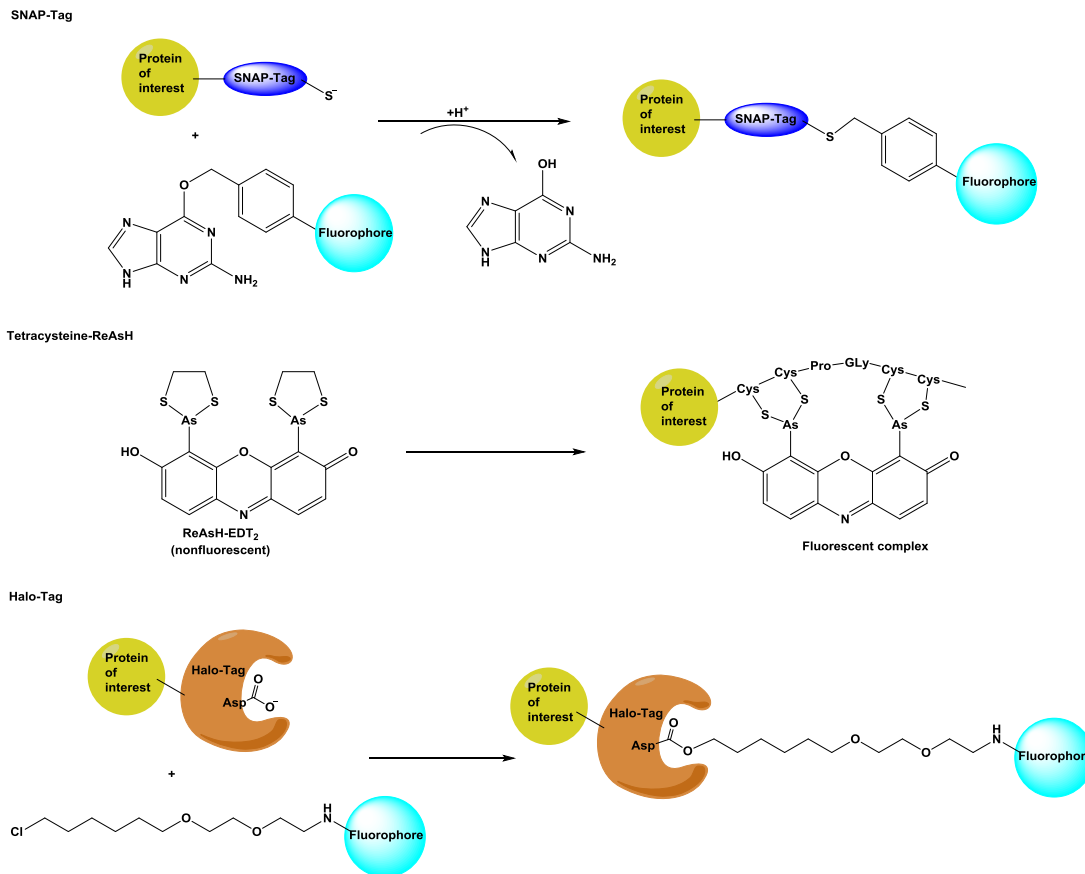


Figure 1.3: Examples of commonly used hybrid tags and their reaction mechanisms.

Nanoparticles

However, two essential properties are still worthy of improvement in fluorescence imaging: brightness and photostability⁷, which would improve the spatial and temporal resolution of fluorescence microscopy. For example, the signaling between neuronal synaptic vesicles (40 nm in size) happens within milliseconds⁴⁶, which requires super resolution microscopies such as stimulated emission depletion (STED) microscopy⁴⁷ and stochastic optical reconstruction

microscopy (STORM)⁴⁸ coupling with suitable fluorescent probes to visualize. Nanoparticles such as semiconducting polymer dots, quantum dots and gold nanoparticles typically have superior brightness and photostability than those of molecular probes^{49,50}. Especially, quantum dots which are nanoscale semiconductor (~1-6 nm) particles with spectral properties that are tunable as a function of particle size and shape for a given material, have been estimated to be 20 times brighter and 100 times more stable than conventional fluorescent reporters⁵¹. Nanoparticles have found successful applications in super-resolution microscopies⁵², multimodal imaging (combination of fluorescence imaging with other methods such as MRI, drug delivery and photodynamic therapy)^{53,54} and intracellular protein labeling^{5,55}, yet they are large in size and require conjugation to protein-targeting molecules, a fact that restricts their practical applications for many experiments.

Fluorogen Activating Proteins (FAPs)

In our group, we have developed novel genetically encoded protein reporters called fluorogen activating proteins that can specifically bind and activate originally non-fluorescent chromophores (fluorogens) to fluoresce⁵⁶. Compared to previous imaging methods (summarized in Table 1.1), the advantage of such technology is that both FAP and fluorogen are non-fluorescent, where only the binding of the complex results in a significant change in the fluorescence brightness, which enables selective ‘switch-on’ of fluorescence without removal of the fluorogenic dyes. A key parameter to assess fluorogenic imaging system is the ‘activation ratio’ (AR)⁵⁷, which is composed of the changes in fluorescence quantum yield ($\Delta\Phi_F$), spectral shift and extinction coefficient ($\Delta\epsilon_{ex}$) between free and bound dye under the same excitation conditions (Figure 1.4). Thus, In order to achieve high performance in labeled cells from FAP-fluorogen complexes, the protein should be easy and stable to express in various cellular

compartments, the free dye should give low background, little non-specific staining and permeate cell freely, and the interaction between them should be specific and happen at low concentration.

Applications	Small organic dyes (antibody-conjugated)	Nanoparticles (antibody-conjugated)	Fluorescent proteins	Hybrid tags	Fluorogen activating proteins
Live cells	Surface	Surface	++	+	++
Animals	<i>Ex vivo</i>	<i>Ex vivo</i>	Transgene live	Transgene <i>Ex vivo</i>	Transgene <i>Ex vivo</i>
Dynamic interactions	+/-	+/-	++	+/-	+/-
CALI	+	-	+	++	++
Super resolution microscopy	++	+	++	++	++
Advantages	Functionality	Brightness Photostability	Live cell Specificity	Live cell Small size	Live cell Functionality
Limitations	Targeting	Targeting Penetration	Ectopic expression	Ectopic expression Background fluorescence	Ectopic expression

Table 1.1: Applications of fluorophores in protein study. ++: optimal, +: applicable, +/-: applicable in some cases, -: not applicable. (Partially adapted from ref. 6)

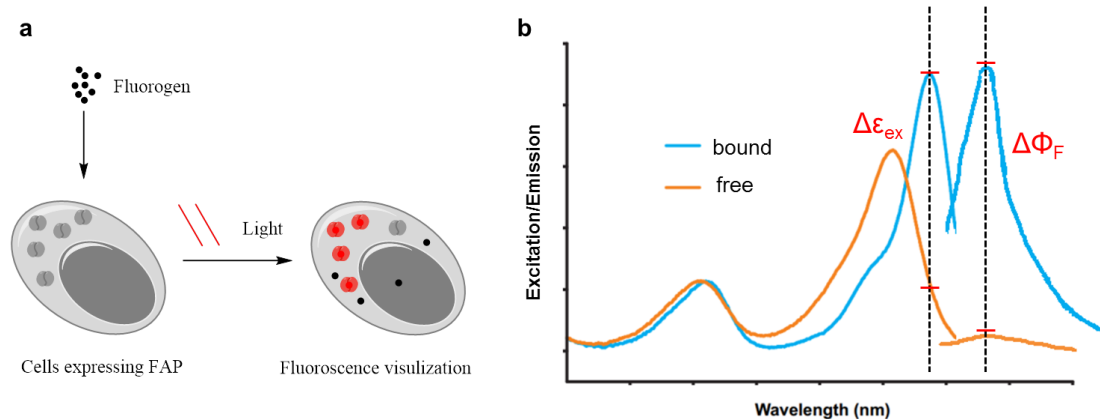


Figure 1.4: Fluorogen activating protein and activation ratio. (a): Fluorogen was added to the cells and activated by genetically targeting FAP to fluoresce when excited by proper laser light; (b): Activation ratio was determined by changes in extinction coefficient at excitation wavelength and fluorescence quantum yield.

A number of FAP-fluorogen complexes have been developed from unrigidized dyes including FAP_{H10}-OTB⁵⁸ (oxazole thiazole blue, ex/em: 400/450 nm), FAP_{HL1.0.1}-TO⁵⁶ (thiazole orange, ex/em: 500/530 nm), FAP_{K7}-DIR⁵⁹ (dimethylindole red, ex/em: 640/670 nm), FAP_{dL5}-MG⁵⁶ (malachite green, ex/em: 633/668 nm), and FAP_{MARS}-SCi1 (ex/em: 703/733 nm) (Figure 1.5). These fluoromodules have distinctive scFv (single-chain variable fragment) compositions, spectral properties, fluorescence brightness and binding properties. MG based fluorogens which bind to FAP_{dL5}** with thousands-fold fluorescence activation and a low-picomolar dissociation constant have found successful applications in many directions and are widely used in our lab in a range of biological problems.

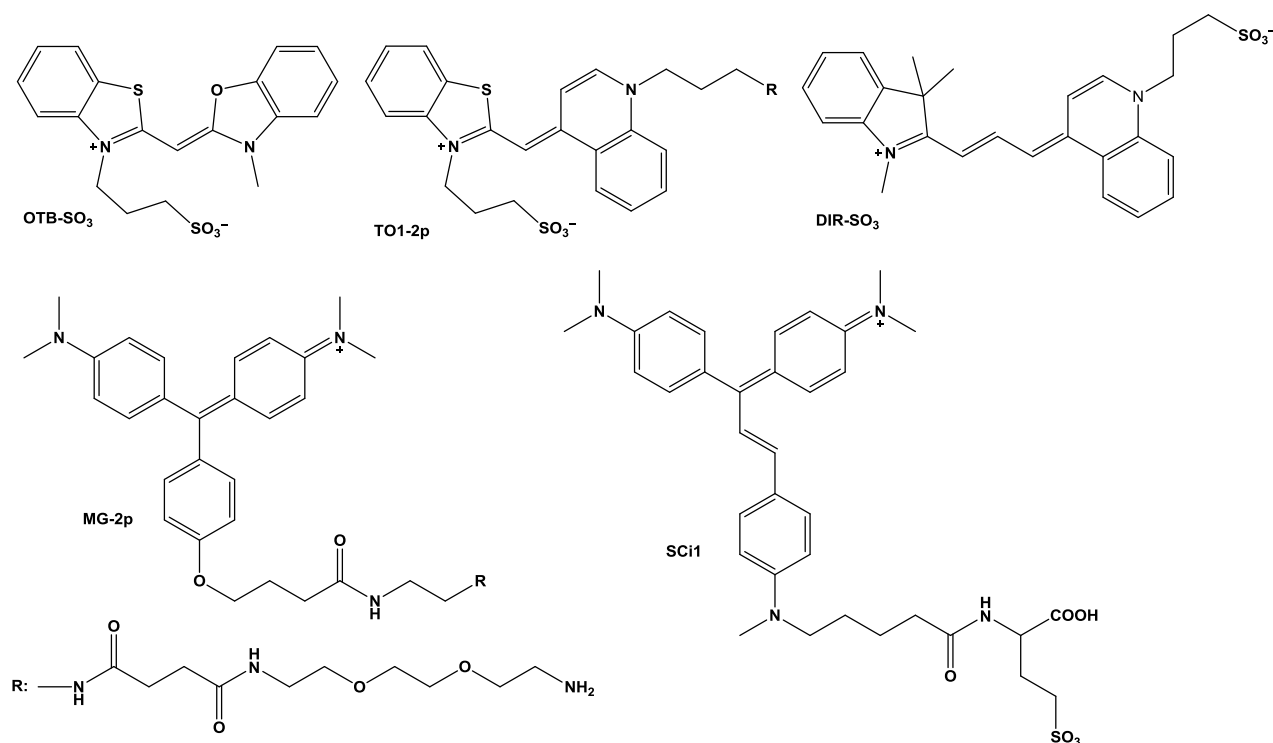


Figure 1.5: Chemical structures of fluorogenic dyes.

Malachite green alone is a cationic cell-permeable dye, which non-specifically stains mitochondria and nuclei with strong fluorescence⁶⁰⁻⁶². By introducing an ether linker at the para-position of the bottom phenyl ring, we have synthesized various MG derivatives with low non-

specific background and tuned cell-permeability, successfully applied to a number of topics (Figure 1.6). As examples, we have demonstrated the first use of FAP-fluorogen with L5/MG-2p complex in STED microscopy in living cells⁶³, providing a 2-3 fold enhancement in resolution over conventional microscopy. We have also coupled multiple cyanine donors (Cy3) to one MG acceptor to create a series of ‘dyedron’ molecules that stoichiometrically increase the fluorescence intensity of MG-dL5 complex up to 10-fold compared to similar size GFP⁶⁴. We have prepared tetramethylrhodamine (TMR) – MG tandem dyes that can penetrate cells and allow two-photon imaging⁶⁵. We have also shown that biotinylated fluorogens enable the specific targeting of streptavidin-conjugated quantum dots to proteins of interest for single molecule experiments⁶⁶.

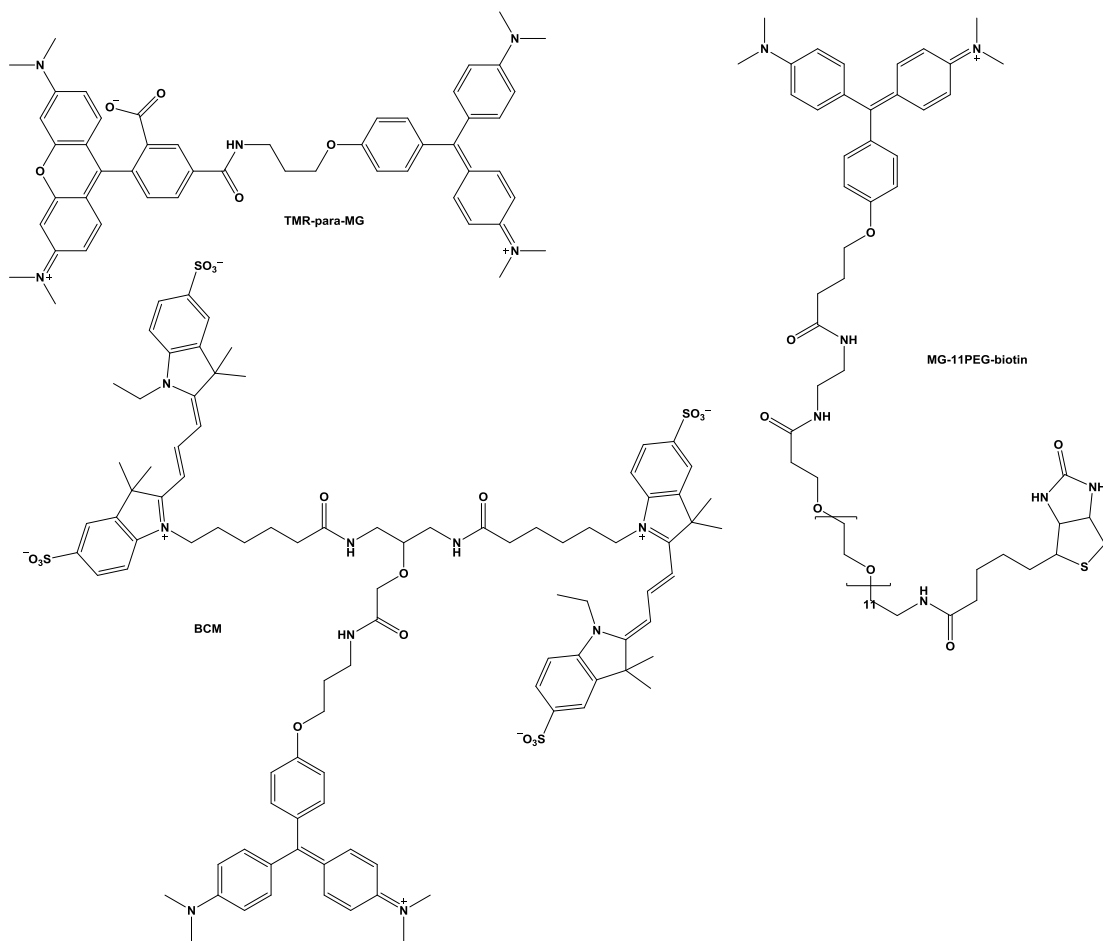


Figure 1.6: Chemical structures of MG derivatives: TMR-para-MG, MG-11PEG-biotin and BCM.

Tailor malachite green into different biological tools

However, in previous applications, the developments of functionalized MG derivatives were focused on energy-transfer pairs where one or multiple fluorophore donors were covalently linked to MG. The donor molecule is often responsible for signaling of environmental change or fluorescence intensity. Little modification has been done to the MG chromophore itself, in part because it is not known whether modifications would preserve binding to the FAP protein, alter the quantum yield of the complex, or otherwise compromise function of the FAP-fluorogen module. It would be very useful and easier to optimize if modifications of the MG chromophore could be used to directly sense or cause the change in biological systems.

Using structural knowledge of the interaction between MG and dL5, several structurally similar series of MG analogues were proposed and synthesized to fulfill a variety of biology applications. First, by varying the charge of the linker, I have synthesized a series of MG derivatives with different net charge that directly alters the cell permeability and specificity of the fluorogen activation on biological targets. Secondly, a series of fluorinated MG derivatives were synthesized to investigate fluorination effect on spectra properties and binding affinity to dL5**, shifting fluorogen-FAP into the near infrared spectral range. Thirdly, a number of MG analogues with distinct absorption spectra were made to serve the purpose of multi-color imaging with tailored cell-permeability properties. Finally, a heavy-atom substituted MG (MG-2I) was made, which greatly increased the rate of singlet generation upon binding to dL5**. This MG-2I/dL5** complex enables protein inactivation and targeted cell killing and rapid targeted lineage ablation in living larval and adult zebrafish.

References:

- 1 Hartwell, L. H., Hopfield, J. J., Leibler, S. & Murray, A. W. From molecular to modular cell biology. *Nature* **402**, C47-C52, doi:Doi 10.1038/35011540 (1999).
- 2 Lippincott-Schwartz, J., Snapp, E. & Kenworthy, A. Studying protein dynamics in living cells. *Nat Rev Mol Cell Bio* **2**, 444-456, doi:Doi 10.1038/35073068 (2001).
- 3 Dulin, D., Lipfert, J., Moolman, M. C. & Dekker, N. H. Studying genomic processes at the single-molecule level: introducing the tools and applications. *Nat Rev Genet* **14**, 9-22, doi:10.1038/nrg3316 (2013).
- 4 Frangioni, J. V. In vivo near-infrared fluorescence imaging. *Curr Opin Chem Biol* **7**, 626-634, doi:10.1016/j.cbpa.2003.08.007 (2003).
- 5 Michalet, X. *et al.* Quantum dots for live cells, in vivo imaging, and diagnostics. *Science* **307**, 538-544, doi:10.1126/science.1104274 (2005).
- 6 Giepmans, B. N. G., Adams, S. R., Ellisman, M. H. & Tsien, R. Y. Review - The fluorescent toolbox for assessing protein location and function. *Science* **312**, 217-224, doi:10.1126/science.1124618 (2006).
- 7 Fernandez-Suarez, M. & Ting, A. Y. Fluorescent probes for super-resolution imaging in living cells. *Nat Rev Mol Cell Bio* **9**, 929-943, doi:10.1038/nrm2531 (2008).
- 8 Chudakov, D. M., Matz, M. V., Lukyanov, S. & Lukyanov, K. A. Fluorescent Proteins and Their Applications in Imaging Living Cells and Tissues. *Physiol Rev* **90**, 1103-1163, doi:10.1152/physrev.00038.2009 (2010).
- 9 Huang, B., Bates, M. & Zhuang, X. W. Super-Resolution Fluorescence Microscopy. *Annu Rev Biochem* **78**, 993-1016, doi:10.1146/annurev.biochem.77.061906.092014 (2009).
- 10 van de Linde, S., Heilemann, M. & Sauer, M. Live-Cell Super-Resolution Imaging with Synthetic Fluorophores. *Annual Review of Physical Chemistry, Vol 63* **63**, 519-540, doi:10.1146/annurev-physchem-032811-112012 (2012).
- 11 Grimm, J. B. *et al.* A general method to improve fluorophores for live-cell and single-molecule microscopy. *Nat Methods* **12**, 244-+, doi:10.1038/Nmeth.3256 (2015).
- 12 Weissleder, R. & Ntziachristos, V. Shedding light onto live molecular targets. *Nat Med* **9**, 123-128, doi:10.1038/nm0103-123 (2003).
- 13 Weissleder, R. & Pittet, M. J. Imaging in the era of molecular oncology. *Nature* **452**, 580-589, doi:10.1038/nature06917 (2008).
- 14 Terai, T. & Nagano, T. Small-molecule fluorophores and fluorescent probes for bioimaging. *Pflug Arch Eur J Phy* **465**, 347-359, doi:10.1007/s00424-013-1234-z (2013).

- 15 Yin, J., Hu, Y. & Yoon, J. Fluorescent probes and bioimaging: alkali metals, alkaline earth metals and pH. *Chem Soc Rev* **44**, 4619-4644, doi:10.1039/c4cs00275j (2015).
- 16 Han, J. Y. & Burgess, K. Fluorescent Indicators for Intracellular pH. *Chem Rev* **110**, 2709-2728, doi:10.1021/cr900249z (2010).
- 17 Ntziachristos, V., Tung, C. H., Bremer, C. & Weissleder, R. Fluorescence molecular tomography resolves protease activity in vivo. *Nat Med* **8**, 757-760, doi:10.1038/nm729 (2002).
- 18 Gomes, A., Fernandes, E. & Lima, J. L. F. C. Fluorescence probes used for detection of reactive oxygen species. *J Biochem Bioph Meth* **65**, 45-80, doi:10.1016/j.jbbm.2005.10.003 (2005).
- 19 Sletten, E. M. & Bertozzi, C. R. Bioorthogonal chemistry: fishing for selectivity in a sea of functionality. *Angew Chem Int Ed Engl* **48**, 6974-6998, doi:10.1002/anie.200900942 (2009).
- 20 Kalia, J. & Raines, R. T. Advances in Bioconjugation. *Curr Org Chem* **14**, 138-147 (2010).
- 21 Hermanson, G. T. *Bioconjugate techniques*. Third edition. edn, (Elsevier/AP, 2013).
- 22 Luo, S. L., Zhang, E. L., Su, Y. P., Cheng, T. M. & Shi, C. M. A review of NIR dyes in cancer targeting and imaging. *Biomaterials* **32**, 7127-7138, doi:10.1016/j.biomaterials.2011.06.024 (2011).
- 23 Takaoka, Y., Ojida, A. & Hamachi, I. Protein organic chemistry and applications for labeling and engineering in live-cell systems. *Angew Chem Int Ed Engl* **52**, 4088-4106, doi:10.1002/anie.201207089 (2013).
- 24 Lavis, L. D. & Raines, R. T. Bright ideas for chemical biology. *Acs Chem Biol* **3**, 142-155, doi:10.1021/cb700248m (2008).
- 25 Goncalves, M. S. Fluorescent labeling of biomolecules with organic probes. *Chem Rev* **109**, 190-212, doi:10.1021/cr0783840 (2009).
- 26 Chan, J., Dodani, S. C. & Chang, C. J. Reaction-based small-molecule fluorescent probes for chemoselective bioimaging. *Nat Chem* **4**, 973-984, doi:10.1038/nchem.1500 (2012).
- 27 Ormo, M. *et al.* Crystal structure of the Aequorea victoria green fluorescent protein. *Science* **273**, 1392-1395 (1996).
- 28 Hein, R. & Tsien, R. Y. Engineering green fluorescent protein for improved brightness, longer wavelengths and fluorescence resonance energy transfer. *Curr Biol* **6**, 178-182 (1996).
- 29 Tsien, R. Y. The green fluorescent protein. *Annu Rev Biochem* **67**, 509-544, doi:10.1146/annurev.biochem.67.1.509 (1998).
- 30 Chalfie, M., Tu, Y., Euskirchen, G., Ward, W. W. & Prasher, D. C. Green Fluorescent Protein as a Marker for Gene-Expression. *Science* **263**, 802-805, doi:DOI 10.1126/science.8303295 (1994).
- 31 Shaner, N. C., Patterson, G. H. & Davidson, M. W. Advances in fluorescent protein technology. *J Cell Sci* **120**, 4247-4260, doi:10.1242/jcs.005801 (2007).

- 32 Yoo, S. D., Cho, Y. H. & Sheen, J. Arabidopsis mesophyll protoplasts: a versatile cell system for transient gene expression analysis. *Nat Protoc* **2**, 1565-1572, doi:10.1038/nprot.2007.199 (2007).
- 33 Revankar, C. M., Cimino, D. F., Sklar, L. A., Arterburn, J. B. & Prossnitz, E. R. A transmembrane intracellular estrogen receptor mediates rapid cell signaling. *Science* **307**, 1625-1630, doi:10.1126/science.1106943 (2005).
- 34 Miesenbock, G., De Angelis, D. A. & Rothman, J. E. Visualizing secretion and synaptic transmission with pH-sensitive green fluorescent proteins. *Nature* **394**, 192-195, doi:10.1038/28190 (1998).
- 35 Bulina, M. E. *et al.* A genetically encoded photosensitizer. *Nat Biotechnol* **24**, 95-99, doi:10.1038/nbt1175 (2006).
- 36 Chen, T. W. *et al.* Ultrasensitive fluorescent proteins for imaging neuronal activity. *Nature* **499**, 295-+, doi:10.1038/nature12354 (2013).
- 37 Dedecker, P., De Schryver, F. C. & Hofkens, J. Fluorescent Proteins: Shine on, You Crazy Diamond. *J Am Chem Soc* **135**, 2387-2402, doi:10.1021/ja309768d (2013).
- 38 Terpe, K. Overview of tag protein fusions: from molecular and biochemical fundamentals to commercial systems. *Appl Microbiol Biotechnol* **60**, 523-533, doi:10.1007/s00253-002-1158-6 (2003).
- 39 Rabuka, D. Chemoenzymatic methods for site-specific protein modification. *Curr Opin Chem Biol* **14**, 790-796, doi:10.1016/j.cbpa.2010.09.020 (2010).
- 40 Los, G. V. *et al.* HatoTag: A novel protein labeling technology for cell imaging and protein analysis. *Acs Chem Biol* **3**, 373-382, doi:10.1021/cb800025k (2008).
- 41 Gautier, A. *et al.* An engineered protein tag for multiprotein labeling in living cells. *Chem Biol* **15**, 128-136, doi:10.1016/j.chembiol.2008.01.007 (2008).
- 42 Adams, S. R. *et al.* New biarsenical Ligands and tetracysteine motifs for protein labeling in vitro and in vivo: Synthesis and biological applications. *J Am Chem Soc* **124**, 6063-6076, doi:UNSP JA017687N10.1021/ja017687n (2002).
- 43 Ju, W. *et al.* Activity-dependent regulation of dendritic synthesis and trafficking of AMPA receptors. *Nat Neurosci* **7**, 244-253, doi:10.1038/nn1189 (2004).
- 44 Gaietta, G. *et al.* Multicolor and electron microscopic imaging of connexin trafficking. *Science* **296**, 503-507, doi:DOI 10.1126/science.1068793 (2002).
- 45 Tour, O., Meijer, R. M., Zacharias, D. A., Adams, S. R. & Tsien, R. Y. Genetically targeted chromophore-assisted light inactivation. *Nat Biotechnol* **21**, 1505-1508, doi:10.1038/nbt914 (2003).

- 46 Willig, K. I., Rizzoli, S. O., Westphal, V., Jahn, R. & Hell, S. W. STED microscopy reveals that synaptotagmin remains clustered after synaptic vesicle exocytosis. *Nature* **440**, 935-939, doi:10.1038/nature04592 (2006).
- 47 Hell, S. W. & Wichmann, J. Breaking the Diffraction Resolution Limit by Stimulated-Emission - Stimulated-Emission-Depletion Fluorescence Microscopy. *Opt Lett* **19**, 780-782, doi:Doi 10.1364/Ol.19.000780 (1994).
- 48 Rust, M. J., Bates, M. & Zhuang, X. W. Sub-diffraction-limit imaging by stochastic optical reconstruction microscopy (STORM). *Nat Methods* **3**, 793-795, doi:10.1038/nmeth929 (2006).
- 49 Resch-Genger, U., Grabolle, M., Cavaliere-Jaricot, S., Nitschke, R. & Nann, T. Quantum dots versus organic dyes as fluorescent labels. *Nat Methods* **5**, 763-775, doi:10.1038/Nmeth.1248 (2008).
- 50 Chaudhuri, R. G. & Paria, S. Core/Shell Nanoparticles: Classes, Properties, Synthesis Mechanisms, Characterization, and Applications. *Chem Rev* **112**, 2373-2433, doi:10.1021/cr100449n (2012).
- 51 Walling, M. A., Novak, J. A. & Shepard, J. R. Quantum dots for live cell and in vivo imaging. *Int J Mol Sci* **10**, 441-491, doi:10.3390/ijms10020441 (2009).
- 52 Huang, B., Wang, W., Bates, M. & Zhuang, X. Three-dimensional super-resolution imaging by stochastic optical reconstruction microscopy. *Science* **319**, 810-813, doi:10.1126/science.1153529 (2008).
- 53 Sun, C., Lee, J. S. & Zhang, M. Magnetic nanoparticles in MR imaging and drug delivery. *Adv Drug Deliv Rev* **60**, 1252-1265, doi:10.1016/j.addr.2008.03.018 (2008).
- 54 Biju, V. Chemical modifications and bioconjugate reactions of nanomaterials for sensing, imaging, drug delivery and therapy. *Chem Soc Rev* **43**, 744-764, doi:10.1039/c3cs60273g (2014).
- 55 Medintz, I. L., Uyeda, H. T., Goldman, E. R. & Mattoussi, H. Quantum dot bioconjugates for imaging, labelling and sensing. *Nat Mater* **4**, 435-446, doi:10.1038/nmat1390 (2005).
- 56 Szent-Gyorgyi, C. *et al.* Fluorogen-activating single-chain antibodies for imaging cell surface proteins (vol 26, pg 235, 2008). *Nat Biotechnol* **26**, 470-470, doi:10.1038/nbt0408-470b (2008).
- 57 Bruchez, M. P. Dark dyes-bright complexes: fluorogenic protein labeling. *Curr Opin Chem Biol* **27**, 18-23, doi:10.1016/j.cbpa.2015.05.014 (2015).
- 58 Zanotti, K. J. *et al.* Blue fluorescent dye-protein complexes based on fluorogenic cyanine dyes and single chain antibody fragments. *Org Biomol Chem* **9**, 1012-1020, doi:10.1039/c0ob00444h (2011).

- 59 Ozhalici-Unal, H. *et al.* A rainbow of fluoromodules: A promiscuous scFv protein binds to and activates a diverse set of fluorogenic cyanine dyes. *J Am Chem Soc* **130**, 12620-+, doi:10.1021/ja805042p (2008).
- 60 Harman, J. W. The Selective Staining of Mitochondria. *Stain Technol* **25**, 69-72 (1950).
- 61 Alfert, M. Studies on Basophilia of Nucleic Acids - the Methyl Green Stainability of Nucleic Acids. *Biol Bull* **103**, 145-156, doi:Doi 10.2307/1538441 (1952).
- 62 Srivastava, S., Sinha, R. & Roy, D. Toxicological effects of malachite green. *Aquat Toxicol* **66**, 319-329, doi:10.1016/j.aquatox.2003.09.008 (2004).
- 63 Fitzpatrick, J. A. J. *et al.* STED Nanoscopy in Living Cells Using Fluorogen Activating Proteins. *Bioconjugate Chem* **20**, 1843-1847, doi:10.1021/bc900249e (2009).
- 64 Szent-Gyorgyi, C., Schmidt, B. F., Fitzpatrick, J. A. J. & Bruchez, M. P. Fluorogenic Dendrons with Multiple Donor Chromophores as Bright Genetically Targeted and Activated Probes. *J Am Chem Soc* **132**, 11103-11109, doi:10.1021/ja9099328 (2010).
- 65 Yushchenko, D. A., Zhang, M., Yan, Q., Waggoner, A. S. & Bruchez, M. P. Genetically Targetable and Color-Switching Fluorescent Probe. *Chembiochem* **13**, 1564-1568, doi:10.1002/cbic.201200334 (2012).
- 66 Saurabh, S. *et al.* Multiplexed Modular Genetic Targeting of Quantum Dots. *Acs Nano* **8**, 11138-11146, doi:10.1021/mn5044367 (2014).

Chapter 2: Charge dependent cell permeability and specificity of malachite green derivatives

Introduction

The net charge of a fluorophore can have great influence over many of its properties such as pH dependence, solubility, sub-cellular localization and fluorescence intensity¹⁻³. By modulating net charge and charge distribution of the fluorophore while maintaining hydrophilicity and structural conformation, the fluorophore's localization and permeability can be altered^{4, 5}. In particular, the permeability of a molecule is believed to be strongly related to its overall charge^{6, 7}. In general, cationic residues are able to interact with negatively charged lipids of plasma membrane to facilitate membrane disruption, inclusion or transportation^{8, 9}. Many modifications of impermeable molecules have been developed to translocate them into cells, including acetate or acetoxymethyl ester¹⁰, polypeptides¹¹, and amine-containing polymers¹². For example, acetylated fluorescein is a quenched, uncharged fluorophore, which can freely diffuse into most cells. Once inside the cell, the ester group will be cleaved by cytoplasmic esterases, giving the fluorescent, negatively charged fluorescein that is retained by cell membrane¹³. This strategy not only allows cell penetration, the cleavage of the ester group can also be employed as an activation event to detect the activity of esterase, which is tightly related to cell viability, for example, calcein AM has been widely used to assess cell adhesion, chemotaxis and multidrug resistance¹⁴⁻¹⁶.

However, the role of charge in cell-permeability and sub-cellular localization is still very intriguing, since the correlations between localization and net charges are not always in agreement from fluorophore to fluorophore. For example, a systematic study conducted by Edelson B *et al.* on the influence of structural variation of polyamide-fluorophores on nuclear localization revealed that fluorophores (fluorescein, rhodamine and bodipy) with the same net

charge (0) performed significantly different in nuclear localization¹⁷. The fluorescein conjugates can effectively access cell nuclei while analogous rhodamine and bodipy conjugates poorly accumulate. Moreover, they found that moving the positive charge from the linker to the dye can prevent nuclear localization. In a recent publication in *Bioconjugate Chemistry*, Sato. K *et al.* reported two NIR heptamethine cyanine dyes with very similar structures yet different charge distributions¹⁸. Their study has shown that the dye's net charge and charge distribution can have significant effects on its bio-distribution of conjugated mAb and can be used to improve its tumor specificity. In Haugland's original description of new Alexa dyes⁴, it was reported that the net negative charges of the fluorophores decreased the interaction between molecules, which had previously strongly limited the fluorescence brightness of rhodamine conjugates. These works suggested that the overall charge and charge distribution on a particular fluorophore may have different effects on its photochemical properties, cellular localization and molecular interactions.

MG/dL5** has been adapted to a wide range of biological applications, from extracellular protein pH sensing to intracellular protein trafficking at different sites¹⁹⁻²². Various MG derived fluorogenic dyes have been made to fulfill those applications²³⁻²⁶. Therefore, it is important to establish the correlation between the net charge of MG derivatives and their cell permeability, FAP_{dL5**} binding affinity and intracellular localization. The MG derivatives that are commonly used in our lab are MG-ester²⁷, MG-2p²⁸ and MG-Btau²⁹ with +1, +2 and -1 overall net charge respectively (Figure 2.1). MG-ester is easy to prepare and can permeate cell quickly, but it has noticeable non-specific fluorescence background when labeling intra-cellular expressed FAPs. This spontaneous non-specific background fluorescence prevents the detection of weakly expressed or dilute proteins. MG-2p has improved signal-to-background fluorescence, however,

its ability to penetrate cell is nearly completely suppressed. MG-Btau is a cell-excluded dye that can specifically label extra-cellular expressed FAPs.

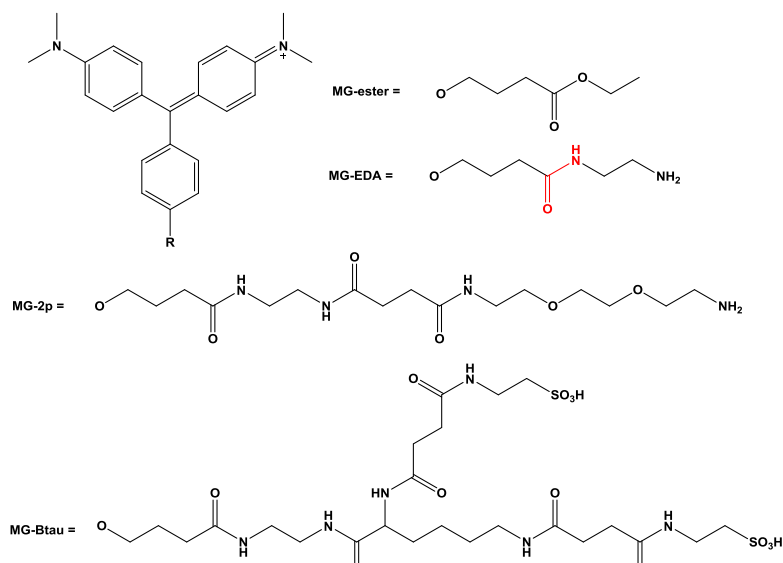


Figure 2.1: Chemical structures of commonly used MG dyes: MG-ester, MG-2p and MG-Btau.

In order to systematically study the effects of net charge on MG derivatives' cell permeability and specificity, we have designed a series of MG derivatives with different charges (from -2 to +3 as shown in Figure 2.2). To minimize the effects of structural variation over fluorogen-FAP interaction, the charged MG derivatives were extended from MG-EDA (Figure 2.1) with a urea bridge since our previous studies have shown that modifications beyond the amide bond have little effect on the fluorescence activation and binding affinity³⁰. These dyes have been extensively characterized and used as alternatives to pre-existing MG dyes and their general properties regarding protein activation, permeability and localization in cells are reported here.

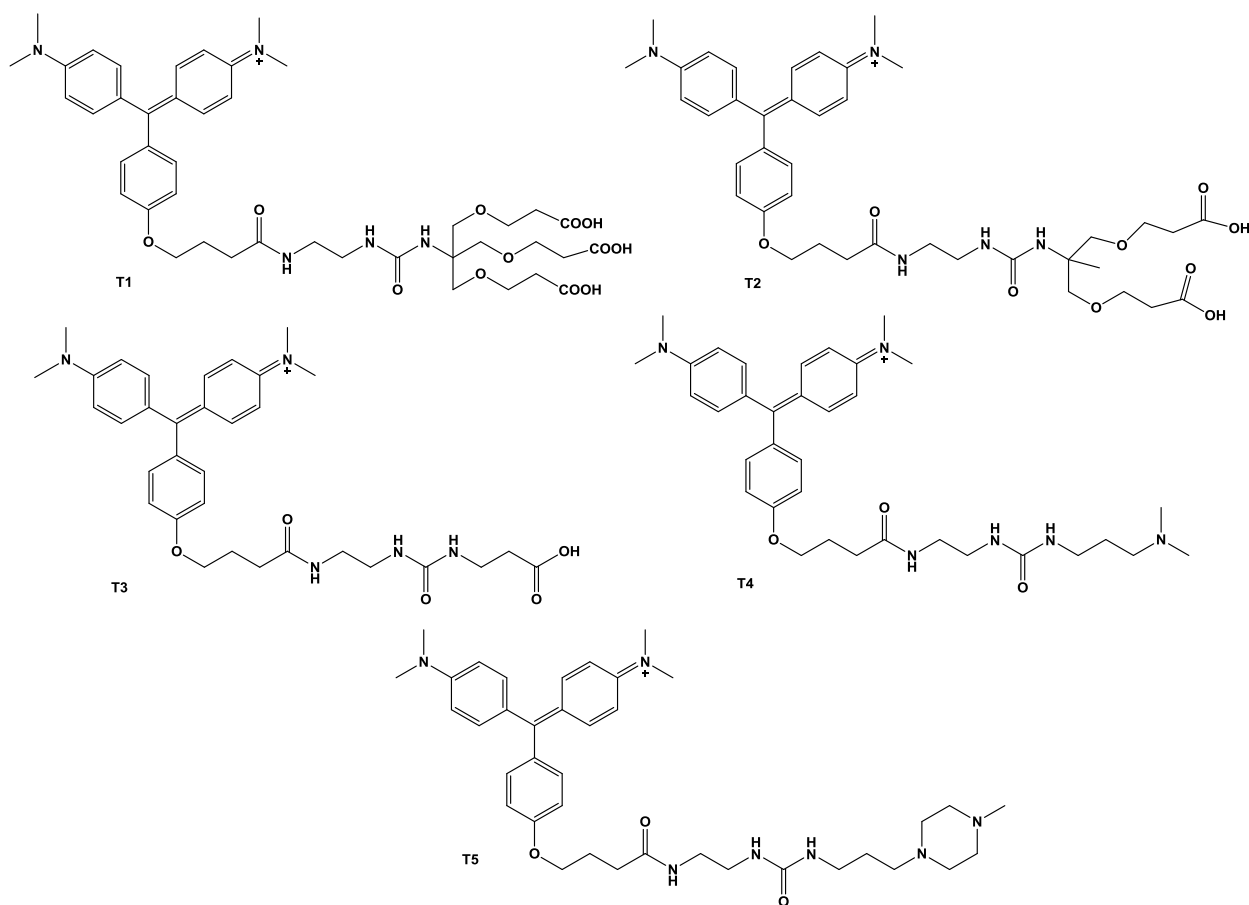


Figure 2.2: Chemical structures of charged MG derivatives

Characterization of charged MG series

We first evaluated whether the variations in linker structure and overall net charges will affect the free dyes' spectral properties and binding properties with dL5**. We found no difference in the absorption spectra of charged MG series compared with MG-ester and MG-2p, nor in the excitation/emission spectra when binding with dL5** compared to MG-ester/dL5**. However, when comparing the fluorescence activation by dL5** under the same condition, we found a weakly increasing trend from T1 to T5 (Figure 2.3), suggesting charged tails may have some effects on the ratio of fluorogen activation.

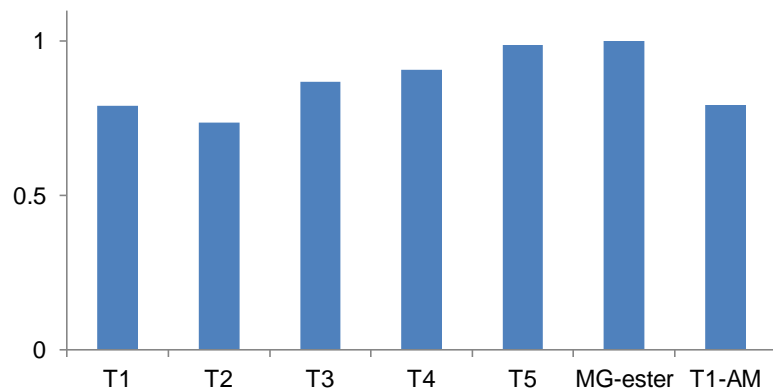


Figure 2.3: Normalized fluorescence quantum yield of charged MG derivatives upon binding to excess dL5** protein, where 500 nM dyes were pre-complexed with 2.5 μ M dL5** at room temperature for 3 hours. The absorbance at 580 nm was adjusted to the same for all complexes, fluorescence emission spectra from 600 to 800 nm excited at 580 nm was measured by Quantamaster monochromator fluorimeter (PTI), integrated and normalized using MG-ester/dL5** as a control.

Like FAP, RNA aptamers can also activate MG and its derivatives to fluoresce, so we also compared the fluorescence activation of charged MG series by MG RNA aptamer³¹. RNA aptamers are polyanion charged molecules, in which a phosphate group (negatively charged at physiological pH) is attached to the 3' position of one ribose and the 5' position of the next one. When measuring the fluorescence activation of charged MG series using MG RNA aptamer, we saw little fluorescence activation from negatively charged MG derivatives (T1, T2) and high activation ratio from positively charged MG derivatives (T4, T5) (Table 2.1). This result is consistent with Coulomb's law, where polyanion RNA aptamer would favor interaction with opposite charged T4 and T5, suggesting electronic interactions can play an important role in MG-aptamer binding process.

Compound (charge)	T1(-2)	T2(-1)	T3(0)	MG-ester(+1)	T4(+2)	T5(+3)	MG-2p(+2)
Fluorescence Intensity	57	57	211	288	939	755	677

Table 2.1: Fluorescence activation of charged MG derivatives by MG RNA aptamer, 200 nM dye and 1 μ M aptamer in pH 7.4 PBS buffer were pre-complexed for 1 hour at room temperature. Fluorescence intensity measured at ex/em: 630/660 nm using Tecan Infinite Plate Spectrometer. (Experiment was done by Dr. Xiaohong Tan)

Charge-dependent cell permeability

The cell permeability of charged MG series was tested with HEK 293 cells expressing with dL5** targeted to transmembrane (TM-dL5**) and to nucleus (NLS-dL5**) ^{22, 29}(Figure 2.4). Cell-permeable MG-ester and cell-impermeable MG-Btau were used to compare the specific targeting and cell permeability. 400 nM dyes were added to the cell culture 30 min prior to imaging; then, all images were taken under the same conditions. Compare to MG-ester, no intracellular fluorescence signals were observed from charged MG series when labeling TM-dL5** cells, suggesting improved specificity from charged linker modifications. In labeling intracellular NLS-dL5** protein, only T4 of the charged MG series can freely penetrate the cell membrane and label the protein as well as MG-ester. Surprisingly, the positively charged T5 failed to permeate inside cells, we hypothesized that the cyclic piperazine moiety might play an opposite role in cell penetration. An alternative structure (see chapter 6) can be synthesized to further investigate this issue.

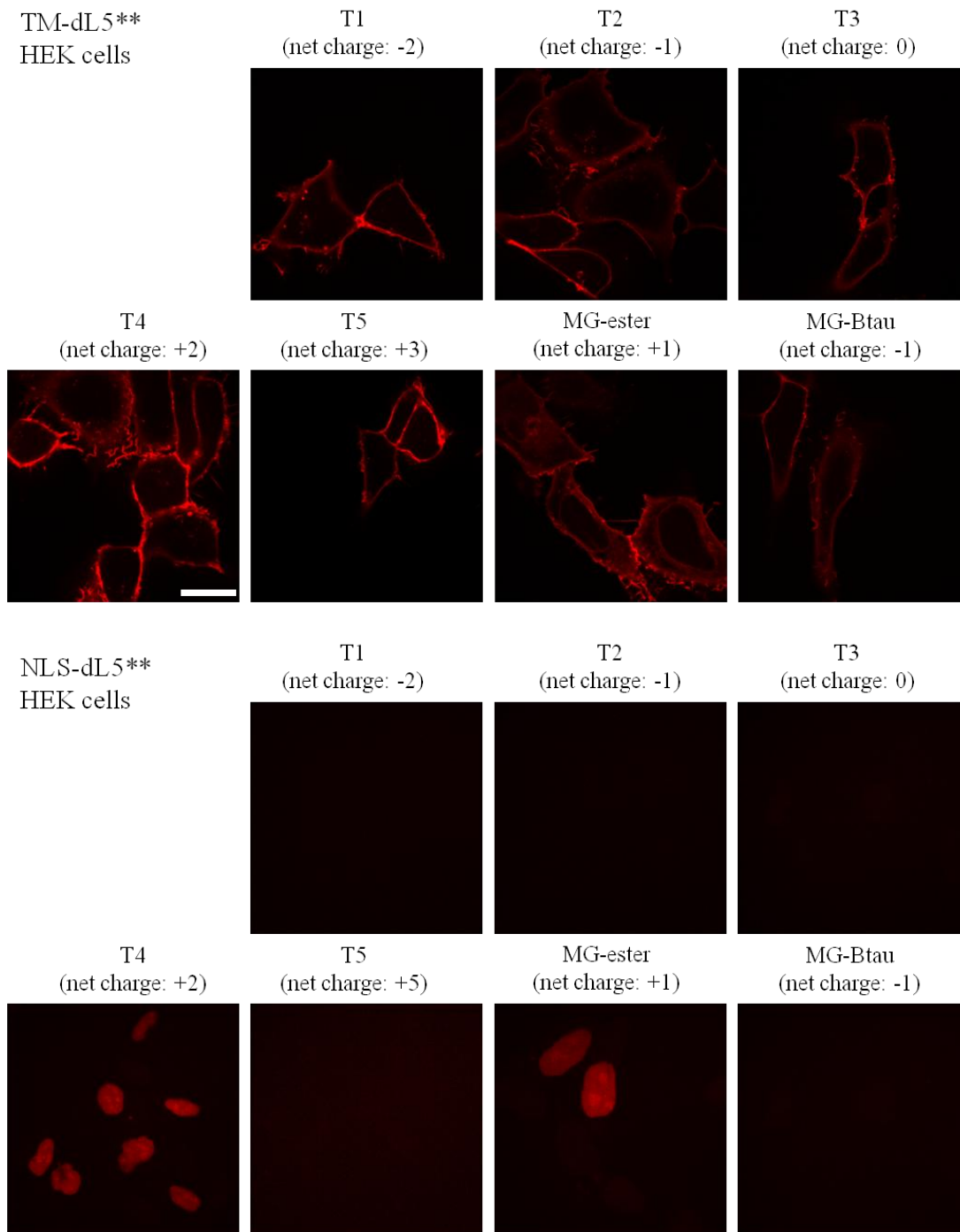


Figure 2.4: Fluorescence imaging of NLS-dL5** and TM-dL5** HEK cells with charged MG derivatives and MG-ester, 400 nM dye was added to the cell culture media without washing 30 minutes prior to the imaging. Scale bar = 10 μ m. (Andor Spinning Disk Confocal Microscope, 60 \times objective, 640 nm excitation, 665/25 nm emission filter, 20 % laser power, 100 ms exposure time)

So far, we only have knowledge of the intracellular behavior of positively charged MG compounds such as MG-ester (+1), MG-2p (+2) and T4 (+2). However, the intracellular pH of different compartments is tightly regulated locally, from acidic lysosomes (as low as pH 5) and Golgi, to neutral endoplasmic reticulum (ER) and mitochondria, to basic nucleus and peroxisomes (as high as pH 8). Ionic interaction is one major cause for non-specific staining; especially the non-specific staining of nuclei from cationic dyes. Triarylmethane dyes, including MG, are mostly cationic dyes and have been reported to non-specifically stain nuclei^{32, 33}. Use of a negatively charged MG derivative to label intracellular sites can provide useful information regarding the effect of net charge over the subcellular localization. As mentioned earlier, many impermeable fluorophores can be loaded into cells in the form of their acetoxymethyl (AM) ester, which has proved to be powerful and versatile in a wide range of applications. To validate this approach, we have synthesized the AM ester form of T1 (T1-AM), the cell permeability was tested with HEK 293 cells expressing with mCer3-dL5** tandem protein targeted to ER (Figure 2.5). By esterification of the carboxylic groups with AM ester, T1-AM can freely penetrate the cell and label dL5** proteins, which can be adapted to tune the permeability of future fluorogens.

This charged MG series can not only be used for study in charge dependent properties, it can also be used as alternatives to other commonly used MG dyes in our lab. For example, when imaging the mouse brain slice expressing dL5** in the BK (big potassium) channel³⁴ with MG-Btau (Figure 2.6), high non-specific nuclear staining background fluorescence was observed, while in the preliminary experiments, using cell-excluded MG-EDA-Tcarb instead of MG-Btau can dramatically reduce the non-specific staining.

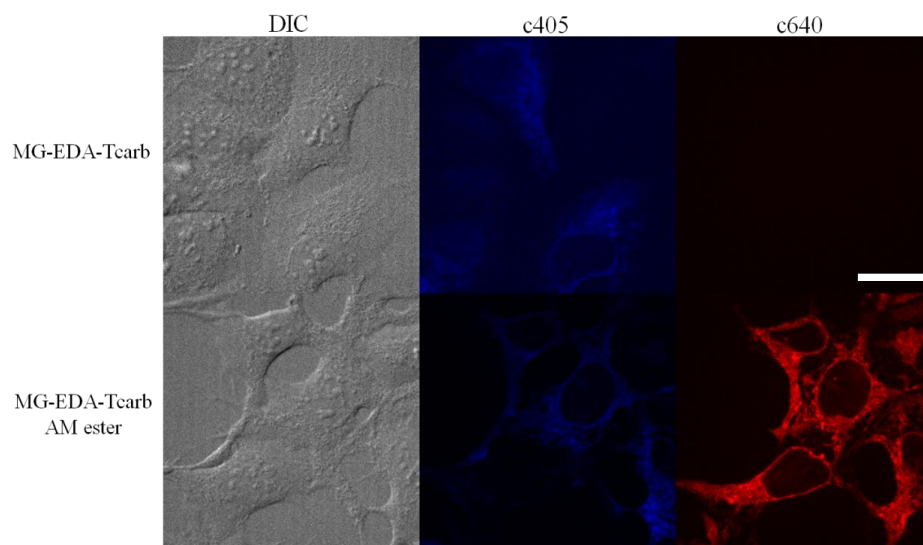


Figure 2.5: Esterification of MG-EDA-Tcarb (T1) with AM ester changes its cell permeability. 400 nM MG-EDA-Tcarb (T1) and MG-EDA-Tcarb (T1 AM) were allowed to pre-complex for 30 minutes prior to fluorescence imaging without washing off the unbound dye. Scale bar = 10 μ m. (Andor Spinning Disk Confocal Microscope, 60 \times objective, c405: 405 nm excitation, 445/25 nm emission, 100% laser power, 100 ms exposure time; c640: 640 nm excitation, 665/25 nm emission, 20% laser power, 20% laser power)

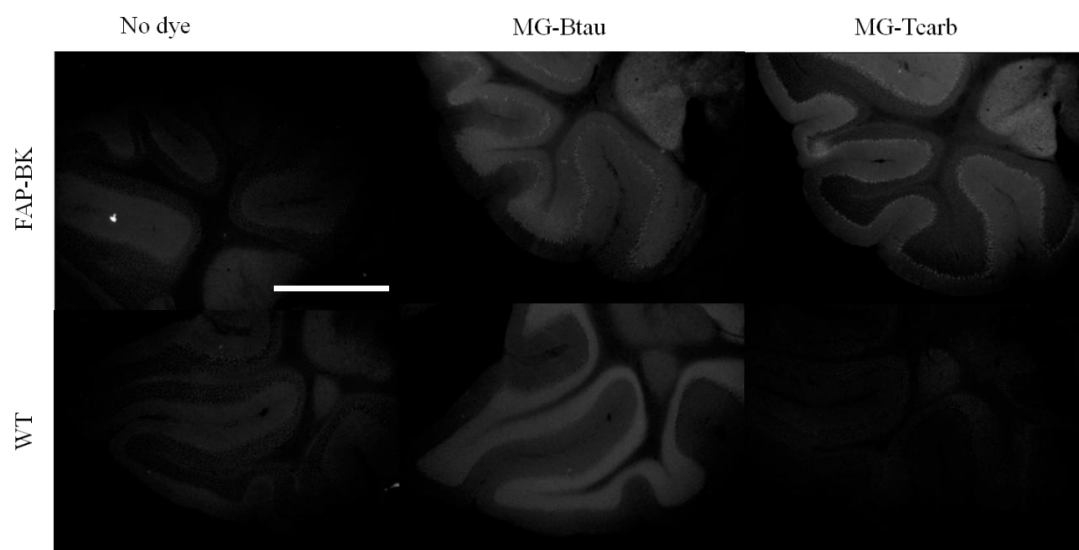


Figure 2.6: Fluorescence imaging of brain slices of FAP-BK expressing mouse and WT mouse, 500 nM dyes were added after fixation with 4% PFA. High signal-to-background ratio was seen when using MG-EDA-Tcarb. Scale bar = 1000 μ m. (Images acquired by EVOS FL Microscopy, 4 \times objective, ex: 628/40 nm, em: 692/40 nm; the experiment was carried out by Christopher P Pratt)

Summary

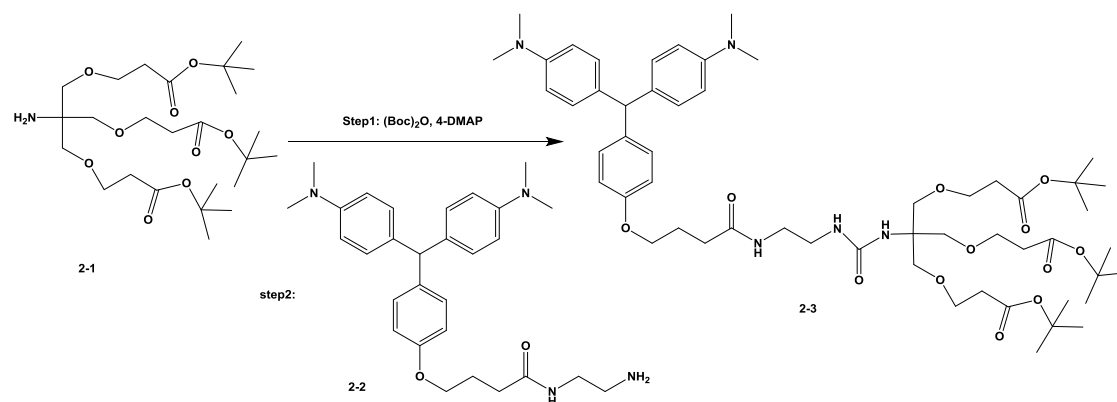
Here we have synthesized a series of charged MG derivatives, and measured their spectral properties and fluorescence activation by dL5** and an MG-binding aptamer. While charge played a minor role in activation by the dL5** protein, the fluorescence activation ratio by MG RNA aptamer appeared to be highly charge dependent, presumably a result of electrostatic selection. The cell permeability of the charged MG series was evaluated using TM-dL5** and NLS-dL5** HEK 293 cells, showing only T4 is readily cell permeable. However, modification of carboxylic group with AM ester allowed effective labeling within living cells. T1 (MG-EDA-Tcarb) has been used as an alternative to MG-Btau in the imaging of mouse brain slice of FAP-BK cells, with improved specificity. Charge can play a role in specificity of fluorogen-FAP interaction and the panel of molecules developed here demonstrated these effects.

Experimental Details

¹H NMR and ¹³C NMR data were recorded from Bruker Avance™ 300 MHz and 500 MHz, *J* coupling results was calculated using MestReNova software (compound 2-9, T4, T5 was calculated directly from hardcopies of the data). Mass spectra were obtained from Thermo-Fisher LCQ ESI/APCI Ion Trap in positive model using EtOH or 0.1% acetic acid EtOH as solvent. Final products were purified by silica, neutral alumina or reverse-phase chromatography, purity was tested by UPLC using a diode array absorbance detector. Absorbance values of respective free dyes and dye-FAP complexes were measured on a PerkinElmer Lambda45 spectrophotometer. Fluorogenic enhancement was measured in 96 well microplates on a Tecan Infinite M1000 Plate Spectrometer. Corrected emission spectra were taken on a Quantamaster monochromator fluorimeter (Photon Technology International). Fluorescence imaging of cell

cultures were taken on a Andor Spinning Disk Confocal Microscope. All electronic files are deposited into the lab folder in Evernote software.

1. The synthesis of MG-EDA-COOH₃ (MG-EDA-Tcarb, T1)

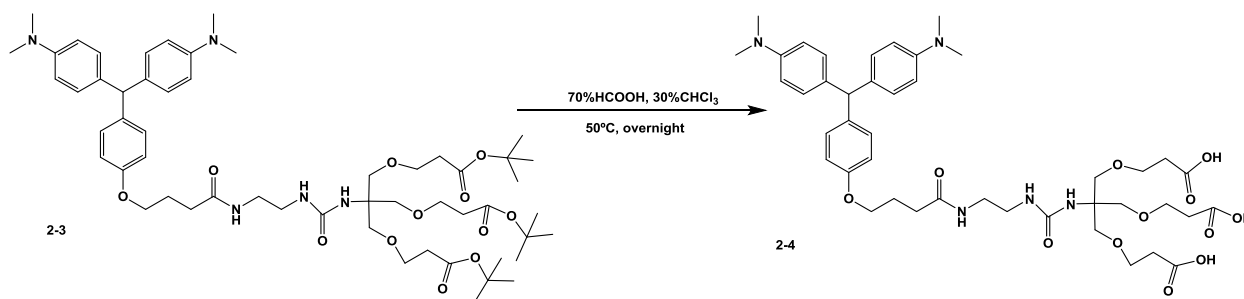


0.917 g (4.2 mmol) di-tert-butyl dicarbonate ((Boc)₂O), were dissolved in 10 mL dry CH₃CN, 0.368 g (3 mmol) 4-DMAP were added. Then, 1.48 g (3 mmol) tripod (2-1, synthesized and provided by Dr. Schmidt³⁵) was dissolved in 10 mL dry CH₃CN and added to the solution. The mixture was allowed to stir for 10 minutes at room temperature. 1.42 g (3 mmol) MG[H]-EDA (2-2, routinely synthesized in the lab following the literature²⁸) was dissolved in 25 mL CH₃CN and added to the reaction mixture. After stirring at room temperature for 5 hours, TLC was used to detect the completion of reaction. The reaction mixture was dried under reduced pressure and purified with silica gel (Eluent: Ethyl acetate)³⁶. The product (2-3) had a chemical composition of C₅₅H₈₃N₅O₁₂ with M.W. of 1005.60 g/mol (yield: 2.25 g, 74%). ¹H NMR (500 MHz, Methanol-*d*₄) δ 7.33 (d, *J* = 9.0 Hz, 4H), 7.27 (d, *J* = 9.2 Hz, 2H), 7.08 (d, *J* = 8.8 Hz, 2H), 6.95 (d, *J* = 9.1 Hz, 4H), 5.52 (s, 1H), 4.11 (t, *J* = 6.3 Hz, 2H), 3.53 (m, 12H), 3.22 (s, 12H), 3.14 (t, *J* = 6.1 Hz, 2H), 3.08 (t, *J* = 6.5 Hz, 2H), 2.34 (m, 8H), 2.06 (m, 2H), 1.35 (s, 27H). (Appendix 7-1)

¹³C NMR (125 MHz, Methanol-*d*₄) δ 172.8, 171.3, 158.8, 157.0, 148.9, 137.6, 133.3, 130.2,

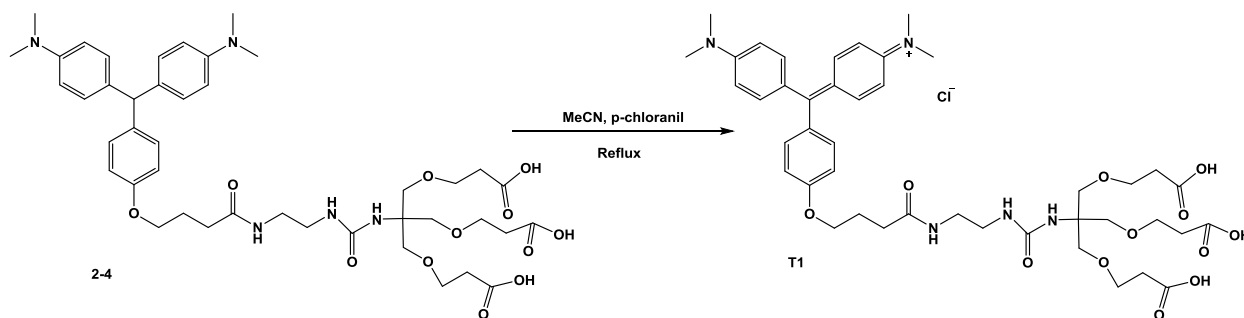
129.9, 114.1, 112.6, 80.7, 70.1, 67.2, 58.9, 54.2, 41.8, 40.8, 39.4, 36.4, 36.2, 31.0, 28.1, 25.4.

ESI-MS (+m/z): 1004.5.



2.01g (2 mmol) MG[H]-EDA-Tripod (2-3) was dissolved in 10 mL 4:1 of HCOOH to CHCl₃ and heated to 50°C overnight. The solvent was then removed under reduced pressure, the raw product was applied to a silica gel column and purified (Eluent: 80% CHCl₃ / 20% MeOH)³⁷.

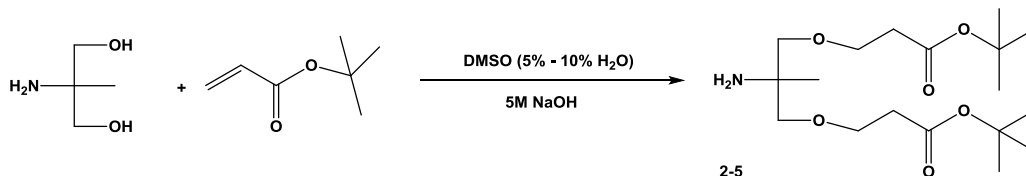
The product (2-4) had a chemical composition of C₄₃H₅₉N₅O₁₂ with M.W. of 837.97 g/mol (yield: 1.51g, 91%). ¹H NMR (500 MHz, Methanol-*d*₄) δ 7.31 (d, *J* = 8.7 Hz, 4H), 7.23 (d, *J* = 9.2 Hz, 4H), 7.02 (d, *J* = 9.0 Hz, 2H), 6.86 (d, *J* = 9.3 Hz, 2H), 5.58 (s, 1H), 4.01 (t, *J* = 6.0 Hz, 2H), 3.67 (m, 12H), 3.33 (t, *J* = 6.3 Hz, 2H), 3.22 (t, *J* = 6.1 Hz, 2H), 3.16 (s, 12H), 2.52 (m, 6H), 2.39 (t, *J* = 6.6 Hz, 2H), 2.08 (m, 2H). ¹³C NMR (125 MHz, Methanol-*d*₄) δ 174.4, 174.1, 159, 157.8, 144, 142, 135.4, 130.5, 130, 117.8, 114.2, 69.8, 66.8, 58.9, 57, 54.7, 43.9, 39.9, 38.7, 34.4, 32.2, 25.3, 17.1. ESI-MS (+m/z): 838.3.



0.838 g (1 mmol) MG[H]-EDA-COOH₃ (2-4) was dissolved in MeCN and heated to reflux, 0.271 g (1.1 mmol) p-chloranil was dissolved in hot MeCN and added to the reaction, it was

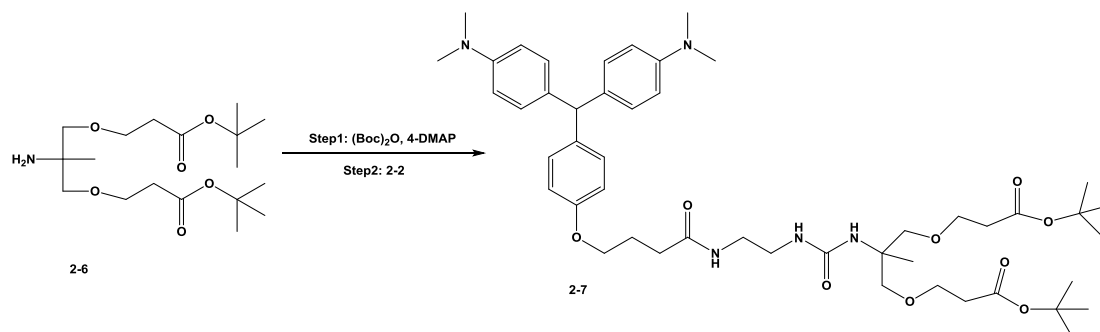
allowed to further reflux for 2-3 hours. This is the standard procedure for the oxidation of reduced malachite green compounds in this thesis unless otherwise stated. The reaction mixture was dried under reduced pressure, purified with silica gel (Eluent: 80% CHCl₃/ 20% MeOH). The product (T1) had a chemical composition of C₄₃H₅₈ClN₅O₁₂ with M.W. of 872.41 g/mol (yield: 0.763 g, 88%). ¹H NMR (500 MHz, Methanol-*d*₄) δ 7.60 (d, *J* = 8.9 Hz, 4H), 7.54 (d, *J* = 8.3 Hz, 2H), 7.38 (d, *J* = 8.7 Hz, 2H), 7.21 (d, *J* = 9.0 Hz, 4H), 4.43 (t, *J* = 6.2 Hz, 2H), 3.93 (t, *J* = 7.2 Hz, 6H), 3.86 (s, 6H), 3.53 (s, 12H), 3.48 (t, *J* = 6.1 Hz, 2H), 3.41 (t, *J* = 5.9 Hz, 2H), 2.80 (t, *J* = 6.0 Hz, 6H), 2.68 (t, *J* = 6.3 Hz, 2H), 2.38 (p, *J* = 6.8 Hz, 2H). (Appendix 7-2) ¹³C NMR (125 MHz, Methanol-*d*₄) δ 177.3, 175.8, 175.5, 164, 159.5, 157.1, 141, 138, 132.3, 126.9, 119.4, 115.2, 113.7, 69.9, 68.3, 67.2, 40.7, 40.2, 39.1, 35, 32.8, 25. ESI-MS (+*m/z*): 836.3.

2. The synthesis of MG-EDA-COOH₂ (MG-EDA-Dcarb, T2) was similar to T1



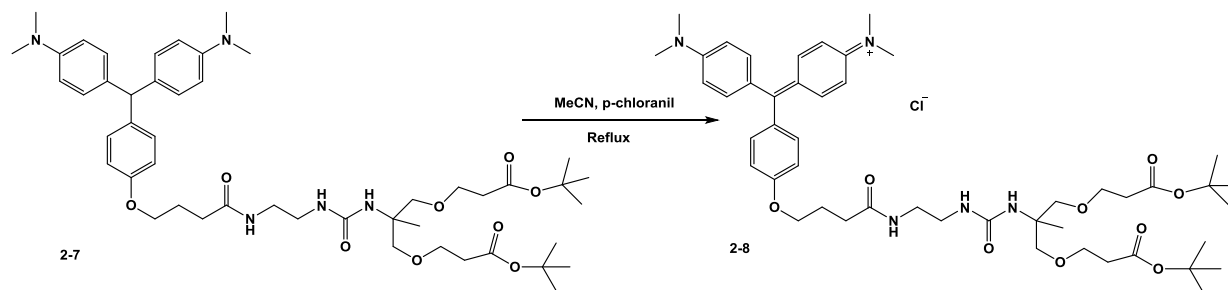
1.05 g (10 mmol) 2-amino-2-methyl-1,3-propanediol dissolved in 3 mL of DMSO (5%-10% water) was cooled to 15.0 °C under Argon. Then, 0.2 mL of 5.0 M NaOH was injected while stirring, followed by the dropwise injection of 3.4 mL (24 mmol) tert-butyl acrylate. The reaction mixture was allowed to reach room temperature and left stirring for 24 h. At this point, the excess reagent and solvent were removed under vacuum at room temperature and the residue was purified by column chromatography (Eluent: 80% hexane/ 20% ethyl acetate) to give 2.53 g (71%) of the product (2-5)³⁸. ¹H NMR (300 MHz, Chloroform-*d*) δ 3.62 (t, *J* = 6.3 Hz, 4H), 3.19 (m, 4H), 2.42 (t, *J* = 6.3 Hz, 4H), 1.40 (s, 18H), 0.96 (s, 3H).

The ¹H NMR data (Appendix 7-3) is consistent with values from reported literatures, ESI/MS or ¹³C NMR was not recorded.



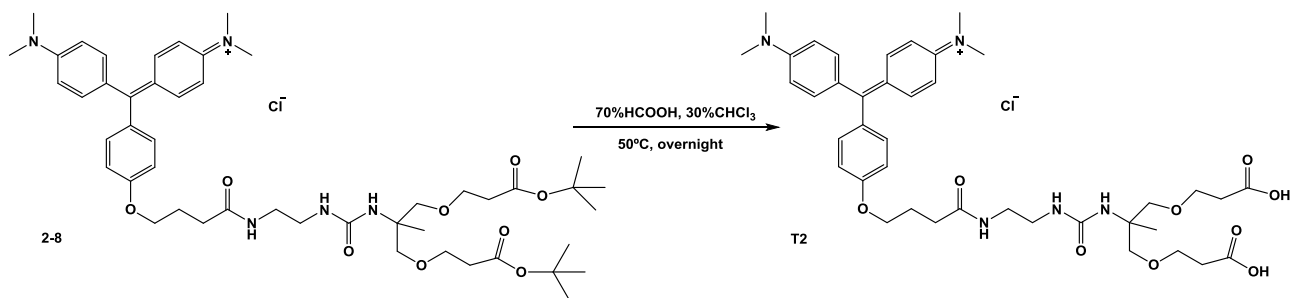
The reaction procedure is the same as the synthesis of 2-3. The product (2-7) had a chemical composition of C₄₈H₇₁N₅O₉ with M.W. of 862.12 g/mol (yield: 67%). ¹H NMR (300 MHz, Methanol-*d*₄) δ 6.96 (d, *J* = 8.9 Hz, 4H), 6.90 (d, *J* = 9.3 Hz, 4H), 6.78 (d, *J* = 8.7 Hz, 2H), 6.68 (d, *J* = 9.1 Hz, 2H), 5.76 (s, 1H), 3.94 (t, *J* = 6.2 Hz, 2H), 3.63 (t, *J* = 6.2 Hz, 4H), 3.51 (dd, 4H), 3.21 (m, 4H), 2.86 (s, 12H), 2.44 (t, *J* = 6.1 Hz, 4H), 2.37 (t, *J* = 7.0 Hz, 2H), 2.05 (m, 2H), 1.44 (s, 18H), 1.25 (s, 3H). (Appendix 7-4) ESI-MS (+*m/z*): 862.4.

Results interpreted from ¹H NMR (Appendix 7-4) and ESI-MS are consistent with the predicted result, no ¹³C NMR was taken.



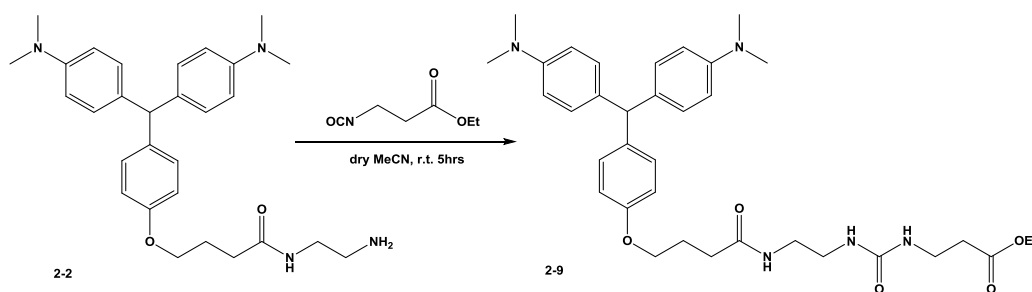
The product (2-8) had a chemical composition of C₄₈H₇₀ClN₅O₉ with M.W. of 896.56 g/mol (yield: 85%). ¹H NMR (300 MHz, Methanol-*d*₄) δ 7.45 (d, *J* = 9.2 Hz, 4H), 7.39 (d, *J* = 9.3 Hz, 2H), 7.19 (m, *J* = 9.1 Hz, 2H), 7.05 (d, *J* = 9.2 Hz, 4H), 4.22 (t, *J* = 6.2 Hz, 2H), 3.68 (t, *J* = 6.3 Hz, 4H), 3.51 (m, 2H), 3.36 (s, 12H), 3.32 (m, 4H), 2.46 (m, *J* = 7.7, 6.9 Hz, 6H), 2.17 (p, *J* = 6.6 Hz, 2H), 1.46 (d, *J* = 1.9 Hz, 18H), 1.28 (s, 3H). ESI-MS (+*m/z*): 860.4.

Results interpreted from ¹H NMR and ESI-MS (Appendix 7-5) are consistent with the predicted result, no ¹³C NMR was taken.



The product (T2) had a chemical composition of $C_{40}H_{54}ClN_5O_9$ with M.W. of 784.35 g/mol (yield: 91%). 1H NMR (300 MHz, Methanol- d_4) δ 7.53 (d, $J = 8.8$ Hz, 4H), 7.46 (d, $J = 9.2$ Hz, 2H), 7.35 (d, $J = 9.0$ Hz, 2H), 7.16 (d, $J = 9.2$ Hz, 4H), 4.41 (t, $J = 6.1$ Hz, 2H), 3.95 (t, $J = 6.4$ Hz, 4H), 3.76 (dd, $J = 21.3$ Hz, 5.9 Hz, 4H), 3.61 (s, 4H), 3.51 (s, 12H), 2.74 (t, $J = 6.1$ Hz, 4H), 2.69 (t, $J = 6.0$ Hz, 2H), 2.37 (m, 2H), 1.48 (s, 3H). (Appendix 7-6) ^{13}C NMR (75 MHz, Methanol- d_4) δ 178, 177.2, 175.4, 164.1, 159.7, 157.1, 140.8, 137.9, 132.1, 127, 119.4, 114.9, 113.7, 73.6, 68.3, 56.3, 40.4, 40, 39, 36.8, 32.8, 25.1, 19.8. ESI-MS (+m/z): 748.3.

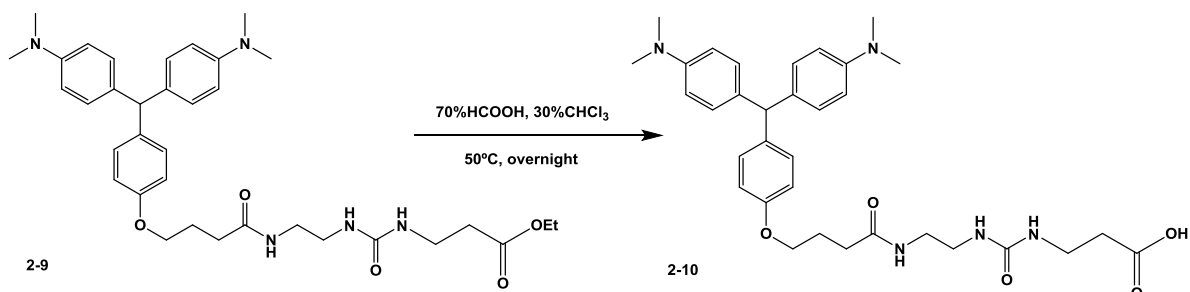
3. The synthesis of MG-EDA-COOH (T3)



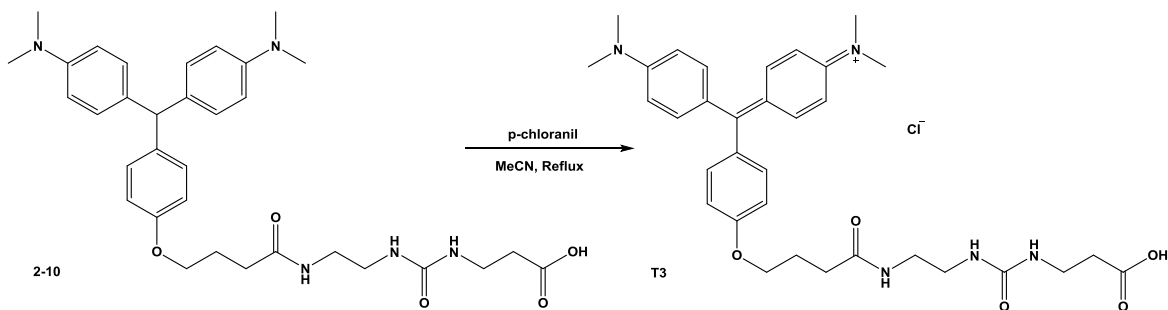
To 0.950 g (2 mmol) of 2-2 in 10 mL dry MeCN, 0.263 mL (2 mmol) of ethyl 3-isocyanatopropanoate in 10 mL dry MeCN was added dropwise. The reaction mixture was allowed to stir at room temperature for 5 hours. The solvent was then removed under reduced pressure to afford the crude product, which was purified by column chromatography on silica gel to give the desired product (eluent: 50% hexane / 50% ethyl acetate). The product (2-9) had a chemical composition of $C_{35}H_{47}N_5O_5$ with M.W. of 617.79 g/mol (yield: 1.07 g, 88%). 1H NMR

(300 MHz, Chloroform-*d*) δ 7.04 (d, $J = 8.3$ Hz, 2H), 6.98 (d, $J = 9.0$ Hz, 4H), 6.79 (d, $J = 8.3$ Hz, 2H), 6.67 (d, $J = 9.7$ Hz, 4H), 5.32 (s, 1H), 4.14(q, $J = 6.7$ Hz, 2H), 3.97 (t, $J = 6.0$ Hz, 2H), 3.42 (q, $J = 5.7$ Hz, 2H), 3.31 (m, 4H), 2.92 (s, 12H), 2.51 (t, $J = 6.0$ Hz, 2H), 2.39 (t, $J = 6.7$ Hz, 2H), 2.10 (p, $J = 6.0$ Hz, 2H), 1.27(t, $J = 6.7$ Hz, 3H). ESI-MS (+m/z): 618.3.

Results interpreted from ^1H NMR and ESI-MS (Appendix 7-7) are consistent with the predicted result, no ^{13}C NMR was taken.



The product (2-10) had a chemical composition of $\text{C}_{33}\text{H}_{43}\text{N}_5\text{O}_5$ with M.W. of 589.74 g/mol (yield: 92%). ^1H NMR (300 MHz, Chloroform-*d*) δ 7.02 (m, 6H), 6.78 (d, $J = 9.2$ Hz, 2H), 6.70 (d, $J = 9.4$ Hz, 4H), 5.95 (s, 1H), 5.33 (s, 1H), 3.92 (t, $J = 6.0$ Hz, 2H), 3.40 (m, 2H), 3.28 (s, 4H), 2.92 (s, 12H), 2.51 (t, $J = 5.7$ Hz, 2H), 2.38 (t, $J = 7.5$ Hz, 2H), 2.06 (s, 2H). ^{13}C NMR (75 MHz, Chloroform-*d*) δ 176.1, 174.8, 159.8, 157.1, 149.1, 137.8, 133.6, 130.3, 129.9, 114.1, 113.0, 68.0, 54.2, 41.2, 40.4, 40.1, 36.1, 35, 32.8, 25.5. ESI-MS (+m/z): 590.3.

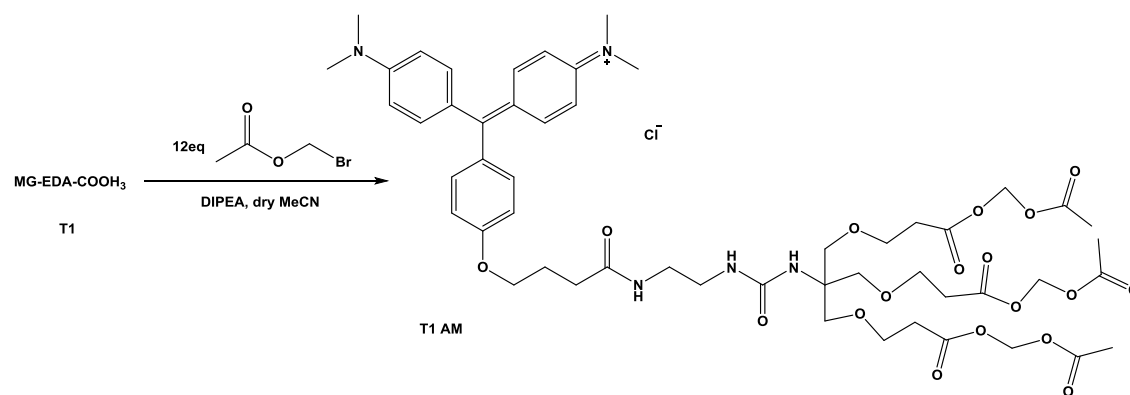


The product (T3) had a chemical composition of $\text{C}_{33}\text{H}_{42}\text{ClN}_5\text{O}_5$ with M.W. of 624.18 g/mol (yield: 78%). ^1H NMR (500 MHz, Methanol-*d*₄) δ 7.54 (d, $J = 8.9$ Hz, 4H), 7.48 (d, $J = 8.3$ Hz, 2H), 7.35 (d, $J = 8.3$ Hz, 2H), 7.17 (d, $J = 8.9$ Hz, 4H), 4.39 (t, $J = 6.3$ Hz, 2H), 3.52 (m, 4H),

The product (T5) had a chemical composition of $C_{33}H_{42}ClN_5O_5$ with M.W. of 624.18 g/mol (overall yield: 33%). 1H NMR (500 MHz, Methanol- d_4) δ 7.63 (d, $J = 10.0$ Hz, 4H), 7.58 (d, $J = 8.7$ Hz, 2H), 7.44 (d, $J = 10.0$ Hz, 2H), 7.25 (d, $J = 8.7$ Hz, 4H), 4.48 (t, $J = 6.2$ Hz, 2H), 3.66 (m, 4H), 3.58 (s, 12H), 3.50 (m, 10H), 3.22 (t, $J = 6.2$ Hz, 2H), 3.09 (s, 3H), 2.53 (t, $J = 7.5$ Hz, 2H), 2.42 (m, 2H), 2.12 (m, 2H). (Appendix 7-10) ^{13}C NMR (125 MHz, Methanol- d_4) δ 177.3, 175.7, 164.1, 160.5, 157, 140.8, 138, 132.3, 127.1, 119.3, 115.1, 113.5, 68.1, 54.8, 52.2, 50, 43.5, 40.3, 39.7, 37.5, 32.9, 25.5, 25.2. ESI-MS (+m/z): 656.3.

1H NMR for the reduced form of T5 was included in the data deposit in lab folder.

6. The synthesis of MG-EDA-COOH₃ AM ester



0.1 mmol MG-EDA-COOH₃ was dissolved in 5 mL dry MeCN under Argon, 12 eq of bromomethyl acetate and 12 eq of DIPEA was added to the system. The reaction was allowed to stir for 18 hours to complete. The product was precipitated in 20 mL ethyl ether. ESI-MS (+m/z): 1052.4. (Appendix 7-11)

Due to the small amount of product synthesized, only ESI-MS was conducted to confirm the esterification of the carboxylic acid.

References:

1. Sitaram, N. & Nagaraj, R. Interaction of antimicrobial peptides with biological and model membranes: structural and charge requirements for activity. *Bba-Biomembranes* **1462**, 29-54 (1999).
2. Madani, F., Lindberg, S., Langel, U., Futaki, S. & Graslund, A. Mechanisms of cellular uptake of cell-penetrating peptides. *J Biophys* **2011**, 414729 (2011).
3. Fischer, R., Waizenegger, T., Kohler, K. & Brock, R. A quantitative validation of fluorophore-labelled cell-permeable peptide conjugates: fluorophore and cargo dependence of import. *Bba-Biomembranes* **1564**, 365-374 (2002).
4. Panchuk-Voloshina, N. et al. Alexa dyes, a series of new fluorescent dyes that yield exceptionally bright, photostable conjugates. *J Histochem Cytochem* **47**, 1179-1188 (1999).
5. Zanetti-Domingues, L.C., Tynan, C.J., Rolfe, D.J., Clarke, D.T. & Martin-Fernandez, M. Hydrophobic Fluorescent Probes Introduce Artifacts into Single Molecule Tracking Experiments Due to Non-Specific Binding. *Plos One* **8** (2013).
6. Dowhan, W., Mileykovskaya, E. & Bogdanov, M. Diversity and versatility of lipid-protein interactions revealed by molecular genetic approaches. *Biochim Biophys Acta* **1666**, 19-39 (2004).
7. Alberts, B. Molecular biology of the cell, Edn. 4th. (Garland Science, New York; 2002).
8. Bhattacharya, S. & Bajaj, A. Advances in gene delivery through molecular design of cationic lipids. *Chem Commun (Camb)*, 4632-4656 (2009).
9. Zuhorn, I.S. & Hoekstra, D. On the mechanism of cationic amphiphile-mediated transfection. To fuse or not to fuse: is that the question? *J Membr Biol* **189**, 167-179 (2002).
10. Lavis, L.D., Chao, T.Y. & Raines, R.T. Synthesis and utility of fluorogenic acetoxymethyl ethers. *Chem Sci* **2**, 521-530 (2011).
11. Fischer, P.M., Krausz, E. & Lane, D.P. Cellular delivery of impermeable effector molecules in the form of conjugates with peptides capable of mediating membrane translocation. *Bioconjug Chem* **12**, 825-841 (2001).
12. Khandare, J. & Minko, T. Polymer-drug conjugates: Progress in polymeric prodrugs. *Prog Polym Sci* **31**, 359-397 (2006).
13. Carter, K.P., Young, A.M. & Palmer, A.E. Fluorescent sensors for measuring metal ions in living systems. *Chem Rev* **114**, 4564-4601 (2014).
14. Hollo, Z., Homolya, L., Davis, C.W. & Sarkadi, B. Calcein Accumulation as a Fluorometric Functional Assay of the Multidrug Transporter. *Bba-Biomembranes* **1191**, 384-388 (1994).

15. Bratosin, D., Mitrofan, L., Pali, C., Estaquier, J. & Montreuil, J. Novel fluorescence assay using calcein-AM for the determination of human erythrocyte viability and aging. *Cytom Part A* **66a**, 78-84 (2005).
16. Hung, P.J., Lee, P.J., Sabounchi, P., Lin, R. & Lee, L.P. Continuous perfusion microfluidic cell culture array for high-throughput cell-based assays. *Biotechnol Bioeng* **89**, 1-8 (2005).
17. Edelson, B.S. et al. Influence of structural variation on nuclear localization of DNA-binding polyamide-fluorophore conjugates. *Nucleic Acids Res* **32**, 2802-2818 (2004).
18. Sato, K. et al. Role of Fluorophore Charge on the In Vivo Optical Imaging Properties of Near-Infrared Cyanine Dye/Monoclonal Antibody Conjugates. *Bioconjug Chem* **27**, 404-413 (2016).
19. Fisher, G.W. et al. Detection and Quantification of beta 2AR Internalization in Living Cells Using FAP-Based Biosensor Technology. *J Biomol Screen* **15**, 703-709 (2010).
20. Grover, A. et al. Genetically Encoded pH Sensor for Tracking Surface Proteins through Endocytosis. *Angew Chem Int Edit* **51**, 4838-4842 (2012).
21. Saunders, M.J. et al. Fluorogen activating proteins in flow cytometry for the study of surface molecules and receptors. *Methods* **57**, 308-317 (2012).
22. Telmer, C.A. et al. Rapid, Specific, No-wash, Far-red Fluorogen Activation in Subcellular Compartments by Targeted Fluorogen Activating Proteins. *Acs Chem Biol* **10**, 1239-1246 (2015).
23. Szent-Gyorgyi, C., Schmidt, B.F., Fitzpatrick, J.A.J. & Bruchez, M.P. Fluorogenic Dendrons with Multiple Donor Chromophores as Bright Genetically Targeted and Activated Probes. *J Am Chem Soc* **132**, 11103-11109 (2010).
24. Yushchenko, D.A., Zhang, M., Yan, Q., Waggoner, A.S. & Bruchez, M.P. Genetically Targetable and Color-Switching Fluorescent Probe. *ChemBiochem* **13**, 1564-1568 (2012).
25. Magenau, A.J.D. et al. Genetically targeted fluorogenic macromolecules for subcellular imaging and cellular perturbation. *Biomaterials* **66**, 1-8 (2015).
26. Saurabh, S. et al. Multiplexed Modular Genetic Targeting of Quantum Dots. *Acs Nano* **8**, 11138-11146 (2014).
27. Holleran, J. et al. Fluorogen-Activating Proteins as Biosensors of Cell-Surface Proteins in Living Cells. *Cytom Part A* **77a**, 776-782 (2010).
28. Szent-Gyorgyi, C. et al. Fluorogen-activating single-chain antibodies for imaging cell surface proteins (vol 26, pg 235, 2008). *Nat Biotechnol* **26**, 470-470 (2008).
29. Yan, Q. et al. Near-instant surface-selective fluorogenic protein quantification using sulfonated triarylmethane dyes and fluorogen activating proteins. *Org Biomol Chem* **13**, 2078-2086 (2015).

30. Szent-Gyorgyi, C. et al. Malachite Green Mediates Homodimerization of Antibody V-L Domains to Form a Fluorescent Ternary Complex with Singular Symmetric Interfaces. *J Mol Biol* **425**, 4595-4613 (2013).
31. Babendure, J.R., Adams, S.R. & Tsien, R.Y. Aptamers switch on fluorescence of triphenylmethane dyes. *J Am Chem Soc* **125**, 14716-14717 (2003).
32. Mckay, R.B. An Investigation of Anomalous Staining of Chromatin by Acid Dyes, Methyl Blue and Aniline Blue. *Q J Microsc Sci* **103**, 519-& (1962).
33. Schulte, E., Wittekind, D. & Kretschmer, V. Victoria Blue-B - a Nuclear Stain for Cytology - a Cytophotometric Study. *Histochemistry* **88**, 427-433 (1988).
34. Pratt, C.P., He, J., Wang, Y., Barth, A.L. & Bruchez, M.P. Fluorogenic Green-Inside Red-Outside (GIRO) Labeling Approach Reveals Adenylyl Cyclase-Dependent Control of BKalpha Surface Expression. *Bioconjug Chem* **26**, 1963-1971 (2015).
35. Szent-Gyorgyi, C., Schmidt, B.F., Fitzpatrick, J.A. & Bruchez, M.P. Fluorogenic dendrons with multiple donor chromophores as bright genetically targeted and activated probes. *J Am Chem Soc* **132**, 11103-11109 (2010).
36. Knolker, H.J., Braxmeier, T. & Schlechtingen, G. A Novel Method for the Synthesis of Isocyanates under Mild Conditions. *Angewandte Chemie-International Edition in English* **34**, 2497-2500 (1995).
37. Han, G., Tamaki, M. & Hruby, V. Fast, efficient and selective deprotection of the tert-butoxycarbonyl (Boc) group using HCl/dioxane (4 M). *J Pept Res* **58**, 338-341 (2001).
38. Cardona, C.M. & Gawley, R.E. An improved synthesis of a trifurcated Newkome-type monomer and orthogonally protected two-generation dendrons. *J Org Chem* **67**, 1411-1413 (2002).

Chapter 3: Study of Fluorinated Malachite Green

Introduction

The substitution of hydrogen with fluorine is commonly seen in modern medicinal chemistry, where C–F is the most conservative replacement of C–H bond in size and shape (Table 3.1)^{1,2}. Because C–F is the most stable single bond in organic chemistry, fluorine is often introduced to increase a drug's metabolic stability^{3,4}. Moreover, since fluorine is also the most electronegative atom, such a replacement often leads to significant electronic consequences over the molecule which results in dramatic changes of the molecule's properties such as pK_a , solubility, stability, hydrogen bonding, and spectral properties, often to its advantage^{5,6}. With the rapid development of new organofluorine compounds and fluorination methods, the field of fluorination chemistry has been greatly advanced in the recent 20 years⁷⁻¹⁰. The availability of commercial fluorinated molecules and fluorination methods has enabled scientists to introduce fluorine to fluorophore structures to develop better fluorescent probes for biological applications.

	Bond dissociation energy(kCal mol ⁻¹)	Bond Length	Van der Waals radii/Å	Electronegativity
C-H	98.8	1.09	1.2	2.1
C-F	105.4	1.35	1.47	4.0
C-O	84.0	1.43	1.52	3.5
C-N	69.7	1.47	1.55	3.0
C-C	83.1	1.54	1.7	2.5

Table 3.1: Bond dissociation energies and bond lengths of C–X covalent bonds; the van der Waals radii and electronegativities of elements (X: H, F, O, N, C) on the Pauling scale.

Despite the continuous emergence of novel fluorophores, improvement of fluorescent probes is still extensively relied on experimental screening. The lack of knowledge in predicting specific

molecular properties regarding photochemical characteristics has limited the progress of fluorophore development. Luckily, many synthetic strategies have been developed to investigate the individual effects brought by different modifications. Fluorination, for example, has been found to be a good substitution since the C–F bond is highly polarized and thus introduces a dramatic electrostatic change of interest. Many fluorinated fluorophores have been successfully developed for biological applications (Figure 3.1a)¹¹⁻¹⁵. For example, Armitage’s group has reported a polyfluorinated cyanine dye (F8-S5) which exhibits greatly reduced aggregation in aqueous media, higher quantum yield and more stability towards photobleaching compared to conventional cyanine dyes¹⁶. Fluorinated fluoresceins have been systematically investigated by several groups (Figure 3.1b)¹⁷⁻²⁰, which they found that fluorination of fluorescein generally ionizes at a lower pH (pK_a 3.3-6.1) with improved photostability and bathochromic shifts of both excitation and emission wavelength compared to fluorescein. However, fluorination at different positions may have totally different impacts on their fluorescence quantum yield, extinction coefficient.

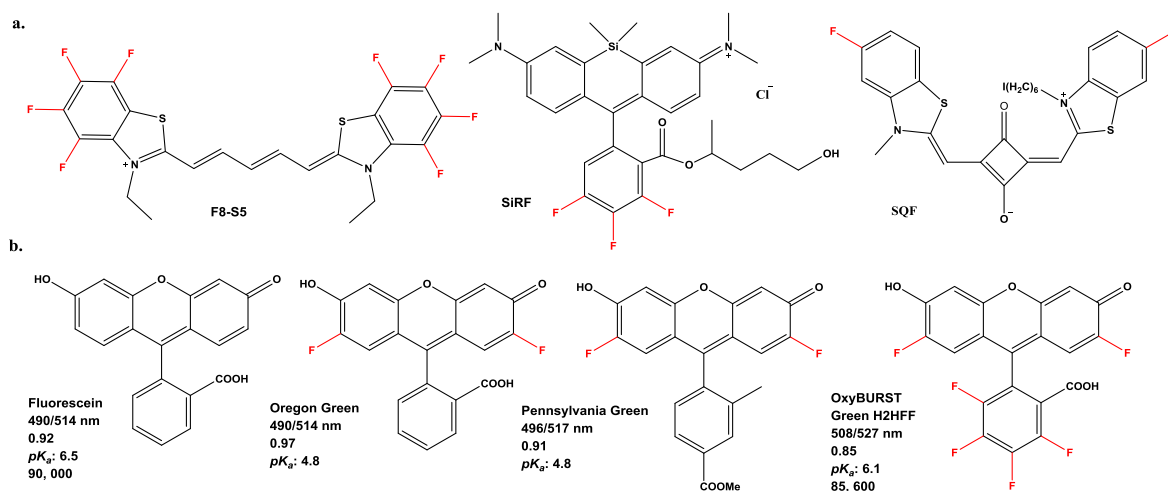


Figure 3.1: a) Structures of selected fluorinated fluorophores: F8-S5¹⁶, SiRF¹⁴, SQF¹⁵; b) fluorinated fluoresceins: Oregon Green, Pennsylvania Green¹⁹ and OxyBURST Green H2HFF²¹ (when oxidized by O_2^-).

A Molecule absorbs in the near infrared (NIR) region (650–900 nm) can be efficiently used to visualize and study *in vivo* molecular targets for the reason of little auto-fluorescence from most tissues (Figure 3.2)²²⁻²⁴. Many efforts have been spent to move commercially available red/far-red emitting chromophores (cyanine, quantum dots and red fluorescent proteins) to the NIR range^{25,26}. Particularly, the infrared-fluorescent proteins (IFP1.4) engineered from *Deinococcus radiodurans*, incorporating biliverdin as the chromophore by Prof. Tsien’s lab has a maximum emission wavelength at 708 nm (extinction coefficient > 90,000 M⁻¹ cm⁻¹; and quantum yield of 0.07) and express well in mammalian cells and mice²⁷. Thus it provides a suitable tool for whole-body imaging. However, the brightness of IFP1.4 is only about 17% of EGFP and it requires exogenous biliverdin addition. Continuous efforts have been made to improve the quantum yield and brightness of near-infrared fluorescent proteins^{28,29}. Thus, to design a genetically targetable NIR fluorescent probe remains an important task in the field of fluorescent imaging, and may find significant applications in many unique clinical situations.

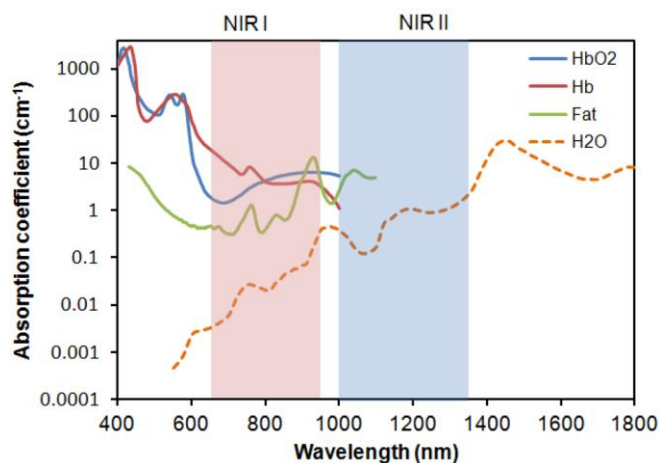


Figure 3.2: Extinction coefficient (on a log scale) of oxygenated hemoglobin, hemoglobin, fatty tissue and water as a function of wavelength. (Image from Figure 2 of Ref. 30)

Introduction of fluorine to fluorogenic dyes that specifically activated by genetically targetable proteins or RNA have also proved to be useful. For example, Armitage’s group has reported a

fluorogenic fluorinated thiazole orange dye (TO-4F) which demonstrated higher fluorescence activation and tighter binding by FAP_{K7} compared to thiazole orange (Figure 3.3a)³¹. In developing GFP mimic RNA-fluorophore (Spinach) imaging, Jaffrey's group found fluorination at the phenol ring (DFHBI) mimics the EGFP with reduced pK_a , 53% brightness of EGFP and improved photostability compared to previously developed DMHBI (Figure 3.3b)³². The fluorescence activation is typically achieved by suppression of free movements of the fluorophore, which promotes fluorescence emission instead of non-radiative de-activation. Thus, we reasoned that potential fluorinations at MG chromophore could be exploited to improve the spectroscopic and photochemical properties of Fluorogen-FAP platform.

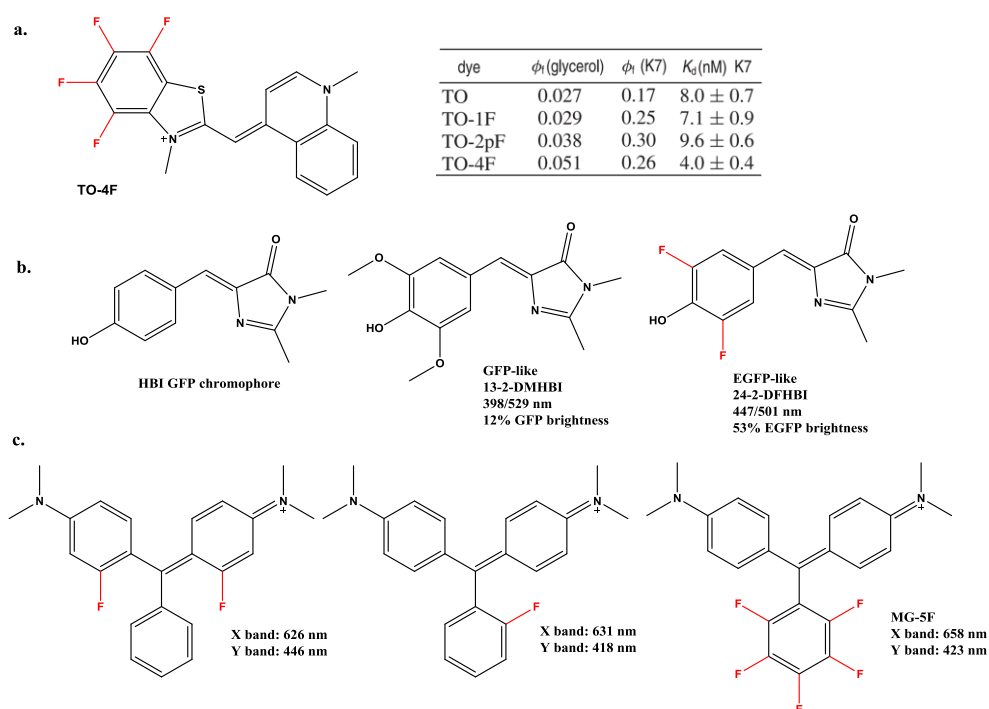


Figure 3.3: a) Structures of fluorinated fluorogenic thiazole orange dyes; b) introduction of fluorine improve the RNA-fluorophore fluorescence performance; c) absorption peak of X (621 nm) and Y (427 nm) band of MG was shift by fluorination.

Previously reports have shown that substitution with a fluorinated moiety of MG will reduce its electron-donating capability, resulting in 10-40 nm bathochromic shift depending on the

fluorination position (Figure 3.3c)^{33,34}. In view of the importance of steric as well as electronic effects in triarylmethane dye spectral properties, the present study was initiated. We hypothesized that fluorination could be introduced at some positions of the MG fluorogen without disrupting its binding affinity to dL5**. Early work performed by Hallas *et al.* has provided us an idea in designing and synthesis of fluorinated MG derivatives with spectral tuning^{33,35-38}. Therefore, we generated a series of spectral varied fluorinated MG ester derivatives (Figure 3.4, 3.5, 3.6). Results showed different fluorination positions have distinct effects in their fluorescence spectra, extinction coefficient, quantum yield and binding affinity. Among those, the emission maximum of MGF2/dL5** reaches 750 nm (80 nm red-shift compare to standard MG ester), which provides potential application for NIR cell imaging.

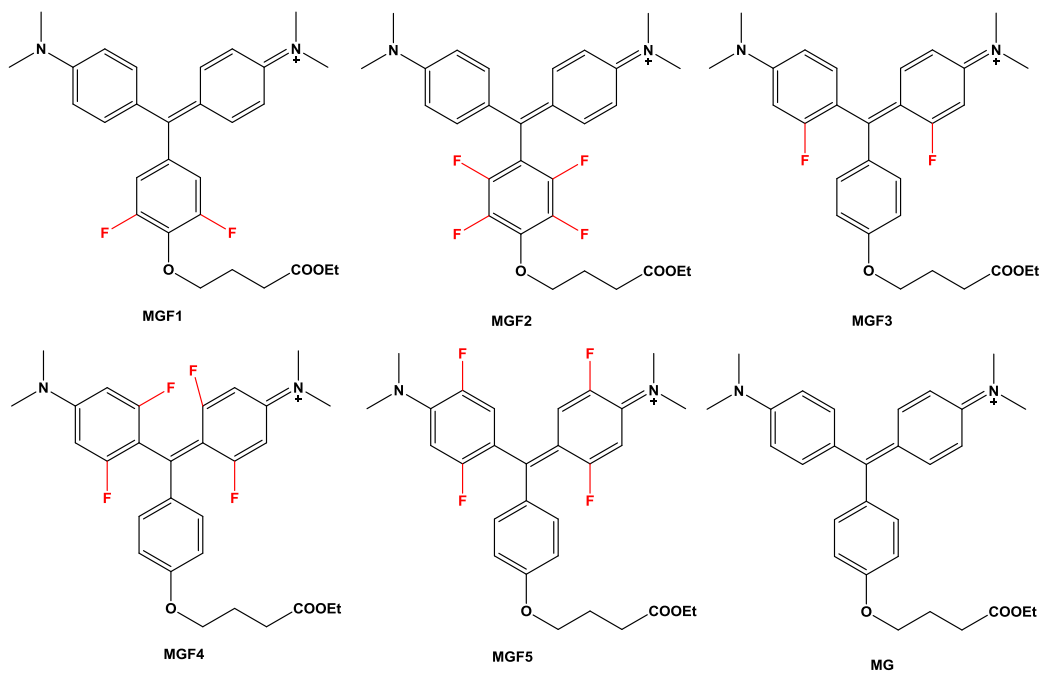


Figure 3.4: Proposed fluorinated MG derivatives

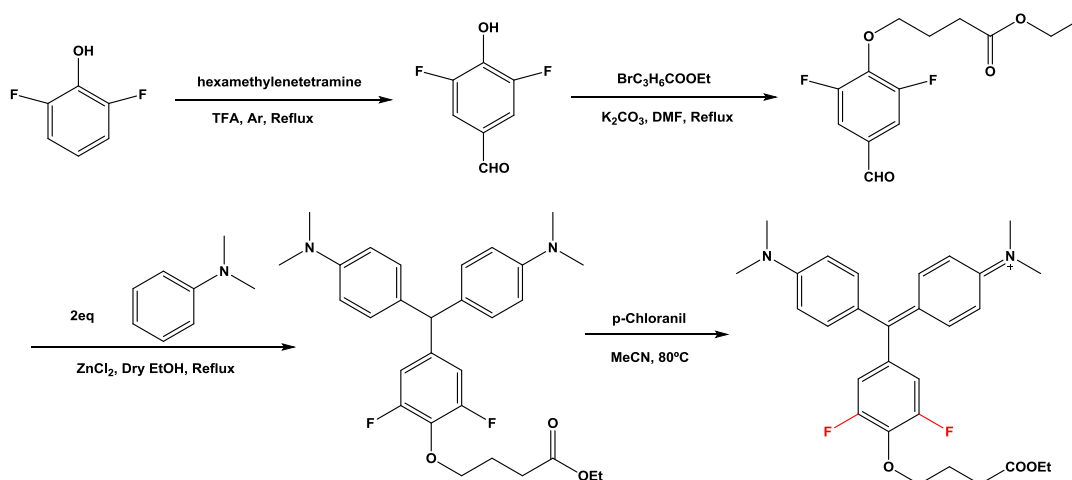


Figure 3.5: Synthetic route for MGF1

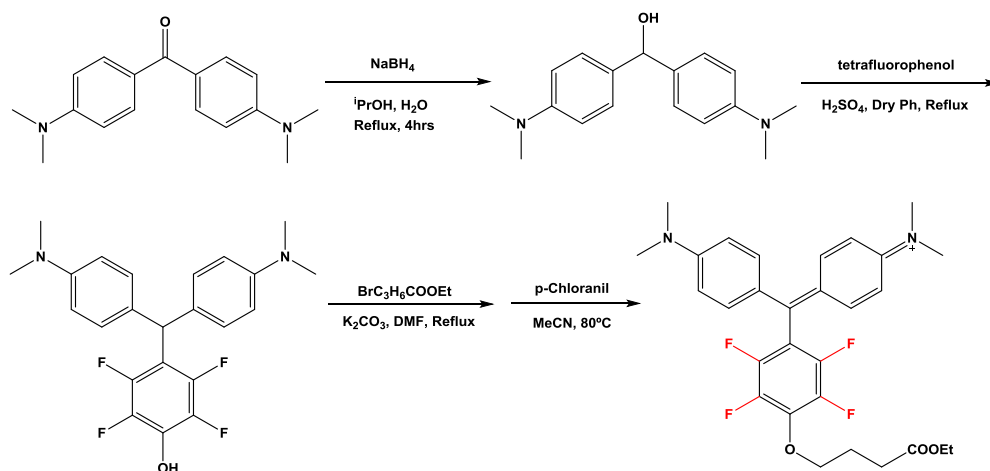


Figure 3.6: Synthetic route for MGF2

Characterization of Fluorinated MG with dL5**

The absorption and fluorescence spectra (Figure 3.7, 3.8), extinction coefficient and fluorescence quantum yield of fluorinated MG series was summarized in Table 3.2. Fluorinations on MG have induced different spectral shifts of free dyes and their fluorescence spectra upon binding with dL5** depending on substitution positions and symmetry. Fluorination of MG can red-shift the X band of excitation spectra from 12 to 46 nm. The shift of Y band is more complicated, a blue shift with decreased intensity is observed when fluorine substitution is on the bottom phenyl ring (MGF1 and MGF2), if hydrogen at the diamino phenyl ring is replaced with

fluorine, the Y band is red-shifted with an increase of intensity (MGF3 and MGF4), brought the X and Y band closer. The excitation/emission maximum of MGF2/dL5** reached 712/750 nm, which is further into NIR range compared to IFP1.4 (685/708 nm). Despite promising spectra change, the fluorinations significantly decreased the quantum yield of the formed complexes, which could be caused by the change of lipophilicity and/or electronegativity in the chromophores. Overall, the fluorinated MG series produced spectra shift, but the impact of fluorination on binding with dL5** is more dramatic than expected.

	Fluorinated positions	Y_{abs} (nm)	X_{abs} (nm)	+dL5** Ex (nm)	+dL5** Em (nm)	ε (M⁻¹cm⁻¹)	+dL5** Φ_F
MGF1	6, 6'-2F	439	630	678	712	7.1	0.037
MGF2	5, 6, 5', 6'-4F	430	652	712	750	11.7	0.0044
MGF3	3,3'-2F	480	618	644	678	5.8	0.033
MGF4	2, 3, 2', 3'-4F	516	628	644(530)	686	4.3	0.003
MGF5	1, 3, 1', 3'-4F	504	636	\	\	<1	\
MG-ester	none	466	606	636(482)	668	9.18	0.123

Table 3.2: Summary of spectral properties of fluorinated MG series free and complexed with excess dL5**, MG-ester is listed as a comparison. (Values are respective absorption maximum of free dye and respective MGF-dL5** complex, ε is the dye alone at its absorption maximum and was measured in pH 7.4 PBS buffer)

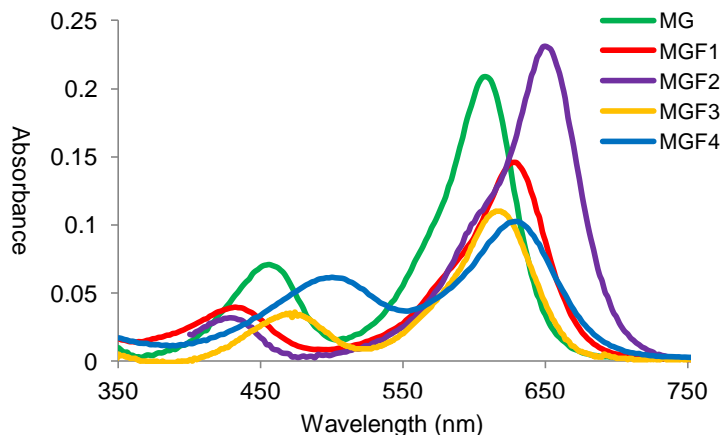


Figure 3.7: Absorption spectra of fluorinated MG series in pH 7.4 PBS buffer at the same concentration.

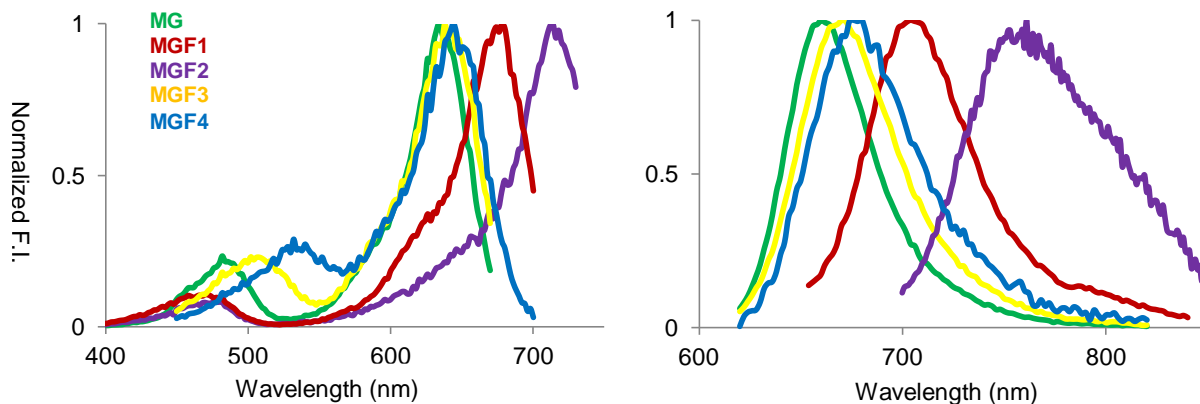


Figure 3.8: Normalized excitation (left) and emission (right) fluorescence spectra of fluorinated MG series upon binding with dL5** (1 μM dye was pre-complexed with 5 μM dL5** for 3 hours)

Upon binding, the absorption peak of MGF2 was significantly red-shifted 60 nm (Figure 3.8), coupling with increased absorbance intensity, where MG-ester only red-shifted 30 nm under the same condition. The large spectral shifts are likely to arise from changes in local electrostatic interactions between the chromophore and surrounding brought by electronegative fluorine atom. While the Stokes shift difference between MGF2/dL5** (38 nm) and MG-ester/dL5** (32 nm) is not that different, it is possible that the large absorption shift upon binding is associated with extremely low fluorescence activation. Further investigation into the difference between the crystal structures of MGF2/dL5** and MG-ester/dL5** might provide us an idea in fluorination effect on binding.

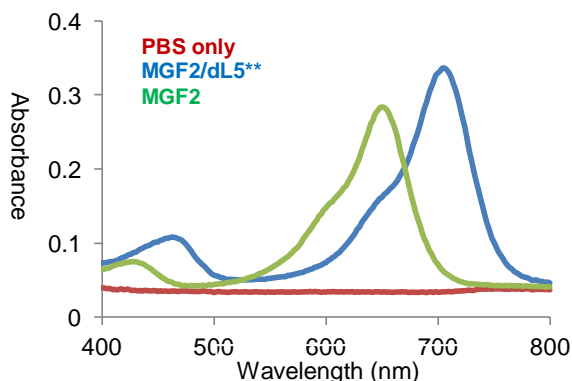


Figure 3.9: Absorption spectra of MGF2 free and bound (5 fold dL5**) at the same concentration in PBS7.4 buffer.

Measuring the binding affinity between fluorinated MG and dL5** become a problem due to the low fluorescence quantum yield from the complexes. So we used MG-ester to compete off the MGF dyes from the pre-complexed equimolar MGF/dL5** complexes (Figure 3.10). Very fast off rate was seen from MGF2 and MGF4, both are tetra-fluorinated derivatives, while di-fluorinated MGF1 and MGF3 are relatively tight binders, indicated that fluorine substitution plays an important role in dye-protein interaction. This result is consistent with corresponding quantum yield results, suggesting loose affinity tend to give a lower quantum yield in this series of dyes.

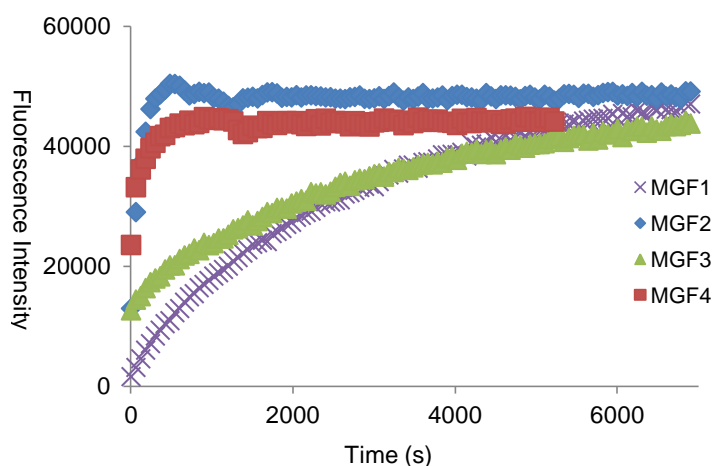


Figure 3.10: 50 nM pre-complexed MGF/dL5** (1:1 ratio) were competing off using 50 nM MG-ester, fluorescence intensity was measured at MG-ester/dL5** channel (ex/em: 633/668 nm) every 1 min for 2 hrs using Tecan Infinite M1000 Plate Spectrometer.

MGF2 has shown promising excitation wavelengths for NIR imaging while maintaining binding properties to the dL5** protein. The Cy5-MGF2 FRET pair was synthesized to improve the brightness of the complex with efficient intramolecular FRET from the Cy5 donor. The absorption spectra of MGF2 and Cy5 alone in PBS buffer is consistent with previous observations (Figure 3.11), it is anticipated that the absorption spectrum of Cy5-MGF2 should simply appear as the sum of corresponding individual spectra. However, when measuring the

absorption spectrum of Cy5-MGF2 in PBS buffer, instead of seeing a sharp peak around 650 nm, the absorption spectrum exhibited two separated peaks at 596 nm (major) and 640 nm (minor).

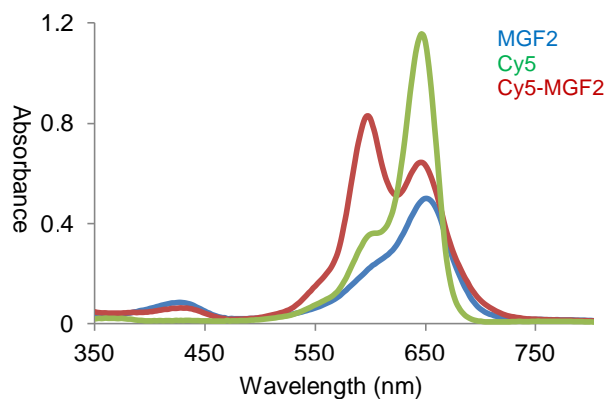


Figure 3.11: absorption spectra of 5 μ M MGF2, Cy5 and Cy5-MGF2 in pH 7.4 PBS buffer. (PerkinElmer Lambda45 spectrophotometer)

We then investigated the appearance of Cy5-MGF2 absorption spectra using mixed DMSO and PBS buffer as solvents. As shown in Figure 3.11, when the percentage of DMSO in the solvent system is increased, the peak at 596 nm generally decreased to the shoulder of Cy5, the other peak at 640 nm is red-shifted with an increase in the absorbance intensity. Finally, the absorption spectrum of Cy5-MGF2 in DMSO is very similar to what we have originally hypothesized. This peak split might be caused by the intra-molecular hetero-H-aggregate through π - π interaction between MGF2 and Cy5, since the fluorescence from Cy5 is quenched, a common feature of H-aggregates³⁹⁻⁴¹. In binding with dL5**, we saw the regeneration of Cy5 fluorescence but minimal energy transfer between Cy5 and MGF2/dL5** pair since we saw no difference between the emission spectra of Cy5 and Cy5-MGF2/dL5** excited at 640 nm.

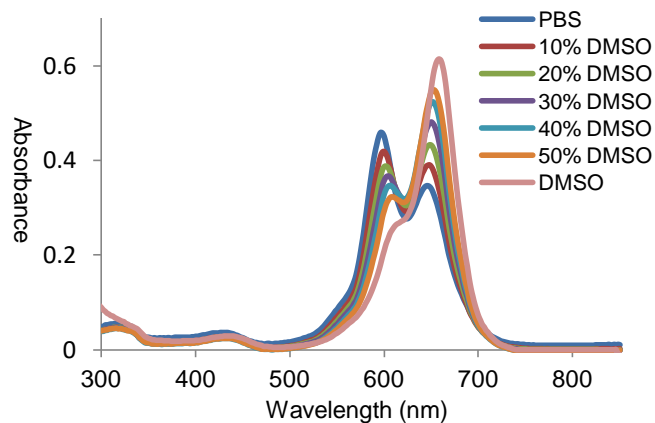


Figure 3.12: Solvent effect on the absorption spectra of Cy5-MGF2 using mixed percentage pH 7.4 PBS buffer and DMSO as co-solvent. (PerkinElmer Lambda45 spectrophotometer)

Summary

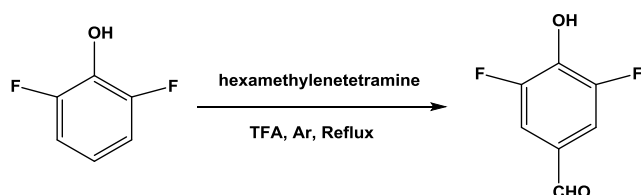
To summarize, we have synthesized a series of fluorinated MG derivatives. Their spectral properties free and bound to dL5** protein were explored in this chapter. While the fluorination provided significant shifts in both x and y bands, it also dramatically affected the fluorescence activation ratio by dL5** protein. Since the fold of activation is dependent upon on effective binding and high quantum yield, the applications of these analogs in complex with dL5** are limited. However, it is possible that through screening of scFv library, tight cognate fluorogen activating proteins for MGF dyes can be discovered.

Experimental Details

^1H NMR and ^{13}C NMR data were recorded from Bruker Avance™ 300 MHz and 500 MHz, J coupling results was calculated using MestReNova software. Mass spectra were obtained from Thermo-Fisher LCQ ESI/APCI Ion Trap using EtOH or 0.1% acetic acid EtOH as solvent. Final products were purified by silica, neutral alumina or reverse-phase chromatography, purity was tested by UPLC using a diode array absorbance detector. Absorbance values of respective free

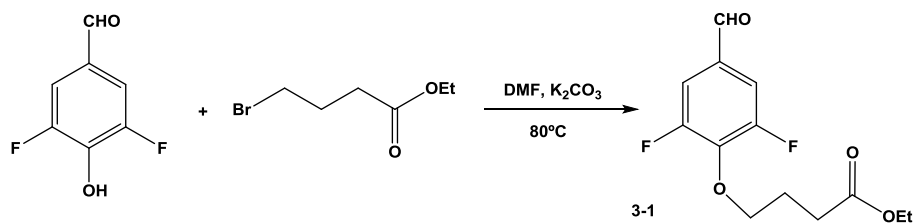
dyes and dye-FAP complexes were measured on a PerkinElmer Lambda45 spectrophotometer. Fluorogenic enhancement was measured in 96 well microplates on a Tecan Infinite M1000 Plate Spectrometer. Corrected emission spectra were taken on a Quantmaster monochromator fluorimeter (Photon Technology International). All electronic files are deposited into the lab folder in Evernote software.

The synthesis of MGF1



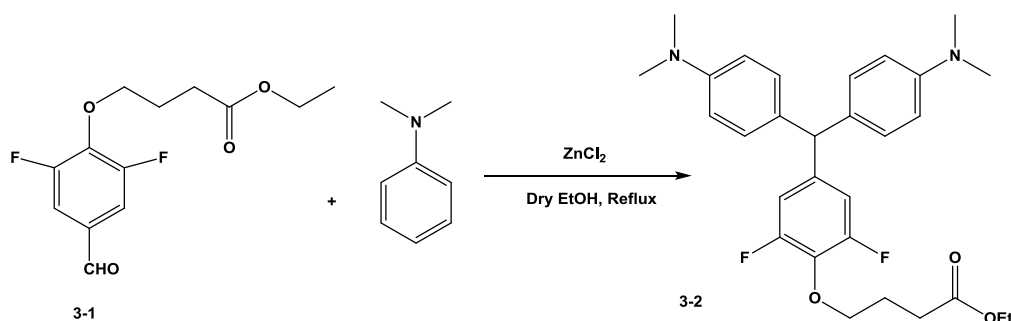
A stirring solution of 4.50 g (34.6 mmol) 2,6-difluorophenol and 4.85 g (34.6 mmol) hexamethylenetetramine in 35 mL TFA was heated at reflux under argon overnight. On cooling to room temperature the solvent was evaporated in vacuum and the crude residue was taken up in 75 mL CH_2Cl_2 . The mixture was washed with a saturated NaHCO_3 aqueous solution (2×50 mL) and the separated aqueous layer was acidified to pH 1 with concentrated HCl. The aqueous layer was extracted with DCM (2×50 mL), the combined organic fractions was dried (MgSO_4) and evaporated in vacuum to give the crude product as cream solid. The crude was purified by column chromatography on silica gel using hexane/ethyl acetate (1/1) to give the product: 3,5-difluoro-4-hydroxybenzaldehyde⁴². The product had a chemical composition of $\text{C}_7\text{H}_4\text{F}_2\text{O}_2$ with M.W. of 158.10 g/mol (yield: 2.90 g, 53%).

^{19}F NMR and ^1H NMR are missed due to untimely backup after facility computer crash (partial data are lost for experiments conducted in-between April 28 2012 and October 2 2012).



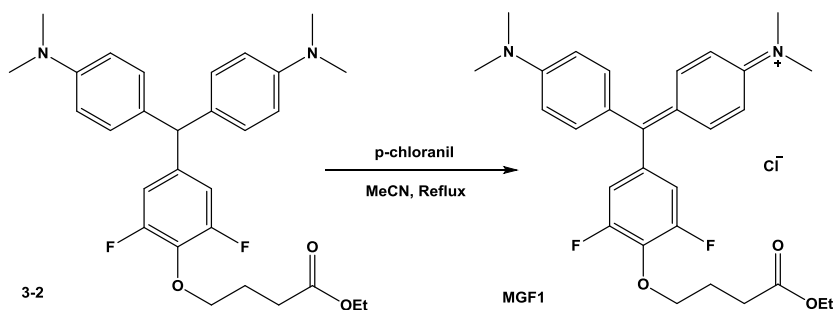
1.60 g (10 mmol) 3,5-difluoro-4-hydroxybenzaldehyde was dissolved in 5 mL dry DMF, added 1.55 g (11 mmol) of finely powdered K_2CO_3 and heated to $80^\circ C$ for 3 hours, the reaction mixture was cooled to room temperature and filtered the precipitate. The solvent was then removed under reduced pressure to afford the crude product, which was purified by column chromatography on silica gel using hexane/ethyl acetate (4/1). The product (3-1) had a chemical composition of $C_{13}H_{14}F_2O_4$ with M.W. of 272.25 g/mol (yield: 2.26 g, 83%). 1H NMR (300 MHz, Chloroform-*d*) δ 9.85 (s, 1H), 7.44 (m, 2H), 4.33 (t, $J = 6.3$ Hz, 2H), 4.17 (q, $J = 6.7$ Hz, 2H), 2.57 (t, $J = 7.0$ Hz, 2H), 2.13 (p, $J = 6.3$ Hz, 2H), 1.38 (t, $J = 7.0$ Hz, 3H). (Appendix 7-12) ESI-MS (+m/z): 273.2.

Results interpreted from 1H NMR and ESI-MS are consistent with the predicted result, no ^{13}C NMR was taken.



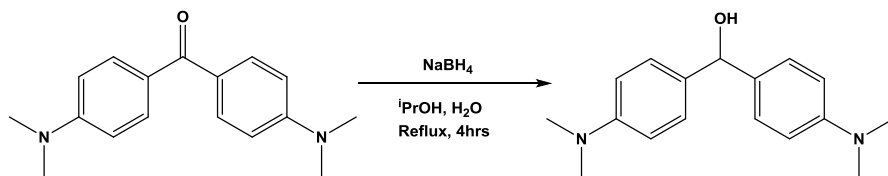
1.36 g (5 mmol) of ethyl 4-(2,6-difluoro-4-formylphenoxy)butanoate (3-1) and 1.27 mL (10 mmol) N,N-dimethylaniline were dissolve in 50 mL dry EtOH, 0.68 g (5 mmol) anhydrous $ZnCl_2$ were added to the solution, it was heated to reflux for 2 days. After the reaction was finished, the reaction mixture was dried under reduced pressure, purified with silica gel (Eluent: 50% hexane / 50% ethyl acetate). The product (3-2) had a chemical composition of $C_{29}H_{34}F_2N_2O_3$ with M.W. of 496.60 g/mol (yield: 1.41 g, 57%). 1H NMR (300 MHz,

Chloroform-*d*) δ 6.97 (d, $J = 9.2$ Hz, 4H), 6.67 (m, 6H), 5.37 (s, 1H), 4.16 (m, 4H), 2.93 (s, 12H), 2.58 (t, $J = 6.7$ Hz, 2H), 2.07 (p, $J = 5.8$ Hz, 2H), 1.29 (t, $J = 6.7$ Hz, 3H). ^{13}C NMR (75 MHz, Chloroform-*d*) δ 173.4, 157.3, 150.7, 135.4, 130.5, 129.7, 118.1, 114.3, 107.7, 99.5, 66.7, 60.6, 40.5, 31, 25.8, 14.3. ESI-MS (+ m/z): 497.2.



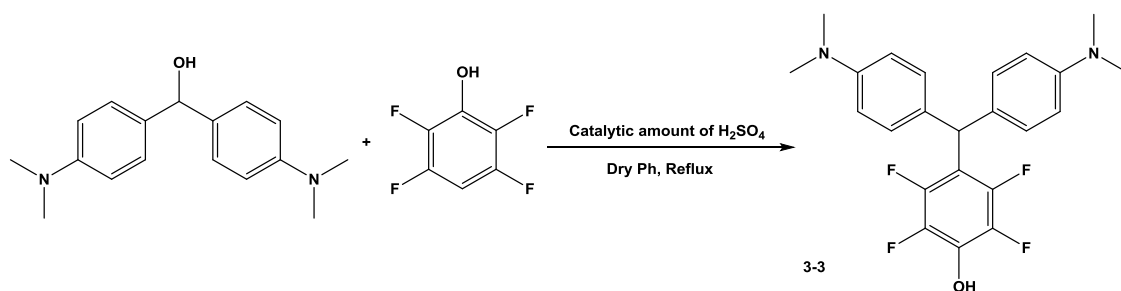
The product (MGF1) had a chemical composition of $\text{C}_{29}\text{H}_{33}\text{ClF}_2\text{N}_2\text{O}_3$ with M.W. of 531.04 g/mol (yield: 82%). ^1H NMR (500 MHz, Chloroform-*d*) δ 7.35 (d, $J = 9.0$ Hz, 4H), 7.01 (d, $J = 9.1$ Hz, 4H), 6.91 (d, $J = 7.9$ Hz, 2H), 4.40 (t, $J = 6.1$ Hz, 2H), 4.15 (q, $J = 7.2$ Hz, 2H), 3.40 (s, 12H), 2.57 (t, $J = 7.3$ Hz, 2H), 2.15 (p, $J = 6.7$ Hz, 2H), 1.27 (d, $J = 7.2$ Hz, 3H). (Appendix 7-13) ^{13}C NMR (125 MHz, Chloroform-*d*) δ 173.1, 157.1, 156.0, 153.8, 140.8, 133.2, 126.8, 118.5, 114.3, 73.7, 60.4, 41.5, 30.3, 25.4, 14.3. ESI-MS (+ m/z): 495.2.

The synthesis of MGF2



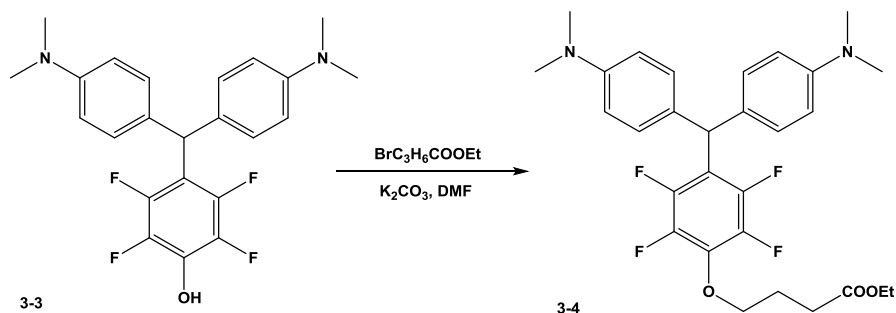
2.68 g of the bis[4-(dimethylamino)phenyl]-benzophenone were dissolved in 12 mL/0.7 mL of $i\text{PrOH}/\text{H}_2\text{O}$, added 0.3 g NaBH_4 . Then, the reaction mixture was heated to reflux for 4 hours. After that, the reaction was cooled down and filtered, wash and recrystallized in EtOH to give the

desired product: 4,4'-Bis(dimethylamino)benzhydryl⁴³. Product was used without further purification.



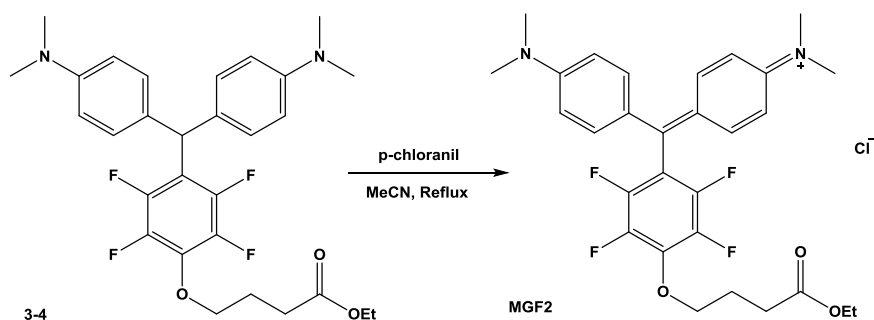
1.08 g (4 mmol) of 4,4'-Bis(dimethylamino)benzhydryl and 0.66 g (4 mmol) of 2,3,5,6-tetrafluorophenol were dissolved in dry benzene, a catalytic amount of H₂SO₄ were added. The reaction was reflux for 1 day. Solvents were then removed under reduced pressure and the crude was washed with water and extract with ethyl acetate. The organic fractions was dried (MgSO₄) and evaporated in vacuum, and then subjected to flash chromatography with 50% hexanes/50% ethyl acetate as eluent to afford product as light yellow oil⁴⁴. The product (3-2) had a chemical composition of C₂₃H₂₂F₄N₂O with M.W. of 418.44 g/mol (53% yield). ¹H NMR (300 MHz, Chloroform-*d*) δ 7.08 (d, *J* = 8.9 Hz, 4H), 6.7 (d, *J* = 8.9 Hz, 4H), 5.7 (s, 1H), 2.94 (s, 12H). (Appendix 7-14) ESI-MS (+*m/z*): 419.2.

Results interpreted from ¹H NMR and ESI-MS are consistent with the predicted result, no ¹³C NMR was taken.



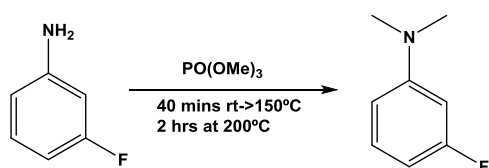
0.93 g (2 mmol) 3-3 was dissolved in 5 mL dry DMF, added 0.31 g (2.2 mmol) of finely powdered K₂CO₃ and heated to 80°C for 3 hours, the reaction mixture was cooled to room

temperature and filtered the precipitate. The solvent was then removed under reduced pressure to afford the crude product, which was purified by column chromatography on silica gel using hexane/ethyl acetate (4/1). The product (3-4) had a chemical composition of $C_{29}H_{32}F_4N_2O_3$ with M.W. of 532.58 g/mol (yield: 0.99 g, 93%). 1H NMR (300 MHz, Chloroform-*d*) δ 7.08 (d, $J = 8.5$ Hz, 4H), 6.69 (m, $J = 9.3$ Hz, 4H), 5.70 (s, 1H), 4.22 (t, $J = 5.9$ Hz, 2H), 3.34 (q, $J = 5.9$ Hz, 2H), 2.94 (s, 12H), 2.45 (t, $J = 7.2$ Hz, 2H), 2.12 (p, $J = 6.5$ Hz, 2H), 1.26 (t, $J = 7.0$ Hz, 3H). ^{13}C NMR (75 MHz, Chloroform-*d*) δ 173.2, 149.6, 145.2, 141.4, 135.8, 129.5, 129.1, 127.5, 112.6, 74.1, 60.7, 44.3, 40.7, 30.5, 25.5, 14.2. ESI-MS (+m/z): 533.3.

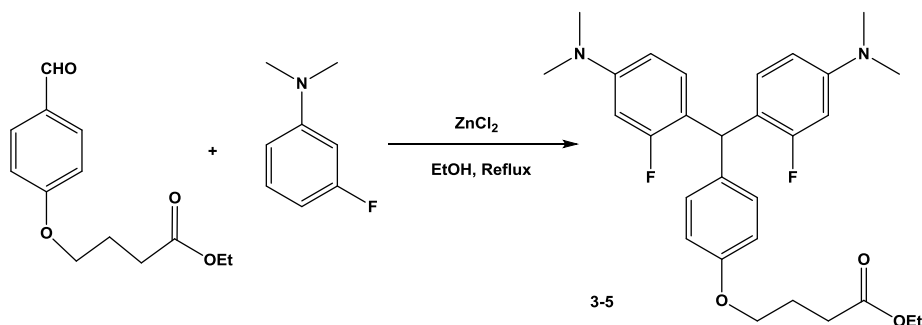


The product (MGF2) had a chemical composition of $C_{29}H_{31}ClF_4N_2O_3$ with M.W. of 567.02 g/mol (yield: 88%). 1H NMR (500 MHz, Chloroform-*d*) δ 7.39 (d, $J = 8.7$ Hz, 4H), 7.03 (m, $J = 9.3$ Hz, 4H), 4.44 (t, $J = 6.1$ Hz, 2H), 3.65 (q, $J = 7.0$ Hz, 2H), 3.39 (s, 12H), 2.54 (t, $J = 7.3$ Hz, 2H), 2.14 (m, 2H), 1.16 (t, $J = 7.0$ Hz, 3H). (Appendix 7-15) ^{13}C NMR (125 MHz, Chloroform-*d*) δ 173, 157.3, 156.7, 145.5, 141.1, 140.4, 139.1, 127.1, 115.3, 111.2, 74.6, 60.7, 41.8, 30.2, 25.3, 14.2. ESI-MS (+m/z): 531.3.

The synthesis of MGF3

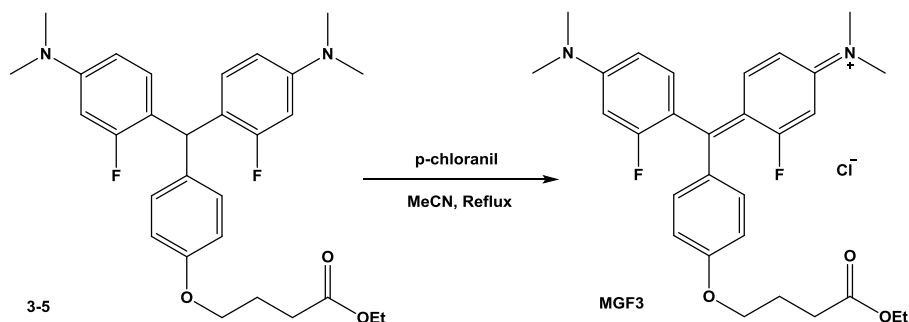


4.81 mL (50 mmol) 3-fluoroaniline were placed under nitrogen atmosphere and combined with 6.1 mL trimethyl phosphate (PO(OMe)₃, 52 mol). The mixture was slowly heated to about 150 °C (over a time period of no less than 40 minutes), and the mixture was refluxed for two hours at a final temperature of about 200°C. The reaction mixture was then cooled to room temperature and slowly added to about 100 mL of NaOH (15 g) aq. solution. The resulting aqueous mixture was then extracted with dichloromethane (DCM) and dried over Na₂SO₄/NaOH. The product was purified by column chromatography on silica gel using hexane/ethyl acetate (4/1) to give (yield: 4.03 g, 58%). This was the common procedure for the preparation of fluorinated dimethylaniline⁴⁵. ¹H NMR (300 MHz, Chloroform-*d*) δ 7.18 (q, *J* = 9.2 Hz, 1H), 6.50 (d, *J* = 9.7 Hz, 1H), 6.44 (m, 2H), 2.97 (s, 6H).



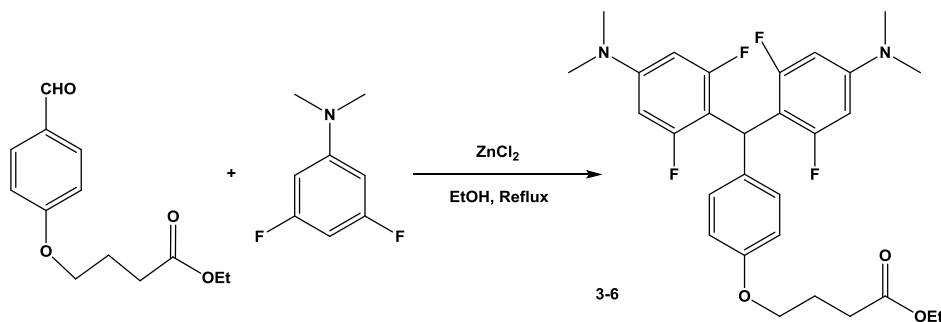
1.18 g (5 mmol) of ethyl 4-(4-formylphenoxy)butanoate and 1.39 g (10 mmol) N,N-dimethyl-3-fluoroaniline were dissolved in 50 mL dry EtOH, 0.68 g (5 mmol) anhydrous ZnCl₂ were added to the solution, it was heated to reflux for 2 days. After the reaction is finished, the reaction mixture was dried under reduced pressure, purified with silica gel (Eluent: 50% ethyl acetate/50% hexane). The product (3-5) had a chemical composition of C₂₉H₃₄F₂N₂O₃ with M.W. of 496.60 g/mol (yield: 0.94 g, 38%). ¹H NMR (300 MHz, Chloroform-*d*) δ 7.04 (d, *J* = 8.3 Hz, 2H), 6.81 (d, *J* = 9.2 Hz, 2H), 6.78 (d, *J* = 9.2 Hz, 2H), 6.39 (m, 4H), 5.82 (s, 1H), 4.16 (q, *J* = 6.6 Hz, 2H), 3.99 (t, *J* = 6.7 Hz, 2H), 2.94 (s, 12H), 2.52 (t, *J* = 7.5 Hz, 2H), 2.12 (p, *J* = 6.6 Hz, 2H), 1.27 (t, *J* = 7.5 Hz, 3H). ESI-MS (+*m/z*): 497.2.

Results interpreted from ^1H NMR and ESI-MS are consistent with the predicted result, no ^{13}C NMR was taken.



The product (MGF3) had a chemical composition of $\text{C}_{29}\text{H}_{33}\text{ClF}_2\text{N}_2\text{O}_3$ with M.W. of 531.04 g/mol (67% yield). ^1H NMR (300 MHz, Chloroform- d) δ 7.30 (d, $J = 8.3$ Hz, 2H), 7.06 (m, 4H), 6.76 (dd, $J = 9.3, 2.5$ Hz, 2H), 6.51 (dd, $J = 15.0, 2.4$ Hz, 2H), 4.17 (qd, $J = 7.2, 6.7, 2.3$ Hz, 4H), 3.37 (s, 12H), 2.55 (t, $J = 7.2$ Hz, 2H), 2.19 (q, $J = 6.6$ Hz, 2H), 1.28 (d, $J = 7.1$ Hz, 3H). (Appendix 7-16) ^{13}C NMR (75 MHz, Chloroform- d) δ 173, 166.8, 165, 158.7, 140.4, 137.7, 132, 128.6, 117.6, 115.3, 110.3, 99.6, 67.8, 60.6, 41.4, 30.6, 24.4, 14.3. ESI-MS (+m/z): 495.2.

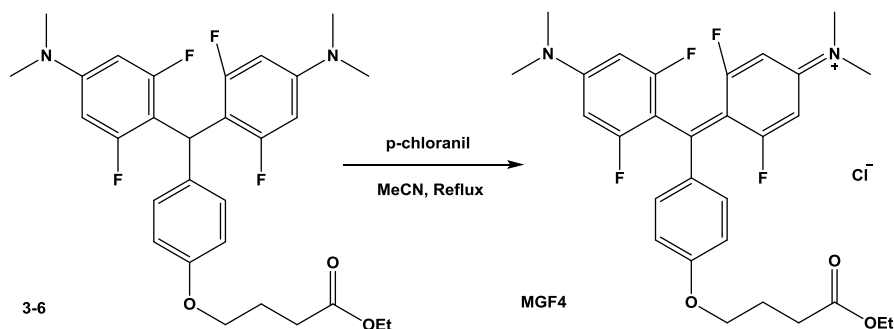
Synthesis of MGF4 and MGF5 are similar to MGF3



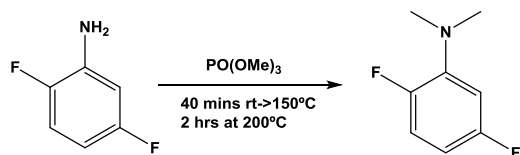
The product (3-6) had a chemical composition of $\text{C}_{29}\text{H}_{32}\text{F}_4\text{N}_2\text{O}_3$ with M.W. of 532.58 g/mol (yield: 43%). ^1H NMR (500 MHz, Chloroform- d) δ 7.10 (d, $J = 8.3$ Hz, 2H), 6.81 (d, $J = 8.7$ Hz, 2H), 6.18 (dd, $J = 8.2, 3.7$ Hz, 4H), 5.95 (s, 1H), 4.17 (q, $J = 7.2$ Hz, 2H), 4.00 (t, $J = 6.1$ Hz, 2H), 2.93 (s, 13H), 2.53 (t, $J = 7.3$ Hz, 2H), 2.11 (p, $J = 6.5$ Hz, 2H), 1.28 (t, $J = 7.1$ Hz, 3H). ^{13}C

NMR (125 MHz, Chloroform-*d*) δ 173.5, 162.5, 157.3, 150.5, 133.7, 128.7, 114.0, 105.4, 95.5, 66.7, 60.4, 40.3, 33.7, 30.9, 24.8, 14.3. ESI-MS (+*m/z*): 533.3.

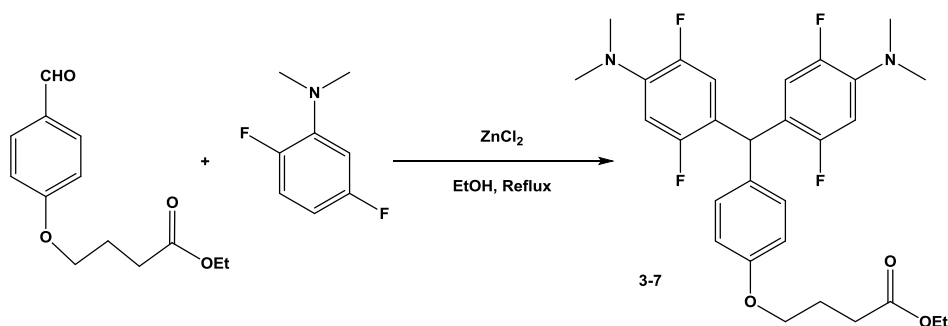
^1H NMR and ^{13}C NMR shifts were compared with predicted value and summarized in appendix 7-17.



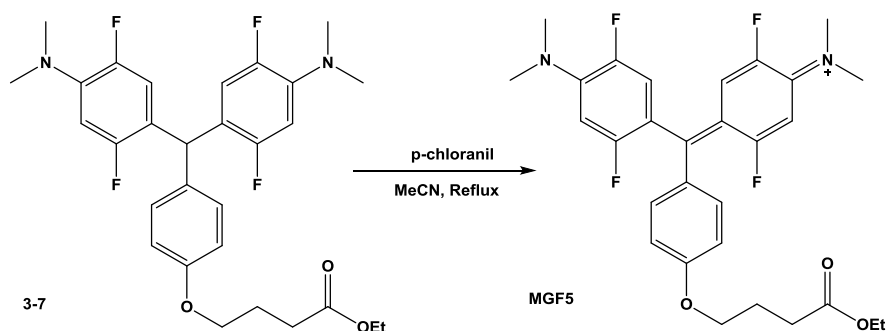
The product (MGF4) had a chemical composition of $\text{C}_{29}\text{H}_{31}\text{ClF}_4\text{N}_2\text{O}_3$ with M.W. of 567.02 g/mol (yield: 44%). ^1H NMR (500 MHz, Chloroform-*d*) δ 7.41 (m, 2H), 7.03 (m, 2H), 6.48 (m, 4H), 4.17 (m, 4H), 3.40 (s, 12H), 2.56 (t, $J = 6.4$ Hz, 2H), 2.22 (t, $J = 7.5$ Hz, 2H), 1.27 (t, $J = 7.5$ Hz, 3H). (Appendix 7-18) ^{13}C NMR (125 MHz, Chloroform-*d*) δ 173.3, 158.2, 156.8, 154.8, 131.1, 129.9, 119.2, 116.1, 115, 114.6, 66.7, 60.5, 45.2, 30.5, 24.3, 14.3. ESI-MS (+*m/z*): 531.3.



^1H NMR (300 MHz, Chloroform-*d*) δ 6.94 (ddd, $J = 12.6, 8.8, 5.4$ Hz, 1H), 6.55 (m, 2H), 2.87 (d, $J = 1.0$ Hz, 6H). ^{13}C NMR (75 MHz, Chloroform-*d*) δ 116.5, 116.2, 106.1, 105.7, 105.3, 104.8, 42.6.

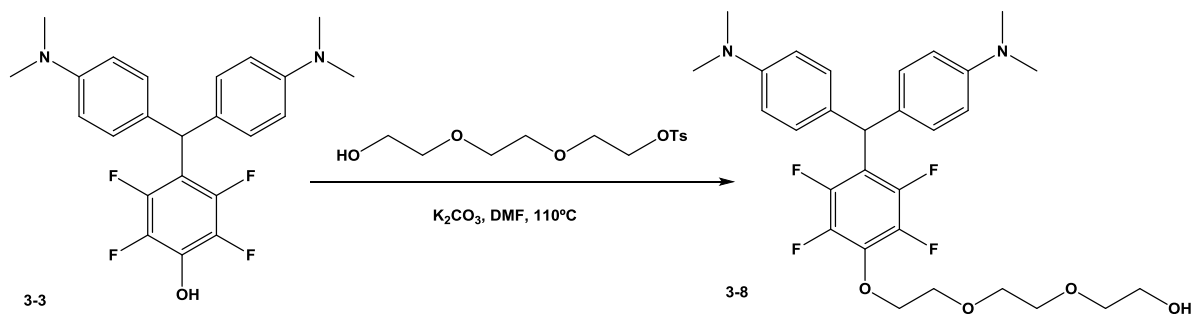


The product (3-7) had a chemical composition of $C_{29}H_{32}F_4N_2O_3$ with M.W. of 567.02 g/mol (yield: 32%). 1H NMR (300 MHz, Chloroform-*d*) δ 7.00 (d, $J = 8.3$ Hz, 2H), 6.83 (d, $J = 8.3$ Hz, 2H), 6.55 (m, 4H), 5.78 (s, 1H), 4.16 (m, 2H), 4.02 (t, $J = 6.7$ Hz, 2H), 2.83 (s, 12H), 2.52 (t, $J = 6.7$ Hz, 2H), 2.13 (m, 2H), 1.27 (t, $J = 6.7$ Hz, 3H). (Appendix 7-19) ^{13}C NMR (75 MHz, Chloroform-*d*) δ 173.3, 157.7, 148.8, 133.5, 129.4, 120.9, 116.8, 114.6, 115.1, 66.7, 60.4, 42.9, 40.8, 31, 24.9, 14.6. ESI-MS (+m/z): 533.2.



No 1H NMR or ^{13}C NMR for MGF5 due to extremely low yield and instability in solvent

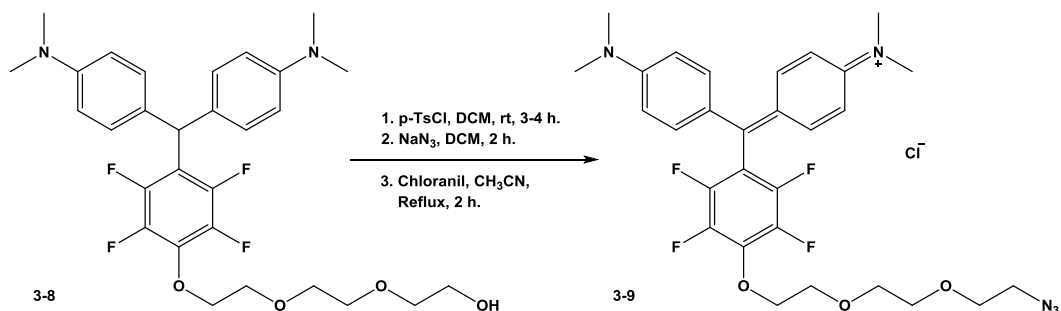
The synthesis of Cy5-MGF2



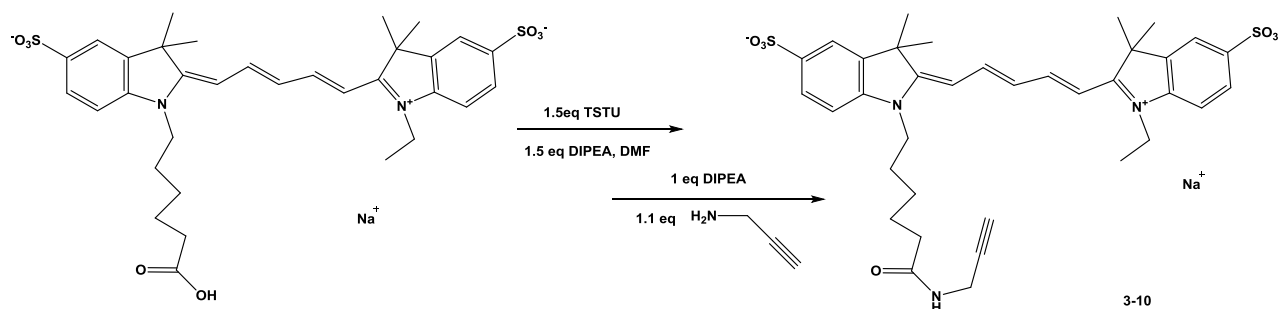
0.94 g (2 mmol) 3-3 was dissolved in 5 mL dry DMF, added 0.31 g (2.2 mmol) finely powdered K_2CO_3 and heated to 80°C for 3 hours. Then, 0.67 g (2.2 mmol) triethylene glycol monotosylate was added to the reaction. The reaction mixture was cooled to room temperature and filtered the precipitate. The solvent was then removed under reduced pressure to afford the crude product, which was purified by column chromatography on silica gel using 75% hexane/25% ethyl acetate. The product (3-8) had a chemical composition of $C_{29}H_{34}F_4N_2O_4$ with M.W. of 567.02

g/mol (yield: 0.93 g, 82%). ^1H NMR (500 MHz, Chloroform-*d*) δ 7.10 (d, $J = 8.6$ Hz, 4H), 6.70 (d, $J = 8.9$ Hz, 4H), 5.72 (s, 1H), 4.36 (m, 2H), 3.85 (m, 2H), 3.74 (m, 4H), 3.68 (m, 2H), 3.60 (m, 2H), 2.95 (s, 12H). (Appendix 7-20) ESI-MS (+ m/z): 551.3.

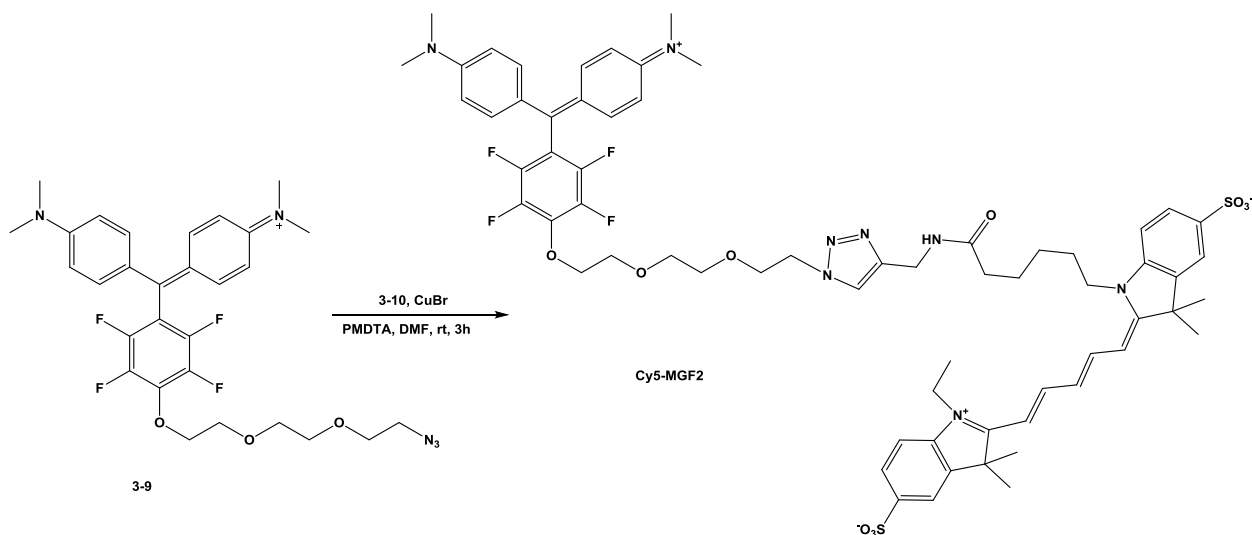
Results interpreted from ^1H NMR and ESI-MS are consistent with the predicted result, no ^{13}C NMR was taken.



0.21 g (1.1 mmol) *p*-TsCl was added to 0.57 g (1 mmol) 3-8 in 10 mL CH_2Cl_2 , the reaction was allowed to stir at room temperature for 3 to 4 hours until it is fully reacted. Then, 0.07 g (1.1 mmol) sodium azide was added to the reaction mixture, and after another 2 hours, TLC was used to determine the completion of the reaction. The solvent were dried under reduced pressure, and the crude was applied to a column, washing with CHCl_3 to give the reduced form of 3-9, which was oxidized in the common process. The product (3-8) had a chemical composition of $\text{C}_{29}\text{H}_{32}\text{ClF}_4\text{N}_5\text{O}_3$ with M.W. of 610.05 g/mol (overall yield: 0.41 g, 66%). ^1H NMR (500 MHz, Chloroform-*d*) δ 7.40 (d, $J = 9.3$ Hz, 2H), 7.03 (d, $J = 9.3$ Hz, 2H), 4.55 (t, $J = 4.5$ Hz, 1H), 3.89 (m, 2H), 3.73 (m, 2H), 3.67 (m, 4H), 3.40 (s, 12H), 3.36 (t, $J = 5.0$ Hz, 2H). ^{13}C NMR (125 MHz, Chloroform-*d*) δ 157.4, 156.8, 145.4, 141.2, 140.8, 139.1, 127.2, 115.1, 111.2, 74.6, 70.9, 70.6, 70.2, 70, 50.8, 41.7. ESI-MS (+ m/z): 574.3.



To 0.068 g (0.1 mmol) Cy5 carboxylic acid (synthesized and provided by Dr. Brigitte Schmidt⁴¹) in 3 mL dry DMF, 0.045 g (0.15 mmol) TSTU was added followed by adding 0.02 g (0.15 mmol) DIPEA. Reverse phase TLC was used to detect the completion of the activation of carboxylic acid. Then, another 0.013 g (0.1 mmol) DIPEA and 0.006 g (0.11 mmol) of propargylamine were added. This should quantitatively afford the Cy5 alkyne as product⁴⁶. The crude was purified in a reverse phase column with MeCN/Water. The product (3-10) had a chemical composition of $C_{36}H_{42}N_3NaO_7S_2$ with M.W. of 715.86 g/mol (overall yield: 0.063 g, 89%). ¹H NMR (300 MHz, Methanol-*d*₄) δ 8.32 (m, 2H), 7.91 (m, 4H), 7.36 (m, 2H), 6.73 (t, *J* = 12.4 Hz, 1H), 6.38 (dd, *J* = 13.7, 4.4 Hz, 2H), 4.17 (dq, *J* = 12.9, 6.9 Hz, 4H), 3.93 (d, *J* = 2.6 Hz, 2H), 3.62 (q, *J* = 7.1 Hz, 2H), 3.31 (m, 1H), 2.22 (t, *J* = 7.3 Hz, 2H), 1.83 (p, *J* = 7.4 Hz, 2H), 1.75 (s, 6H), 1.68 (q, *J* = 7.4 Hz, 2H), 1.39 (m, 8H), 1.19 (t, *J* = 7.0 Hz, 3H). (Appendix 7-21) ESI-MS (-*m/z*): 692.4.



0.061 g (0.1 mmol 3-9) was dissolved in 5 mL dry DMF under Argon, catalytic amount of CuBr and PMDTA was added. Then, 0.063 g (0.09 mmol) 3-10 was added to the reaction. After stirred at room temperature for 3 hours, the reaction mixture was washed with CHCl_3 (50 mL) and water (50 mL) for 3 times, and 1 more time with Brine (50 mL). The final product was purified with reverse phase column using MeCN/Water as eluents. The product (Cy5-MGF2) had a chemical composition of $\text{C}_{65}\text{H}_{74}\text{N}_4\text{F}_8\text{O}_{10}\text{S}_2$ with M.W. of 1267.47 g/mol (overall yield: 0.094 g, 83%). ESI-MS (-m/z): 1266.5.

Due to the hydrophilic and hydrophobic moieties from the molecule and small amount of product, ^1H NMR was taken but not resolvable for all peaks.

After a series of reactions have been conducted, their reactivity is shown in Figure 3.13. To conclude, fluorination on the ortho position decreases the reactivity of dimethylaminophenyl in the condensation reaction with aldehyde. This is the biggest effect compared to the hindrance caused by the C-F bond on the meta position. The last two show no reactions after 2 days.

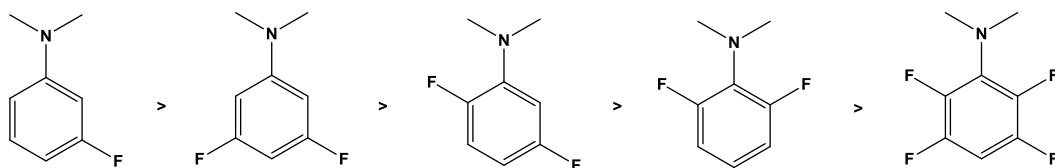


Figure 3.13: Reactivity of fluorinated dimethylaminophenyl in condensation reaction with benzaldehyde.

References:

- 1 Bohm, H. J. *et al.* Fluorine in medicinal chemistry. *Chembiochem* **5**, 637-643, doi:10.1002/cbic.200301023 (2004).
- 2 O'Hagan, D. Understanding organofluorine chemistry. An introduction to the C-F bond. *Chem Soc Rev* **37**, 308-319, doi:10.1039/b711844a (2008).
- 3 Furuya, T., Kuttruff, C. A. & Ritter, T. Carbon-fluorine bond formation. *Curr Opin Drug Disc* **11**, 803-819 (2008).
- 4 O'Hagan, D. Fluorine in health care Organofluorine containing blockbuster drugs. *J Fluorine Chem* **131**, 1071-1081, doi:10.1016/j.jfluchem.2010.03.003 (2010).
- 5 Hagmann, W. K. The many roles for fluorine in medicinal chemistry. *J Med Chem* **51**, 4359-4369, doi:10.1021/jm800219f (2008).
- 6 Lin, J. H. & Lu, A. Y. H. Role of pharmacokinetics and metabolism in drug discovery and development. *Pharmacol Rev* **49**, 403-449 (1997).
- 7 Purser, S., Moore, P. R., Swallow, S. & Gouverneur, V. Fluorine in medicinal chemistry. *Chem Soc Rev* **37**, 320-330, doi:10.1039/b610213c (2008).
- 8 Nagib, D. A. & MacMillan, D. W. C. Trifluoromethylation of arenes and heteroarenes by means of photoredox catalysis. *Nature* **480**, 224-228, doi:10.1038/nature10647 (2011).
- 9 Furuya, T., Kamlet, A. S. & Ritter, T. Catalysis for fluorination and trifluoromethylation. *Nature* **473**, 470-477, doi:10.1038/nature10108 (2011).
- 10 Liang, T., Neumann, C. N. & Ritter, T. Introduction of Fluorine and Fluorine-Containing Functional Groups. *Angew Chem Int Edit* **52**, 8214-8264, doi:10.1002/anie.201206566 (2013).
- 11 Mitronova, G. Y. *et al.* New fluorinated rhodamines for optical microscopy and nanoscopy. *Chemistry* **16**, 4477-4488, doi:10.1002/chem.200903272 (2010).
- 12 Spagnuolo, C. C., Vermeij, R. J. & Jares-Erijman, E. A. Improved photostable FRET-competent biarsenical-tetracysteine probes based on fluorinated fluoresceins. *J Am Chem Soc* **128**, 12040-12041, doi:10.1021/ja063212q (2006).
- 13 Hirano, T., Kikuchi, K., Urano, Y. & Nagano, T. Improvement and biological applications of fluorescent probes for zinc, ZnAFs. *J Am Chem Soc* **124**, 6555-6562 (2002).
- 14 Kolmakov, K. *et al.* Far-Red Emitting Fluorescent Dyes for Optical Nanoscopy: Fluorinated Silicon-Rhodamines (SiRF Dyes) and Phosphorylated Oxazines. *Chem-Eur J* **21**, 13344-13356, doi:10.1002/chem.201501394 (2015).

- 15 Renard, B. L., Aubert, Y. & Asseline, U. Fluorinated squaraine as near-IR label with improved properties for the labeling of oligonucleotides. *Tetrahedron Lett* **50**, 1897-1901, doi:10.1016/j.tetlet.2009.02.029 (2009).
- 16 Renikuntla, B. R., Rose, H. C., Eldo, J., Waggoner, A. S. & Armitage, B. A. Improved photostability and fluorescence properties through polyfluorination of a cyanine dye. *Org Lett* **6**, 909-912, doi:10.1021/ol036081w (2004).
- 17 Sun, W. C., Gee, K. R., Klaubert, D. H. & Haugland, R. P. Synthesis of fluorinated fluoresceins. *J Org Chem* **62**, 6469-6475, doi:DOI 10.1021/jo9706178 (1997).
- 18 Spagnuolo, C. C. *et al.* Photostability and Spectral Properties of Fluorinated Fluoresceins and their Biarsenical Derivatives: A Combined Experimental and Theoretical Study. *Photochem Photobiol* **85**, 1082-1088, doi:10.1111/j.1751-1097.2009.00565.x (2009).
- 19 Mottram, L. F., Boonyarattanakalin, S., Kovel, R. E. & Peterson, B. R. The Pennsylvania green fluorophore: A hybrid of Oregon Green and Tokyo Green for the construction of hydrophobic and pH-insensitive molecular probes. *Org Lett* **8**, 581-584, doi:10.1021/ol052655g (2006).
- 20 Funabiki, K. *et al.* Ring-fluorinated fluoresceins as an organic photosensitizer for dye-sensitized solar cells using nanocrystalline zinc oxide. *J Fluorine Chem* **127**, 257-262, doi:10.1016/j.jfluchem.2005.12.009 (2006).
- 21 Chen, C. S. & Chen, W. N. U. Phorbol ester induces elevated oxidative activity and alkalization in a subset of lysosomes. *Mol Biol Cell* **11**, 524a-524a (2000).
- 22 Weissleder, R. A clearer vision for in vivo imaging. *Nat Biotechnol* **19**, 316-317, doi:Doi 10.1038/86684 (2001).
- 23 Schaafsma, B. E. *et al.* The Clinical Use of Indocyanine Green as a Near-Infrared Fluorescent Contrast Agent for Image-Guided Oncologic Surgery. *J Surg Oncol* **104**, 323-332, doi:10.1002/jso.21943 (2011).
- 24 Vahrmeijer, A. L., Hutteman, M., van der Vorst, J. R., van de Velde, C. J. H. & Frangioni, J. V. Image-guided cancer surgery using near-infrared fluorescence. *Nat Rev Clin Oncol* **10**, 507-518, doi:10.1038/nrclinonc.2013.123 (2013).
- 25 Frangioni, J. V. In vivo near-infrared fluorescence imaging. *Curr Opin Chem Biol* **7**, 626-634, doi:10.1016/j.cbpa.2003.08.007 (2003).
- 26 Luo, S. L., Zhang, E. L., Su, Y. P., Cheng, T. M. & Shi, C. M. A review of NIR dyes in cancer targeting and imaging. *Biomaterials* **32**, 7127-7138, doi:10.1016/j.biomaterials.2011.06.024 (2011).
- 27 Shu, X. *et al.* Mammalian expression of infrared fluorescent proteins engineered from a bacterial phytochrome. *Science* **324**, 804-807, doi:10.1126/science.1168683 (2009).

- 28 Yu, D. *et al.* An improved monomeric infrared fluorescent protein for neuronal and tumour brain imaging. *Nature Communications* **5**, doi:ARTN 362610.1038/ncomms4626 (2014).
- 29 Filonov, G. S. *et al.* Bright and stable near-infrared fluorescent protein for in vivo imaging. *Nat Biotechnol* **29**, 757-U133, doi:10.1038/nbt.1918 (2011).
- 30 Quek, C. H. & Leong, K. W. Near-Infrared Fluorescent Nanoprobes for in Vivo Optical Imaging. *Nanomaterials-Basel* **2**, 92-112, doi:10.3390/nano2020092 (2012).
- 31 Shank, N. I., Zanotti, K. J., Lanni, F., Berget, P. B. & Armitage, B. A. Enhanced Photostability of Genetically Encodable Fluoromodules Based on Fluorogenic Cyanine Dyes and a Promiscuous Protein Partner. *J Am Chem Soc* **131**, 12960-12969, doi:10.1021/ja9016864 (2009).
- 32 Paige, J. S., Wu, K. Y. & Jaffrey, S. R. RNA Mimics of Green Fluorescent Protein. *Science* **333**, 642-646, doi:10.1126/science.1207339 (2011).
- 33 Hallas, G., Grocock, D. E., Hepworth, J. D. & Jones, A. M. Dyes Containing Fluorine .1. Electronic Absorption-Spectrum of 2,3,4,5,6-Pentafluoro Malachite Green and Electronic Effect of Pentafluorophenyl Group. *Tetrahedron* **28**, 893-&, doi:Doi 10.1016/0040-4020(72)84048-1 (1972).
- 34 Kraus, G. A. *et al.* Fluorinated analogs of malachite green: Synthesis and toxicity. *Molecules* **13**, 986-994, doi:DOI 10.3390/molecules13040986 (2008).
- 35 Hallas, G., Grocock, D. E. & Hepworth, J. D. Steric and Electronic Effects in Basic Dyes .1. Electronic Absorption Spectra of Derivatives of Malachite Green Containing Trifluoromethyl Groups in Phenyl Ring. *J Soc Dyers Colour* **86**, 200-& (1970).
- 36 Ferguson, A. S. & Hallas, G. Steric and Electronic Effects in Basic Dyes .2. Electronic Absorption Spectra of Derivatives of Malachite Green Containing Electron-Withdrawing Substituents in Phenyl Ring. *J Soc Dyers Colour* **87**, 187-& (1971).
- 37 Castelin.Rw, Taylor, D. C. & Hallas, G. Steric and Electronic Effects in Basic Dyes .3. Electronic Absorption-Spectra of Lilolidine and 1-Methylindoline Analogs of Michlers Hydrol Blue, Malachite Green and Crystal Violet. *J Soc Dyers Colour* **88**, 25-& (1972).
- 38 Ferguson, A. S. & Hallas, G. Steric and Electronic Effects in Basic Dyes .4. Electronic Absorption-Spectra of Derivatives of Malachite Green Containing More Than One Substituent in Phenyl Ring. *J Soc Dyers Colour* **89**, 22-24 (1973).
- 39 Rosch, U., Yao, S., Wortmann, R. & Wurthner, F. Fluorescent H-aggregates of merocyanine dyes. *Angew Chem Int Ed Engl* **45**, 7026-7030, doi:10.1002/anie.200602286 (2006).

- 40 Yushchenko, D. A., Zhang, M., Yan, Q., Waggoner, A. S. & Bruchez, M. P. Genetically Targetable and Color-Switching Fluorescent Probe. *Chembiochem* **13**, 1564-1568, doi:10.1002/cbic.201200334 (2012).
- 41 Szent-Gyorgyi, C., Schmidt, B. F., Fitzpatrick, J. A. J. & Bruchez, M. P. Fluorogenic Dendrons with Multiple Donor Chromophores as Bright Genetically Targeted and Activated Probes. *J Am Chem Soc* **132**, 11103-11109, doi:10.1021/ja9099328 (2010).
- 42 Lawrence, N. J., Hepworth, L. A., Rennison, D., McGown, A. T. & Hadfield, J. A. Synthesis and anticancer activity of fluorinated analogues of combretastatin A-4. *J Fluorine Chem* **123**, 101-108, doi:10.1016/S0022-1139(03)00117-9 (2003).
- 43 Dumur, F. *et al.* New chelating stilbazonium-like dyes from Michler's ketone. *Org Lett* **10**, 321-324, doi:10.1021/ol7027931 (2008).
- 44 Malpert, J. H. *et al.* Color intensity control in polymers using triarylmethane leuconitriles as color formers. *Tetrahedron* **57**, 967-974, doi:Doi 10.1016/S0040-4020(00)01088-7 (2001).
- 45 Brown, S. B. T. T., 15 Southway Manor Par, Burley-in-Wharfedale West Yorkshire, GB), O'grady, Cassandra Claire. DEVELOPMENTS IN BIOLOGICALLY ACTIVE METHYLENE BLUE DERIVATIVES (2). (2005).
- 46 Uzagare, M. C., Claussnitzer, I., Gerrits, M. & Bannwarth, W. Site specific chemoselective labelling of proteins with robust and highly sensitive Ru(II) bathophenanthroline complexes. *Organic & Biomolecular Chemistry* **10**, 2223-2226, doi:10.1039/c2ob06684j (2012).

Chapter 4: From One, Many: Structurally derived malachite green analogues for multicolor cell labeling using dL5**

A part of this chapter was adapted from a paper published in *Bioconjugate Chem.*, **2015**, 26 (9), pp 1963–1971. Experiments done by others are appropriately acknowledged in the corresponding paragraphs.

Introduction

Molecular fluorescence detection stands as a valid approach to visualize events of biology from a single molecule to the entire organism¹⁻³. With numerous fluorescent probes that were chemically tailored or biologically recognized, the breadth of applications has been truly integrated to every aspect of life science research⁴⁻⁶. Using fluorescence microscopy, we are able to simultaneously visualize multiple cellular compartments in live cell experiments with suitable fluorescent probes^{7,8}. Multicolor imaging approaches enable us to track cell movement, visualize individual molecules and specify biological events⁹⁻¹¹. For example, Wang S *et al.* have developed a multicolor cell imaging approach to discriminate different type of cancer cells with fluorophore conjugated aptamers that interacted with different cancer cell lines in different degree¹².

However, few examples have been demonstrated with multi-color imaging of the same protein in live cells. Gaietta G *et al.* reported the use of FIAsh/ReAsH to label older and newer copies of the same species (connexin43), where the sequential addition of spectrally separable FIAsh and ReAsH provided a real-time analysis of protein synthesis¹³. Protein trafficking is tightly regulated in all cells and mediates important functions such as receptor signaling, cell adhesion and ion channel activities¹⁴⁻¹⁶. In particular, the regulation of surface levels of protein is influenced by a number of cellular mechanisms including changes in gene expression, protein synthesis, trafficking, and degradation. However, analysis of protein surface expression is

limited by cumbersome techniques, including biotinylation of surface proteins¹⁷, immunofluorescence using ectofacial epitopes¹⁸, and the use of pH-dependent fluorophores¹⁹. Real-time dynamics of surface protein trafficking have been difficult to visualize.

The MG/dL5** complex possesses high affinity, resistance to photobleaching and high brightness, and functions within the cytoplasm of living cells^{20,21}. The spectral and binding properties are determined by the interactions of these proteins and fluorogens, which represent a new class of fluorescent sensors with context-specific activation. Unlike original fluorescent proteins (GFP etc.) or small organic fluorophores (Cy5 and Rhodamine), these binding complexes are genetically encoded for expression in and on the cell and have advantages in versatility over fluorescent proteins. Suitable chemical modifications of the fluorogen can create the same FAP-bound fluorogenic dyes with alternative colors and distinct permeability properties^{22,23}. We sought to create a method that enables quantitation of surface and internal protein levels in living cells.

The MG fluorogen resides in the cavity created by dimerized anti-parallel L5* (Figure 4.1a), this scFv binding pocket physically constrains the free rotation around the central carbon atom of the chromophore, promoting fluorescence emission instead of non-radiative de-activation²⁴. MG is oriented so that the proximal oxygen atom of the linker points outward from the binding pocket. MG and the homodimer share a single C2 rotation axis through the oxygen atom of the dye (Figure 4.1b), and MG is almost entirely encapsulated between the two re-arranged V_L domains. Although MG is almost entirely encapsulated in FAP_{dL5**}, major contacts are made by the dimethylamine carbons from ring R2 and R3 (Figure 4.1c), raising the possibility that modifications or even removal of the bottom phenol ring R1 may still preserve high affinity binding to the protein.

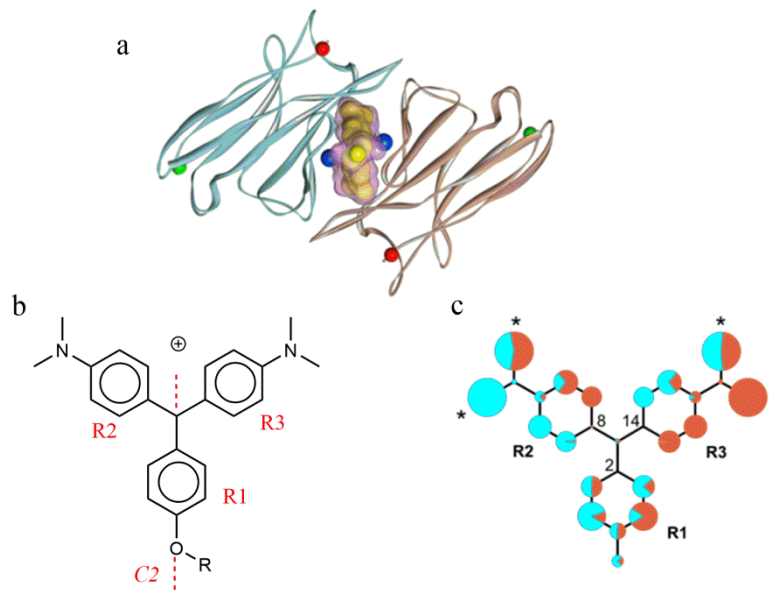


Figure 4.1: MG forming complex with dL5**. (a): Main-chain views of liganded L5* homodimers, MG atomic contacts made to L5* are symmetrical and complex. (b): Chemical structure of MG fluorogen. (c): Size of circle at each non-hydrogen atom position represents total surface area of contacts to L5* made by that atom; contacts to $V_L A$ are shown in light blue and contacts to $V_L B$ are shown in orange. Major contacts made by the dimethylamine carbons are marked (*). (adapted from ref. 24)

On the basis of previous work, we have proposed and synthesized a series of MG analogues with unchanged R2 and R3 rings but linked to different groups to give distinct spectral properties (Figure 4.2), hoping to retain the binding to dL5** but produce varied excitation and emission properties. FAPs can be easily engineered and expressed in different intra/extra-cellular compartments. By using cell-permeable or impermeable fluorogens, we can selectively visualize proteins of interest inside cells, on the cell surface or within trafficking vesicles. With spectrally distinguishable MG analogues in both cell-permeant and cell-excluded form, we are able to simultaneous label the surface and intracellular pools with different colors in living cells, and provide a real-time readout of biosynthetic trafficking to the cell surface.

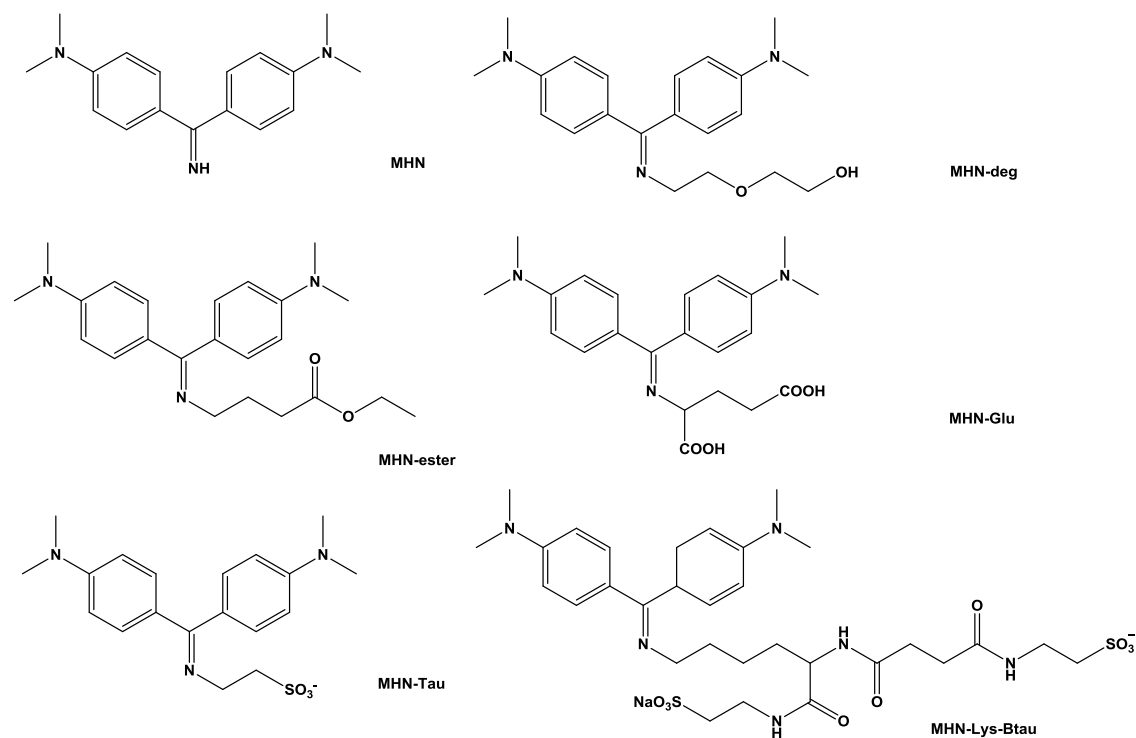


Figure 4.2: Chemical structures of MG analogues: N-substituted Michler's Hydrol (MHN) derivatives.

Synthesis of spectrally varied MG analogues

MG displays two absorbance (excitation) bands, a main (X) band contributed by rings R2 and R3 and a minor (Y) band contributed by ring R1. Olsen reported trends in solution state absorbance bands and transition dipole moments associated with the first two electronic excitations can be described within reasonable accuracy by the model (Figure 4.3)²⁵. In particular, the X= -NH₂ derivative of Michler's Hydrol Blue has an absorption peak at around 450 nm, where we hypothesized when binding with dL5** can be red-shifted to around 488 nm, an excitation wavelength that was commonly equipped among the 4 laser lines for microscopy.

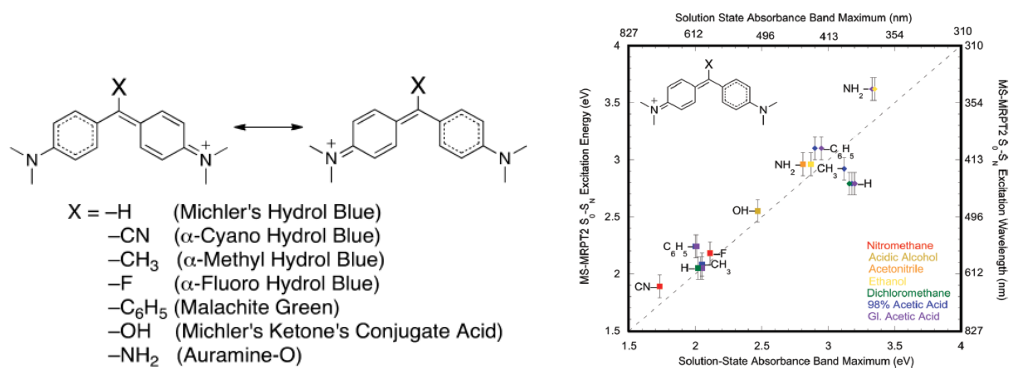


Figure 4.3: Structures of cationic diarylmethanes dyes (left); comparison between calculated and experimental excitation energies for dyes, experimental data of first (x band, squares) and second (y band, diamonds) absorbance band maxima. (adapted from Ref. 25)

The formation of imine bonds (Schiff base when R is not hydrogen) are typically through the condensation of primary amines and aldehydes or ketones in some rare cases (Figure 4.4)^{26,27}. The reactions proceeded via the nucleophilic addition, followed by an elimination of water to yield the imine. However, the reaction equilibrium usually favors the reverse direction, so that the removal of water is necessary to drive the reaction toward imine formation. Other commonly employed imine synthesis includes oxidation of secondary amine²⁸, oxidative condensation between alcohol with primary amine²⁹, Stieglitz rearrangement³⁰ and Schmidt reaction³¹.

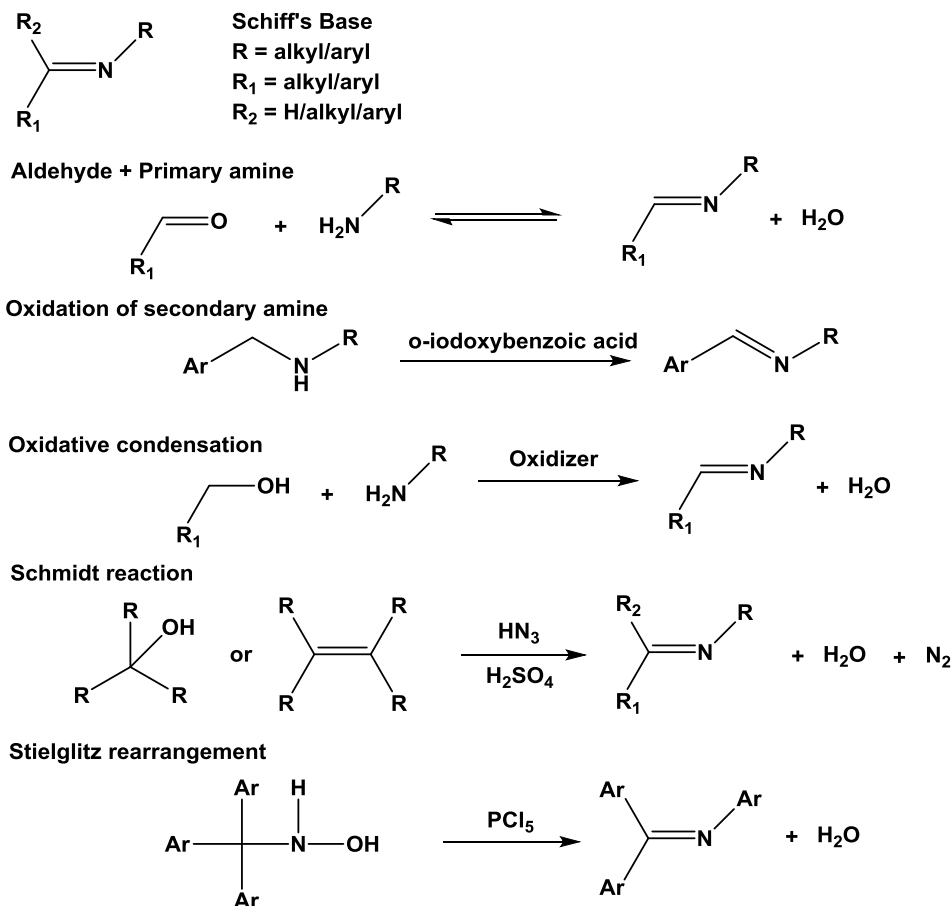


Figure 4.4: Structure of Schiff base, commonly employed synthesis reactions for imide bond formation.

However, the imine bond is not very stable, especially when treated with the presence of electrophiles or acids, which lead to the hydrolysis to aldehydes (or ketones) and amines. As a precaution, the formation of the imine bond is often completed at the end of the total synthesis. In the case of MHN derivative synthesis, we found the condensation reaction between Michler's Ketone and corresponding amines proceeded poorly and is hard to purify. This is probably because of the low nucleophilicity of the aromatic ketone. Higher reaction temperatures led to side products. So, we planned to first synthesize the precursor amine and then oxidized to the imine compound through mild oxidation. The reaction was illustrated in Figure 4.5, where the Michler's Ketone was converted to highly electrophilic benzhydrylium ions, followed the addition of primary amine and oxidation using p-chloranil.

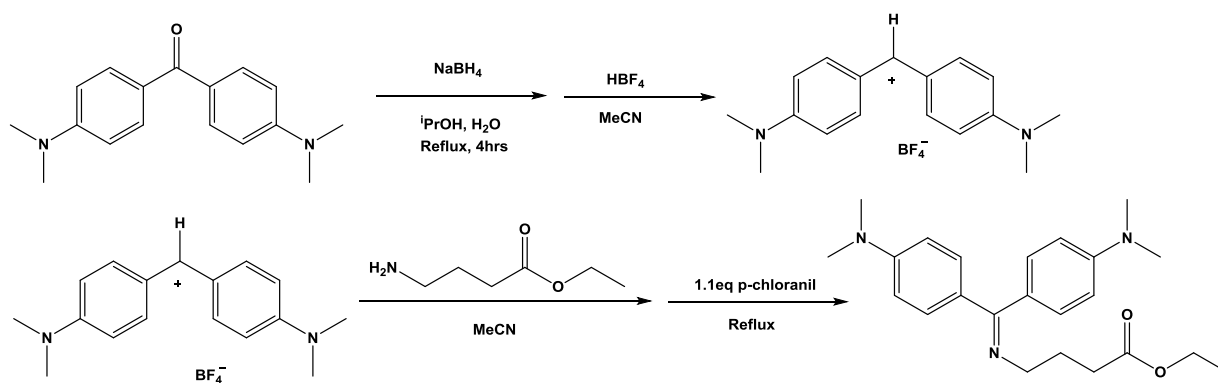


Figure 4.5: Representative synthesis route of MHN derivatives (MHN-Ester)

Characterization of MHN derivatives with dL5**

MHN derivatives were synthesized as potential spectrally distinct counterparts, in testing their binding with dL5**, we found that despite sharing the same chromophore, the length and function group of the linker can significantly affect their ratio of fluorescence activation (Table 4.1 and Figure 4.6). Among these MHN derivatives, MHN-ester is a stable, cell-permeable dye with high activation ratio (Table 4.2). MHN-ester and MG-Btau pose distinctive fluorescence spectra and cell-permeability but bind to the same protein (dL5**) with similar activation ratio and binding affinity (Table 4.1 and Figure 4.7), which is useful in labeling proteins that are expressed both extra/intra-cellularly with dual-color fluorescence.

	MHN	Lys-Tau	Tau	Deg	Ester	Glu
$\lambda_{\text{ex}} / \lambda_{\text{em}}$ (nm)	459/535	458/527	476/533	459/540	456/532	459/535
Φ_{F}	N.A	0.197	0.149	0.079	0.30	N.A

Table 4.1: Excitation and emission maxima, and fluorescence quantum yield of MHN dyes/dL5** complexes. (N.A: data was not measured)

	λ_{\max} (nm)	λ_{ex} (nm)	λ_{em} (nm)	ϵ_{\max} ($\text{M}^{-1}\text{cm}^{-1}$)	Φ	$\epsilon_{\text{B}} / \epsilon_{\text{F}}^{\#}$	$\Phi_{\text{B}} / \Phi_{\text{F}}$	$\text{AR}^{\$}$	K_{d} (pM)
MHN-ester	422	(422)	(488)	$5.9 \cdot 10^4$	$4.2 \cdot 10^{-4}$	12	710	8520	42.5
MHN-ester/dL5**	456	456	532	$6.4 \cdot 10^4$	0.30				
MG-Btau	606	(606)	(636)	$9.1 \cdot 10^4$	$9.5 \cdot 10^{-5}$	3.5	2010	7035	18
MG-Btau/dL5**	633	633	668	$1.1 \cdot 10^5$	0.19				

Table 4.2: Properties of dL5** FAP Fluorogen Activation. #: ϵ_{B} and ϵ_{F} are the extinction coefficient of bound and free dye at the laser excitation wavelength (488 and 640 nm); \$: AR refers to activation ratio; it is the product of the extinction coefficient ratio and quantum yield ratio.

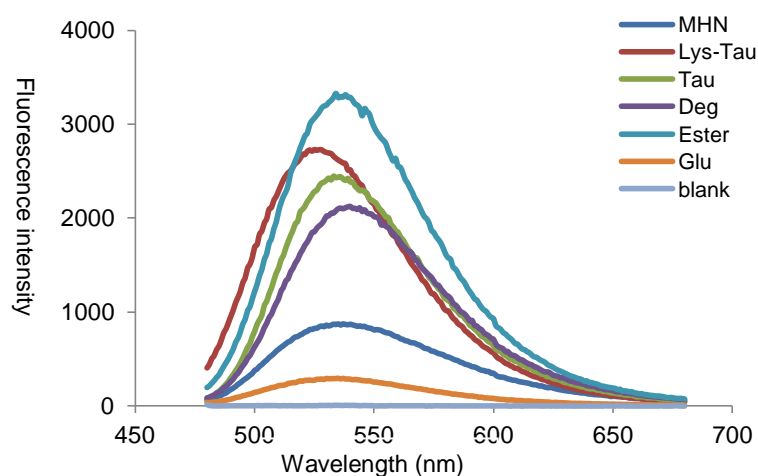


Figure 4.6: Fluorescence emission spectra of 1 μM MHN dyes with 5 μM dL5** excited at 450 nm measured with Tecan Infinite M1000 Plate Spectrometer.

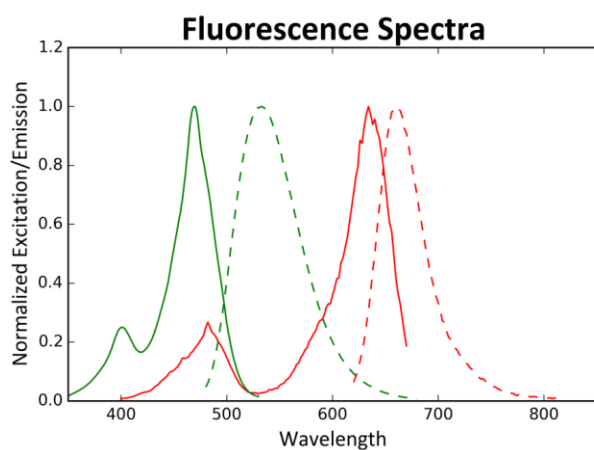


Figure 4.7: MHN-ester (green) and MG-Btau (red) excitation (solid lines) and emission (dashed lines) spectra bound to excess dL5** protein.

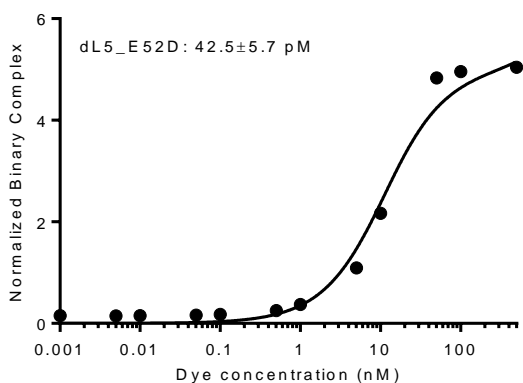


Figure 4.8: K_d determination using purified dL5**, where 5 nM of protein was complexed with a series of MHN-ester dilutions overnight. Fluorescent intensity was measured, normalized and analyzed by a one-site binding ligand depletion model. (Experiment conducted by Dr. Yi Wang)

The dL5** was originally developed as a tight binder and activator of MG-Btau with a picomolar affinity ($K_d = 18$ pM). To our surprise, despite the large difference in structure, MHN-ester can still bind to dL5** with a high affinity. This confirmed our previous observation that dimethylamino group play a major role in dL5** protein binding.

The fluorescence quantum yield (Φ_F) was determined by comparing integrated emission spectra of MHN-ester/dL5** complex to reference Rhodamine 6G dye (Figure 4.9). Corrected emission spectra were taken on a Quantamaster monochromator fluorimeter (Photon Technology International). The emission spectra (500-700 nm) of a set of five concentrations were integrated and plotted against absorbance at 480 nm and the Φ_F was then calculated from the slopes using Equation 1. Where Φ_X is the sample quantum yield, Φ_{ST} is the standard quantum yield, $Grad_X$ is the sample slope, $Grad_{ST}$ is the standard slope, η_X is the refraction index of the sample solvent, and η_{ST} is the refraction index of the standard solvent.

$$\Phi_X = \Phi_{ST} \left(\frac{Grad_X}{Grad_{ST}} \right) \left(\frac{\eta_X^2}{\eta_{ST}^2} \right) \quad \text{Equation. 1}$$

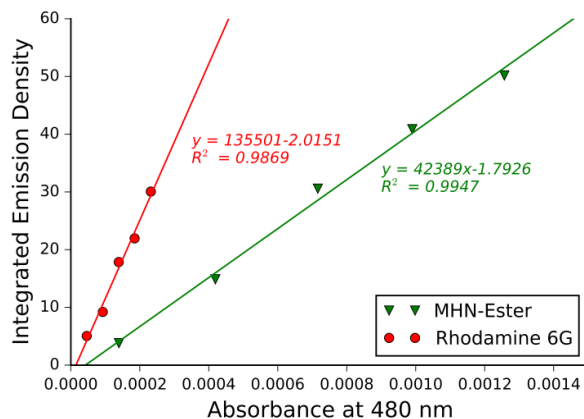


Figure 4.9: Quantum yield measurement of MHN-ester/dL5** complex was determined using Rhodamine 6G ($\Phi_F = 0.95$ in EtOH) to yield $\Phi_F = 0.30$.

Dual-color imaging of FAP-BK α HEK293 cells

This part of work are done by Christopher P. Pratt, for more information regarding using MHN-ester, MG-Btau as a Green-inside Red-outside (GIRO) labeling approach for BK α protein trafficking, please read: *Bioconjugate Chem.*, 2015, 26 (9), pp 1963–1971

The green cell-permeable MHN-ester and far-red cell-excluded MG-Btau are spectrally resolved and tight in binding dL5**. It is plausible to use the dual-color imaging to study extra- and intracellular stores of protein of interest. Hence, we examined the dynamics of BK α subunit using HEK293 cells that stably express FAP-BK α both on the surface and inside the cell. MG-Btau (300 nM) was added first to saturate surface-exposed FAP. After 5 min incubation, MHN-ester (300 nM) was added to label the internal portion of protein. With its low K_d and slow off-rate, MG-Btau labeling is effectively irreversible over these short experimental time scales. Thus, FAP-BK α channel can be distinctively labeled within 7 min, which enables simultaneous detection and quantitation of two sub-populations of FAP-BK α depending on bound dye's fluorescence (Figure 4.10). This real-time green-inside red-outside (GIRO) labeling strategy allow us to analyze protein distribution in living cells.

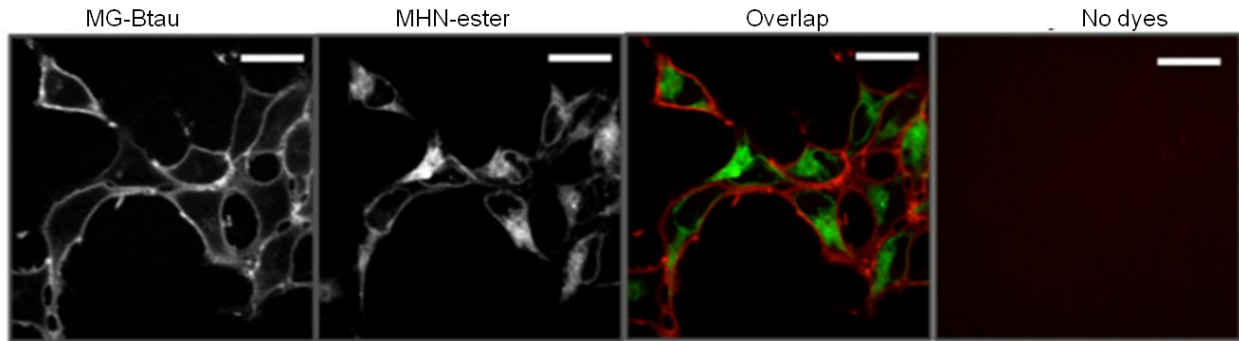
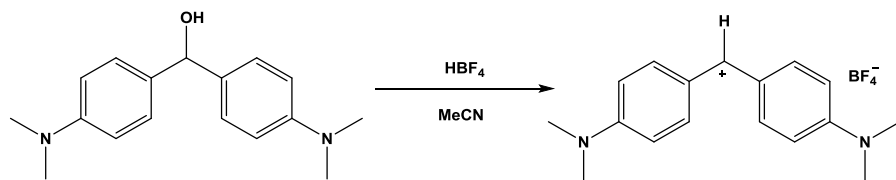


Figure 4.10: Live cells labeled with MG-Btau (red) and MHN-ester (green) to label surface and internal protein in FAP-BK α expressing live cells. Scale bar = 10 μ m (Experiment conducted by Christopher P. Pratt)

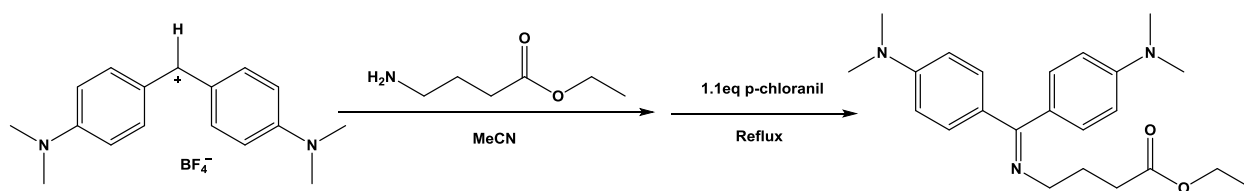
Summary

A series of MHN dyes have been synthesized to explore the fluorescence activation by dL5** at a distinct excitation wavelength compared with MG dyes. We found out that the removal of the bottom phenol ring of MG still preserve significant activations by dL5**, and different replacing linkers results in different ex/em wavelength and quantum yield of the complexes, suggesting interaction between linker and the protein. Further investigations including crystal structure, linker length and charge are required to provide guidance in designing novel fluorogen structures. The MHN-ester has been used together with MG-Btau as a dual-color labeling method for BK α channel trafficking. Due to the instability of imine bond in the aqueous solution, we found noticeable change of spectra shape when MHN dyes were kept in buffer solution for more than 30 min. The formation of the complex can greatly stabilize MHN dyes, but the complex is susceptible to photobleaching and is phototoxic to some extent.

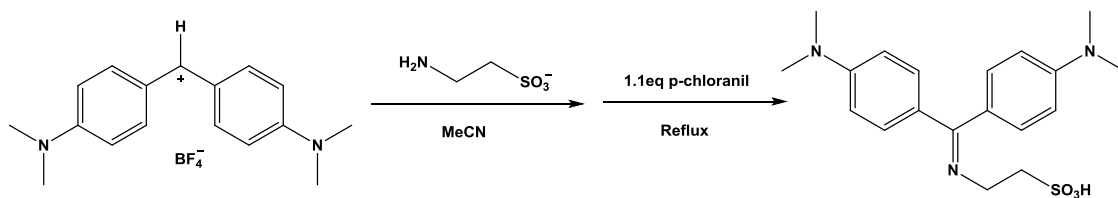
Experimental details



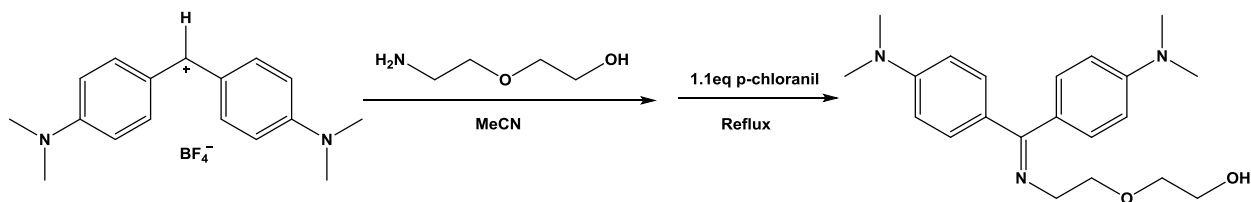
270 mg bis[4-(dimethylamino)phenyl]-Benzophenol (Michler's hydrol) was dissolved in 20 mL MeCN, 1 equivalence HBF₄ (50% in water) was added to the solution. The reaction was allowed to stir at room temperature for 30 minutes. After that, the reaction mixture was dried for later use^{32,33}.



MHN-ester: To 0.34 g (1 mmol) 4,4-bis(dimethylamino)benzhydrylium tetrafluoroborate MeCN solution, added 4 fold excess of the amine. When the solution color changed from deep violet to colorless, 0.27 g (1.1 mmol) of p-chloranil was added and heated to 50°C for 2 hours. The reaction mixture was directly poured onto the silica gel, 50 % EtOAc/50% EtOH was used as eluent to separate the final product. The product (MHN-ester) had a chemical composition of C₂₃H₃₁N₃O₂ with M.W. of 381.52 g/mol (yield: 0.092 g, 24%). (Appendix 7-22) ¹H NMR (300 MHz, Methanol-*d*₄) δ 7.48 (d, *J* = 9.2 Hz, 2H), 7.36 (d, *J* = 8.9 Hz, 2H), 6.86 (m, 4H), 4.07 (q, *J* = 7.1 Hz, 2H), 3.82 (t, *J* = 7.1 Hz, 2H), 3.14 (s, 12H), 2.41 (t, *J* = 7.0 Hz, 2H), 2.09 (p, *J* = 7.1 Hz, 2H), 1.19 (t, *J* = 7.1 Hz, 3H). ¹³C NMR (75 MHz, Methanol-*d*₄) δ 176.3, 172.9, 155.0, 153.9, 133.4, 133.1, 119.6, 116.3, 111.3, 111.0, 60.5, 39, 30.8, 24.6, 13.1. ESI-MS (+*m/z*): 382.3.



MHN-tau: To 0.34 g (1 mmol) 4,4-bis(dimethylamino)benzhydrylium tetrafluoroborate MeCN/H₂O (50% / 50%) solution, added 5 fold excess of sodium taurate. When the solution color changed from deep violet to colorless, 0.27 g (1.1 mmol) p-chloranil was added and heated to 50°C for 2 hours. The reaction mixture was directly poured onto the silica gel, 60% EtOAc/40% EtOH was used as eluent to separate the final product. The product (MHN-tau) had a chemical composition of C₁₉H₂₅N₃O₃S with M.W. of 375.49 g/mol (yield: 0.16 g, 44%). ¹H NMR (300 MHz, Methanol-*d*₄) δ 7.57 (d, *J* = 9.2 Hz, 2H), 7.47(d, *J* = 9.1 Hz, 2H), 6.90 (m, 4H), 4.22 (t, *J* = 6.1 Hz, 2H), 3.33(m, 1H), 3.21(t, *J* = 6.0 Hz, 2H), 3.16 (s, 12H). ¹³C NMR (75 MHz, Methanol-*d*₄) δ 176.5, 155.3, 154.3, 134.1, 118.9, 115.2, 111.3, 110.8, 49.0, 45.0, 38.8. ESI-MS (-*m/z*): 375.2.



The product (MHN-deg) had a chemical composition of C₂₁H₂₉N₃O₂ with M.W. of 355.48 g/mol (yield: 47%). ¹H NMR (300 MHz, Methanol-*d*₄) δ 7.50 (m, 4H), 6.89 (m, 4H), 4.01 (t, *J* = 5.6 Hz, 2H), 3.83 (t, *J* = 5.6 Hz, 2H), 3.67 (m, 4H), 3.16 (d, *J* = 2.4 Hz, 12H). ¹³C NMR (75 MHz, MeOD) δ 177.5, 155.4, 154.3, 134.1, 119.0, 115.5, 111.2, 110.9, 72.1, 68.3, 60.7, 38.8. ESI-MS (+*m/z*): 382.3.

References:

- 1 Du, W., Wang, Y., Luo, Q. M. & Liu, B. F. Optical molecular imaging for systems biology: from molecule to organism. *Anal Bioanal Chem* **386**, 444-457, doi:10.1007/s00216-006-0541-z (2006).
- 2 Giepmans, B. N. G., Adams, S. R., Ellisman, M. H. & Tsien, R. Y. Review - The fluorescent toolbox for assessing protein location and function. *Science* **312**, 217-224, doi:10.1126/science.1124618 (2006).
- 3 Liu, Z., Lavis, L. D. & Betzig, E. Imaging Live-Cell Dynamics and Structure at the Single-Molecule Level. *Mol Cell* **58**, 644-659, doi:10.1016/j.molcel.2015.02.033 (2015).
- 4 Lavis, L. D. & Raines, R. T. Bright ideas for chemical biology. *Acs Chem Biol* **3**, 142-155, doi:10.1021/cb700248m (2008).
- 5 Shaner, N. C., Patterson, G. H. & Davidson, M. W. Advances in fluorescent protein technology. *J Cell Sci* **120**, 4247-4260, doi:10.1242/jcs.005801 (2007).
- 6 Terai, T. & Nagano, T. Small-molecule fluorophores and fluorescent probes for bioimaging. *Pflug Arch Eur J Phys* **465**, 347-359, doi:10.1007/s00424-013-1234-z (2013).
- 7 Gautier, A. *et al.* An engineered protein tag for multiprotein labeling in living cells. *Chem Biol* **15**, 128-136, doi:10.1016/j.chembiol.2008.01.007 (2008).
- 8 Chudakov, D. M., Lukyanov, S. & Lukyanov, K. A. Fluorescent proteins as a toolkit for in vivo imaging. *Trends Biotechnol* **23**, 605-613, doi:10.1016/j.tibtech.2005.10.005 (2005).
- 9 Patterson, G., Davidson, M., Manley, S. & Lippincott-Schwartz, J. Superresolution Imaging using Single-Molecule Localization. *Annu Rev Phys Chem* **61**, 345-367, doi:10.1146/annurev.physchem.012809.103444 (2010).
- 10 Hu, C. D. & Kerppola, T. K. Simultaneous visualization of multiple protein interactions in living cells using multicolor fluorescence complementation analysis. *Nat Biotechnol* **21**, 539-545, doi:10.1038/nbt816 (2003).
- 11 Bates, M., Huang, B., Dempsey, G. T. & Zhuang, X. W. Multicolor super-resolution imaging with photo-switchable fluorescent probes. *Science* **317**, 1749-1753, doi:10.1126/science.1146598 (2007).
- 12 Wang, S., Kong, H., Gong, X. Y., Zhang, S. C. & Zhang, X. R. Multicolor Imaging of Cancer Cells with Fluorophore-Tagged Aptamers for Single Cell Typing. *Anal Chem* **86**, 8261-8266, doi:10.1021/ac501657g (2014).
- 13 Gaietta, G. *et al.* Multicolor and electron microscopic imaging of connexin trafficking. *Science* **296**, 503-507, doi:DOI 10.1126/science.1068793 (2002).
- 14 Clapham, D. E. Calcium signaling. *Cell* **131**, 1047-1058, doi:10.1016/j.cell.2007.11.028 (2007).

- 15 Funke, L., Dakoji, S. & Bredt, D. S. Membrane-associated guanylate kinases regulate adhesion and plasticity at cell junctions. *Annu Rev Biochem* **74**, 219-245, doi:10.1146/annurev.biochem.74.082803.133339 (2005).
- 16 Hicke, L. & Dunn, R. Regulation of membrane protein transport by ubiquitin and ubiquitin-binding proteins. *Annu Rev Cell Dev Bi* **19**, 141-172, doi:10.1146/annurev.cellbio.19.110701.154617 (2003).
- 17 Elia, G. Biotinylation reagents for the study of cell surface proteins. *Proteomics* **8**, 4012-4024, doi:10.1002/pmic.200800097 (2008).
- 18 Kast, C., Canfield, V., Levenson, R. & Gros, P. Transmembrane organization of mouse P-glycoprotein determined by epitope insertion and immunofluorescence. *J Biol Chem* **271**, 9240-9248 (1996).
- 19 Miesenbock, G., De Angelis, D. A. & Rothman, J. E. Visualizing secretion and synaptic transmission with pH-sensitive green fluorescent proteins. *Nature* **394**, 192-195, doi:10.1038/28190 (1998).
- 20 Szent-Gyorgyi, C. *et al.* Fluorogen-activating single-chain antibodies for imaging cell surface proteins (vol 26, pg 235, 2008). *Nat Biotechnol* **26**, 470-470, doi:10.1038/nbt0408-470b (2008).
- 21 Telmer, C. A. *et al.* Rapid, Specific, No-wash, Far-red Fluorogen Activation in Subcellular Compartments by Targeted Fluorogen Activating Proteins. *Acs Chem Biol* **10**, 1239-1246, doi:10.1021/cb500957k (2015).
- 22 Yan, Q. *et al.* Near-instant surface-selective fluorogenic protein quantification using sulfonated triarylmethane dyes and fluorogen activating proteins. *Org Biomol Chem* **13**, 2078-2086, doi:10.1039/c4ob02309a (2015).
- 23 Zhang, M. *et al.* Fluoromodule-based reporter/probes designed for in vivo fluorescence imaging. *J Clin Invest* **125**, 3915-3927, doi:10.1172/Jci81086 (2015).
- 24 Szent-Gyorgyi, C. *et al.* Malachite green mediates homodimerization of antibody VL domains to form a fluorescent ternary complex with singular symmetric interfaces. *J Mol Biol* **425**, 4595-4613, doi:10.1016/j.jmb.2013.08.014 (2013).
- 25 Olsen, S. Four-Electron, Three-Orbital Model for the Low-Energy Electronic Structure of Cationic Diarylmethanes: Notes on a "Pauling Point". *J Phys Chem A* **116**, 1486-1492, doi:10.1021/jp212295s (2012).
- 26 Layer, R. W. Chemistry of Imines. *Chem Rev* **63**, 489-&, doi:DOI 10.1021/cr60225a003 (1963).
- 27 Albrecht, S., Defoin, A. & Tarnus, C. Simple preparation of O-substituted hydroxylamines from alcohols. *Synthesis-Stuttgart*, 1635-1638, doi:10.1055/s-2006-926440 (2006).

- 28 Nicolaou, K. C., Mathison, C. J. N. & Montagnon, T. New reactions of IBX: Oxidation of nitrogen- and sulfur-containing substrates to afford useful synthetic intermediates. *Angew Chem Int Edit* **42**, 4077-4082, doi:10.1002/anie.200352076 (2003).
- 29 Zhang, E. L., Tian, H. W., Xu, S. D., Yu, X. C. & Xu, Q. Iron-Catalyzed Direct Synthesis of Imines from Amines or Alcohols and Amines via Aerobic Oxidative Reactions under Air. *Org Lett* **15**, 2704-2707, doi:10.1021/ol4010118 (2013).
- 30 Stagner, B. A. The molecular rearrangement of triarylmethyl-hydroxylamines. *J Am Chem Soc* **38**, 2069-2081, doi:DOI 10.1021/ja02267a018 (1916).
- 31 Boyer, J. H. & Hamer, J. The Acid-Catalyzed Reaction of Alkyl Azides Upon Carbonyl Compounds. *J Am Chem Soc* **77**, 951-954, doi:DOI 10.1021/ja01609a045 (1955).
- 32 Kanzian, T., Nigst, T. A., Maier, A., Pichl, S. & Mayr, H. Nucleophilic Reactivities of Primary and Secondary Amines in Acetonitrile. *Eur J Org Chem*, 6379-6385, doi:10.1002/ejoc.200900925 (2009).
- 33 Brotzel, F., Chu, Y. C. & Mayr, H. Nucleophilicities of primary and secondary amines in water. *J Org Chem* **72**, 3679-3688, doi:10.1021/jo062586z (2007).

Chapter 5: MG-2I/dL5** as a targetable and activatable photosensitizer

This chapter is adapted from a previously published paper (*Nature Methods*, 2016, **13**, 263-268).

Supplemental information and additional data is also incorporated in this chapter. Experiments done by others are appropriately acknowledged in the corresponding paragraphs.

Introduction

When combined with suitable genetic constructs or chemical reagents, light can provide precise temporal and spatial control of many biological processes¹⁻³. Photosensitizer (PS) dyes and proteins are able to create short-lived reactive oxygen species (ROS) when exposed to light of appropriate wavelengths (Figure 5.1)^{4,5}. ROS generated by PS can be utilized for functional manipulation of living cells, including protein inactivation⁶, targeted damage introduction⁷, and cellular ablation (Figure 5.2)⁸. In particular, with the development of lasers and the improvement of photosensitizers, photodynamic therapy (PDT) has been well established as a therapeutic technique against various types of cancers⁹. The minimal invasion and promising tumor-specific immunostimulatory effects of PDT offer great alternatives in treatment for localized superficial malignant and premalignant tumors^{10,11}. Although widely used for many years, conventional photosensitizers such as Photofrin have little tumor selectivity and require long clearance time, making patients photosensitive and causing serious off-target damage to normal tissues upon incidental exposure to light^{12,13}. The off-target phototoxicity produced during light exposure has not only limited its applications as a cancer therapy, but also in places where precise and specific introduction of ROS damage is desired¹⁴.

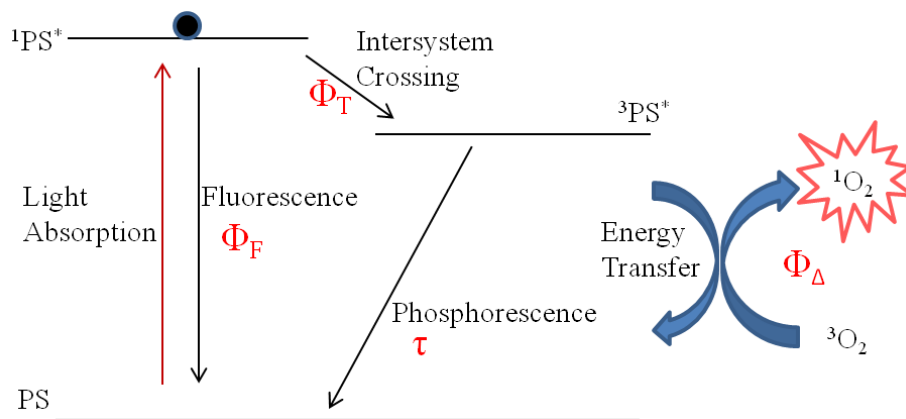


Figure 5.1: The mechanism of ROS generation by PS illustrated by Jablonski energy diagram.

Newer photosensitizers have been developed with higher ROS generating efficiency, better photostability, along with near-infrared (NIR) absorption and fluorescent imaging ability to enhance tissue penetration and facilitate *in vivo* tumor visualization during PDT and other applications^{15,16}. More recently, a number of genetically targeted photosensitizers have been developed to improve targeting and specificity in living cells, including FIAsh and ReAsH¹⁷, KillerRed¹⁸ and MiniSOG¹⁹. These fluorescent photosensitizers display good chromophore-assisted light inactivation (CALI) of directly linked proteins. Particularly, KillerRed that developed from anm2CP (a homolog of GFP) has found successful applications in a range of biological problems^{6,20,21}. It can efficiently generate superoxide (O_2^-) upon green/yellow light excitation through a Type-I photosensitization facilitated by a marked long internal hydrogen-bonded water channel²²⁻²⁴. Despite showing spatially restricted ROS generation, these photosensitizer proteins require a very high light dose to reach effective inactivation or cell killing. Moreover, for deep tissue applications, and to avoid autofluorescent photosensitization, genetically encoded photosensitizers with far-red/NIR excitation wavelengths (> 620 nm for tissue penetration purpose) are required, yet no efficient genetically targeted photosensitizers are available in this spectral range.

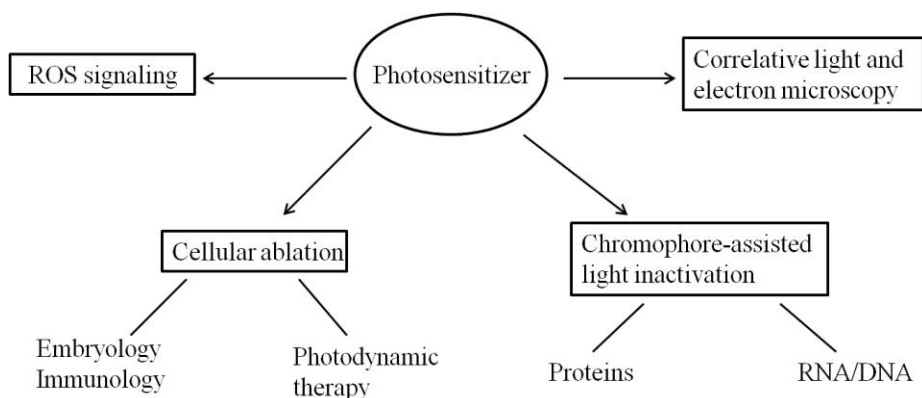


Figure 5.2: Photosensitizers' applications in different fields.

To reduce non-specific phototoxicity in normal tissues, one approach is to develop photosensitizers that can only be activated for ROS generation with the presence of both light illumination and cell-specific targeting²⁵. Cellularly targeted and activated photosensitizers are expected to improve the specificity by restraining the ROS generation at the targeted site and minimizing the damage to the surrounding non-targeted tissue, where the photosensitizer remains inactive. Currently, activatable photosensitizers are either responsive to local environmental changes such as pH or hydrophilicity, or contain a quenching group that is cleaved, releasing an active photosensitizer²⁶⁻²⁸. These activation events typically increase the ROS production by 10–50-fold, providing enhanced photosensitizing contrast, but still showing some off-target effects from non-specifically localized materials. Selectively targeting and significantly activating a photosensitizer at a site of interest remains a significant goal to advance photosensitizers and photosensitizing proteins.

To target and activate a ROS-generating photosensitizer, we exploited the high molecular specificity and selective fluorescence activation of fluorogenic dye upon binding a specific FAP partner^{29,30} and extended this fluorescence activation concept to ROS activation with a chemically tailored dye. We reasoned that the suppression of non-radiative relaxation of the electronic excited state by which the FAP enhances fluorescence in MG fluorogens could be

exploited to modify other photochemical properties³¹, in particular intersystem crossing, when combined with properly designed fluorogens. We found that heavy-atom substitutions, which are known to increase the spin-orbit coupling for efficient intersystem crossing^{32,33}, do not abolish FAP-fluorogen interactions and dramatically increase the rate of singlet oxygen generation (Figure 5.3). This iodinated MG analog (MG-2I) has low fluorescence and ROS generation in free form, and produces a NIR excitable fluorescent complex with high singlet oxygen quantum yield (Φ_{Δ}) when bind to dL5^{**}. This protein-dye complex has been successfully demonstrated in inactivation of fused proteins, selective killing of cells expressing dL5^{**} at the plasma membrane, cytosol, mitochondrial matrix or nucleus in culture, and ablation of cardiac cells within living larval/adult zebrafish expressing dL5^{**} in the cytoplasm. We have also applied this method to A431 tumor ablation in nude mice by using a recombinant FAP conjugated affinity probe (AffiFAP). This FAP-targeted and activated photosensitizer (TAPs) approach along with NIR excitation and emission provides a new spectral range for photosensitizer proteins, useful for imaging, manipulation and cellular ablation deep within living organisms.

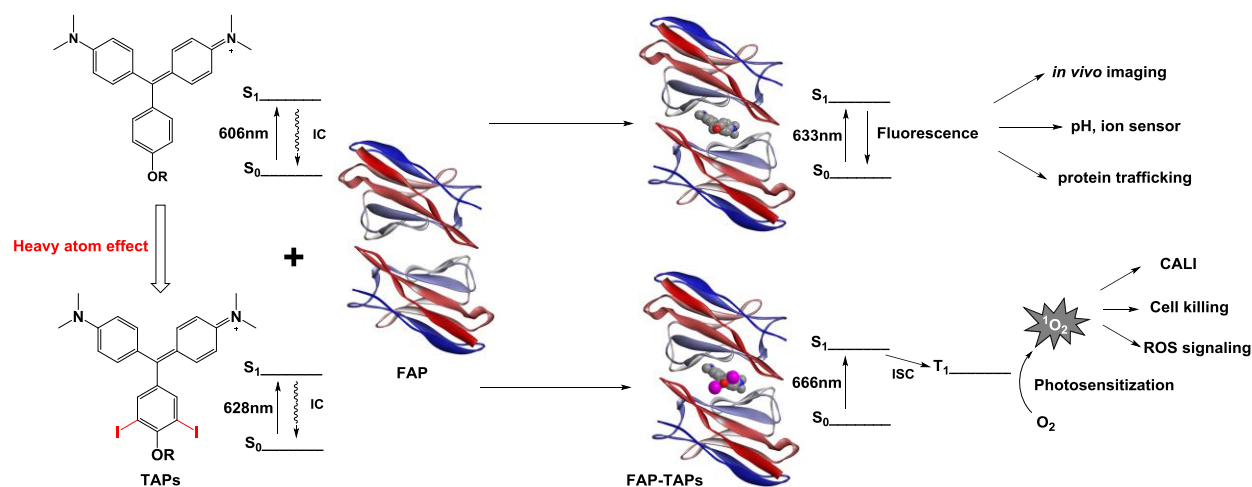


Figure 5.3: Illustration of the ROS generating mechanism of FAP-TAPs. IC: internal conversion by molecule's free rotation, ISC: intersystem crossing.

Synthesis route for MG-2I

Photophysical heavy-atom effects was first discovered at 1949 by McClure³⁴, who found that internal heavy atoms appear to have a significant effect on both the rate of population of the triplet state and the rate of triplet decay, which increase the quantum yields ratio of phosphorescence to fluorescence Φ_P/Φ_F . Heavy atom such as iodine or bromine increases the spin and orbital interaction and the spin become more favorable, which promote intersystem crossing between singlet state and triplet state (S_1 to T_1). This effect has been widely used to transform a general fluorophore to an efficient photosensitizer without significant change of its spectral characteristics^{33,35}. We proposed a series of heavy-atom substituted MG derivatives and tried to synthesize them (Figure 5.4). The synthesis of several molecules is still carried by other group member. The detailed synthesis route and characterizations of MG-2I (3) is described below.

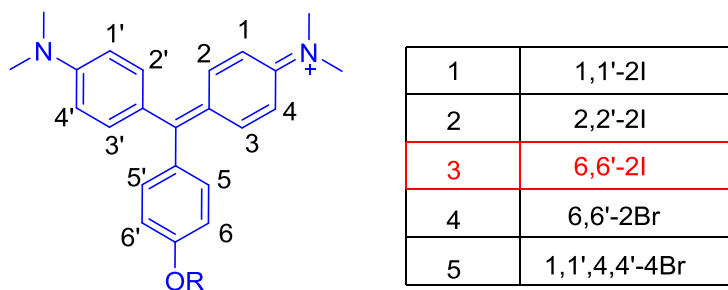


Figure 5.4: Proposed iodinated/brominated MG derivatives.

Characterization of MG-2I/dL5** complex

After MG-2I was synthesized and purified, its photochemical properties in both free and bound form were measured and summarized in Table 5.1. Details about experimental conditions and adapted protocols are discussed in the following paragraphs.

	$\lambda_{\text{Abs}}^{\text{a}}$ (nm)	λ_{ex} (nm)	λ_{em} (nm)	K_{d} (μM)	$\epsilon_{\text{max}}^{\text{b}}$ ($10^4 \text{ M}^{-1} \text{ cm}^{-1}$)	Φ_{F}	Φ_{Δ}	DAB photoconversion ^c
MG-ester/dL5**	606	633	668	7	10.3(9.18)	0.12	<0.005	-
MG-2I/dL5**	628	666	693	122	10.1(9.02)	0.037	0.13	+
KillerRed	585	585	610	NA	4.5	0.25	0	-

Table 5.1: Summary of spectral, FAP binding and ROS generating properties between MG-ester and MG-2I complexed with dL5**, KillerRed is listed as a comparison.

a: Values are respective absorption maximum of fluorogen only; b: The values in parentheses are for the unbound fluorogen at its respective maximum. c: For DAB photoconversion: - indicates no precipitate, + indicates brown precipitate.

Upon binding to dL5**, the absorption peak of MG-2I was red-shifted from 628 nm to 666 nm, accompanying with an increase of extinction coefficient ($10^4 \text{ M}^{-1} \text{ cm}^{-1}$) from 9.02 to 10.1 (Figure 5.5a), which was similar to previous report of MG-ester binding to dL5 protein²⁹. Compared to MG-ester, the iodination effect also produced a 22 nm bathochromic shift to the major absorption peak of free MG, moving the excitation maximum of the complex into the NIR range (666 nm) (Figure 5.5b).

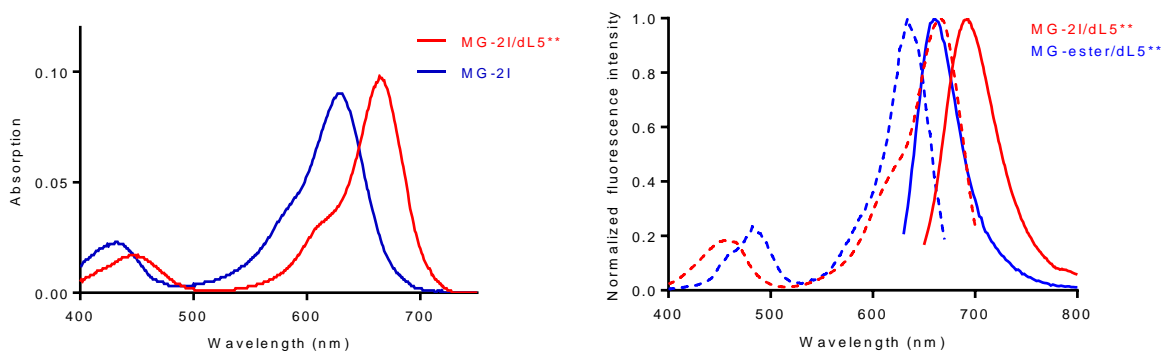


Figure 5.5: (a) Absorption spectra of unbound and FAP-bound MG-2I, where the absorption of $1 \mu\text{M}$ MG-2I was measured with or without $5 \mu\text{M}$ dL5**; (b) Normalized excitation (dotted lines) and emission (solid lines) spectra of MG-ester and MG-2I binding to dL5**, where 500 nM fluorogen was complexed with $3 \mu\text{M}$ dL5** and the fluorescence intensity was individually normalized to the peak maxima.

The fluorescence quantum yield (Φ_{F}) was determined by comparing integrated emission spectra

of MG-2I/dL5** complex to reference Cy5 dye. Corrected emission spectra were taken on a Quantamaster monochromator fluorimeter (Photon Technology International). The emission spectra (620-820 nm) of a set of five concentrations were integrated and plotted against absorbance at 600 nm and the Φ_F was then calculated from the slopes using Equation 1³⁶.

Where Φ_X is the sample quantum yield, Φ_{ST} is the standard quantum yield, $Grad_X$ is the sample slope, $Grad_{ST}$ is the standard slope, η_X is the refraction index of the sample solvent, and η_{ST} is the refraction index of the standard solvent.

$$\Phi_X = \Phi_{ST} \left(\frac{Grad_X}{Grad_{ST}} \right) \left(\frac{\eta_X^2}{\eta_{ST}^2} \right) \quad \text{Equation. 1}$$

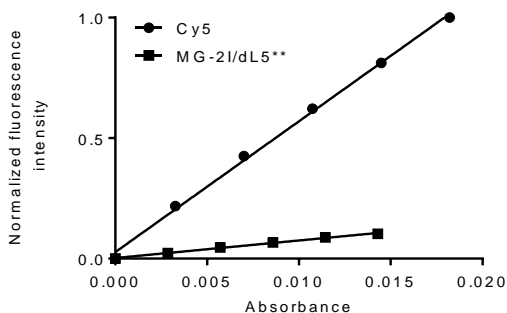


Figure 5.6: Fluorescent quantum yield measurement of MG-2I/dL5** using Cy5 as standard (emission spectra were integrated, normalized to the maximum value and plotted against absorbance at 600 nm).

The dissociation constant was determined by pre-complexing 5 nM of purified dL5** with a series of dye dilutions overnight and measuring the resulting fluorescence intensity. The fluorescence of free dye at each concentration was also measured and subtracted as background. Based on the plateau intensity in the binding curve calculated from a hyperbolic binding model, the results were normalized to the concentration of protein-dye complex. Using this scaled data, the dissociation constant was calculated from a one-site binding ligand depletion model in GraphPad Prism 6. Despite the large size of diiodo-substitution, the binding affinity of MG-2I with dL5** remains in pM range.

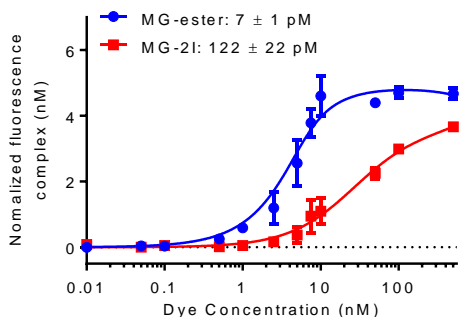


Figure 5.7: Dissociation equilibrium constant (K_d) of MG-ester/dL5** and MG-2I/dL5**, where 5 nM of protein was complexed with various concentrations of dyes. Fluorescent intensity was measured, normalized and analyzed by a one-site binding ligand depletion model. ($n = 4$, mean and S.E.M. plotted)

The generation of singlet oxygen was first evaluated by bleaching of anthracene-9,10-dipropionic acid (ADPA), a commonly used singlet oxygen scavenger³⁷, using aluminum phthalocyanine tetrasulfonate (AlPcS₄)³⁸ as the standard. PBS (pH 7.4) buffer containing optically matched samples and 0.1 mM ADPA were illuminated by 669 nm LED light box. The fluorescence intensity of ADPA was monitored with an excitation of 374 nm and an emission of 402 nm by Tecan Infinite M1000 plate spectrometer. The normalized fluorescence intensity was plotted against exposure time at 669 nm, and the Φ_{Δ} was then calculated from the slopes using equation 2. Here k_r is the chemical quenching of singlet oxygen by ADPA and k_d is the constant of deactivation of singlet oxygen via the solvent; both values are constant regardless of the photosensitizer being used. $[A]$ is the ADPA concentration, and I_{abs} is the absorbance at excitation wavelength. The Φ_{Δ} of the FAP-TAPs was determined to be 0.13, while the singlet oxygen generation from the MG-ester/dL5** was not detectable under the same conditions.

$$-\frac{d[A]}{dt} = I_{abs}\Phi_{\Delta}\frac{k_r}{k_d}[A] \quad \text{Equation. 2}$$

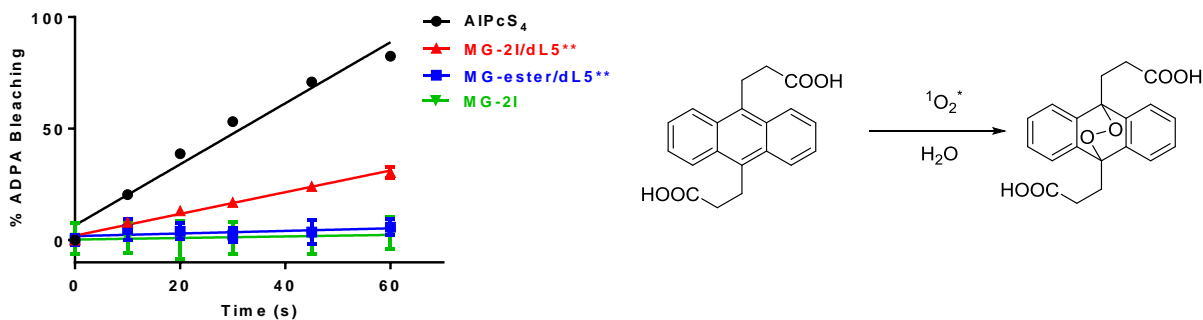


Figure 5.8: Measurement of $^1\text{O}_2$ generation by MG-2I/dL5** by ADPA, where bleaching of ADPA fluorescence was monitored at 374/402 nm as a function of 669 nm exposure time. AlPcS₄ was used as standard for the $^1\text{O}_2$ generation ($\Phi_{\Delta} = 0.34$). Optically matched solutions of MG-2I, MG-ester/dL5**, MG-2I/dL5** and AlPcS₄ at 669 nm were used. (n = 4, mean and S.E.M. plotted)

When bleaching the ADPA, we also noticed a change in the absorption spectra of FAP-TAPs. After 10 min of illumination, the fluorescence of ADPA in solution was completely bleached by FAP-TAPs. We compared the absorption spectra of before and after illumination, we noticed the major peak of the complex was blue-shifted 10 nm, coupled with a decrease in absorbance (Figure 5.9a). This could be caused by the photobleaching of the MG-2I. It is also possible that the complex itself has been photo-oxidized to a stable form. There is no significant difference between the bleaching rate of MG-ester/dL5** and MG-2I/dL5** (Figure 5.9b). Further experiments are required to understand the singlet oxygen generation pathway and how the complex itself withstands the strong oxidation environment.

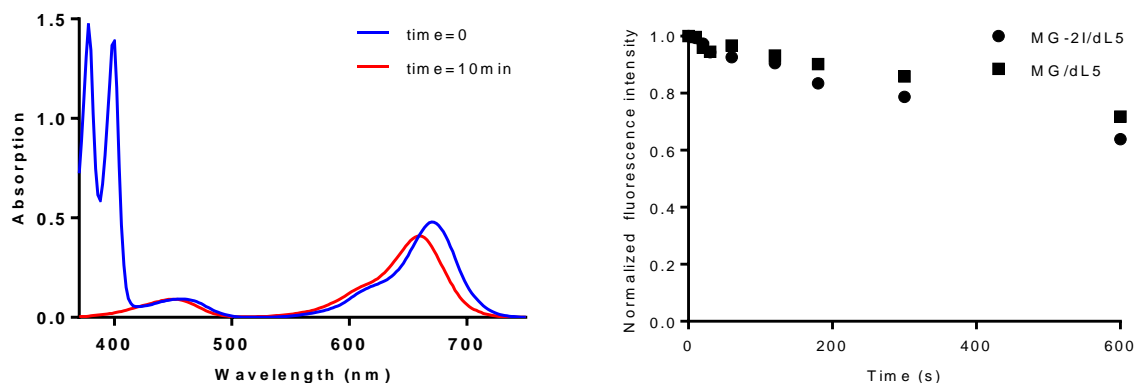


Figure 5.9: (a) Absorption spectra of MG-2I/dL5** with ADPA before and after 10 minutes of LED illumination at 669 nm. (b) Fluorescence intensity in corresponding channel (668/700 nm for MG-2I/dL5**, and 633/668 nm for MG-ester/dL5**) was monitored over 10 min and individually normalized to its initial fluorescence intensity.

Since D₂O is known to greatly increase the lifetime of ¹O₂ (4 μs to 52 μs)³⁹ while exerting little effect on other reactive oxygen species, the same ADPA bleaching assay was conducted in D₂O to further confirm that the ROS generated by FAP-TAPs was singlet oxygen (Figure 5.10). In deuterated PBS buffer, the bleaching rate of ADPA by FAP-TAPs was significantly enhanced (at 30 s, 86% ADPA was bleached by FAP-TAPs in dPBS while only 27% in PBS), indicating ADPA bleaching was a result of specific generation of singlet oxygen from the complex.

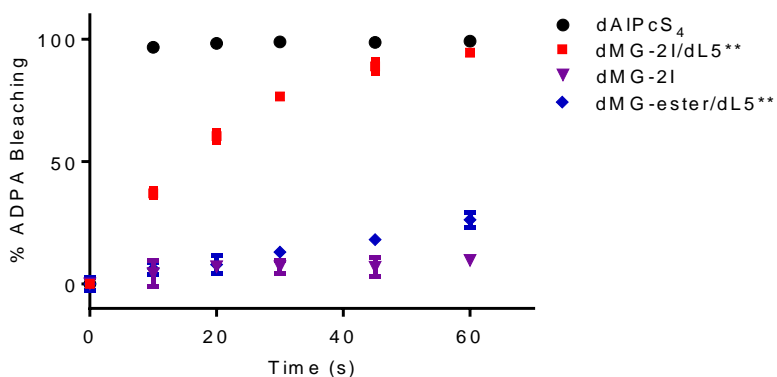


Figure 5.10: % ADPA bleaching by FAP-TAPs in deuterated PBS buffer, conditions are maintained the same as in Figure 5.8. (n = 4, mean and S.E.M. plotted)

In order to estimate the fold of activation of singlet oxygen generation, we made a concentration series of free MG-2I (in dPBS) and MG-2I/dL5** (in 1 : 9, H₂O: dPBS), and plotted the absorbance at 669 nm against the ADPA bleaching. However, in the same absorbance range, MG-2I/dL5** is much faster in bleaching ADPA than MG-2I, so we applied different light exposure time to the samples (60 s exposure time for MG-2I and 10 s exposure time for MG-2I/dL5**). Assuming the bleaching rate does not change within 60 s for MG-2I, we estimated the change of singlet oxygen generation is > ~100-fold based on the ratio of the slopes, scaled by a factor of 6 to account for the 6-fold longer exposure of the MG-2I (Figure 5.11). Due to the change of absorption maximum upon binding, the OD₆₆₆ of an equimolar solution of MG-2I dye is 4.5-fold lower than that of a MG-2I/dL5** (0.022 vs 0.097). Taken together, the overall activation for singlet oxygen production (R_{Δ}) upon binding is estimated to be higher than 450-fold calculating from equation 3 (R_{ϵ} : extinction coefficient (ϵ) activation at the excitation maximum of the complex, $R_{\Phi_{\Delta}}$: singlet oxygen quantum yield activation (Φ_{Δ})).

$$R_{\Delta} = R_{\epsilon} R_{\Phi_{\Delta}}$$

Equation. 3

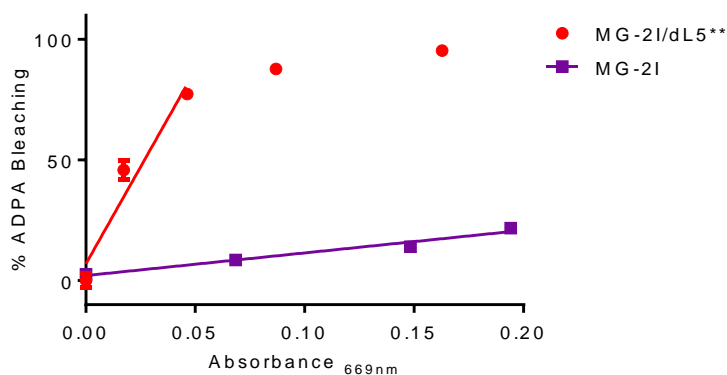


Figure 5.11: Estimated fold of activation of singlet oxygen generation from MG-2I bound to FAP, % ADPA bleaching by free MG-2I (in dPBS) (OD = 0.017, 0.041, 0.087, 0.163) at 669 nm after 60 s illumination, and by MG-2I/dL5** (in 1 : 9 H₂O: dPBS) (OD = 0.068, 0.148, 0.194) at 669 nm after 10 s illumination was plotted against 669 nm absorbance. (n = 4, mean and S.E.M. plotted)

To evaluate FAP-TAPs ability to generate singlet oxygen under different wavelength illumination, we compared the relative ADPA bleaching rate using excitation filters for various fluorescent proteins, including CFP (445/45 nm), GFP (470/22 nm), YFP (500/24 nm), RFP(531/40 nm), Cy5 (628/40 nm) and a 659 nm laser (Figure 5.12). When excited with identical light flux, the excitation with GFP poses the most significant problem for excitation of the FAP-TAPs, while using YFP or RFP excitation filters shows very little singlet oxygen activation. This result is in consistent with the excitation spectrum of the FAP-TAPs, suggesting these fluorescent proteins are optimal for use with FAP-TAPs.

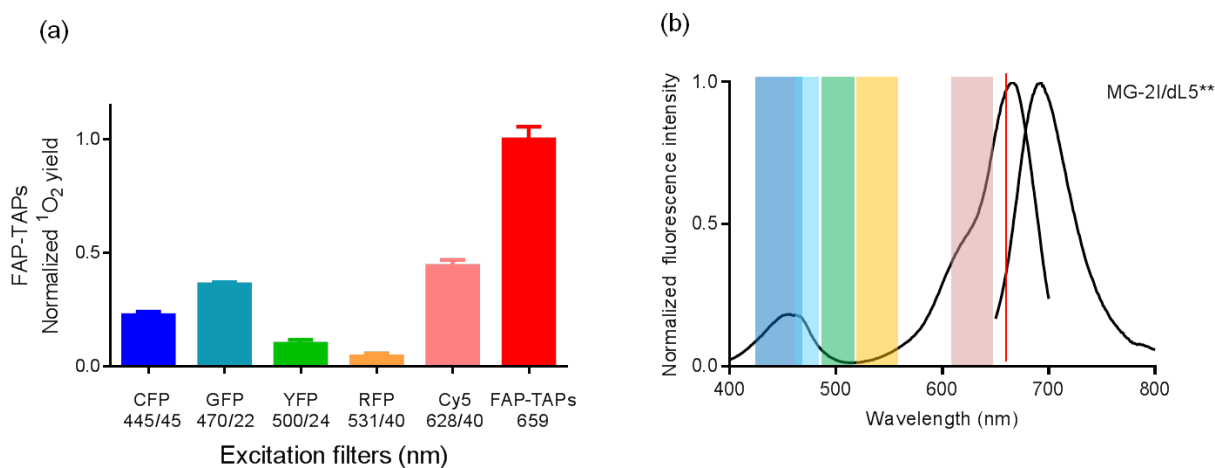


Figure 5.12: **(a)** Normalized singlet oxygen yield using % ADPA bleaching by FAP-TAPs in PBS buffer with different excitation wavelengths, YFP and RFP excitation resulted in little ADPA bleaching. (n = 4, mean and S.E.M. plotted) **(b)** Overlap of common fluorescent proteins' excitations with MG-2I/dL5** spectrum.

ROS generation is useful in Correlative Light and Electron Microscopy (CLEM)¹⁹, where 3,3'-Diaminobenzidine (DAB) can be photo-oxidized by ROS to produce brown precipitate and bind to electron-dense osmium during subsequent electron microscopy fixation, which will then provide contrast in electron microscopy (Figure 5.13a). To find FAP-TAPs' potential use in CLEM, we evaluated its ability to cause DAB precipitate *in vitro*. 100 μ L samples (AlPcS₄, MG-

2I/dL5**, MG-ester/dL5**, MG-2I) in pH 7.4 sodium cacodylate buffer with the same optical density at 669 nm were mixed with 100 μ L 1mg/mL DAB in pH 7.4 sodium cacodylate buffer for 5 minutes. Then, all samples were transferred to a 96-well plate and subject to 2 hours illumination using the LED light box. Clear brown precipitate were seen from MG-2I/dL5** complex after 1 h illumination, suggesting these constructs could be potentially useful for CLEM (Figure 5.13b).

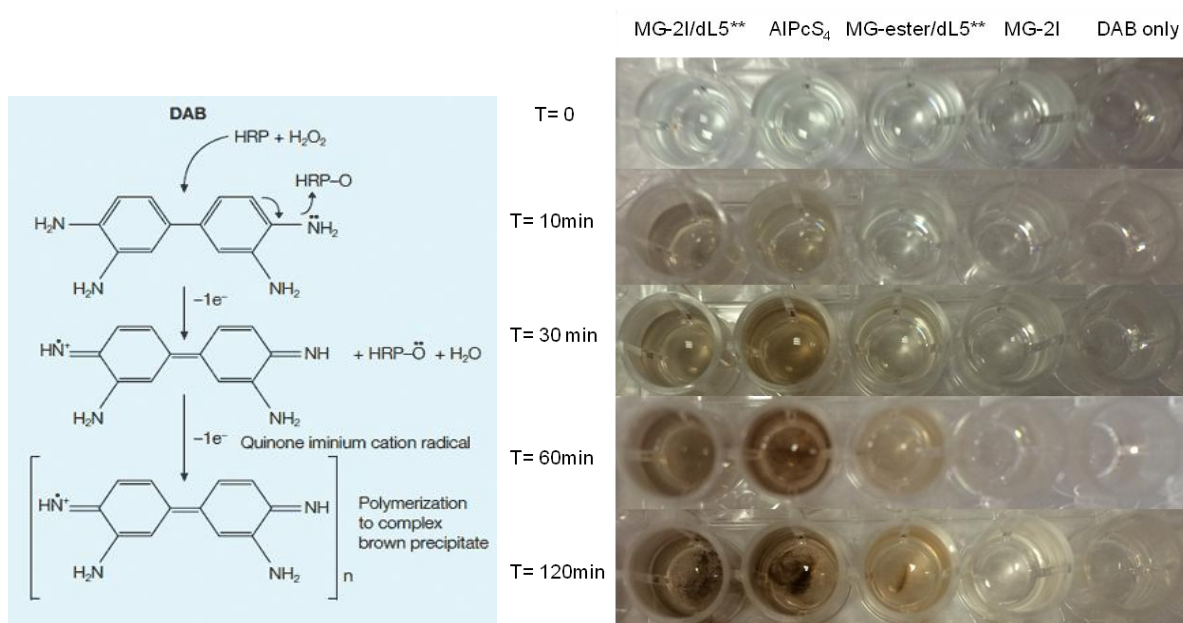


Figure 5.13: (a) Mechanism of DAB photoconversion by ROS. (b) Photoconversion of DAB by FAP-TAPs. The absorbance for each group at 669 nm was adjusted to the same. Illumination light source: LED, 669 nm, 89 mW/cm². Clear precipitates were observed from MG-2I/dL5** and AIPcS₄ after 1 hour illumination.

FAP-TAPs mediated CALI of the PLC δ 1 PH domain

Chromophore-assisted light inactivation (CALI) is a technique where biologists use a photosensizing molecule (genetic fused or conjugated to an antibody) to precisely inactivate protein of interest^{40,41}. Because of the short lifetime of ROS, the damage radius is usually well-controlled and restricted to proteins that are adjacent to the illuminated chromophore. This

method provides a spatially and temporally precise inactivation tool for studies of protein functions and protein-protein interactions. To assess FAP-TAPs utility for targeted protein inactivation, we compared release from the membrane of EGFP-PH-KillerRed and EGFP-PH-dL5** fusion proteins upon suitable illumination in HEK 293 cells (constructed by Dr. Yi Wang)¹⁸. When the pleckstrin homology (PH) domain from PLC δ 1 is inactivated by CALI, it translocates from the membrane to the cytoplasm, increasing the cytoplasmic/membrane EGFP signal (Figure 5.14).

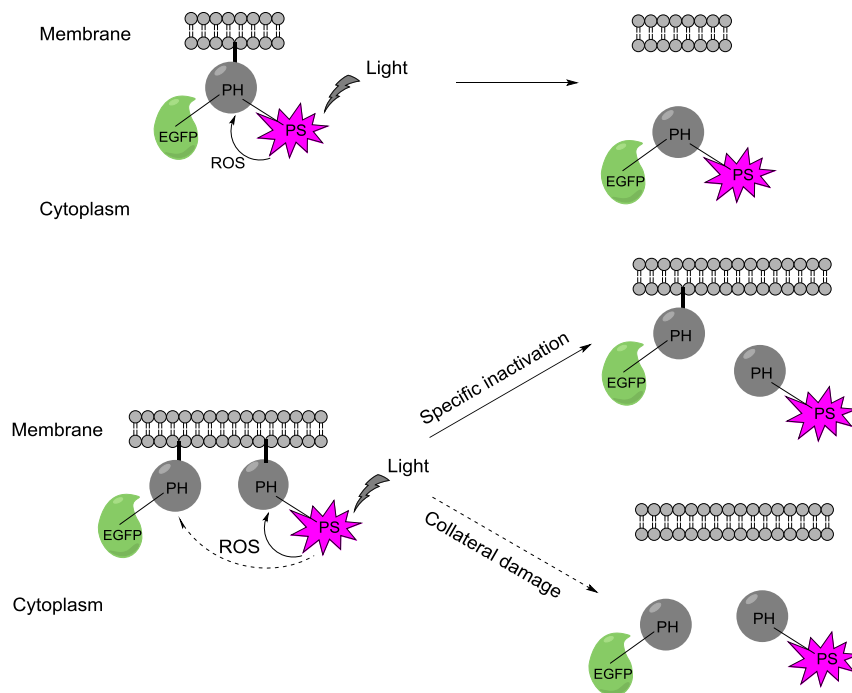


Figure 5.14: Schematic outline of the experimental design. Top: EGFP-PH-KillerRed or EGFP-PH-dL5** triple fusion protein was constructed to evaluate the effectiveness of specific protein inactivation from KillerRed and FAP-TAPs. Bottom: EGFP-PH was co-expressed with PH-KillerRed or PH-dL5** to estimate the collateral damage from KillerRed and FAP-TAPs.

After 5 min illumination with 560 nm ($60\times$ objective, 2.03 W/cm^2), the cytoplasm-to-membrane signal ratio changed 37% under KillerRed-mediated CALI, similar to previous reports (Figure 5.15a)¹⁸. The fluorescence of KillerRed is significantly bleached ($> 75\%$) after 1 min illumination. In contrast, FAP-TAPs illumination resulted in a 33% ratio change after 10 s of 640

nm laser illumination ($60\times$ objective, 2.07 W/cm^2). Further illumination of FAP-TAPs induced no EGFP ratio change but noticeable morphology change and minor photobleaching (Figure 5.15b and Figure 5.16). The potential collateral damage was also assayed by co-expressing EGFP-PH with PH-KillerRed or PH-dL5** (Figure 5.14). Although the timescales of illumination were ~ 30 -fold different, Both KillerRed and FAP-TAPs induced similar inter-molecule inactivation of PH domain in proportion to the amount of target inactivation, indicating the FAP-TAPs are spatially restricted similarly to KillerRed under CALI conditions.

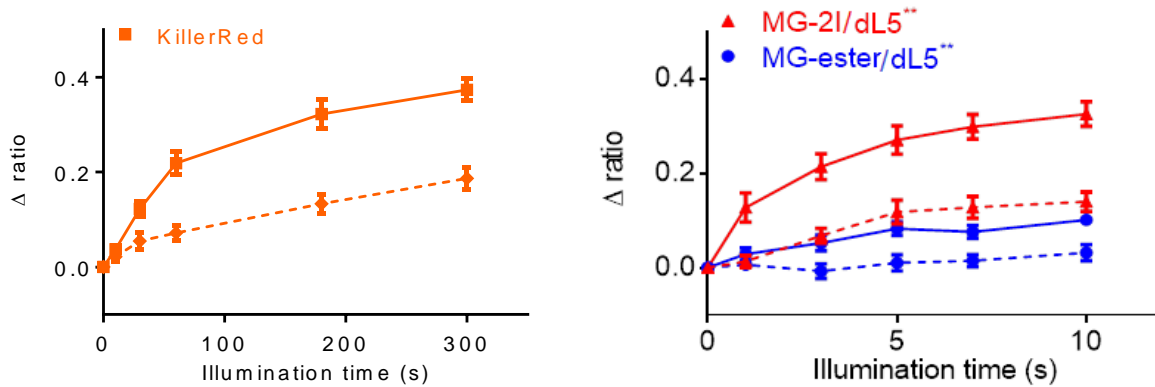


Figure 5.15: EGFP cytoplasm to membrane ratio change upon illumination of (a): EGFP-PH-KillerRed and (b): MG-2I with EGFP-PH-dL5**, MG-ester with EGFP-PH-dL5** (Solid lines). Dashed lines are corresponding collateral damage from co-expressed proteins. ($n = 8$, mean and S.E.M. plotted)

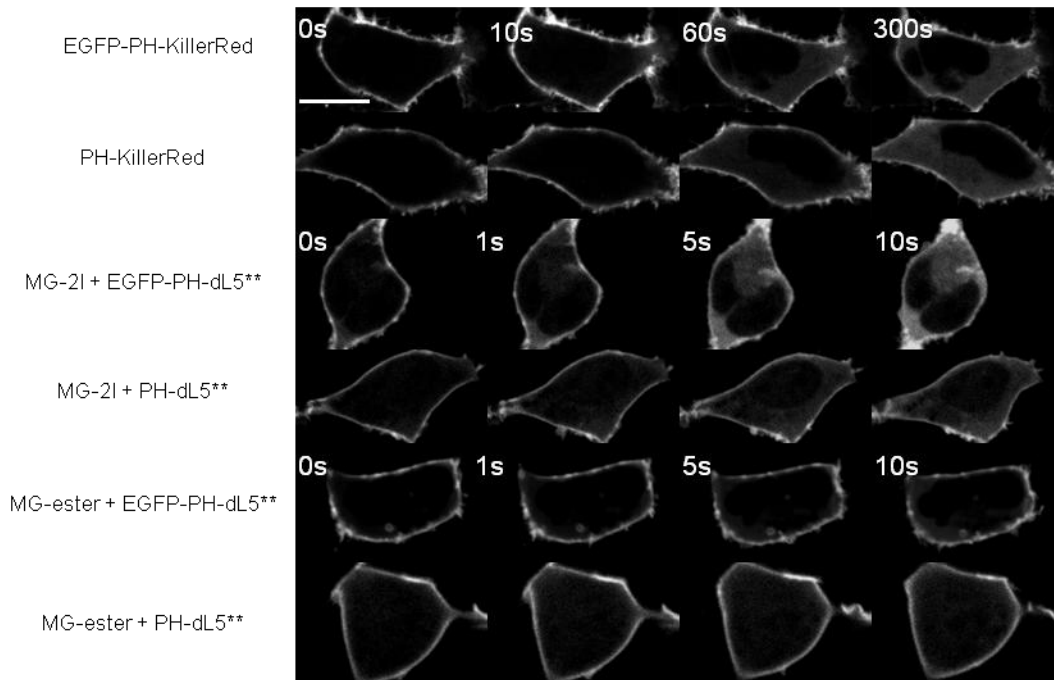


Figure 5.16: FAP-TAPs mediated light-induced protein inactivation of the PLC $\delta 1$ PH domain. Representative EGFP fluorescent signal change from each condition, with imaging at fixed intervals. Scale bar = 5 μm and applied to all images. Illumination condition: KillerRed: 560 nm laser, 60 \times objective, 2.03 W/cm^2 ; MG-ester/dL5** and MG-2I/dL5**: 640 nm laser, 60 \times objective, 2.07 W/cm^2 .

FAP-TAPs mediated cellular photoablation

The light-induced cytotoxicity of FAP-TAPs was evaluated on HEK 293 cells expressing a cell-surface anchored FAP (TM-dL5** HEK), where the FAP was anchored in the plasma membrane by a single PGFR-derived transmembrane helix (cell line constructed and provided by Dr. Yi Wang). A mixed population of TM-dL5** expressing HEK cells and wild-type HEK cells was incubated with 400 nM of MG-ester or MG-2I dye for 30 minutes and then illuminated with a continuous laser source (40 \times objective, 640 nm excitation, 0.76 W/cm^2) for 1 minute. As shown in Figure 5.17, only fluorescently labeled TM-dL5** HEK cells that were treated with MG-2I and light were stained dead within 30 minutes using a LIVE/DEAD cell viability kit (Invitrogen, L-3224), while the wild-type HEK cells in the illumination field remained alive and

metabolically active. The labeled cells began to lose cell morphology with swelling and blebbing within a very short period upon illumination. MG-ester bound to TM- dL5** HEK cells, MG-2I treated WT HEK cells and non-targeted MG-2I/dL5** complex added to the media showed no apparent cytotoxicity or phototoxicity upon illumination. These results clearly established the dual requirements of targeted FAP expression and activated TAPs recognition in order to achieve efficient photosensitization. Moreover, these results also revealed that close contact of FAP-TAPs on target cells was critical for effective delivery of ROS due to the very short radius of action of singlet oxygen.

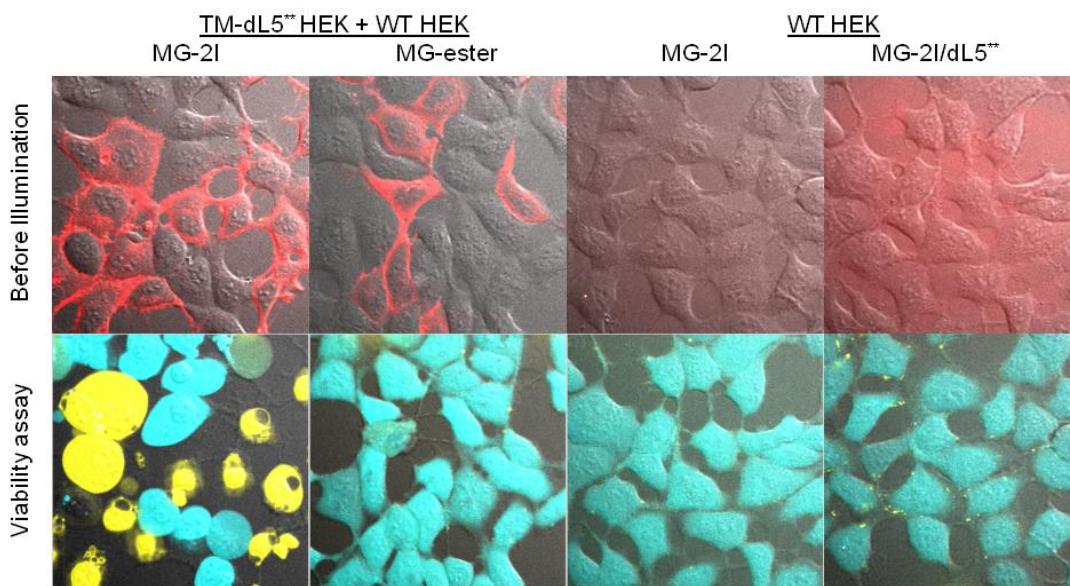


Figure 5.17: Photo-induced cell death required both the binding of MG-2I to dL5** and the cellular targeting of the complex. Top panel: images taken before laser illumination, merge of c640 (red) and DIC; bottom panel: Live/Dead cell viability assay 30 min after illumination, merge of c488 (live cells in cyan), c560 (dead cells in yellow) and DIC. Scale bar = 10 μ m and applied to all images.

Limited self-bleaching (< 30%) was observed during photosensitization (the first minute of continuous illumination) of FAP-TAPs (Supplementary Movie 1), allowing high ROS dose delivery and real-time monitoring of site targeting. Under prolonged illumination times, WT HEK cells that are adjacent to FAP-TAPs expressing cells begin to lose viability (Figure 5.18).

The high photostability of the FAP-TAPs allows a high degree of tuning in the delivered ROS dose, allowing illumination conditions ranging from those selectively kill only a fraction of the expressing cells to prolonged exposures that extend the phototoxicity to nearby, non-targeted cells.

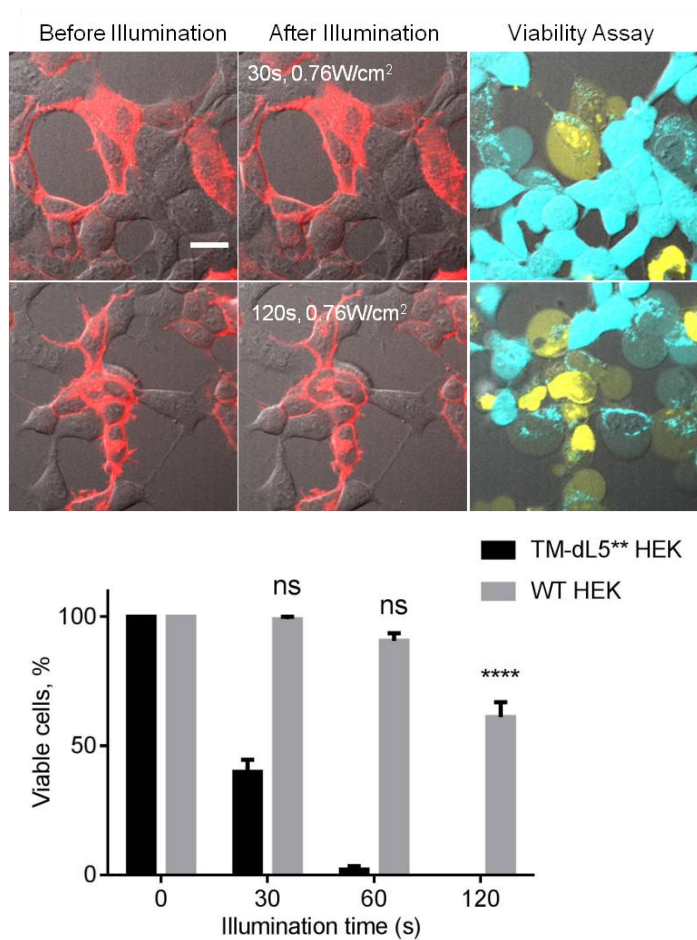


Figure 5.18: Photo-induced cell death required both the binding of MG-2I to dL5** and the cellular targeting of the complex. Top panel: images taken before laser illumination, merge of c640 (red) and DIC; bottom panel: Live/Dead cell viability assay 30 min after illumination, merge of c488 (live cells in cyan), c560 (dead cells in yellow) and DIC. Scale bar = 10 μ m and applied to all images.

dL5** targeted to the cytosol, mitochondria and nuclei of HEK cells (cell lines constructed and provided by Dr. Yi Wang) have also successfully induced phototoxicity from the FAP-TAPs at distinct subcellular locations. Cellular death pathways induced by oxidative stress from high

singlet oxygen production of photosensitizer are reported to be dependent on the localization site of photosensitizer in the cell and the amount of singlet oxygen generated^{5,9}. Unlike targeting to TM, dL5** targeted to the above compartments tended to require higher light dose (2-fold more) and longer incubation time after illumination (3 hours) to observe clear cell death. The change of morphology is also not as drastic as TM-dL5** cells, indicating possible different death pathways were induced by targeting to different sites.

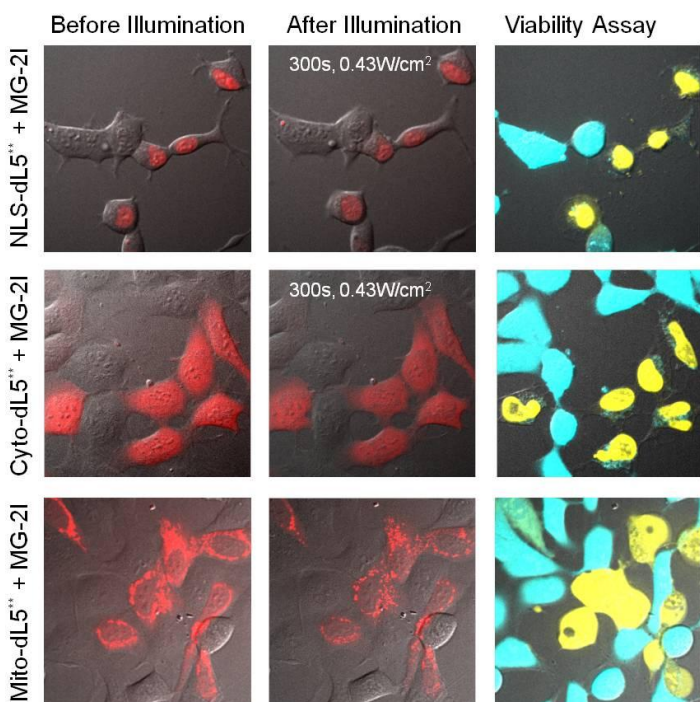


Figure 5.19: Representative MG-2I induced cytotoxicity on HEK cells expressing FAP in transmembrane, mitochondria, nucleus and cytosol.

Use of KillerRed targeted mitochondria has been reported to allow effective cell killing by inducing apoptosis. To compare the cell killing effectiveness between FAP-TAPs and KillerRed, we transfected HEK cells to express KillerRed in the mitochondria in the same manner as dL5** (cell line constructed and provided by Dr. Yi Wang). Mito-KillerRed HEK cells required 90 minutes of 560 nm laser illumination ($60\times$ objective, 2.03 W/cm^2) to induce about 50% effective cell killing, and higher light doses are required to achieve 100% killing which resulted in

significant killing of neighboring non-expressing cells. Using the same laser power, mitochondrially targeted FAP-TAPs illuminated for 90 seconds induced 100% effective cell killing, without damage to neighboring cells (Table 5.2). The light dose required for cellular ablation is at least 60-fold less than KillerRed.

Illumination time			Repeat 1		Repeat 2		Repeat 3		Repeat 4	
			total	dead	total	dead	total	dead	total	dead
FAP-TAPs	1.5min	Mito-dL5	3	3	4	4	6	5	4	4
		WT	5	0	9	0	9	0	9	0
	5min	Mito-dL5	4	4	3	3	3	3	4	4
		WT	9	2	5	4	4	4	11	3
KillerRed	60min	mito-KR	7	0	4	0	4	1	6	0
		WT	6	0	4	0	5	0	3	0
	90min	Mito-KR	4	2	7	4	7	2	5	1
		WT	4	0	6	0	9	0	3	0
	120min	Mito-KR	4	4	6	6	5	4	5	5
		WT	5	5	5	5	7	0	3	2

Table 5.2: Summary of cell death induced by FAP-TAPs and KillerRed targeted to mitochondria of HEK cells. A mixture of Mito-dL5** or Mito-KillerRed and WT HEK cells were subjected to continuous laser illumination, for FAP-TAPs: 640 nm, 60× objective, 2.07 W/cm², KillerRed: 560 nm, 60× objective, 2.03 W/cm². Viability assay was carried 3 hours post illumination.

Using a custom-built light-box emitting at 669 nm (89 mW/cm² at specimen), we quantitatively determined the light-induced cytotoxicity on TM-dL5** HEK cells under varied illumination times and intensities (Figure 5.20). Different light doses were achieved by changing of light intensity (using 10 × 10 cm neutral density filters placed over the sample in the light box, power density was measured at the sample for each condition) or illumination time. For dead cell counting, the media was replaced with PBS containing 2 μM propidium iodide (PI) and 8 μM Hoechst after illumination. Allowing 30 min of staining, the ratio of cell death was calculated from the cell count stained by PI (dead cells) to Hoechst (total cells). WT HEK cells incubated

with MG-2I and TM-dL5** HEK cells labeled with MG-ester showed no detectable light-induced cytotoxicity. The LD₅₀ of illumination for FAP-TAPs labeled cells was measured to be 50 J/cm² in the light box, and in the microscope (Figure 5.21). A linear response was observed with changes in illumination duration, while changes in light intensity revealed a more sigmoidal process, similar to threshold responses to ROS reported in bacteria and mammalian cells, a result of cellular buffering systems that can mitigate the effects of some excess toxic ROS^{42,43}.

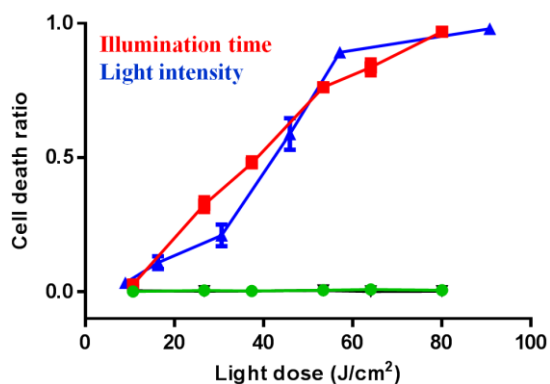


Figure 5.20: Light dose dependent cytotoxicity is seen on TM-dL5** cells labeled with MG-2I under variable light intensity (blue) or variable illumination duration (red). In contrast, no phototoxic effect is seen for MG-ester with TM-dL5** HEK cells (dotted black) or MG-2I with WT HEK cells (dashed green). Cells were illuminated using a LED light box. Cells were stained with propidium iodide (dead) and Hoechst (total) and over 300 cells were counted for each data point (n = 4, mean and S.E.M. plotted).

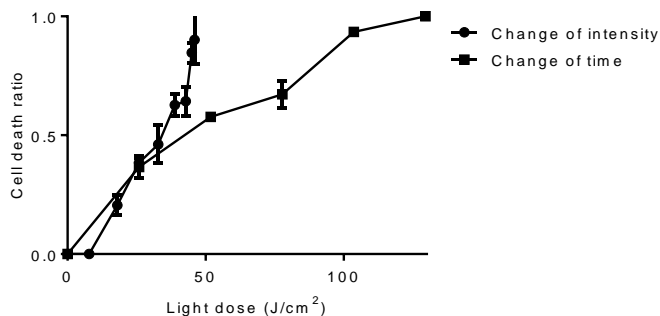


Figure 5.21: Dose dependent cytotoxicity by MG-2I on HEK cells expressing cell surface dL5** with various illumination intensity (1 minute illumination time with 25%, 40%, 50%, 60%, 70%, 80%, 90%, 100% laser power) or illumination duration (50% laser power with 1, 2, 3, 4, 5 minutes illumination time) using confocal microscopy (40× objective, 640 nm). (n = 3, mean and S.E.M. plotted)

In order to specify the ROS generated by FAP-TAPs in cells, we examined the suppression of FAP-TAPs mediated phototoxicity by adding different ROS quenchers to TM-dL5** HEK cells complexed with MG-2I using the light-box mentioned earlier. Sodium azide (NaN_3), a known selective quencher of singlet oxygen, demonstrated a dose-dependent inhibition of the phototoxic response⁴⁴. The phototoxic effect of FAP-TAPs was almost completely suppressed at a sodium azide concentration of 10 mM, consistent with other reports of sodium azide-mediated suppression of cytotoxicity (Figure 5.22). Meanwhile, no significant suppression of phototoxicity was observed when cells were incubated with high concentrations of catalase (a peroxide quencher, 1,000 U/mL) or superoxide dismutase (SOD, a superoxide quencher, 500 U/mL)⁴⁵. Up to 2,000 U/mL catalase and 1,000 U/mL SOD were used under continuous illumination in a confocal microscope, resulting in a modest reduction in dead cell staining, but a persistent loss of viability and metabolic activity (Figure 5.23). Results from these quenching experiments along with the *in vitro* ADPA bleaching assay indicated that singlet oxygen generated from FAP-TAPs was the primary ROS mediating the observed phototoxic responses.

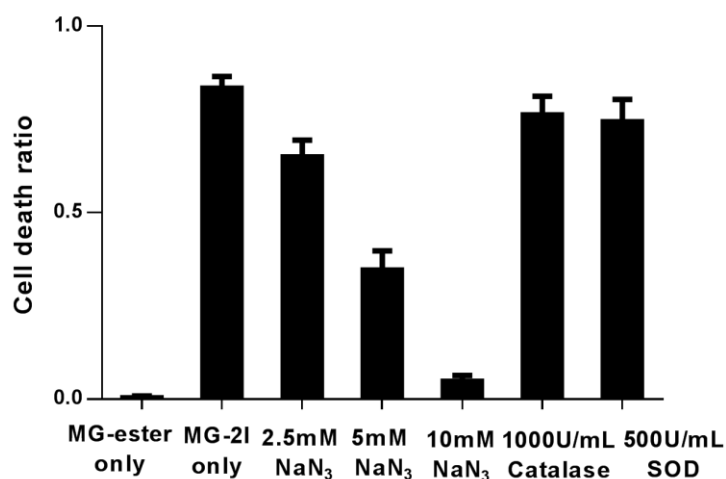


Figure 5.22: TM -dL5** HEK cells were labeled with 400 nM of MG-2I and various ROS quenchers. After 1 minute of illumination ($40\times$ objective, 640 nm, 0.76 W/cm^2), cell viability was determined with Live/Dead cell fluorescent assay. (Scale bar = 10 μm and applied to all images)

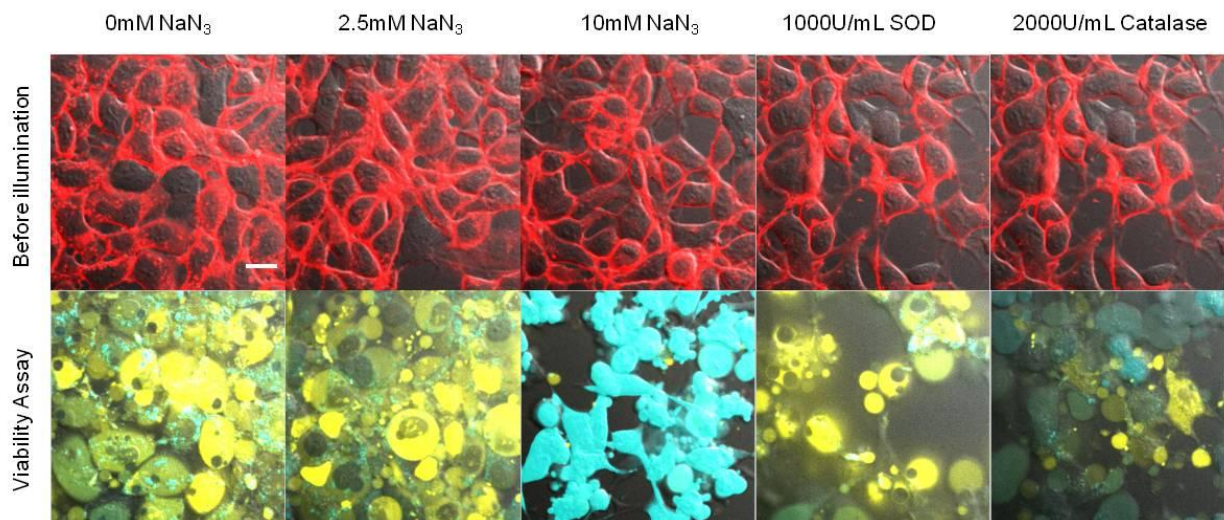


Figure 5.23: Phototoxicity was suppressed only by sodium azide, but not catalase or SOD, indicating the cytotoxicity was singlet oxygen mediated. ROS quenchers were added to cells 5 minutes prior to illumination and allowed 5 minutes rescue after illumination before Live/Dead staining as above. (n = 4, mean and S.E.M. plotted)

$^1\text{O}_2$ is known to react with nearby molecules to produce secondary peroxide species as initial products, which then create other reactive species and lead to cytotoxicity⁴⁶. Hence, chemical sensors can be used to identify the cascade generation of ROS after photosensitization.

Dihydroethidium (DHE), which reacts with superoxide (O_2^-) to form a DNA intercalating fluorescent species (2-hydroxyethidium, 490 nm excitation and 567 nm emission), was used to detect other ROS in HEK cells expressing the FAP-TAPs in the nucleus⁴⁷. NLS-dL5** HEK cells were incubated with 400 nM of dyes and then exposed to 2 μM dihydroethidium (diluted from freshly prepared ethanol stock solution) for 10 min. Then cells were illuminated for 2 min (60 \times objective, 640 nm, 2.43 W/cm²). The activation of DHE was monitored with an excitation of 488 nm and emission of 535/25 nm immediately after photosensitizing illumination.

Significant ROS-dependent activation of DHE in the nucleus was only observed when MG-2I with dL5** and light were present, but not in control cells or FAP-expressing cells labeled and illuminated in the presence of MG-ester dye (Figure 5.24).

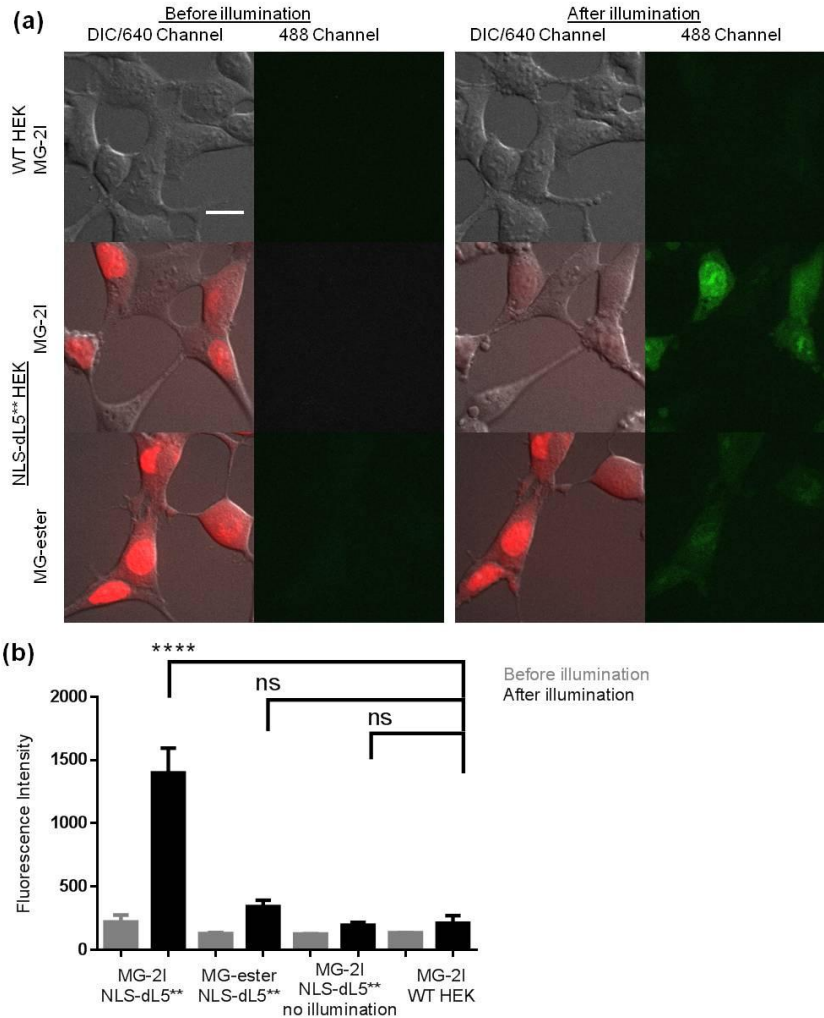


Figure 5.24: **(a)** Wild type HEK cells or cells expressing FAP with a nuclear localization signal (NLS-dL5** HEK) were first labeled with 400 nM of dye, and then 2 μ M of DHE was added to cells 10 minutes prior to 2 minutes of illumination (60 \times objective, 640 nm, 2.43 W/cm²). Imaging was carried out immediately after photosensitization. **(b)** Mean fluorescence intensity change after illumination of each group. (n = 6, mean and S.E.M plotted. Scale bar = 10 μ m and applied to all images, 488 channel: 488 nm excitation and 535/25 nm emission filter).

FAP-TAPs mediated cardiac ablation in larval zebrafish

Transgenic zebrafish lines were produced by our collaborators at University of Pittsburgh (Dr. Maria A. Missinato, Dr. Ezenwa Onuoha and Dr. Michael Tsang), the photoablation and analysis of adult zebrafish were carried out by Dr. Maria A. Missinato and Dr. Michael Tsang

In vivo cellular ablation has been used to study cell-niche relationships, cellular roles in development and replacement of damaged cells and tissues in regeneration⁴⁸. Zebrafish (*danio*

rerio) is a frequently used vertebrate model organism because it is optically transparent, easily genetically manipulated, and shows conserved developmental processes with other vertebrates^{49,50}. Lineage ablation can be accomplished in zebrafish by tissue specific expression of a bacterial nitroreductase (*ntr*) and subsequent treatment for ~12-24 h with metronidazole, a prodrug that is reduced in *ntr*⁺ cells to a DNA synthesis inhibitor, resulting in cell death⁵¹. Because of the rapid zebrafish development, 12-24 hours represents a relatively large ablation timeframe, which can limit the temporal resolution of lineage ablation studies. Given the rapid phototoxic response from targeted cells in culture, we sought to test the timescale of cellular ablation in living larval zebrafish. Transgenic zebrafish lines were produced that expressed a cytoplasmic dL5***-mCer3* (dL5***-mCer3*) tandem protein under control of the heart-specific *myosin light chain 7* (*myl7*, also known as *cmlc2*) promoter, *Tg(myl7: dL5***-mCer3*)*⁵². 3 founder lines that expressed mCer3 at 28 hpf in the beating cardiac tube were identified, *Tg(myl7:MBIC5-mCer3)*^{pt22} (*Tg*^{pt22}) and *Tg(myl7:MBIC5-mCer3)*^{pt23} (*Tg*^{pt23}) were used in this study. Expression of dL5***-mCer3* was confirmed by fluorescence imaging of mCer3 and MG-ester/dL5** or MG-2I/dL5** complexes, and was restricted to the beating heart (Figure 5.25).

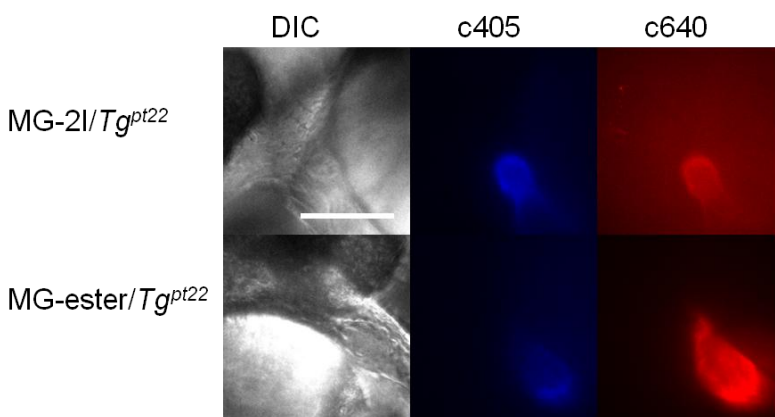


Figure 5.25: Specific expression of *Tg*^{pt22} and labeling by MG-2I or MG-ester, images were taken by a confocal microscope, 20×, 100% laser power. Scale bar = 50 μm and applied to all images.

To test the effectiveness of FAP-TAPs, we treated Tg^{pt22} embryos at 48 hour post fertilization (hpf) with 500 nM fluorogen (MG-2I or MG-ester) for 3 hours. Then, larvae are subjected to 12 minutes laser illumination (659 nm, 242 mW/cm²). Immediately after illumination, irradiated transgenic zebrafish treated with MG-2I showed no sign of heart beat or blood circulation, while MG-ester treated transgenic larvae and wild-type zebrafish with MG-2I were normal. At 24 hours post illumination (hpi), we did not detect any new cardiac cells as indicated by expression of *mCer3* fluorescence in the transgenic larvae (Figure 5.26). Tg^{pt22} larvae treated with MG-2I and light were developmentally delayed relative to control groups, showing smaller eyes and larger yolk at 96 hpi (Figure 5.27). At 48 hpi, we found that photo-treated MG-2I/ Tg^{pt22} larvae exhibited cardiac edema and lower *mCer3* fluorescence than at 24hpi. At 96 hpi, no *mCer3*⁺ cells were detected from photo-treated MG-2I/ Tg^{pt22} larvae, indicating that acute loss of *myl7* lineage cells was not renewed later in development.

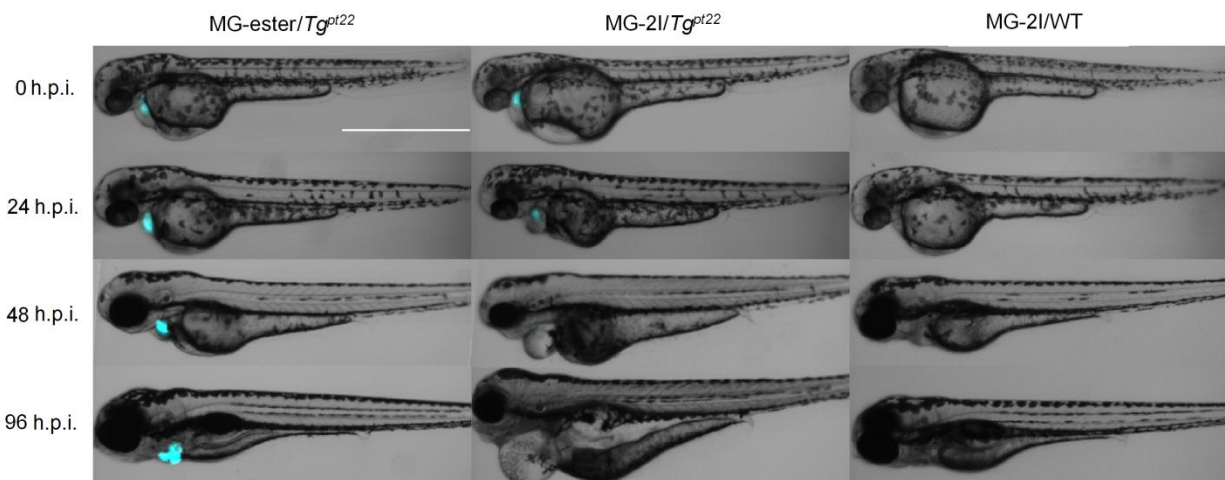


Figure 5.26: Phenotype development from 0 hpi to 96 hpi of larval zebrafish (Merge of DIC and *mCer3* fluorescence (cyan), n = 20 for each group): MG-ester/ Tg^{pt22} , MG-2I/ Tg^{pt22} and MG-2I/WT. In MG-2I/ Tg^{pt22} group, the larvae developed a range of visible defects: large cardiac edema, small eyes, and collapsed, nonfunctional heart chambers. In both control groups, development proceeded normally. Scale Bar = 1000 μ m and applied to all images.

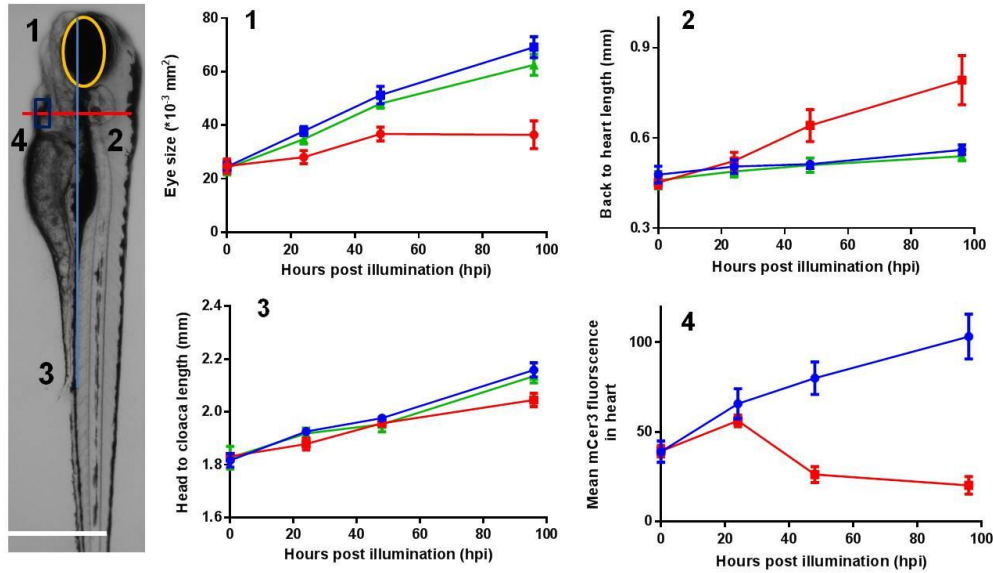


Figure 5.27: Region of interest selected to quantitatively analyze development of zebrafish from 0hpi to 96hpi. Red: MG-2I/*Tg^{pt22}*, blue: MG-ester/*Tg^{pt22}*, green: MG-2I/WT. In MG-2I/*Tg^{pt22}* group, the fish developed smaller eyes (****), shorter body length (*), larger edema (****) compared to MG-2I/WT and loss of mCer3 positive cell (****) compared to MG-ester/*Tg^{pt22}*. Scale bar = 500 μ m, n = 6, mean and S.E.M. plotted, unpaired t test, * $P < 0.05$, ** $P < 0.01$; *** $P < 0.001$.

To evaluate ablation, we used deoxynucleotidyl transferase-mediated deoxyuridinetriphosphate nick end-labeling (TUNEL) assay with anti-GFP staining to assess on and off-target cell death in whole-mount *Tg^{pt22}* larvae at 24 hpi (Figure 5.28). Larval zebrafish were fixed 24 h after illumination in 4% paraformaldehyde (PFA) overnight. Whole-mount apoptosis was measured via TUNEL assay (Invitrogen, C10617) according to the manufacturer's instructions. mCerulean3 was labeled by a primary rabbit anti-GFP antibody (Abcam, ab6556); the secondary antibody in use was donkey anti-rabbit IgG H&L (Alexa Fluor 555) (Abcam, ab150074). Reduced mCer3⁺ cells and an increased number of TUNEL⁺mCer3⁺ cells were seen in 12 min MG-2I/*Tg^{pt22}* larvae, without any increase in TUNEL⁺mCer3⁻ cell death compared with 12 min MG-ester/*Tg^{pt22}* larvae (Figure 5.29). The fraction of TUNEL⁺mCer⁺ cells in 12 min MG-2I/*Tg^{pt22}* group was increased compared to 12 min MG-ester/*Tg^{pt22}* group (31% vs 4.4%, $P <$

0.01). Shorter illumination time (4 min MG-2I/ Tg^{pt22}) resulted in reduced specific cytotoxicity, confirming the light-dose dependence of the FAP-TAPs ablation.

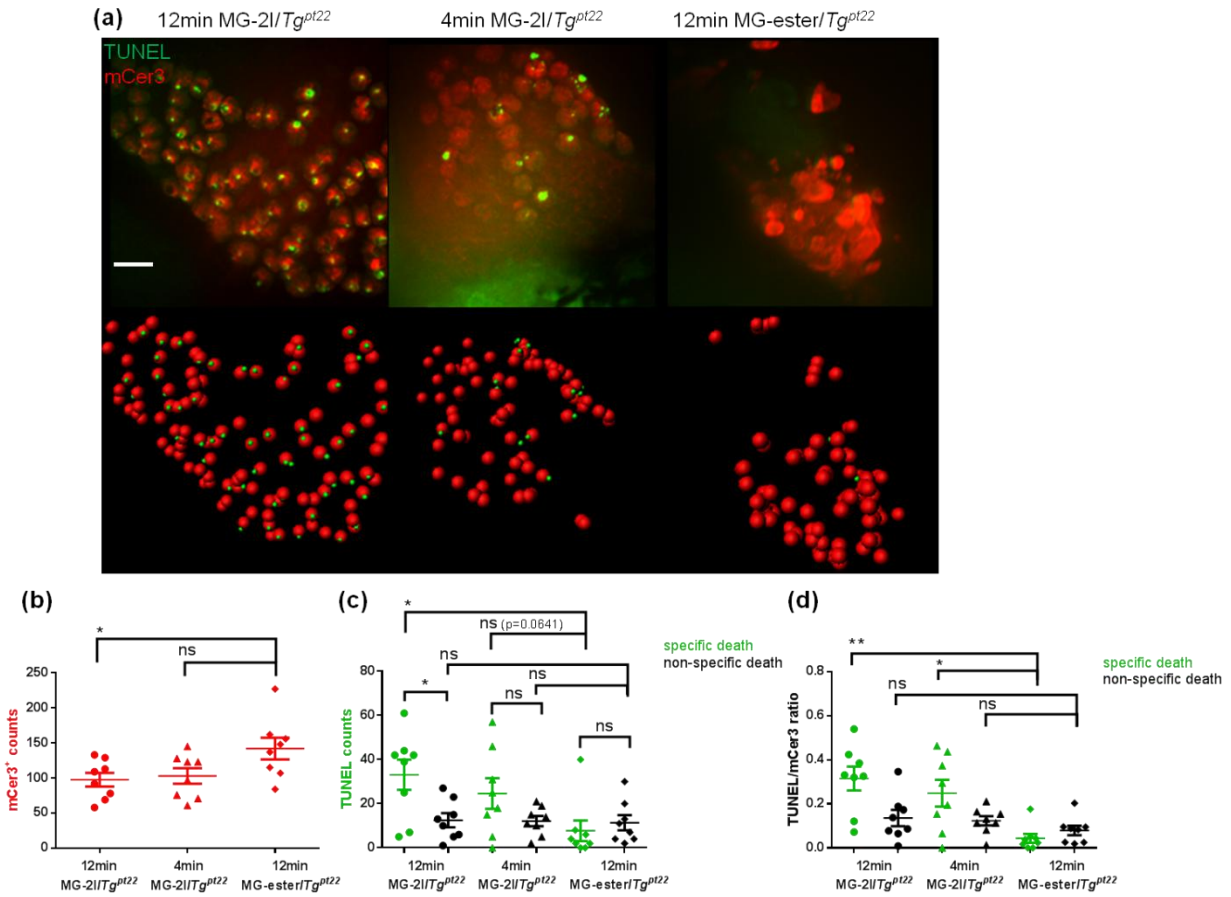


Figure 5.28: Fish were fixed 24 hpi and stained using a whole mount TUNEL assay and immunolabeling of the mCer3 with anti-GFP antibodies and a secondary Alexa555 conjugated donkey anti-rabbit antibody. **(a)** Representative imaging of orthogonal view and sphere reconstruction of TUNEL/mCer3 fluorescence. **(b)** mCer3⁺ cell count, fewer mCer3⁺ cells are seen in 12 min MG-2I/ Tg^{pt22} group (*). **(c)** TUNEL positive cell count, green represents TUNEL signals that colocalized with mCer3 signals; black represents TUNEL signals that were not associated with mCer3⁺ cells. (NS for all groups) **(d)** TUNEL/mCer3⁺ ratio, MG-2I with 12 min illumination induced 31.5% (**) cell death of mCer3⁺ cells compared to MG-ester with 12 min group. A reduced fraction of mCer3⁺ cells are killed (24.8%) when 4 min illumination is applied (*). Scale Bar = 10 μ m and applied to all images, n = 8, mean and S.E.M plotted. One-way ANOVA, Tukey post hoc tests were performed with multiple comparisons of mean for each group. Paired t test was used for comparisons between specific death and non-specific death. * $P < 0.05$, ** $P < 0.01$.

To demonstrate the utility of FAP-TAPs in deep tissue, we performed cardiomyocyte photo-ablation experiments in adult zebrafish (experiments and analysis were carried by Dr. Maria A. Missinato and Dr. Michael Tsang). Tg^{pt23} zebrafish that uniformly express CFP in the heart at the adult stage was used in this study (Figure 5.29a). Zebrafish were anesthetized for 3 minutes in Tricaine (0.168 mg/L of MS222, Sigma) and retro-orbital injected with 3 μ L of 12 μ M MG-ester (0.06 mg/kg) or MG-2I (0.09 mg/kg) solutions dissolved in filtered 1 \times PBS⁵³. Fish were returned into water and stimulate to breathe by vigorously squirting water over the gills with a pipette. 20-30 minutes after retro-orbital injection, 5 fish will were placed in a 100 mL beaker containing 50 mL of fish water and illuminated with the LED light-box (669 nm, 2.5 W/cm² illumination from below the fish) for 30 minutes (Figure 5.29b). The fish water in the beaker was replaced with fresh water every 10 minutes.

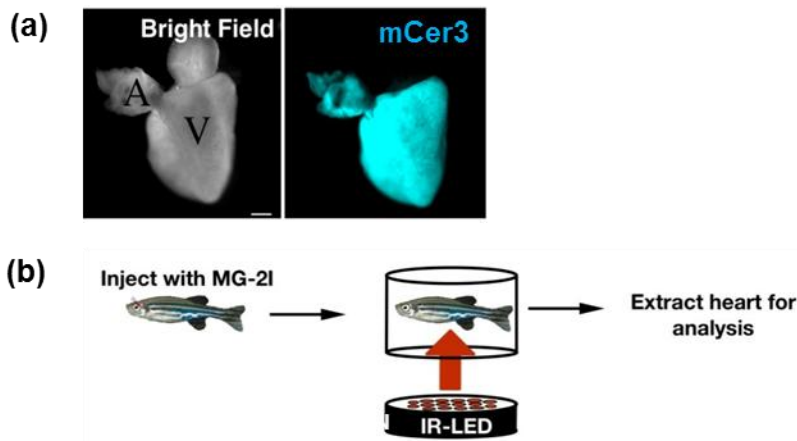


Figure 5.29: (a) Tg^{pt23} zebrafish uniformly express mCer3-dL5^{**} at the adult stage in the atrium (A) and in the ventricle (V) (Experiments were carried out by Dr. Maria A. Missinato); (b) Schematic illustration of experimental setup for photo-ablation of adult zebrafish (illustration was drawn by Dr. Michael Tsang).

The fish were then returned to the water system and monitored daily. Fish were lethally euthanized at determined time point after the illumination, and hearts, livers and intestines were

extracted and fixed in 4% paraformaldehyde for histochemical analysis. At 3 days post illumination (dpi), hearts, livers and intestine were extracted and fixed with 4% PFA. Fixed hearts, livers and intestines were cryopreserved in 30% sucrose in PBS before immersion in embedding medium (Leica). Apoptosis was measured via TUNEL assay (Millipore; S7165) according to the manufacturer's instructions. Primary antibodies used for immunostaining were anti-Mef2c (Santa Cruz Biotechnology; sc-313) (1:500) and anti-PCNA (Sigma; P8825) (1:1,000). Secondary antibodies used were Alexa Fluor 488 goat anti-rabbit IgG peroxidase conjugate (Thermo Fisher; A-11008) (1:1,000) and Alexa Fluor 594 goat anti-mouse IgG (H + L) (Thermo Fisher; A-11036) (1:1,000). Slides were mounted with Vectashield mounting medium with DAPI (Vector Laboratories; H-1200). For each experiment, two to six sections were analyzed for each heart, liver and intestine. The cardiomyocyte proliferation index was calculated as the percentage of the number of Mef2c⁺PCNA⁺ cells divided by the number of total Mef2c⁺ cells.

Increases cell death was observed in the hearts of transgenic zebrafish injected with MG-2I, compared to all the controls groups (Figure 5.30a), suggesting the efficiency of the ablation in deep tissue. In contrast, no difference of apoptotic rate was observed in livers and intestines between all the treatments, showing the specificity of the ablation system for the heart (Figure 5.31a). To confirm cardiomyocyte ablation, we extracted the hearts at 5 dpi and stained with Acid Fuchsin Orange G (AFOG) staining that labels the intact cardiac muscle in orange⁵⁴. Fourteen-micrometer cryosections were stained with AFOG as previously described. We measured the myofiber area by imaging four sections for each heart stained with AFOG and quantifying the total ventricular area and the cardiac tissue using ImageJ software (NIH). Transgenic hearts injected with MG-2I showed a damaged cardiac structure and a reduction of

the percentage of cardiac muscle in the ventricle, compared to the controls (Figure 5.30b). Importantly, no structural defects were observed in livers and intestine (Figure 5.31b). Adult zebrafish has a remarkable ability to regenerate damaged cardiac muscle throughout proliferation of pre-existing cardiomyocyte⁵⁵⁻⁵⁷. To determine whether the system that we generated caused enough damage to activate a regenerative response, we performed cardiomyocyte proliferation assay. At 5 dpi, only illuminated transgenic zebrafish injected with MG-2I had significantly increased numbers of proliferating cardiomyocytes compared to similarly treated wild-type zebrafish ($P < 0.001$, MG-2I-treated Tg^{pt23} versus MG-2I-treated wild-type; $P > 0.05$ MG-ester-treated Tg^{pt23} versus MG-ester-treated wild-type) (Figure 5.30c), showing that the ablation inflicted sufficient damage to induce a regenerative response. Notably, proliferation rate in livers and intestine was comparable in all the groups (Figure 5.31c), showing the specificity of the ablation for the cardiac muscle.

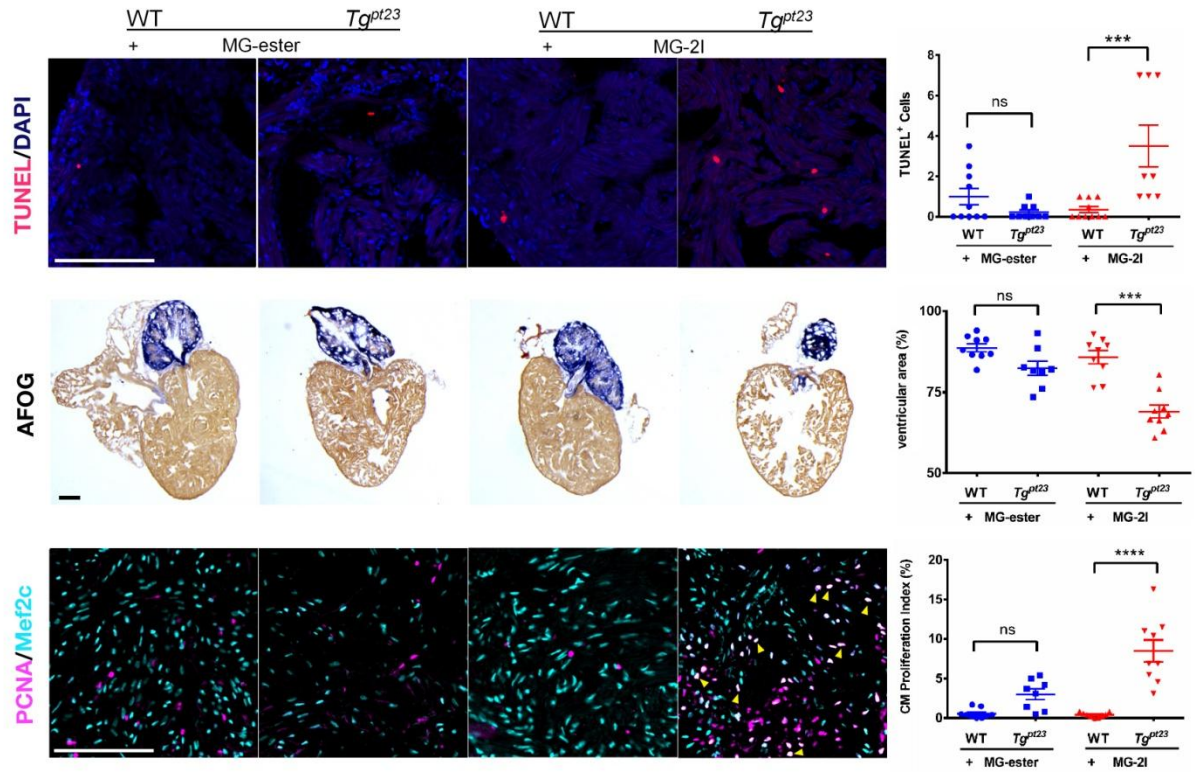


Figure 5.30: (a) FAP-TAPs photo-induced cardiac damage in adult zebrafish. Hearts were extracted at 3 dpi and TUNEL was performed to assess cell death. (b) Acid Fuchsin Orange G (AFOG) staining of hearts at 5 dpi showing the damaged cardiac structure in transgenic fish injected with MG-2I. (c) Mef2c (cardiomyocyte) and PCNA (proliferation) staining at 5 dpi shows enhanced cardiomyocyte proliferation (yellow arrow) in transgenic fish injected with MG-2I. Scale bar = 100 μ m and applied to all images, n = 9 for all groups, One-way ANOVA, Tukey post hoc tests were performed with multiple comparisons of mean for each group. *P*-values were considered significant when < 0.05 , shown as mean \pm S.E.M. (Experiments and analysis were carried out by Dr. Maria A. Missinato)

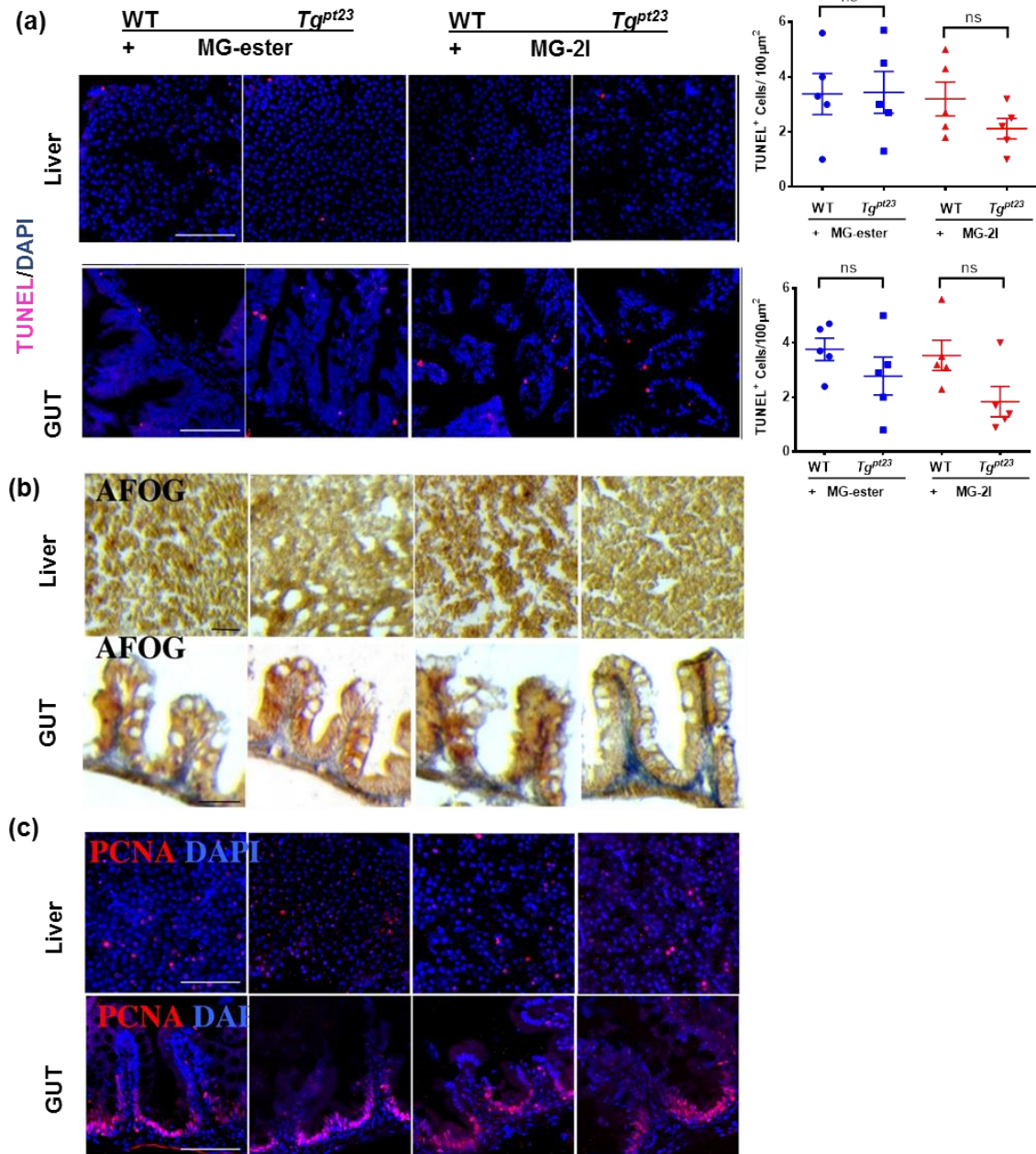


Figure 5.31: FAP-TAPs induced photo-ablation is specific to the cardiac tissue in adult zebrafish. (a): TUNEL assay in liver and intestine (Gut) at 3 dpi showed no differences between the four groups. (b): AFOG staining of liver and Gut at 5 dpi showing no structural damage in all groups. (c): Mef2c (cardiomyocyte) and PCNA (proliferation) staining in liver and Gut at 5 dpi was comparable in all the groups. $n = 5$ for each group, One-way ANOVA, $*P < 0.05$, $**P < 0.01$, $***P < 0.001$; scale bar = 100 μm . (Experiments and analysis were carried out by Dr. Maria A. Missinato)

Targeting FAP-TAPs to selective ablate cancer cells

Numerous efforts have been made to improve tumor specificity by conjugating photosensitizers to tumor-recognizing moieties (3rd generation)^{14,58}. For example, photosensitizers have been coupled to monoclonal antibodies (mAbs) specific to tumor-associated markers, so that the conjugate can be delivered to the tumor site with improved specificity⁵⁹⁻⁶¹. However, the large size of antibodies results in slow systemic clearance rates and limited tissue penetration. Moreover, the highly specific antigen recognition by mAbs is often compromised by the high ratio of photosensitizer substitution, which alters the overall charge and biodistribution of these conjugates^{8,11}. Additionally, non-human derived immunoconjugates are usually neutralized by the human immune system, resulting in further reduction of tumor accumulation.

To reduce nonspecific phototoxicity in normal tissues, one approach is to develop photosensitizers that can only be activated for ROS generation with the presence of both light illumination and cell-specific targeting^{25,62}. Cellularly targeted and activated photosensitizers are expected to improve the specificity in PDT by restraining the ROS generation to tumor tissues and minimizing the damage to the surrounding non-targeted tissue, where the photosensitizer remains inactive. Spring *et. al* reported an activatable photoimmunotherapy for targeting A431 cancer cells, in which multiple self-quenching photosensitizers were conjugated to an antibody against EGFR⁶³. Upon binding, the phototoxicity and fluorescence of photosensitizer were activated by lysosomal proteolysis with 7-fold activation. However, lysosome-targeted ROS generation is less effective for inducing cytotoxicity and the relatively low activation efficiency suggests both high dose illuminations would be required and limited selectivity would be obtained. The problem of robustly targeting and activating photosensitizer selectively at tumor sites remains an unmet technical challenge, and a significant goal to advance PDT.

To illustrate FAP-TAPs targeting endogenous cellular proteins for photosensitization, we delivered FAP-TAPs to cancer cells for phototoxic effect through a recombinant affinity probe (AffiFAP) (Figure 5.32a), where FAP was conjugated to two copies of an EGFR specific affibody⁶⁴. Affibody is a compact affinity scaffold and has been developed as an antibody alternative for *in vivo* targeting due to faster clearance rates and improved tissue penetration as a result of the small size (6 kDa). Using cultured cells, we demonstrated highly selective targeting of the AffiFAP to tumor cells and the resulting targeted cell-specific cytotoxicity (Figure 5.32b). A mix of wild-type HEK and A431 cells was first labeled with 200 nM of AffiFAP followed by 200 nM of the respective dye without washing off unbound AffiFAP-dye complexes. After 1 minute illumination (60× objective, 640 nm, 2.43 W/cm²), A431 cells labeled by EGFR-specific AffiFAP and MG-2I showed significant and highly specific light-induced cytotoxicity. No detectable cell death was observed among cells incubated with MG-2I bound to non-conjugated dL5** or among cells incubated with MG-ester bound to EGFR targeted AffiFAP. A separate HER2 specific AffiFAP also failed to target and induce cytotoxicity of A431 cells, indicating the molecular selectivity of this targeting approach. These results revealed that close contact of FAP-TAPs to target cells was critical for effective delivery of ROS due to the very short radius of action of singlet oxygen (< 0.2 μm). These results clearly established the dual requirements of FAP-TAPs targeted by cancer-specific affinity probes and activated by FAP/fluorogen recognition in order to achieve efficient cancer photosensitization. Similar results were also observed with HER2-specific AffiFAP labeled SKBR3 cancer cells (Figure 5.33). Thus, through AffiFAP constructs, FAP-TAPs were shown to target endogenous cancer cell markers and limit nonspecific damage to normal cells by spatially restricting the singlet oxygen generation to the cancer cells.

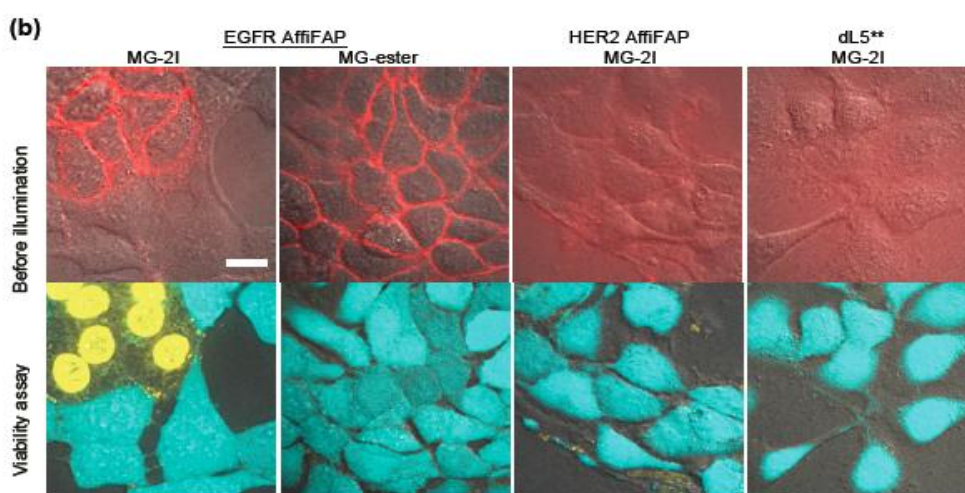
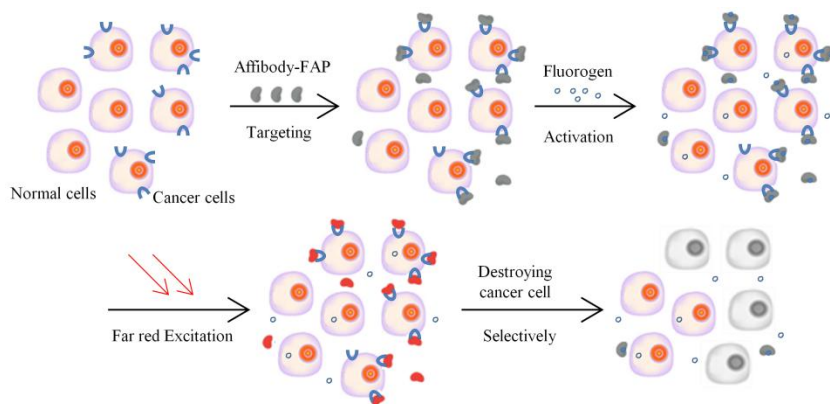


Figure 5.32: Highly specific and activatable phototoxicity of TAPs on A431 cancer cells targeted by AffiFAP. (a): Schematic illustration of TAPs targeting and selectively destroying cancer cells by AffiFAP; (b): Cancer cell selective killing effect by FAP-TAPs. A mixture of A431 and HEK cells was first labeled with 200 nM of AffiFAP for 15 minutes followed by 200 nM of dyes for another 15 minutes. Without washing, cells were illuminated for 1min ($60\times$ objective, 640 nm, 2.43 W/cm^2) and then stained with a Live/Dead cell viability kit (top panel: DIC and 640 channel (red), bottom panel: DIC, 488 channel (live cells in cyan) and 560 channel (dead cells in yellow)). Scale bar = 10 μm and applied to all images. Images are representative of typical results from > 4 independent replicates.

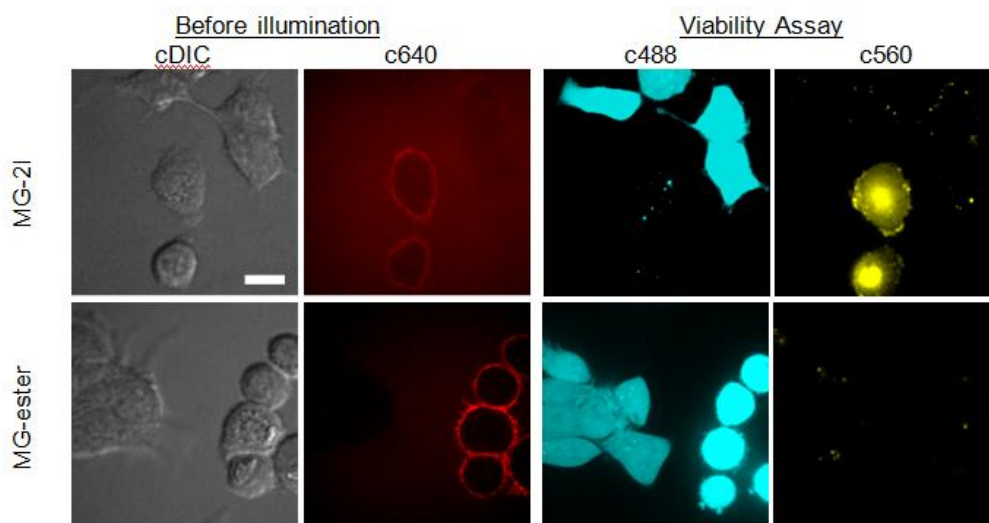


Figure 5.33: Selective cytotoxicity of HER2 AffiFAP targeting SKBR3 cancer cells. A mixed culture of SKBR3 and HEK cells was first incubated with 100 nM of dL5** conjugated affibody against HER2 for 15 minutes followed by 100 nM of MG-2I or MG-ester for another 15 minutes. 1 hour after 3 minutes of illumination ($60\times$ objective, 640 nm, $2.43\text{W}/\text{cm}^2$), cell viability was determined with Live/Dead cell fluorescent assay. (Scale bar, 10 μm)

Summary

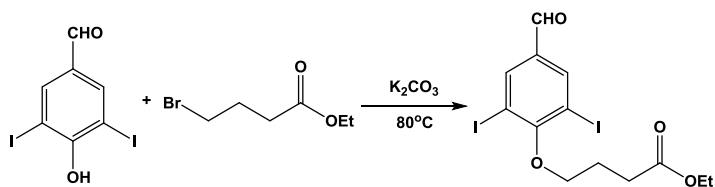
We have reported a two-component photosensitizing approach that enables robust and target-specific NIR light-mediated cytotoxicity of FAP expressing cells and AffiFAP targeted cancer cells. Different from conventional photosensitizers, the fluorogen (MG-2I) or FAP (dL5**) alone has no significant photosensitizing effect until they are bound to each other. The activation of photosensitization is achieved by ‘active’ addition of fluorogens to the targeted cells instead of the ‘passive’ cleavage of quenching groups by cellular components. The flexible genetic targeting strategy of the FAP along with efficient activation of ROS generation makes FAP-TAPs an immediately useful tool for targeted cellular ablation and subcellular protein inactivation, which can potentially be multiplexed with other photosensitizers (e.g. KillerRed and MiniSOG). With molecular targeting strategy of the AffiFAP along with efficient activation of

ROS generation makes FAP-TAPs a potential alternative for cancer ablation in PDT and surgical applications. The fact that the same FAP (dL5**) can be used to bind a non-photosensitizing dye (the MG-ester), allows many studies that rely on imaging to be extended to photosensitization only when the researcher or clinician desires. This alternative labeling strategy can facilitate the selection of stable cells and transgenic animals, which are primed for imaging, photoablation or photosensitization studies.

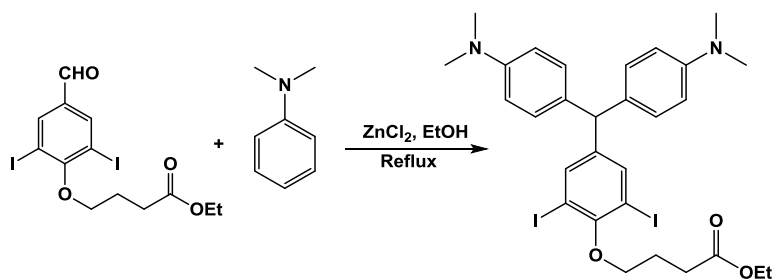
Experimental Details

The 3, 5-diiodo-4-hydroxybenzaldehyde was purchased from VWR International; anthracene-9, 10-dipropionic acid disodium salt (ADPA), Catalase–polyethylene glycol and SOD–polyethylene glycol from Sigma-Aldrich; tetrasulfonated aluminum phthalocyanine (AlPcS₄) from Frontier Scientific; Hoechst dye 33342, Live/dead cell viability/cytotoxicity kit (L-3224) and Dihydroethidium (hydroethidine) (D11347) were from Invitrogen. ¹H NMR and ¹³C NMR data were recorded from Bruker Avance™ 300 MHz and 500 MHz. Mass spectra were obtained from Thermo-Fisher LCQ ESI/APCI Ion Trap. Final products were purified by silica, neutral alumina and reverse-phase chromatography. Raw absorbance values of respective free dyes and dye-FAP complex were measured on a PerkinElmer Lambda45 spectrophotometer. Fluorogenic enhancement was measured in 96-well microplates on a Tecan Infinite Plate Spectrometer. Corrected emission spectra were taken on a Quantamaster monochromator fluorimeter (Photon Technology International). Live zebrafish imaging was acquired by an EVOS FL Manual microscope. For details regarding cell culture and generation of transgenic zebrafish line, please read *Nature Methods*, 13, 263-168 (2016).

Synthesis of MG-2I

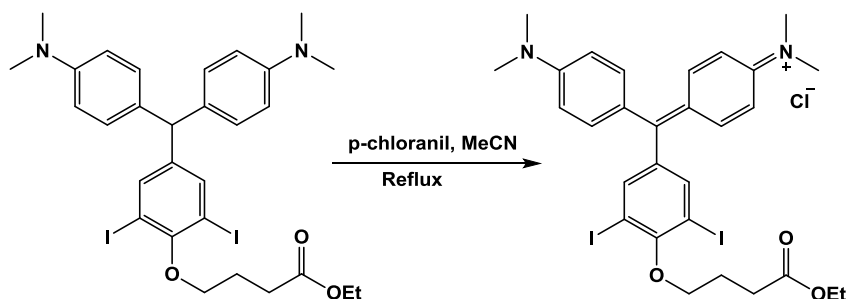


Ethyl 4-(2,6-diiodo-4-formylphenoxy)butanoate: 3.74 g (10 mmol) 3,5-Diiodo-4-hydroxybenzaldehyde and 2.0 g (10 mmol) ethyl, 4-bromobutyrate were dissolved in 5 mL dry DMF, 1.52 g (11 mmol) of finely powdered K_2CO_3 added and heated to $80^\circ C$ for 3 hours. The reaction mixture was cooled to room temperature and filtered to remove the precipitate. The solvent was then removed under reduced pressure to afford the crude product, which was purified by column chromatography on silica gel using 80% Hexane/20% Ethyl acetate. The product had a chemical composition of $C_{13}H_{14}I_2O_4$ with M.W. of 488.06 g/mol (yield: 4.58 g, 94%). 1H NMR (300 MHz, Chloroform-*d*) δ 9.82 (s, 1H), 8.28 (s, 2H), 4.17 (q, $J = 7.1$ Hz, 2H), 4.10 (d, $J = 6.0$ Hz, 2H), 2.72 (t, $J = 7.4$ Hz, 2H), 2.29 (q, $J = 6.6$ Hz, 2H), 1.30 (t, $J = 7.2$ Hz, 3H). ^{13}C NMR (75 MHz, Chloroform-*d*) δ 188.1, 173.3, 162.7, 141.6, 135.4, 91.7, 72.4, 60.4, 80.6, 25.3, 14.4, ESI-MS (+m/z): 488.2.



MG[H]-2I ester: 2.44 g (5 mmol) ethyl 4-(2,6-diiodo-4-formylphenoxy)butanoate and 1.22 g (10 mmol) N,N-dimethylaniline were dissolved in 50 mL dry EtOH, 0.70 g (5 mmol) anhydrous $ZnCl_2$ was added to the solution and it was heated to reflux for 2 days. The reaction mixture was then dried under reduced pressure, purified with silica gel (Eluent: 50% ethyl acetate/50%

hexane) to give MG[H]-2I ester. The product had a chemical composition of $C_{29}H_{34}I_2N_2O_3$ with M.W. of 712.41 g/mol (yield: 2.31 g, 65%). 1H NMR (300 MHz, Chloroform-*d*) δ 7.53 (s, 2H), 6.96 (d, $J = 8.6$ Hz, 4H), 6.69 (d, $J = 8.8$ Hz, 4H), 5.24 (s, 1H), 4.19 (q, $J = 7.1$ Hz, 2H), 4.02 (t, $J = 6.0$ Hz, 2H), 2.95 (s, 12H), 2.71 (t, $J = 7.5$ Hz, 2H), 2.23 (p, $J = 6.4$ Hz, 2H), 1.30 (t, $J = 7.1$ Hz, 3H). ^{13}C NMR (75 MHz, $CDCl_3$): δ 155.6, 149.4, 145.7, 140.7, 131.5, 129.8, 112.8, 90.7, 71.9, 60.5, 53.7, 40.9, 31.2, 25.5, 14.4, ESI-MS (+m/z): 712.3.



MG-2I: 0.71 g (1 mmol) MG[H]-2I ester was dissolved in 5 mL MeCN and heated to reflux, 0.27 g (1.1 mmol) p-chloranil was dissolved in 5 mL hot MeCN and added to the reaction, it was allowed to further reflux for 2-3 hours. The reaction mixture was dried under reduced pressure, purified with silica gel to get methylium, bis[4-(dimethylamino)phenyl](4-(3-carboethoxypropyl)-3,5-diiodo-phenyl)-chloride (MG-2I) (Eluent: 80% $CHCl_3$ /20% MeOH).

The product had a chemical composition of $C_{29}H_{33}ClI_2N_2O_3$ with M.W. of 746.85 g/mol (yield: 0.67 g, 90%). 1H NMR (300 MHz, Chloroform-*d*) δ 7.68 (s, 2H), 7.35 (d, $J = 8.6$ Hz, 4H), 7.02 (d, $J = 8.3$ Hz, 4H), 4.17 (m, 4H) 3.41 (s, 12H), 2.7 (t, $J = 6.6$ Hz, 2H), 2.26 (m, 2H), 1.28 (t, $J = 7.0$ Hz, 3H). ^{13}C NMR (75 MHz, Chloroform-*d*) δ 174.2, 171.7, 161.3, 157.2, 145, 140.6, 138.9, 128, 114.4, 91.3, 72.8, 61.6, 41.5, 30.9, 25.5, 14.6, ESI-MS (+m/z): 710.3.

References:

- 1 Lee, H. M., Larson, D. R. & Lawrence, D. S. Illuminating the Chemistry of Life: Design, Synthesis, and Applications of "Caged" and Related Photoresponsive Compounds. *Acs Chem Biol* **4**, 409-427, doi:10.1021/cb900036s (2009).
- 2 Jacobson, K., Rajfur, Z., Vitriol, E. & Hahn, K. Chromophore-assisted laser inactivation in cell biology. *Trends Cell Biol* **18**, 443-450, doi:10.1016/j.tcb.2008.07.001 (2008).
- 3 Levskaya, A., Weiner, O. D., Lim, W. A. & Voigt, C. A. Spatiotemporal control of cell signalling using a light-switchable protein interaction. *Nature* **461**, 997-1001, doi:10.1038/nature08446 (2009).
- 4 Dolmans, D. E. J. G. J., Fukumura, D. & Jain, R. K. Photodynamic therapy for cancer. *Nat Rev Cancer* **3**, 380-387, doi:10.1038/nrc1071 (2003).
- 5 Robertson, C. A., Evans, D. H. & Abrahamse, H. Photodynamic therapy (PDT): a short review on cellular mechanisms and cancer research applications for PDT. *J Photochem Photobiol B* **96**, 1-8, doi:10.1016/j.jphotobiol.2009.04.001 (2009).
- 6 Lin, J. Y. *et al.* Optogenetic Inhibition of Synaptic Release with Chromophore-Assisted Light Inactivation (CALI). *Neuron* **79**, 241-253, doi:10.1016/j.neuron.2013.05.022 (2013).
- 7 Qi, Y. C. B., Garren, E. J., Shu, X. K., Tsien, R. Y. & Jin, Y. S. Photo-inducible cell ablation in *Caenorhabditis elegans* using the genetically encoded singlet oxygen generating protein miniSOG. *P Natl Acad Sci USA* **109**, 7499-7504, doi:10.1073/pnas.1204096109 (2012).
- 8 Allison, R. R. *et al.* Photosensitizers in clinical PDT. *Photodiagnosis Photodyn Ther* **1**, 27-42, doi:10.1016/S1572-1000(04)00007-9 (2004).
- 9 Castano, A. P., Demidova, T. N. & Hamblin, M. R. Mechanisms in photodynamic therapy: part one-photosensitizers, photochemistry and cellular localization. *Photodiagnosis Photodyn Ther* **1**, 279-293, doi:10.1016/S1572-1000(05)00007-4 (2004).
- 10 Qiang, Y. G., Yow, C. M. N. & Huang, Z. Combination of photodynamic therapy and immunomodulation: Current status and future trends. *Med Res Rev* **28**, 632-644, doi:10.1002/med.20121 (2008).
- 11 Firczuk, M. *et al.* Approaches to improve photodynamic therapy of cancer. *Front Biosci-Landmark* **16**, 208-224, doi:10.2741/3684 (2011).
- 12 Sharman, W. M., Allen, C. M. & van Lier, J. E. Photodynamic therapeutics: basic principles and clinical applications. *Drug Discov Today* **4**, 507-517, doi:Doi 10.1016/S1359-6446(99)01412-9 (1999).

- 13 Ethirajan, M., Chen, Y. H., Joshi, P. & Pandey, R. K. The role of porphyrin chemistry in tumor imaging and photodynamic therapy. *Chem Soc Rev* **40**, 340-362, doi:10.1039/b915149b (2011).
- 14 Josefsen, L. B. & Boyle, R. W. Photodynamic therapy: novel third-generation photosensitizers one step closer? *Br J Pharmacol* **154**, 1-3, doi:10.1038/bjp.2008.98 (2008).
- 15 Liu, K. *et al.* Covalently Assembled NIR Nanoplatfrom for Simultaneous Fluorescence Imaging and Photodynamic Therapy of Cancer Cells. *Acs Nano* **6**, 4054-4062, doi:10.1021/nn300436b (2012).
- 16 Vahrmeijer, A. L., Hutteman, M., van der Vorst, J. R., van de Velde, C. J. H. & Frangioni, J. V. Image-guided cancer surgery using near-infrared fluorescence. *Nat Rev Clin Oncol* **10**, 507-518, doi:10.1038/nrclinonc.2013.123 (2013).
- 17 Tour, O., Meijer, R. M., Zacharias, D. A., Adams, S. R. & Tsien, R. Y. Genetically targeted chromophore-assisted light inactivation. *Nat Biotechnol* **21**, 1505-1508, doi:10.1038/nbt914 (2003).
- 18 Bulina, M. E. *et al.* A genetically encoded photosensitizer. *Nat Biotechnol* **24**, 95-99, doi:10.1038/nbt1175 (2006).
- 19 Shu, X. *et al.* A genetically encoded tag for correlated light and electron microscopy of intact cells, tissues, and organisms. *PLoS Biol* **9**, e1001041, doi:10.1371/journal.pbio.1001041 (2011).
- 20 Vitriol, E. A., Wise, A. L., Berginski, M. E., Bamburg, J. R. & Zheng, J. Q. Instantaneous inactivation of cofilin reveals its function of F-actin disassembly in lamellipodia. *Mol Biol Cell* **24**, 2238-2247, doi:10.1091/mbc.E13-03-0156 (2013).
- 21 Teh, C. *et al.* Optogenetic in vivo cell manipulation in KillerRed-expressing zebrafish transgenics. *Bmc Dev Biol* **10**, doi:Artn 11010.1186/1471-213x-10-110 (2010).
- 22 Pletnev, S. *et al.* Structural Basis for Phototoxicity of the Genetically Encoded Photosensitizer KillerRed. *J Biol Chem* **284**, 32028-32039, doi:10.1074/jbc.M109.054973 (2009).
- 23 de Rosny, E. & Carpentier, P. GFP-Like Phototransformation Mechanisms in the Cytotoxic Fluorescent Protein KillerRed Unraveled by Structural and Spectroscopic Investigations. *J Am Chem Soc* **134**, 18015-18021, doi:10.1021/ja3073337 (2012).
- 24 Vegh, R. B. *et al.* Reactive oxygen species in photochemistry of the red fluorescent protein "Killer Red". *Chem Commun* **47**, 4887-4889, doi:10.1039/c0cc05713d (2011).
- 25 Lovell, J. F., Liu, T. W., Chen, J. & Zheng, G. Activatable photosensitizers for imaging and therapy. *Chem Rev* **110**, 2839-2857, doi:10.1021/cr900236h (2010).
- 26 McDonnell, S. O. *et al.* Supramolecular photonic therapeutic agents. *J Am Chem Soc* **127**, 16360-16361, doi:10.1021/ja0553497 (2005).

- 27 Zheng, G. *et al.* Photodynamic molecular beacon as an activatable photosensitizer based on protease-controlled singlet oxygen quenching and activation. *Proc Natl Acad Sci U S A* **104**, 8989-8994, doi:10.1073/pnas.0611142104 (2007).
- 28 Tian, J. *et al.* Cell-specific and pH-activatable rubyrin-loaded nanoparticles for highly selective near-infrared photodynamic therapy against cancer. *J Am Chem Soc* **135**, 18850-18858, doi:10.1021/ja408286k (2013).
- 29 Szent-Gyorgyi, C. *et al.* Fluorogen-activating single-chain antibodies for imaging cell surface proteins (vol 26, pg 235, 2008). *Nat Biotechnol* **26**, 470-470, doi:10.1038/nbt0408-470b (2008).
- 30 Szent-Gyorgyi, C. *et al.* Malachite green mediates homodimerization of antibody VL domains to form a fluorescent ternary complex with singular symmetric interfaces. *J Mol Biol* **425**, 4595-4613, doi:10.1016/j.jmb.2013.08.014 (2013).
- 31 Plummer, B. F. & Ferree, W. I. Photochemical Heavy-Atom Effects. *Abstr Pap Am Chem S* **164**, 98-& (1972).
- 32 Gandin, E., Lion, Y. & Vandevorst, A. Quantum Yield of Singlet Oxygen Production by Xanthene Derivatives. *Photochem Photobiol* **37**, 271-278, doi:DOI 10.1111/j.1751-1097.1983.tb04472.x (1983).
- 33 Yogo, T., Urano, Y., Ishitsuka, Y., Maniwa, F. & Nagano, T. Highly efficient and photostable photosensitizer based on BODIPY chromophore. *J Am Chem Soc* **127**, 12162-12163, doi:10.1021/ja0528533 (2005).
- 34 McClure, D. S. Triplet-Singlet Transitions in Organic Molecules - Lifetime Measurements of the Triplet State. *J Chem Phys* **17**, 905-913, doi:Doi 10.1063/1.1747085 (1949).
- 35 Gorman, A. *et al.* In vitro demonstration of the heavy-atom effect for photodynamic therapy. *J Am Chem Soc* **126**, 10619-10631, doi:10.1021/ja047649e (2004).
- 36 Mielenz, K. D., Velapoldi, R. A., Mavrodineanu, R. & Institute for Materials Research (U.S.). Analytical Chemistry Division. *Standardization in Spectrophotometry and luminescence measurements : proceedings of a workshop seminar held at the National Bureau of Standards, Gaithersburg, Maryland, November, November 19-20, 1975.* (U.S. Dept. of Commerce, National Bureau of Standards : for sale by the Supt. of Docs., U.S. Govt. Print. Off., 1977).
- 37 Lindig, B. A., Rodgers, M. A. J. & Schaap, A. P. Determination of the Lifetime of Singlet Oxygen in D₂O Using 9,10-Anthracenedipropionic Acid, a Water-Soluble Probe. *J Am Chem Soc* **102**, 5590-5593, doi:DOI 10.1021/ja00537a030 (1980).
- 38 Davila, J. & Harriman, A. Photosensitized Oxidation of Biomaterials and Related Model Compounds. *Photochem Photobiol* **50**, 29-35, doi:DOI 10.1111/j.1751-1097.1989.tb04126.x (1989).

- 39 Ogilby, P. R. Singlet oxygen: there is indeed something new under the sun. *Chem Soc Rev* **39**, 3181-3209, doi:10.1039/b926014p (2010).
- 40 Takei, K. Chromophore/fluorophore-assisted light inactivation method. *Nihon Yakurigaku Zasshi* **140**, 226-230 (2012).
- 41 Wojtovich, A. P. & Foster, T. H. Optogenetic control of ROS production. *Redox Biol* **2**, 368-376, doi:10.1016/j.redox.2014.01.019 (2014).
- 42 Patterson, M. S., Wilson, B. C. & Graff, R. In vivo tests of the concept of photodynamic threshold dose in normal rat liver photosensitized by aluminum chlorosulphonated phthalocyanine. *Photochem Photobiol* **51**, 343-349 (1990).
- 43 Schafer, M. *et al.* Systematic study of parameters influencing the action of Rose Bengal with visible light on bacterial cells: Comparison between the biological effect and singlet-oxygen production. *Photochem Photobiol* **71**, 514-523, doi:Doi 10.1562/0031-8655(2000)071<0514:Sopit>2.0.Co;2 (2000).
- 44 Kuimova, M. K., Yahioglu, G. & Ogilby, P. R. Singlet Oxygen in a Cell: Spatially Dependent Lifetimes and Quenching Rate Constants. *J Am Chem Soc* **131**, 332-340, doi:10.1021/ja807484b (2009).
- 45 Tilly, J. L. & Tilly, K. I. Inhibitors of Oxidative Stress Mimic the Ability of Follicle-Stimulating-Hormone to Suppress Apoptosis in Cultured Rat Ovarian Follicles. *Endocrinology* **136**, 242-252, doi:DOI 10.1210/en.136.1.242 (1995).
- 46 Simon, H. U., Haj-Yehia, A. & Levi-Schaffer, F. Role of reactive oxygen species (ROS) in apoptosis induction. *Apoptosis* **5**, 415-418, doi:Doi 10.1023/A:1009616228304 (2000).
- 47 Zhao, H. T. *et al.* Superoxide reacts with hydroethidine but forms a fluorescent product that is distinctly different from ethidium: Potential implications in intracellular fluorescence detection of superoxide. *Free Radical Bio Med* **34**, 1359-1368, doi:10.1016/S0891-5849(03)00142-4 (2003).
- 48 Fuchs, Y. & Steller, H. Programmed Cell Death in Animal Development and Disease. *Cell* **147**, 742-758, doi:10.1016/j.cell.2011.10.033 (2011).
- 49 Dodd, A., Curtis, P. M., Williams, L. C. & Love, D. A. Zebrafish: bridging the gap between development and disease. *Hum Mol Genet* **9**, 2443-2449, doi:DOI 10.1093/hmg/9.16.2443 (2000).
- 50 Lieschke, G. J. & Currie, P. D. Animal models of human disease: zebrafish swim into view. *Nat Rev Genet* **8**, 353-367, doi:10.1038/nrg2091 (2007).
- 51 Curado, S., Stainier, D. Y. R. & Anderson, R. M. Nitroreductase-mediated cell/tissue ablation in zebrafish: a spatially and temporally controlled ablation method with applications in developmental and regeneration studies. *Nature Protocols* **3**, 948-954, doi:10.1038/nprot.2008.58 (2008).

- 52 Molina, G. A., Watkins, S. C. & Tsang, M. Generation of FGF reporter transgenic zebrafish and their utility in chemical screens. *BMC Dev Biol* **7**, 62, doi:10.1186/1471-213X-7-62 (2007).
- 53 Pugach, E. K., Li, P., White, R. & Zon, L. Retro-orbital injection in adult zebrafish. *J Vis Exp*, doi:10.3791/1645 (2009).
- 54 Missinato, M. A., Tobita, K., Romano, N., Carroll, J. A. & Tsang, M. Extracellular component hyaluronic acid and its receptor Hmmer are required for epicardial EMT during heart regeneration. *Cardiovasc Res* **107**, 487-498, doi:10.1093/cvr/cvv190 (2015).
- 55 Poss, K. D., Wilson, L. G. & Keating, M. T. Heart regeneration in zebrafish. *Science* **298**, 2188-2190, doi:DOI 10.1126/science.1077857 (2002).
- 56 Kikuchi, K. *et al.* Primary contribution to zebrafish heart regeneration by gata4(+) cardiomyocytes. *Nature* **464**, 601-605, doi:10.1038/nature08804 (2010).
- 57 Jopling, C. *et al.* Zebrafish heart regeneration occurs by cardiomyocyte dedifferentiation and proliferation. *Nature* **464**, 606-609, doi:10.1038/nature08899 (2010).
- 58 van Dongen, G. A., Visser, G. W. & Vrouenraets, M. B. Photosensitizer-antibody conjugates for detection and therapy of cancer. *Adv Drug Deliv Rev* **56**, 31-52 (2004).
- 59 Vrouenraets, M. B. *et al.* Development of meta-tetrahydroxyphenylchlorin-mono-clonal antibody conjugates for photoimmunotherapy. *Cancer Res* **59**, 1505-1513 (1999).
- 60 Mitsunaga, M. *et al.* Cancer cell-selective in vivo near infrared photoimmunotherapy targeting specific membrane molecules. *Nat Med* **17**, 1685-1691, doi:10.1038/nm.2554 (2011).
- 61 Savellano, M. D., Pogue, B. W., Hoopes, P. J., Vitetta, E. S. & Paulsen, K. D. Multiepitope HER2 targeting enhances photoimmunotherapy of HER2-overexpressing cancer cells with pyropheophorbide-a immunoconjugates. *Cancer Res* **65**, 6371-6379, doi:10.1158/0008-5472.CAN-05-0426 (2005).
- 62 Bugaj, A. M. Targeted photodynamic therapy--a promising strategy of tumor treatment. *Photochem Photobiol Sci* **10**, 1097-1109, doi:10.1039/c0pp00147c (2011).
- 63 Spring, B. Q. *et al.* Selective treatment and monitoring of disseminated cancer micrometastases in vivo using dual-function, activatable immunoconjugates. *P Natl Acad Sci USA* **111**, E933-E942, doi:10.1073/pnas.1319493111 (2014).
- 64 Wang, Y. *et al.* Fluorogen activating protein-affibody probes: modular, no-wash measurement of epidermal growth factor receptors. *Bioconjug Chem* **26**, 137-144, doi:10.1021/bc500525b (2015).

Thesis summary

Fluorescence microscopy is essential for cell imaging and bio-sensing. Various targeting strategies have been developed to visualize molecules of interest¹. Fluorogen activating proteins (FAPs) can activate dark fluorogens to fluoresce and have been applied to a wide range of fields including pH sensing, protein trafficking, STED super-resolution microscopy and *in vivo* imaging^{2,3}. In this thesis, I have focused on developing malachite green based fluorogenic dyes to study the fluorogen-FAP interaction and to explore the photochemical properties of fluorogens, for applications such as tuned cell permeability, NIR imaging, multi-color imaging and ROS generation. Especially, the FAP-mediated targetable and activatable photosensitizer (FAP-TAPs) was established and validated to induce acute and localized phototoxicity by production of singlet oxygen, and has been successfully applied to photo-inactivate fused proteins; to photosensitize cells expressing dL5** at the plasma membrane, cytosol, mitochondrial matrix or nucleus in culture; and to ablate cardiac cells in living larval and adult zebrafish expressing dL5** in the cytoplasm⁴.

Future directions

Completion of charged MG study

To help better understanding the effect of net charge of MG derivatives, two compounds have been proposed to synthesis in the future (Figure 6.1). MG-EDA-OH has a +1 overall charge that is missing in the charged MG series, MG-EDA-PPT is an alternative version of MG-EDA-piperazine (T5) with +3 overall charge without the cyclic tail.

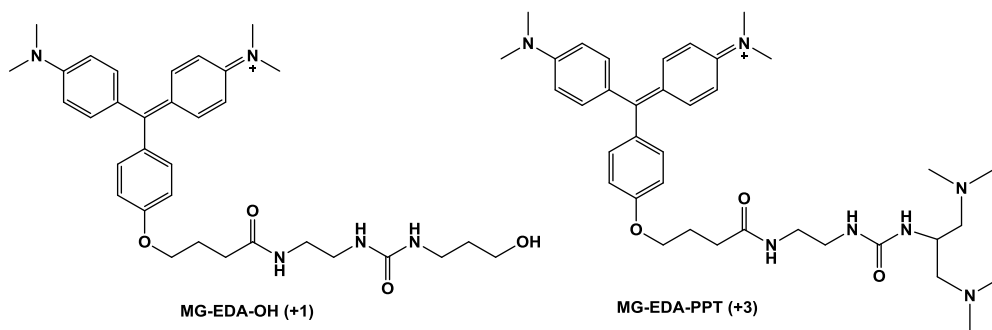


Figure 6.1: Two proposed charged MG derivatives.

Selection of FAPs to activate MGF2

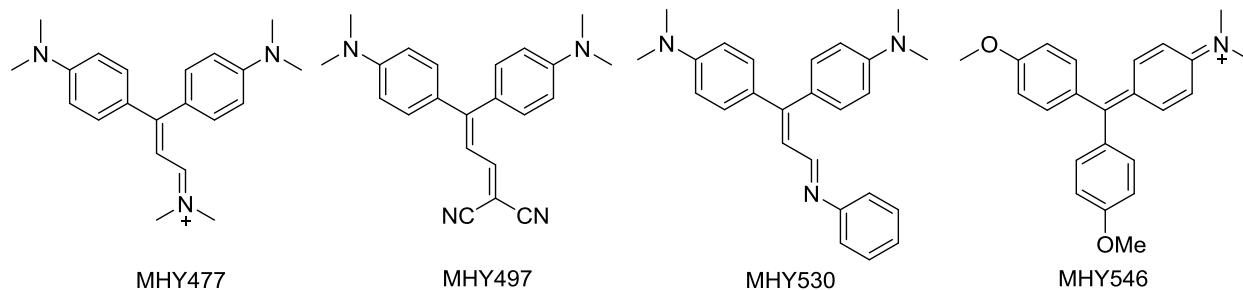
Even though dL5** can bind and activate MGF2 to fluoresce, the activation ratio is poor and hardly detectable with confocal microscopy. The free MGF2 is chemically stable and doesn't decolorize in physiologic pH (pH 5 – 8.5). It is plausible to develop FAPs from the naive scFv library to specifically activate MGF2 fluorogen with improved binding and fluorescence activation through randomly mutagenizing and screening using a yeast expression system and cell sorting⁵. The selected MGF2 activating FAPs are likely to also activate MG because of similar but smaller structures. With a bright NIR functioning MGF2-FAP, we would be able to image cellular compartments in deep tissues *in vivo*.

Develop fluorogen that emits yellow fluorescence when binding dL5**

MHN-ester, MG-Btau have been used together with dL5** as green-inside red-outside labeling approach for protein trafficking⁶. A fluorogen that can be activated by dL5** to emit yellow fluorescence can not only offer more choice in multi-color imaging of protein of interest, but also provide alternatives when using together with other fluorescent probes. In fact, several structurally mimics of MG have been proposed and synthesized (Figure 6.2). Their binding properties were tested against dL5** and several FAP_{MARS} proteins, we found little fluorescence activation by dL5** but promising activation from FAP_{MARS} proteins. In designing future MHY

compounds, factors such as symmetry, solubility and lipophilic linker should be taken into consideration based on previous experience.

MHY compounds synthesized



Proposed MHY structures

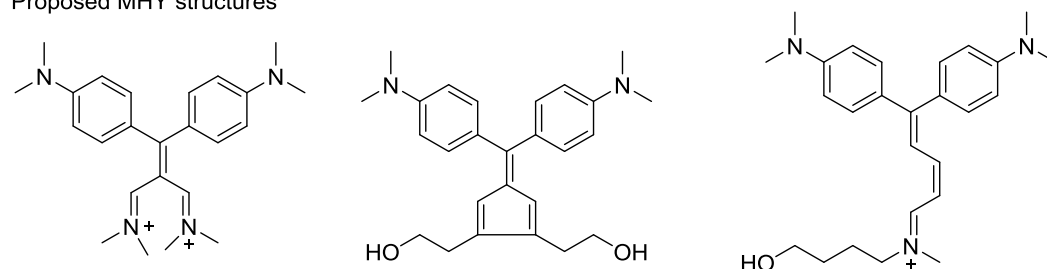


Figure 6.2: Several MHY compounds were synthesized for potential yellow fluorescence activation when bound with dL5**, proposed MHY structures to improve the fluorescence activation ratio

Develop Fluorogen-FAP platform in NIR-II imaging window

Fluorescence imaging in the NIR-II (1000-1700 nm) has dramatically higher resolution and depth compared to in the NIR-I (750-900 nm) window⁷. So far, no genetically targetable fluorescent probes are available in the NIR-II window. We propose that MG analogues with incorporating lengthened double band(s) that extend the charge delocalization will red-shift the absorption spectrum (Figure 6.3)⁸. These non-fluorescent MG analogues would also become fluorescent if bound and rigidized by dL5** or other suitable FAPs, and can provide a NIR spectra range no fluorogen-FAP complexes were able to achieve so far.

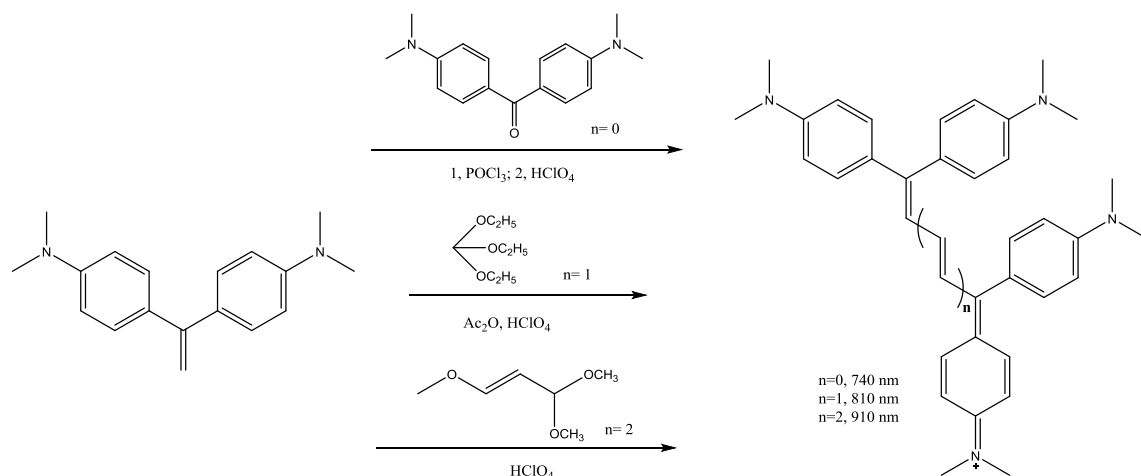


Figure 6.3: Proposed MG analogues for NIR-II fluorescence imaging and their synthesis routes.

Develop TAPs with higher Φ_{Δ} and further shifted excitation wavelength

The FAP-TAPs strategy using MG-2I/dL5** has been demonstrated to be effective and useful in target ablation with a 0.13 singlet oxygen quantum yield and a 666 nm excitation maximum. The dramatic increase of Φ_{Δ} was brought by the intermolecular heavy-atom effect from the diiodo-substituted bottom phenyl ring which prolonged the triplet lifetime of MG-2I/dL5**. New TAPs dyes with higher Φ_{Δ} and further red-shifted absorption spectrum can access deep tissue and require less light dose to achieve effective ablation. Intramolecular heavy-atom substitutions is known to be more effective in prolonging the triplet lifetime than intermolecular⁹, higher Φ_{Δ} can be achieved by introducing iodo/bromo heavy-atom at the dimethylaniline rings (Figure 6.4). The absorption spectrum can be red-shifted by introducing electron-withdrawing group at the chromophore.

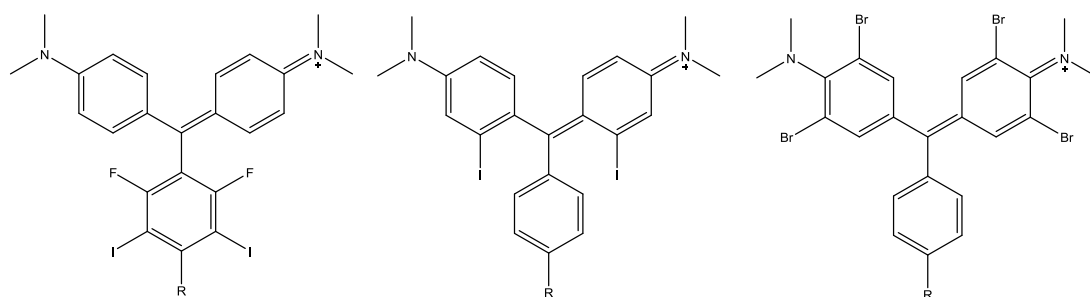
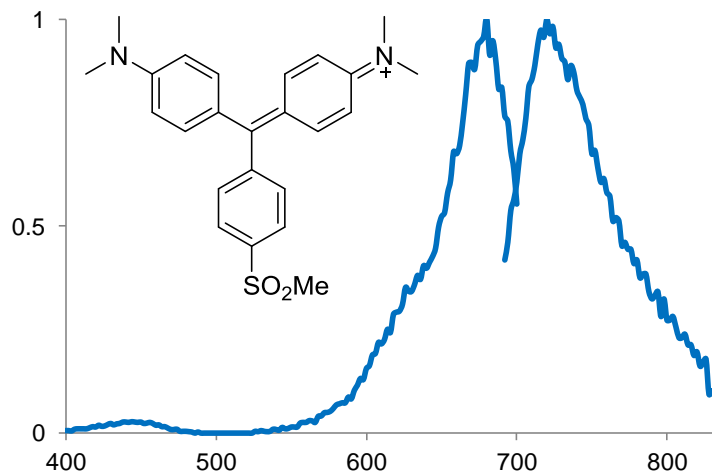


Figure 6.4: Proposed structures for 2nd generation TAPs

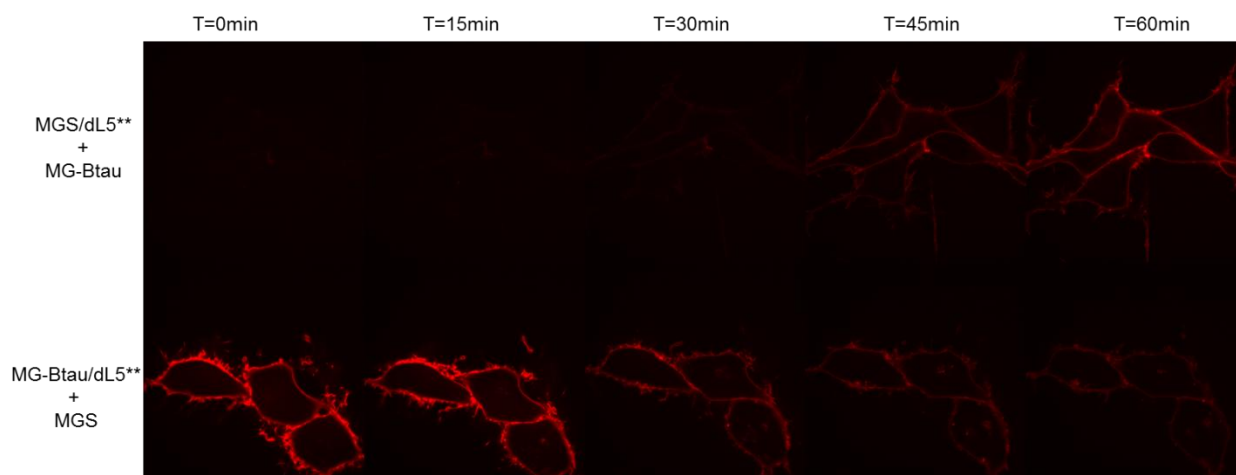
References:

- 1 Giepmans, B. N. G., Adams, S. R., Ellisman, M. H. & Tsien, R. Y. Review - The fluorescent toolbox for assessing protein location and function. *Science* **312**, 217-224, doi:10.1126/science.1124618 (2006).
- 2 Bruchez, M. P. Dark dyes-bright complexes: fluorogenic protein labeling. *Curr Opin Chem Biol* **27**, 18-23, doi:10.1016/j.cbpa.2015.05.014 (2015).
- 3 Yan, Q. & Bruchez, M. P. Advances in chemical labeling of proteins in living cells. *Cell Tissue Res* **360**, 179-194, doi:10.1007/s00441-015-2145-4 (2015).
- 4 He, J. *et al.* A genetically targetable near-infrared photosensitizer. *Nat Methods* **13**, 263-268, doi:10.1038/nmeth.3735 (2016).
- 5 Zhang, M. *et al.* Fluoromodule-based reporter/probes designed for in vivo fluorescence imaging. *J Clin Invest* **125**, 3915-3927, doi:10.1172/Jci81086 (2015).
- 6 Pratt, C. P., He, J., Wang, Y., Barth, A. L. & Bruchez, M. P. Fluorogenic Green-Inside Red-Outside (GIRO) Labeling Approach Reveals Adenylyl Cyclase-Dependent Control of BKalpha Surface Expression. *Bioconjug Chem* **26**, 1963-1971, doi:10.1021/acs.bioconjchem.5b00409 (2015).
- 7 Antaris, A. L. *et al.* A small-molecule dye for NIR-II imaging. *Nat Mater* **15**, 235-242, doi:10.1038/nmat4476 (2016).
- 8 Tuemmler, W. B. & Wildi, B. S. Polymethine Dyes .1. A Comparison of Several Vinylogous Series in Which the Polymethine Chains Are Terminated by Aryl Groups. *J Am Chem Soc* **80**, 3772-3777, doi:DOI 10.1021/ja01547a077 (1958).
- 9 Gandin, E., Lion, Y. & Vandevorst, A. Quantum Yield of Singlet Oxygen Production by Xanthene Derivatives. *Photochem Photobiol* **37**, 271-278, doi:DOI 10.1111/j.1751-1097.1983.tb04472.x (1983).

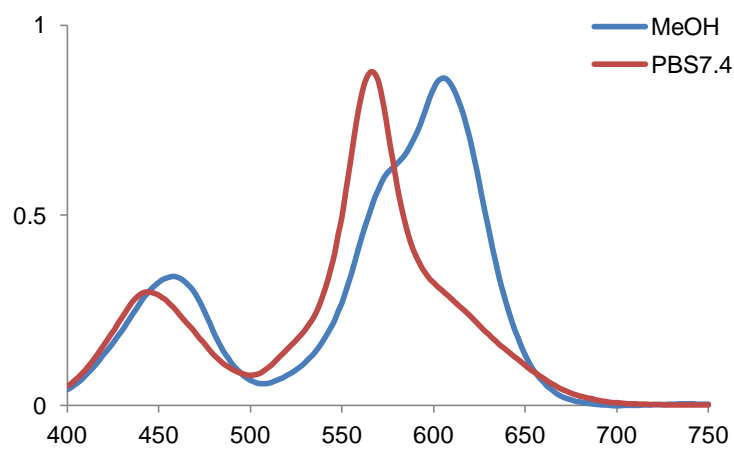
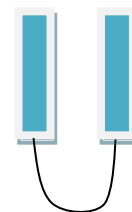
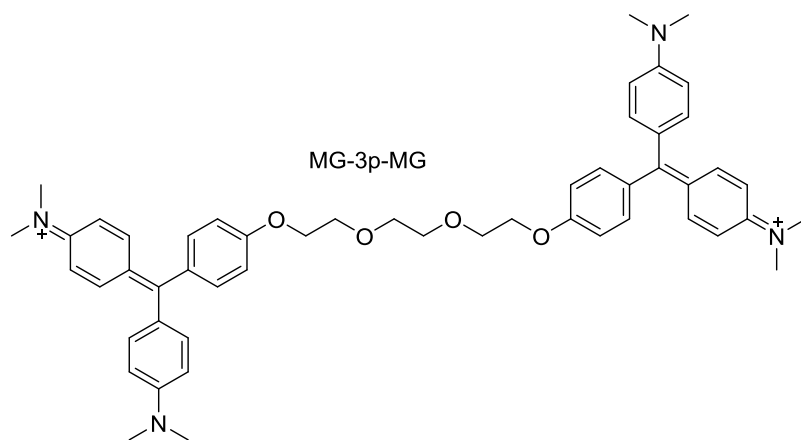
Appendix



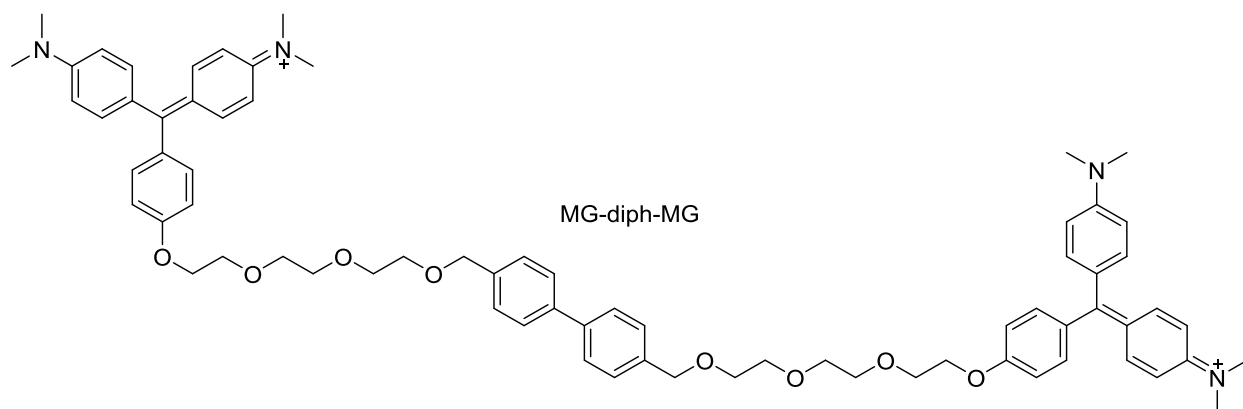
Structure of MGS and normalized fluorescence spectrum of MGS/dL5** complex ($\Phi_F < 1\%$)



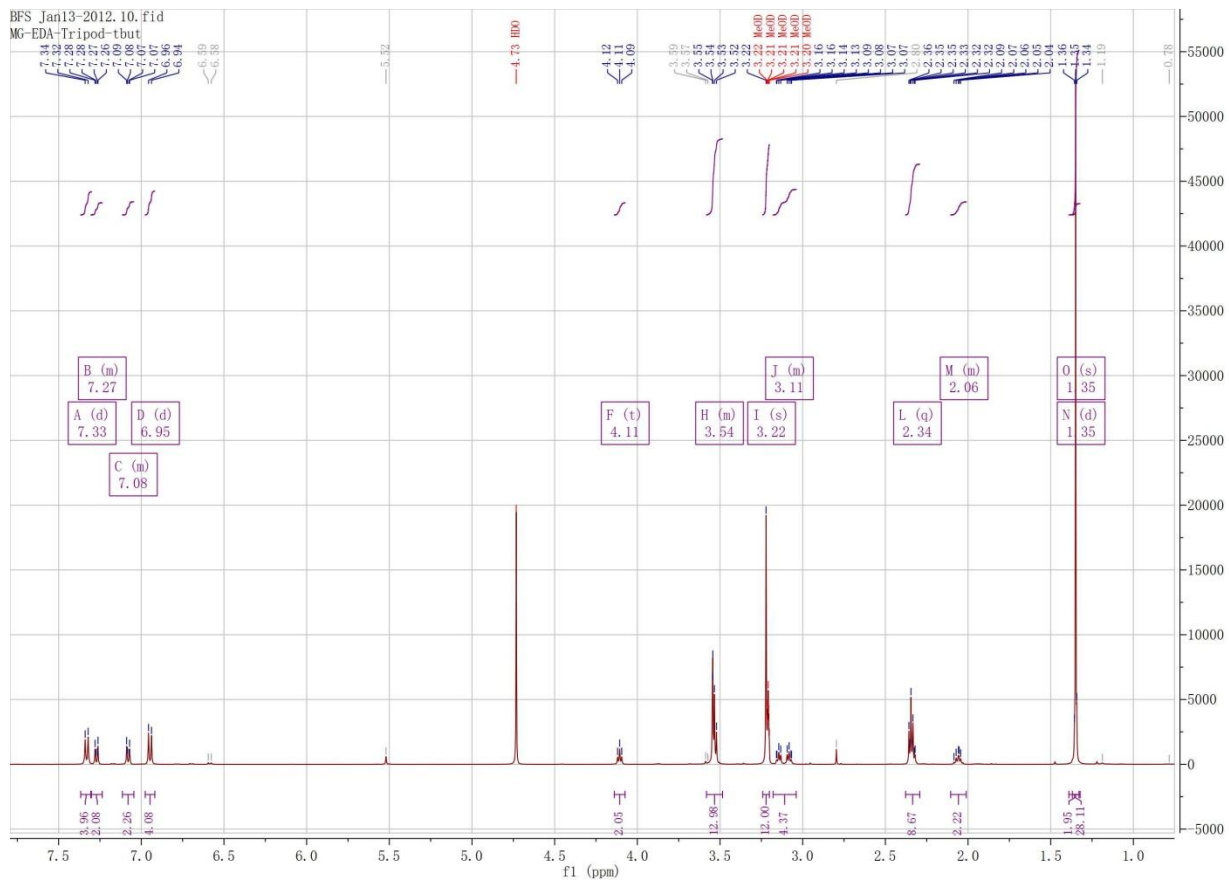
MGS as a non-fluorescent marker for dL5** protein, it can effectively block surface dL5** for 30 minutes. (Top: 500 nM MGS was pre-complexed with TM-dL5** HEK cells for 30 minutes, then 500 nM MG-Btau was added to the cell culture; Bottom: 500 nM MG-Btau was pre-complexed with TM-dL5** HEK cells for 30 minutes, then 500 nM MGS was added to the cell culture)



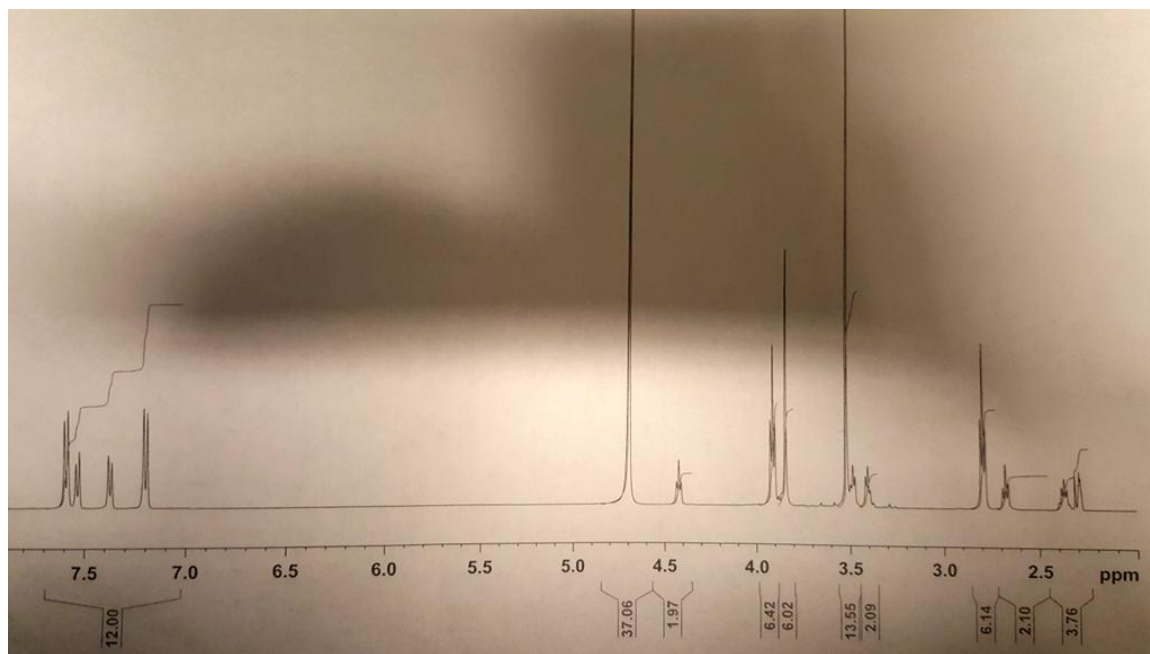
Absorption spectrum of MG-3p-MG in pH7.4 PBS buffer and in MeOH, intramolecular folding was seen in aqueous solution.



Introduction of rigid diphenyl linker prevent the intramolecular folding between MG

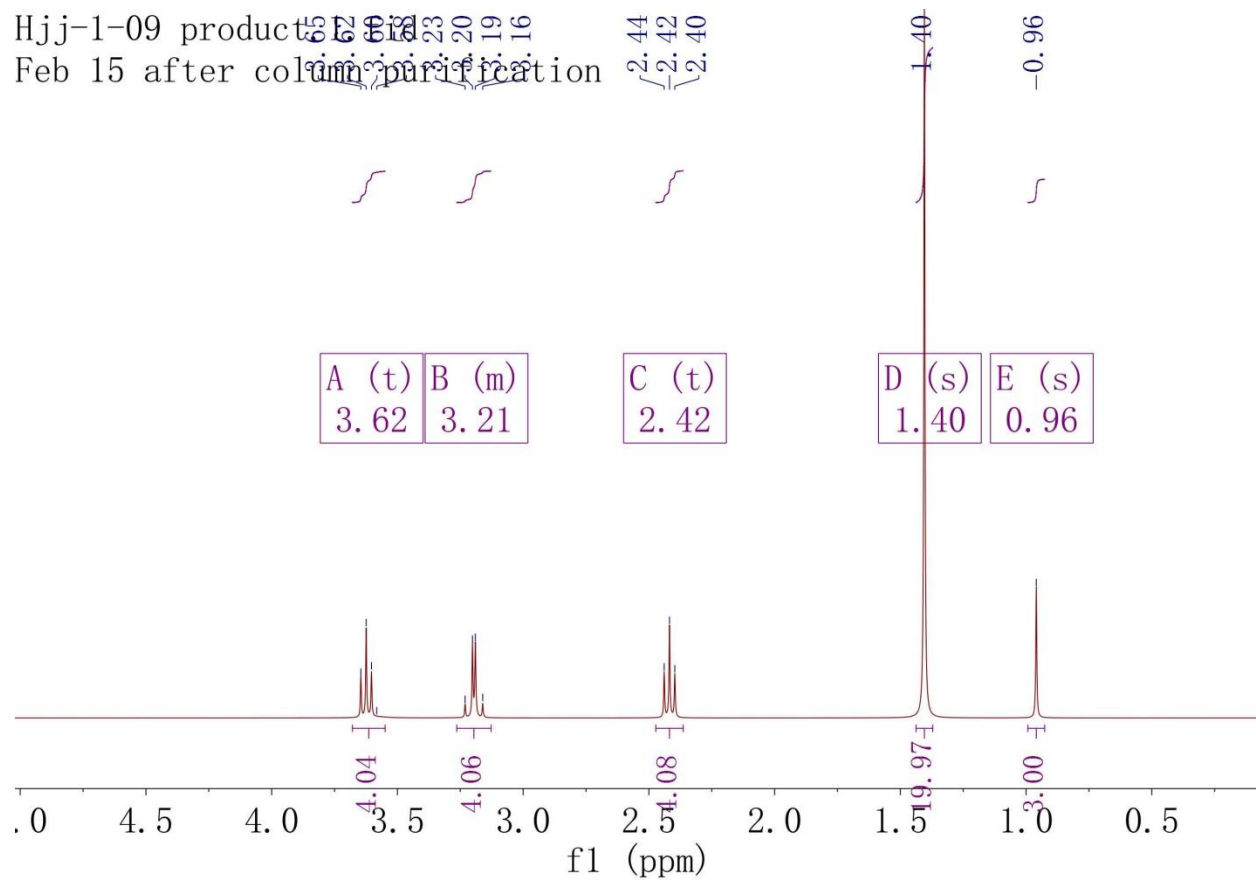


Appendix 7-1 (product: 2-3)

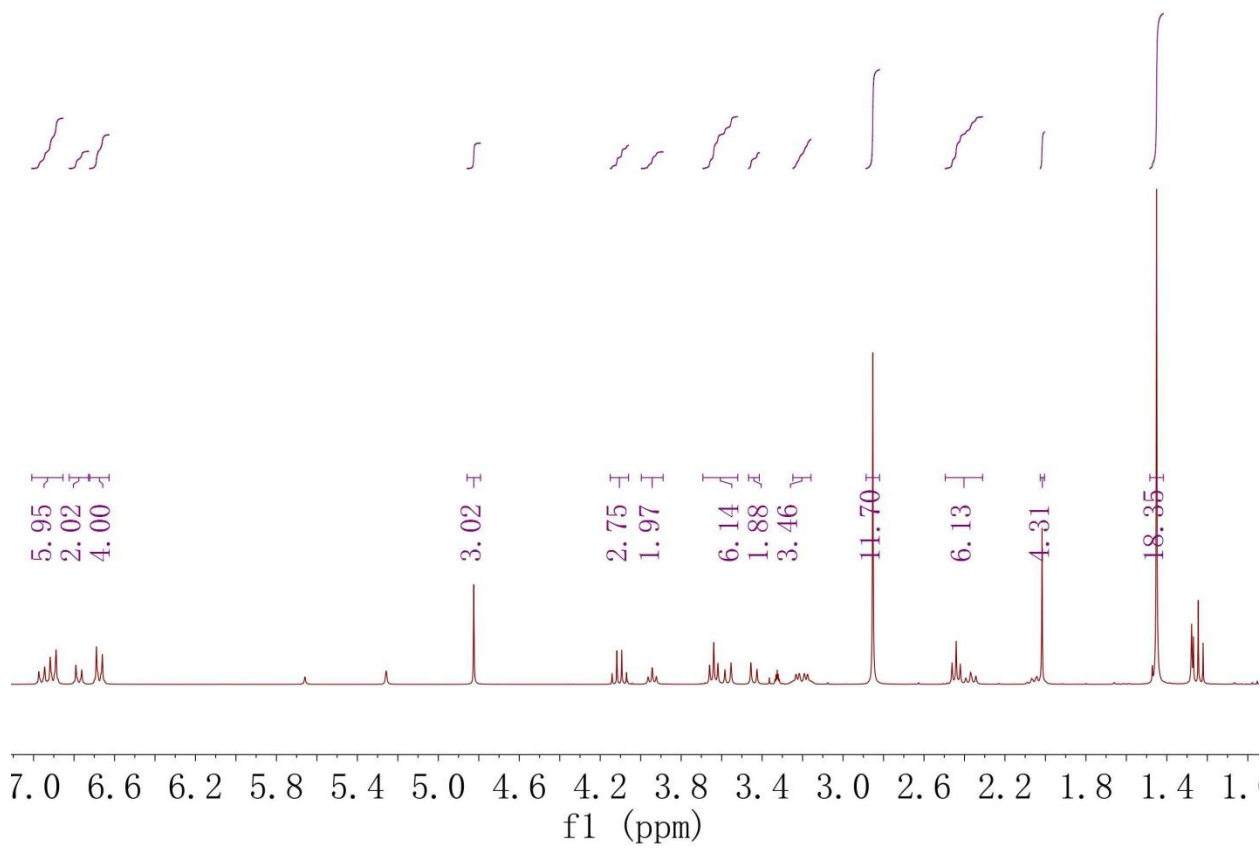


Appendix 7-2 (product: T1)

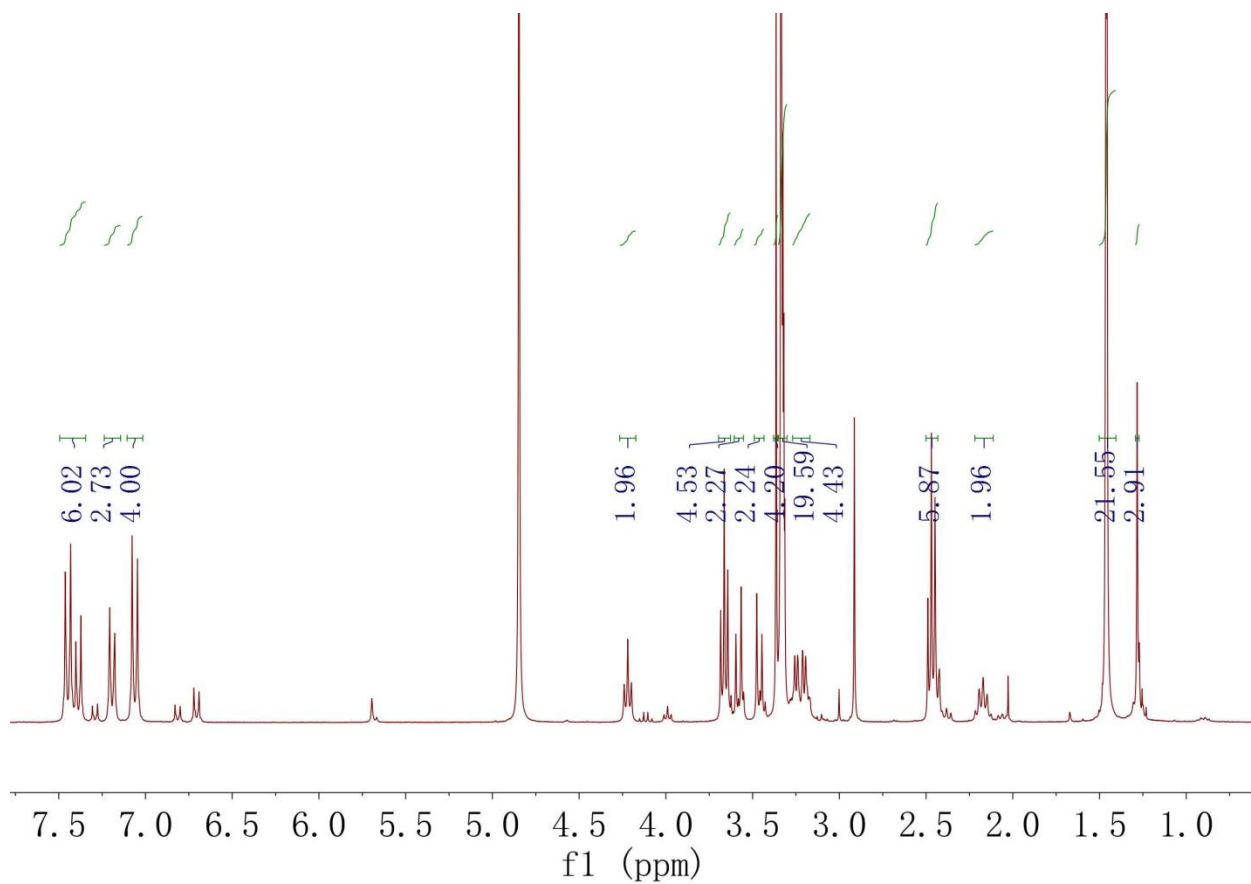
Hjj-1-09 product 2-5
 Feb 15 after column purification



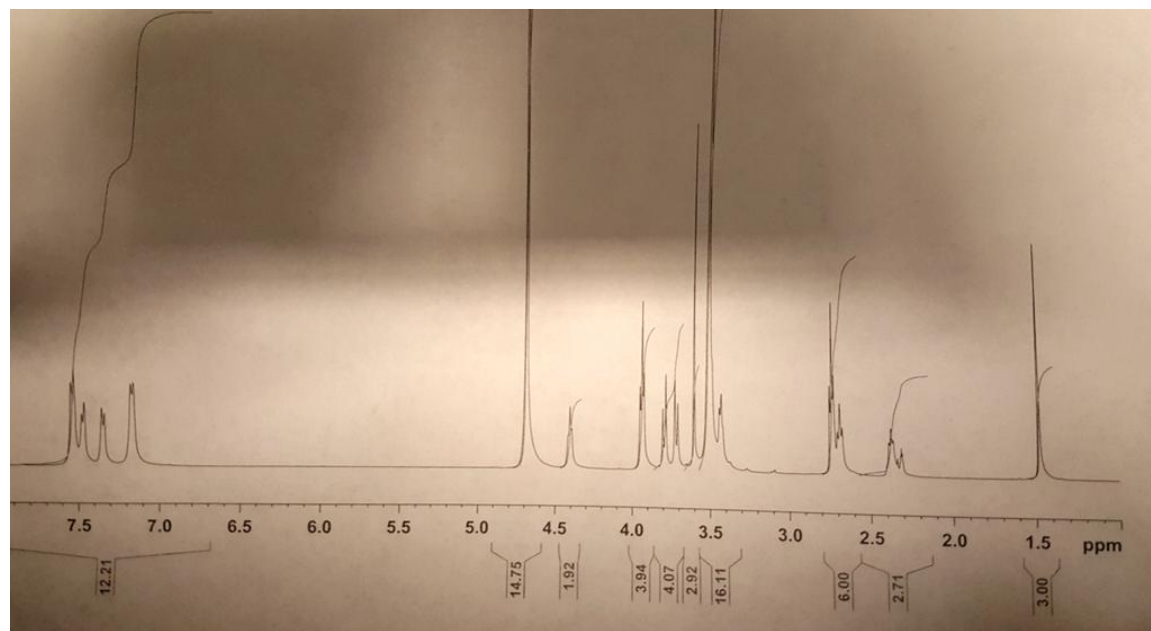
Appendix 7-3 (product: 2-5)



Appendix 7-4 (product: 2-7)

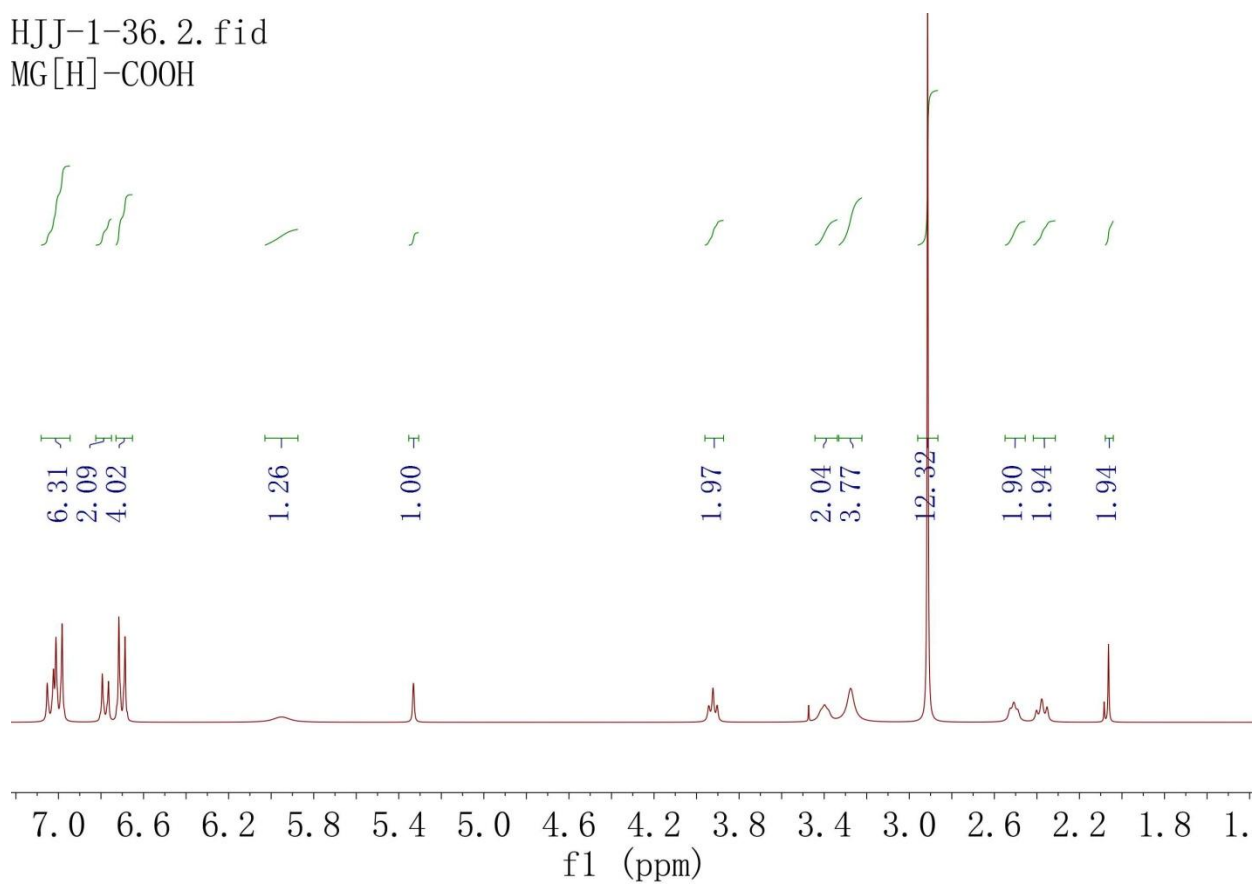


Appendix 7-5 (product: 2-8)

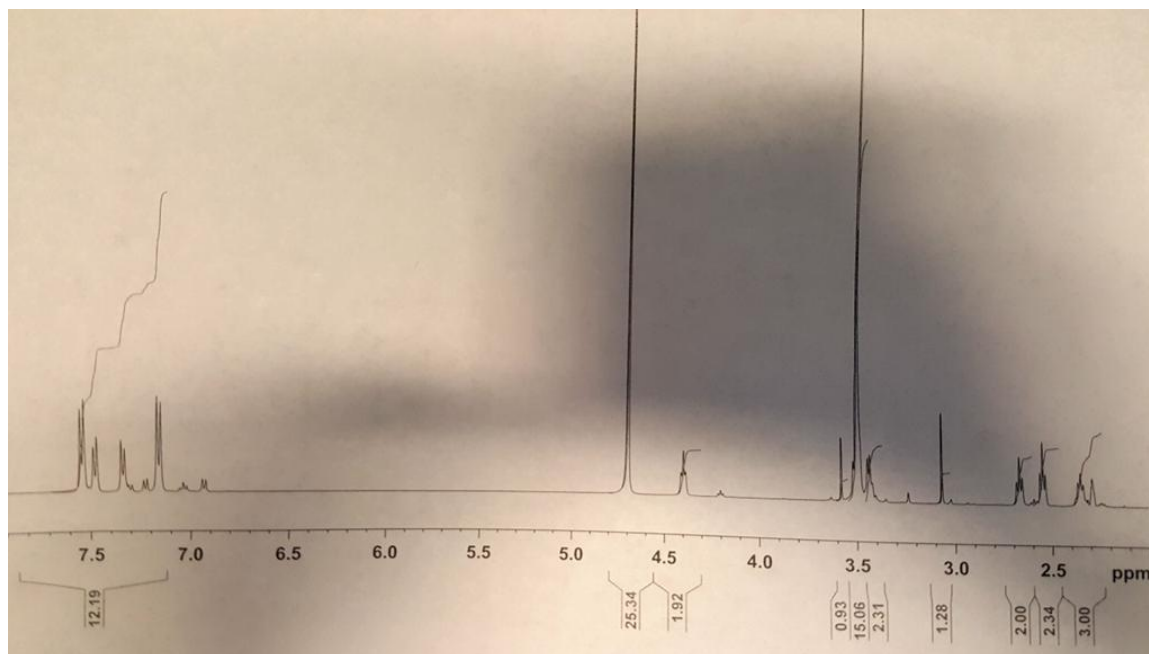


Appendix 7-6 (product: T2)

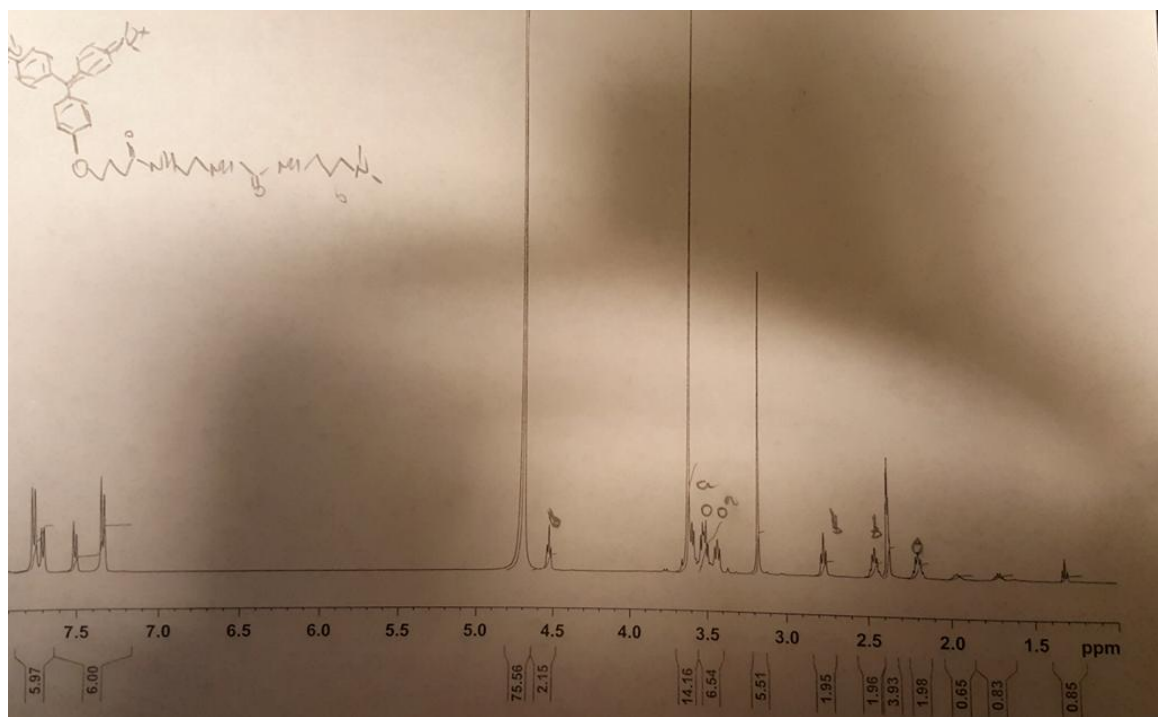
HJJ-1-36. 2. fid
MG[H]-COOH



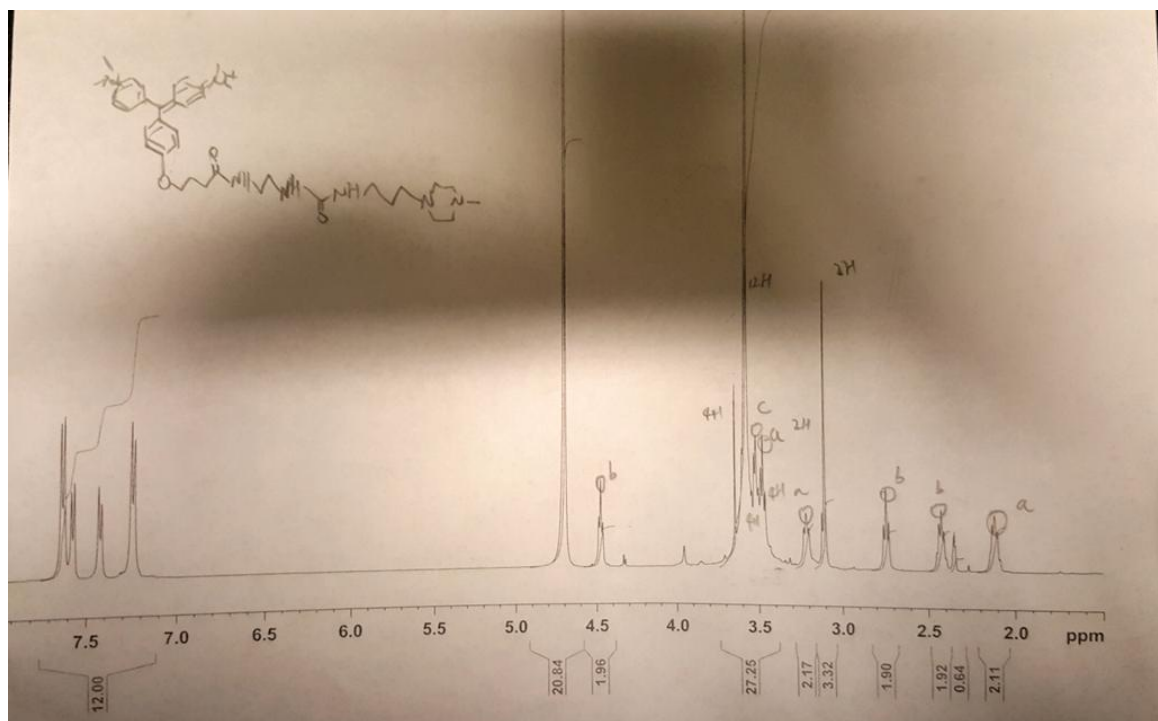
Appendix 7-7 (product: 2-9)



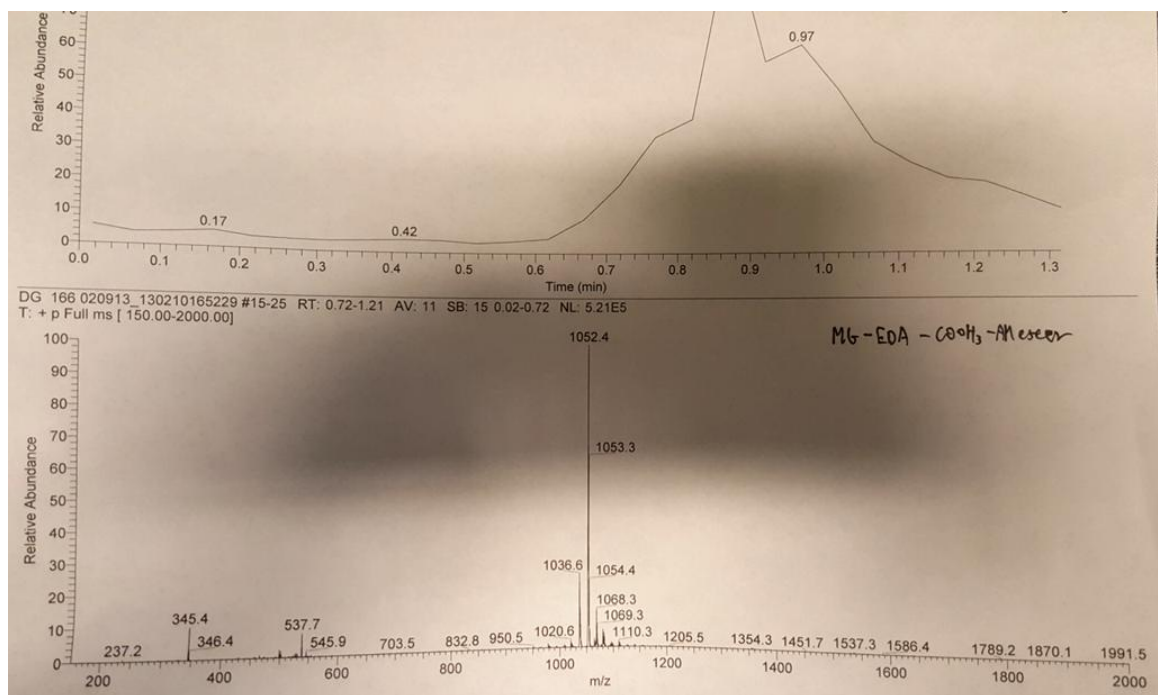
Appendix 7-8 (product: T3)



Appendix 7-9 (product: T4)

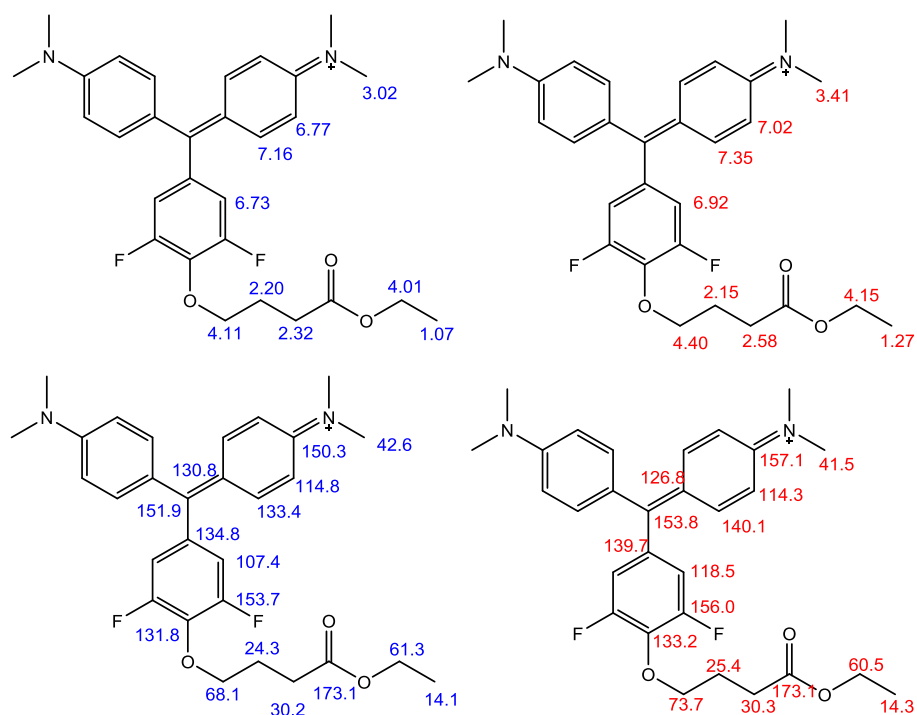
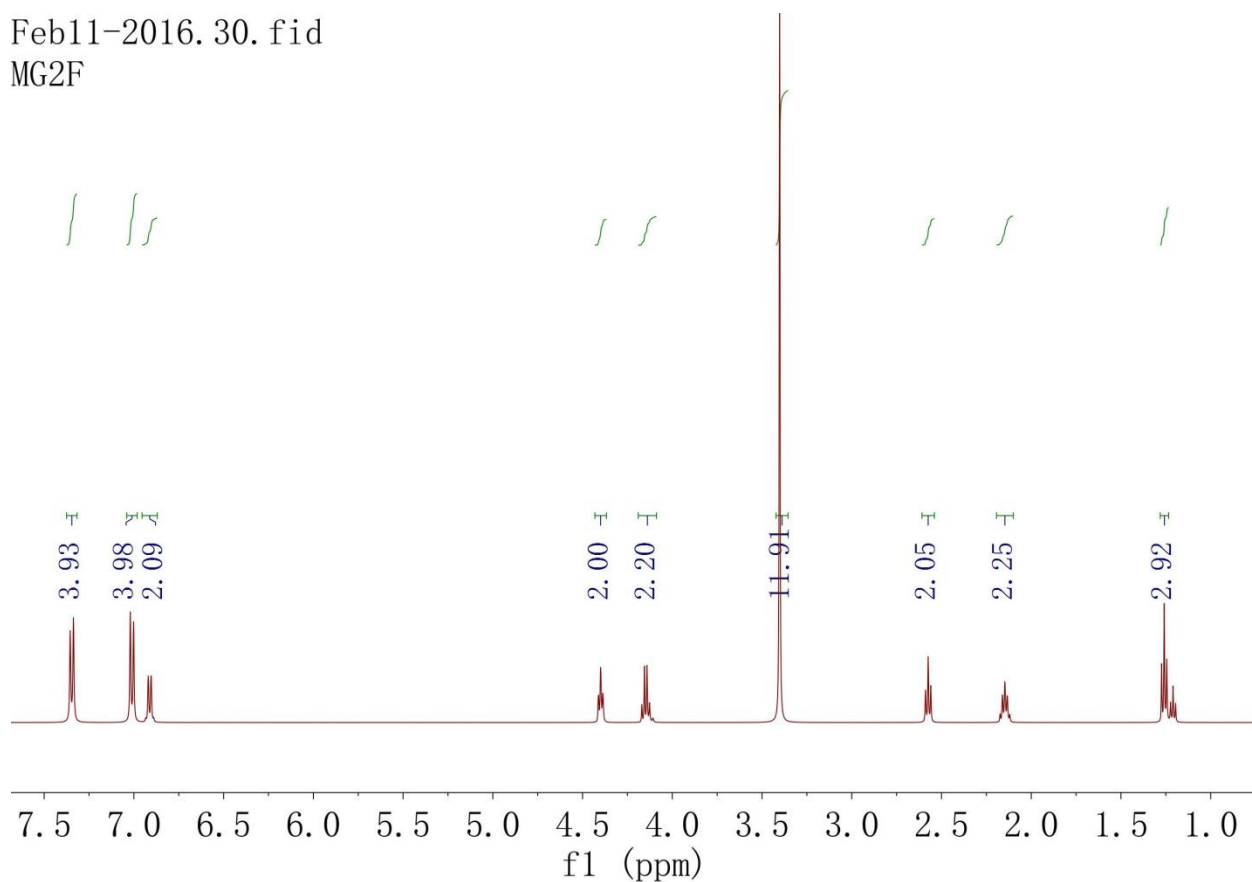


Appendix 7-10 (product: T5)

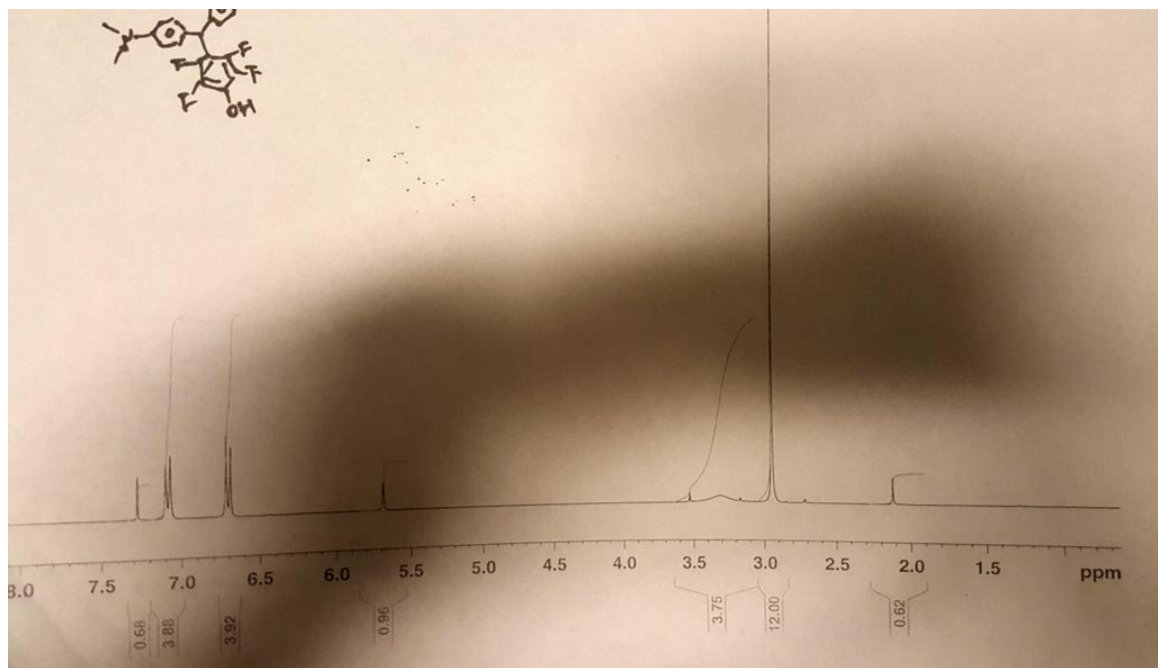


Appendix 7-11 (product: T1-AM)

Feb11-2016. 30. fid
MG2F

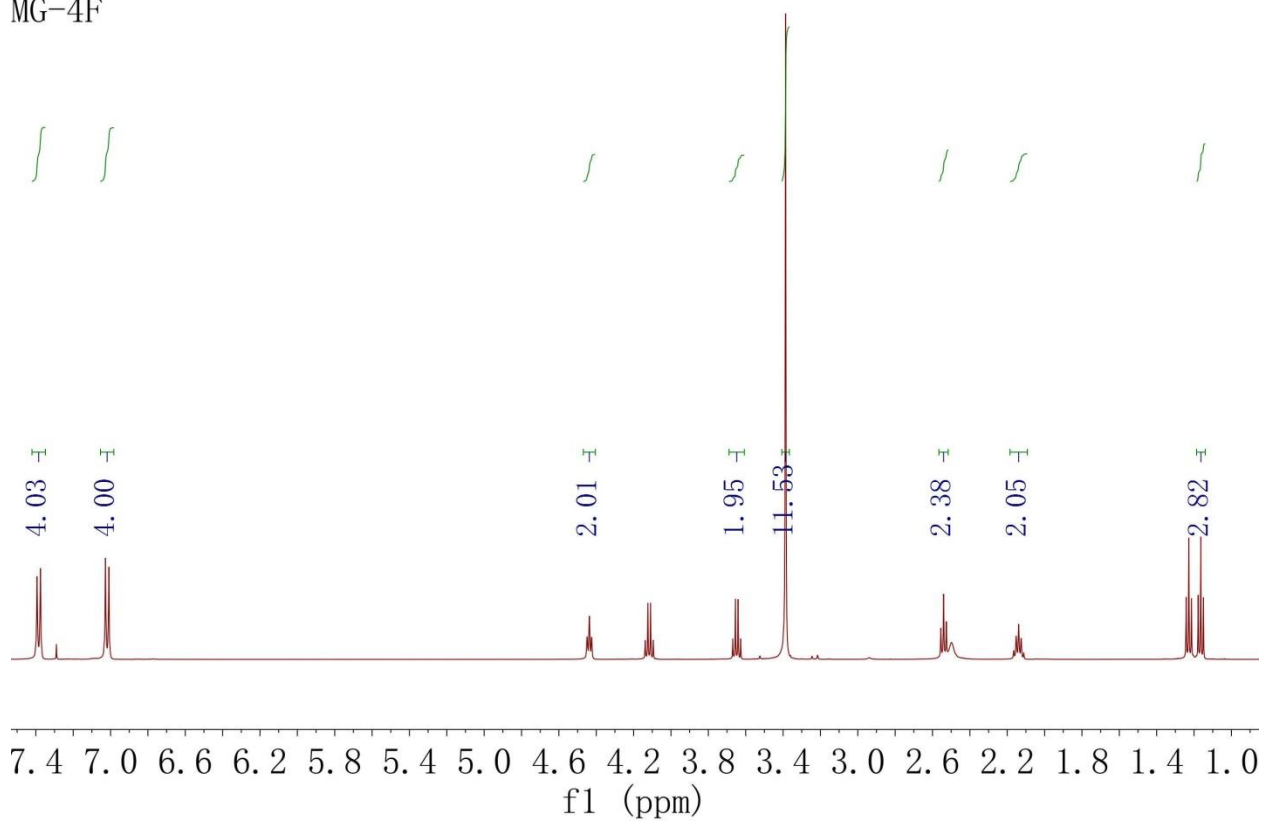


Appendix 7-13 (product: MGF1, predicted ^1H NMR and ^{13}C NMR of MGF1 and obtained ^1H NMR and ^{13}C NMR)

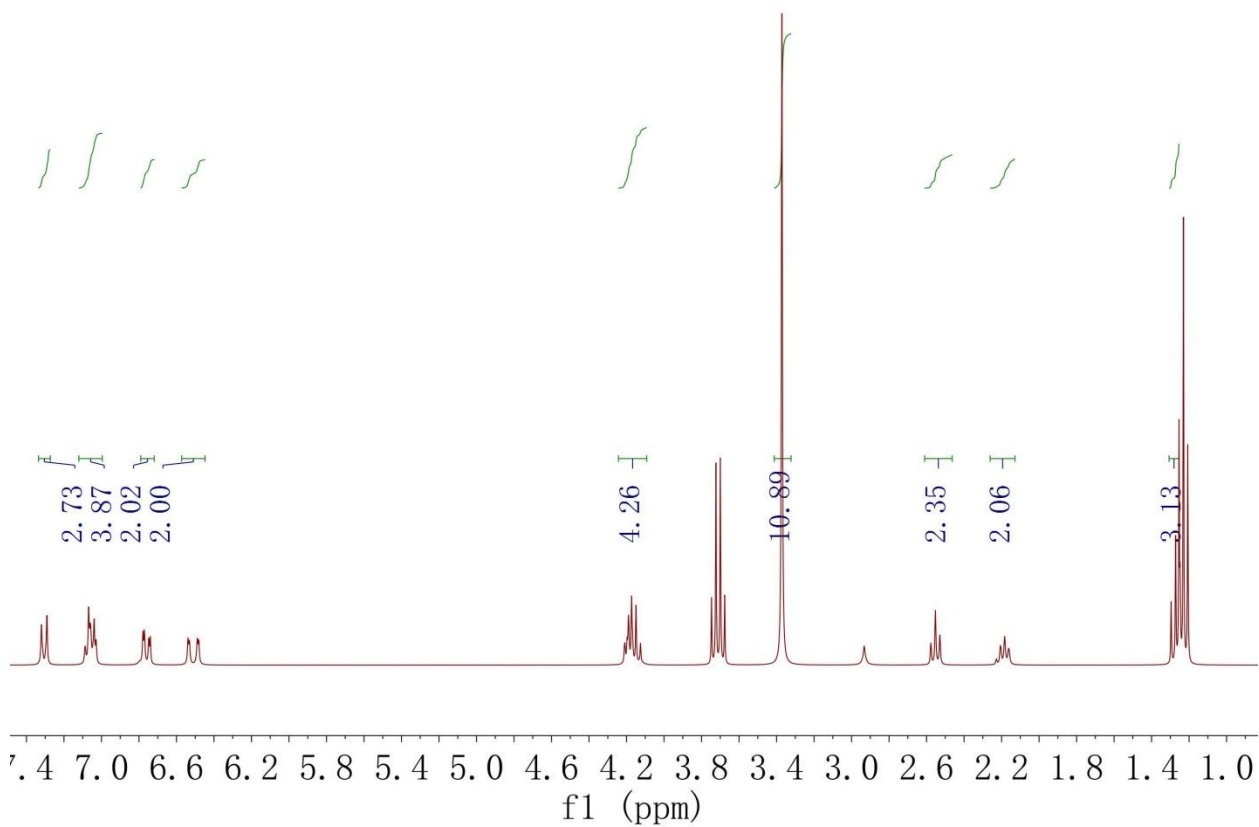


Appendix 7-14 (product: 3-2)

Dec11-2012. 10. fid
MG-4F

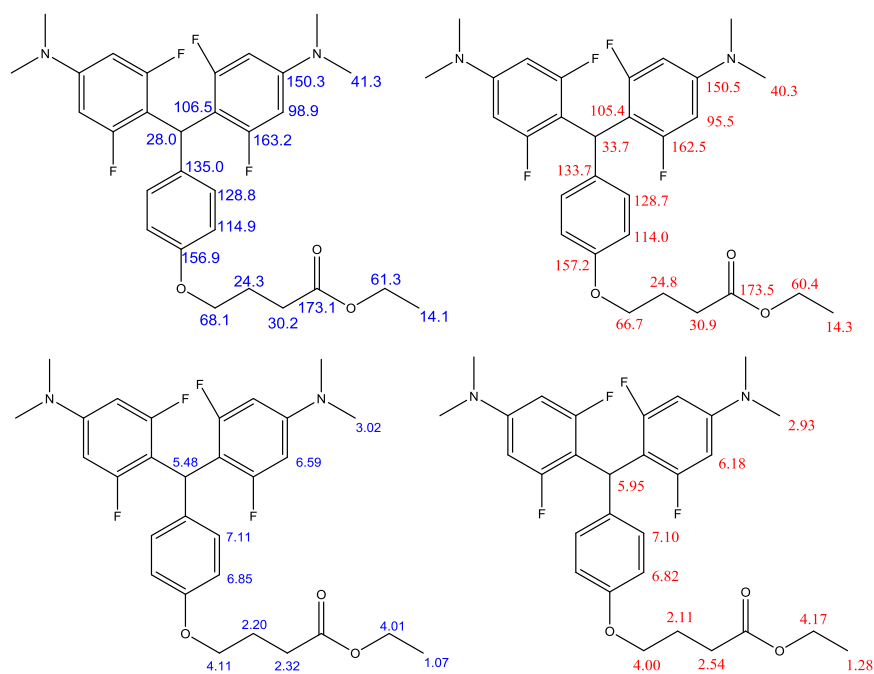
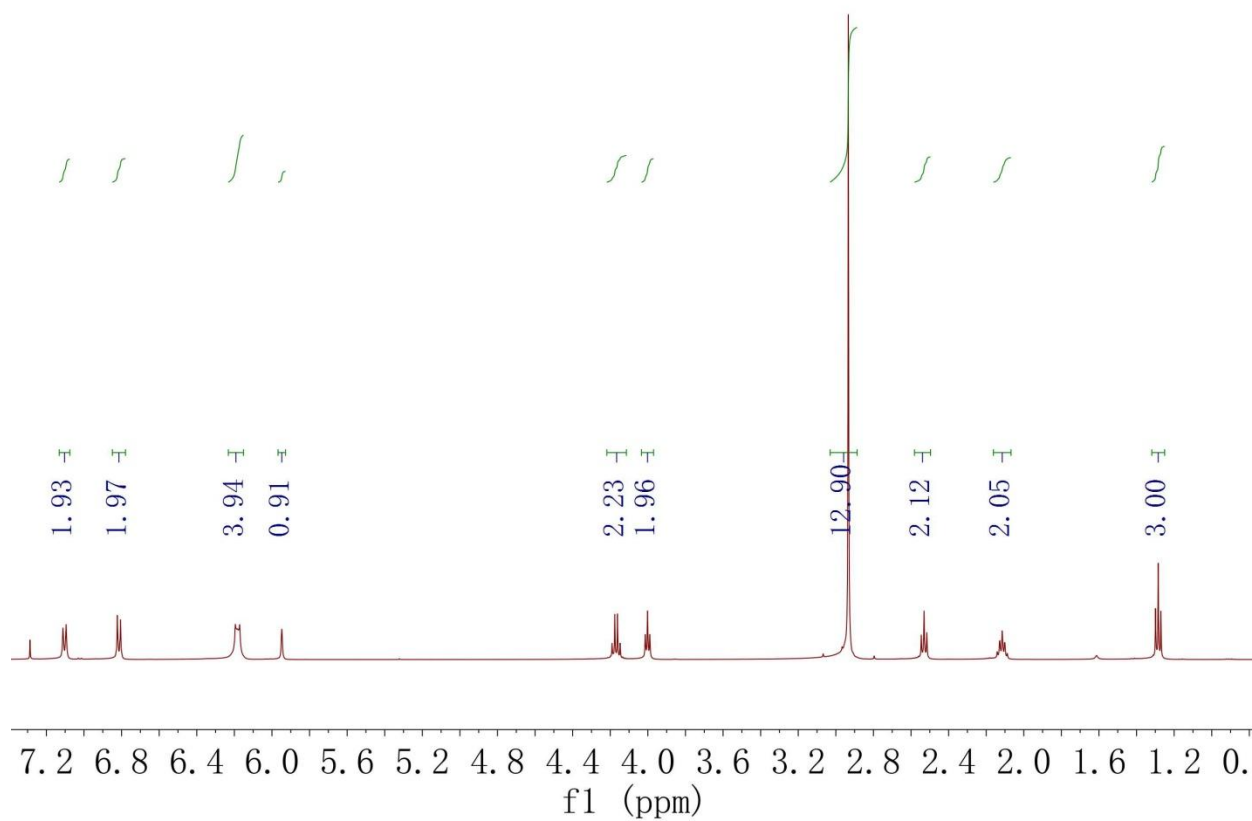


Appendix 7-15 (product: MGF2)

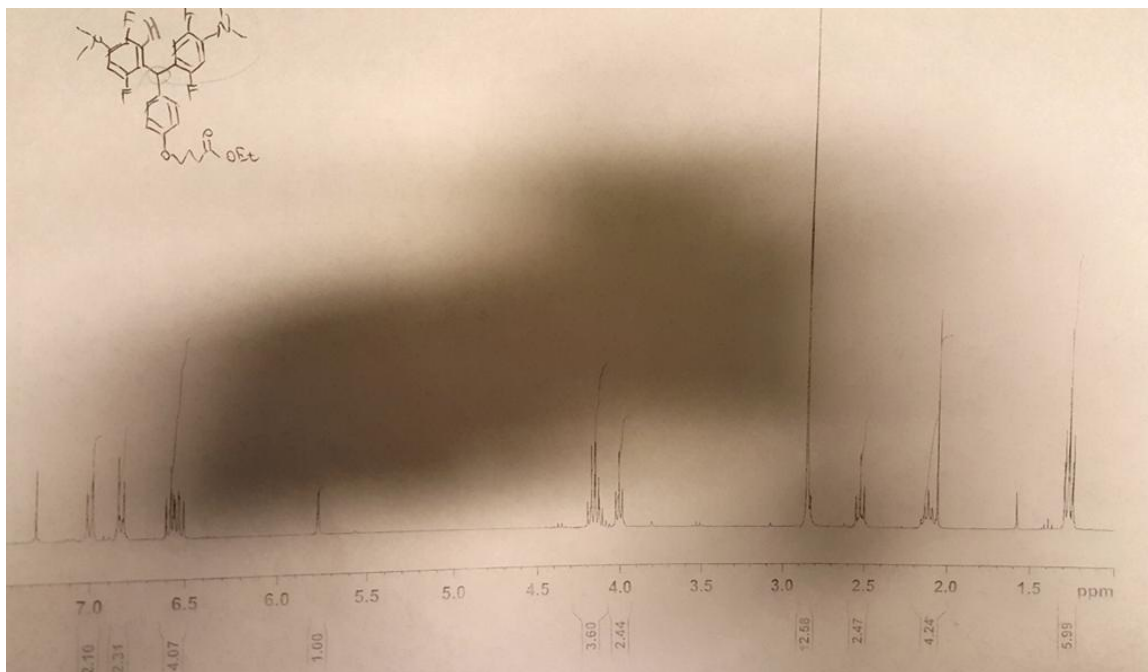


Appendix 7-16 (product: MGF3)

Feb11-2016. 20. fid



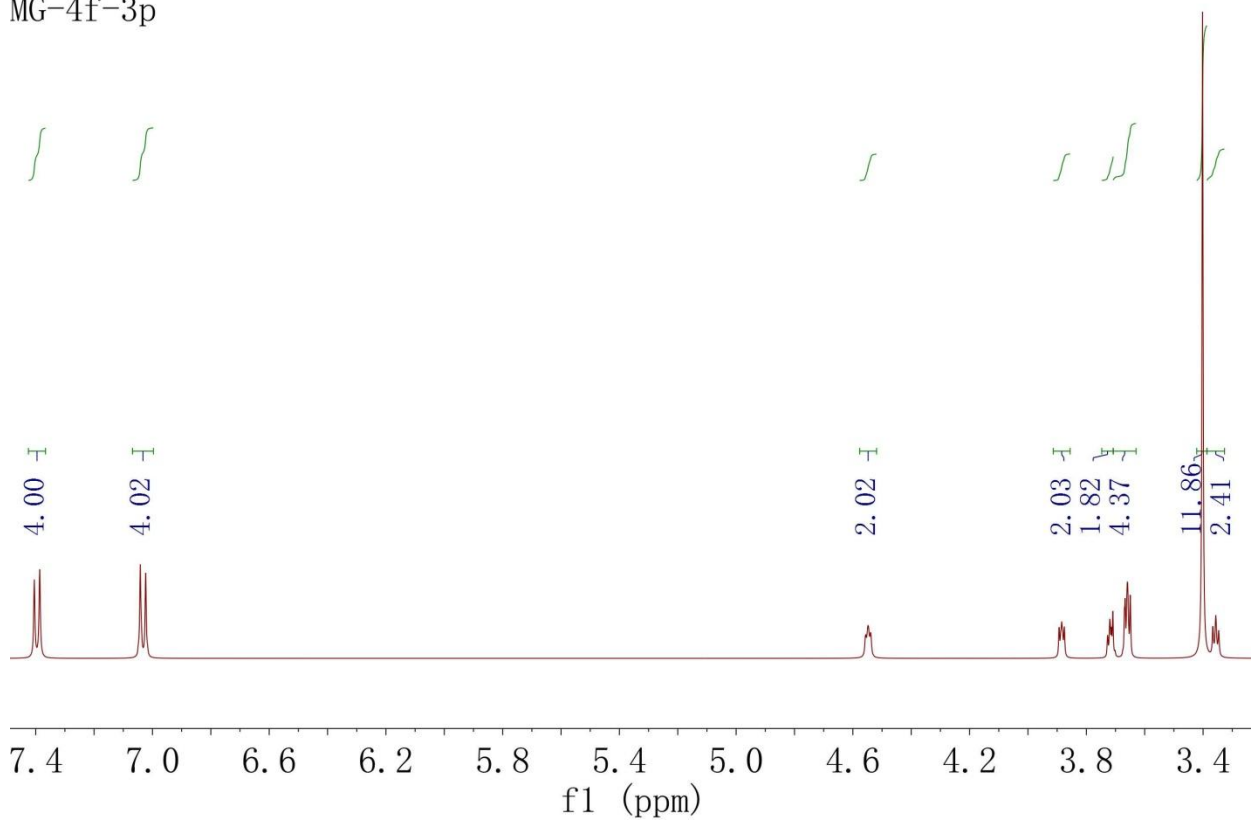
Appendix 7-17: (product: MGF4[H], predicted ^1H NMR and ^{13}C NMR of MGF4[H] and obtained ^1H NMR and ^{13}C NMR)



Appendix 7-19 (product: 3-7)

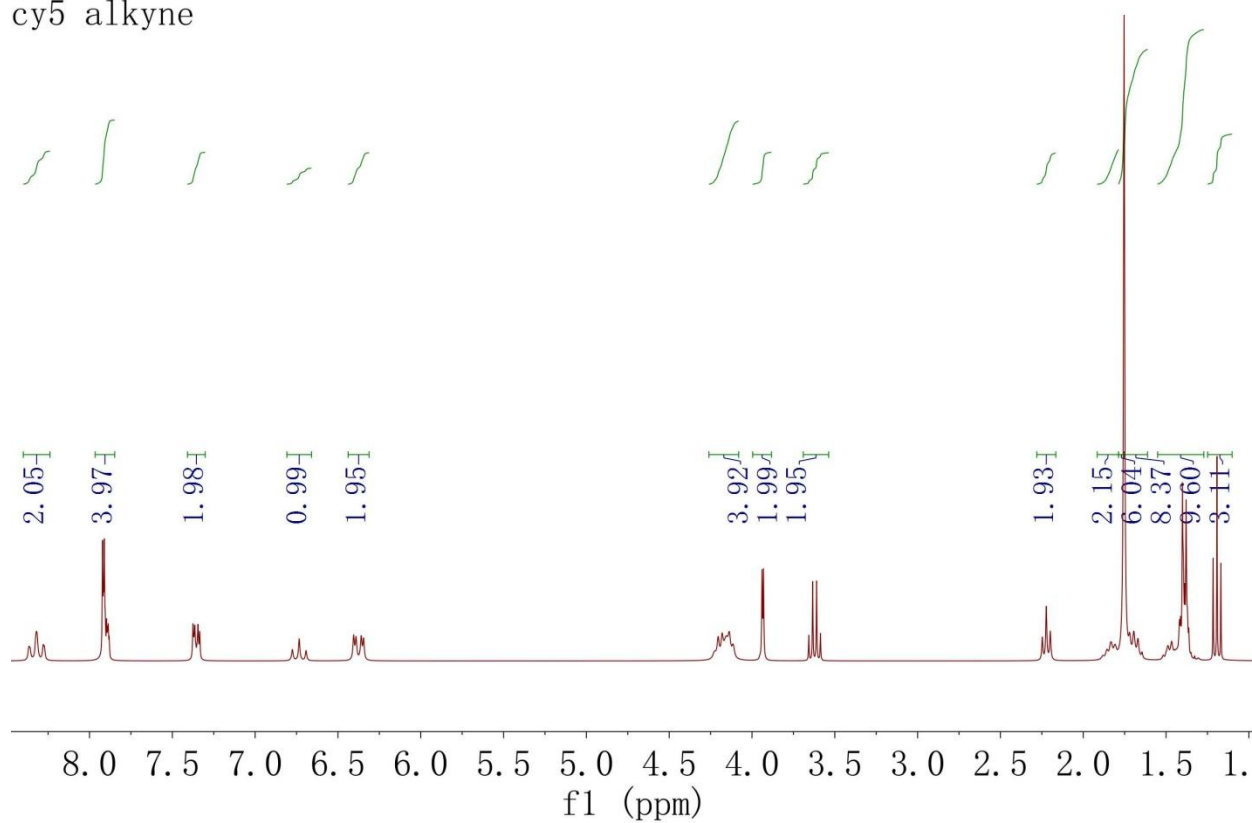
MG4F-3p. 10. fid

MG-4f-3p

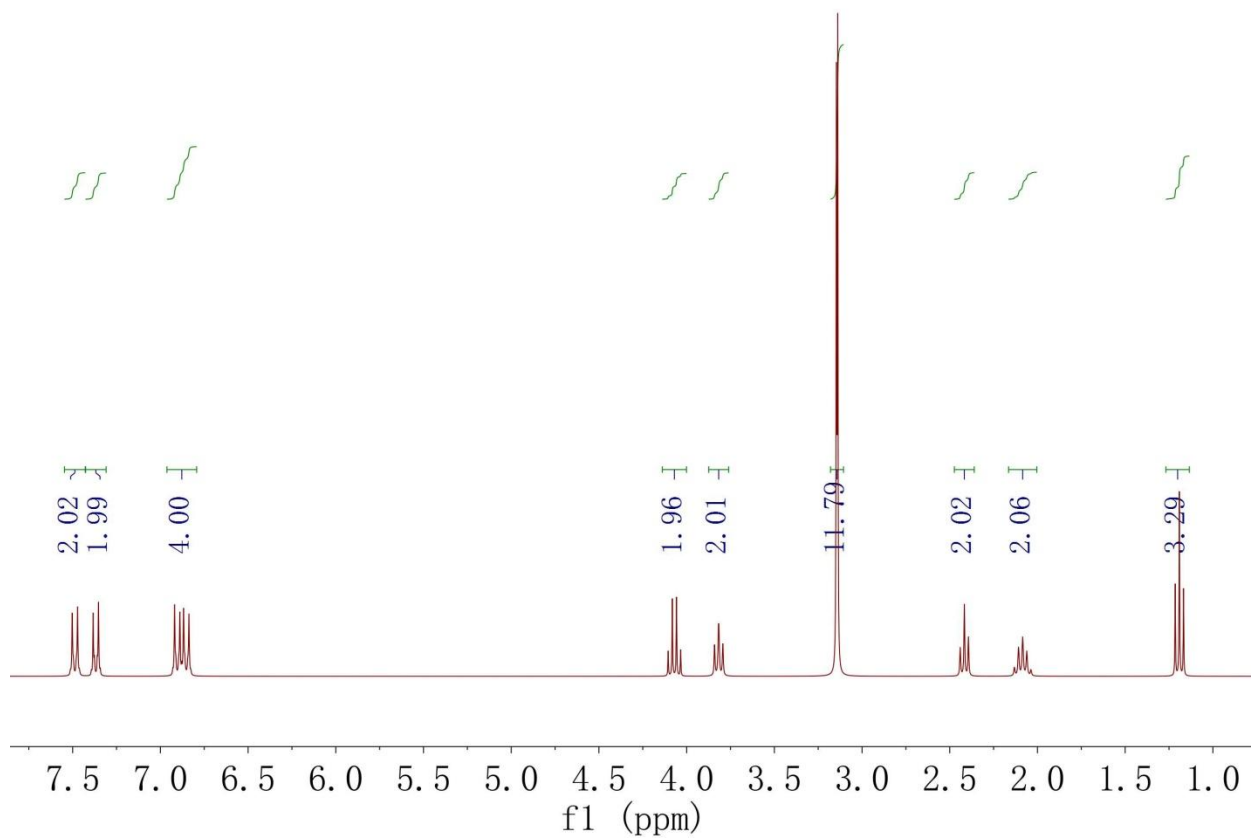


Appendix 7-20 (product: 3-8)

cy5-alkyne. 1. fid
cy5 alkyne



Appendix 7-21 (product: 3-10)



Appendix 7-22 (product: MHN-ester)